Advanced beam shaping for spatially fractionated proton beam therapy

Fardous Reaz

Thesis submitted for the degree of

Master of Science

Department of Physics

Faculty of Mathematics and Natural Sciences

UNIVERSITY OF OSLO

Autumn 2021

Advanced beam shaping for spatially fractionated proton beam therapy

Fardous Reaz

Advanced beam shaping for spatially fractionated proton beam therapy

http://www.duo.uio.no/

Printed: Reprosentralen, University of Oslo

Abstract

External beam radiotherapy (EBRT) is one of the major tools in the arsenal to fight cancer. The main objective of this treatment modality is to utilize the curative potential of ionizing radiation combined with minimal radiation-induced damage to healthy tissue and sensitive organs. Cutting-edge technologies like proton therapy, which exhibits higher dose conformity, have been developed to precisely deposit dose at the tumors. Despite the several advantages of proton beams over photon beams, its performance is still limited when treating small tumors without affecting the surrounding tissue. Using small beam spots at the target can overcome this limitation. Moreover, distinct small spots can be used for fundamental radiobiological studies to reveal the mechanisms of the bystander effect. In addition, narrow beams are also desirable for different proton-based treatment modalities, including GRID therapy.

The primary aim of this work is to develop techniques to produce a narrow beam and small spot to increase treatment efficacy of proton therapy. Based on Monte Carlo simulation, we have assessed three different beam shaping techniques. Metal collimators can produce a narrow beam of protons. However, it can not produce a very small spot at a deep-seated target. The smallest transverse size (σ) of a collimated proton beam at 155 mm depth was more than 1.5 mm observed with a 0.5 mm collimator. The performance could not be improved with smaller collimators. In addition, a narrow collimator reduces the Bragg peak to surface dose ratio by decreasing the dose at the spot. In contrast, a magnetically focused beam of conventional energy could produce a large Bragg peak to surface dose ratio, even though it could not practically further reduce the spot size. Considering high-energy focused beams, our assessment revealed their superiority in producing small transverse spots. This approach can produce a submillimetric spot at 155 mm depth in water.

In our study, the magnetically focused beams produced less than 0.2% of neutrons generated by the collimated beams. It uses the protons produced by the accelerator (much) more efficiently, which enables them to deliver a higher dose rate. We also demonstrate their potential to produce inhomogeneous dose distribution for GRID therapy. Additionally, we developed a novel irradiation modality to deliver high doses at distinct points of a tumor to study immunogenic response of cells.

To produce our proposed magnetically focused beam for experimental validation, an elementary magnetic lattice design was developed. It was found that a suitable combination of quadrupoles can produce the desired focused beams when inserted right after the nozzle of a conventional proton therapy beamline.

From this study, magnetically focused beams therefore appear to be a potentially highly interesting candidate to be implemented in treatment. Due to low losses of accelerated protons, it could facilitate FLASH irradiation. With their ability to deliver a very high dose rate, our proposed irradiation modalities can bring a paradigm change in the current ideas of GRID irradiation.

Acknowledgements

I am sincerely grateful to my esteemed supervisor Erik Adli without whom this journey would not have been possible. His incredible patience, invaluable knowledge, and constant guidance during my Masters helped me complete this work.

I would like to express my sincere gratitude towards my supervisors Eirik Malinen, Kyrre Ness Sjøbæk, and Nina Frederike Jeppesen Edin. Your support and guidance are highly appreciated. Kyrre, thank you for your help in each step of this long journey. Discussion with you has been illuminating and encouraging. Eirik and Nina, your constant feedback, insightful comments, and invaluable suggestions assisted me a lot in improving my work at all phases.

I would also like to appreciate all the supports I have received from Julian Ersland Vevik, Shailendra Bhandari, and Tellef Storebakken. Without you guys, I could not have had all those fun and cherished memories during the program.

Additionally, I would like to extend my sincere thanks to all the members of the Nuclear Physics group who have been very supportive and helped me adapt to my new life here in Oslo, miles away from home.

Contents

List of abbreviations

BK	Bragg-Kleeman (rule)
BP	Bragg peak
CB	Collimated beam
CEFB	Conventional energy focused beam
CSDE	Continuous-slowing-down approximation
c-t-c	Center-to-center (distance)
DADR	Dose-averaged dose rate
DNA	Deoxyribonucleic acid
DSB	Double-strand break
EBRT	External beam radiation therapy
HEFB	High energy focused beam
IDD	Integral depth dose
IORT	Intraoperative radiotherapy
LET	Linear energy transfer
LQ	Linear-quadratic (model)
MAD-X	Methodical Accelerator Design -X
MBRT	Minibeam radiotherapy
MC	Monte Carlo
MCS	Multiple Coulomb scattering
MRT	Microbeam radiotherapy
NTCP	Normal tissue complication probability
PDD	Percentage depth dose
PVDR	Peak-to-valley dose ratio
RBE	Relative biological effectiveness
RF	Radio frequency
RMT	Radiometabolic therapy
ROS	Reactive oxygen species
RT	Radiotherapy/Radiation therapy
SFRT	Spatially fractionated radiation therapy
SOBP	Spread-out Bragg peak
SSB	Single-strand break
TCP	Tumor control probability
TI	Therapeutic index
VHEE	Very high energy electron

List of nomenclature

$\boldsymbol{\alpha}$, $\boldsymbol{\beta}$, $\boldsymbol{\gamma}$	Twiss parameters
$\boldsymbol{D_{Sur}}$	Surface dose
$\boldsymbol{D_{BP}}$	Dose at the Bragg peak/focal point
$\boldsymbol{D_{Peak}}$	Peak dose of GRID irradiation
$\boldsymbol{D_{Valley}}$	Valley dose of GRID irradiation
$\boldsymbol{D_{BP}/D_{Sur}}$	Bragg peak to surface dose ratio
ε	Geometrical emittance
$\boldsymbol{LET_d}$	Dose-averaged LET
$\boldsymbol{LET_t}$	Track-averaged LET
$\boldsymbol{\sigma}$, $\boldsymbol{\sigma_u}$	Transverse beam size
$\boldsymbol{\sigma_{u'}}$	Beam divergence
$\boldsymbol{\sigma_{BP}}$	Transverse beam size at the Bragg peak/focal point
θ_0	RMS value of scattering angles

Chapter 1

Introduction

The term cancer is used to describe a group of diseases that can be initiated at any tissue or organ [1]. It is characterized by the rapid and uncontrolled growth of mutated cells. Cell proliferation and increase in their size are natural processes in growth of tissue [2]. It is regulated strictly in a healthy cell by a complex system of biological signals. Uncontrolled cell growth can lead to cancer, and It has the potential to invade nearby tissue and other parts of the body through the blood and lymphatic systems [3, 4]. Cancers introduced by migrated primary tumor cells are called metastases [5], which are a major cause of cancer-induced death [6]. With over 18 million new cases and 9.6 million estimated deaths in 2018 globally, cancer is the second leading cause of death [7]. Due to the increase in world population and average life expectancy, the predicted global incidence will rise to 27.5 million new cases and 16.3 million cancer deaths by 2040 [8].

Radiotherapy (RT) is one of the most frequently used cancer treatment modalities. More than half of the patients are treated with RT either exclusively or in conjunction with other forms of treatment [9, 10, 11]. X-rays are most commonly used for external beam radiation therapy (EBRT). However, during the last decades, an increasing number of Proton therapy centers have been built, and Norway will get its first proton therapy unit around 2024. The motivation for using proton irradiation is the superior dose profile. In contrast to the exponential drop in the dose profile for x-rays, a proton beam completely stops after having deposited most of the energy in the last few millimeters of its range. This makes it possible to irradiate in front of an organ at risk. In addition, it can limit the irradiated volume of normal tissue with a lesser dose and still ensure a high tumor dose [12]. Thus, proton therapy has higher conformity compared to photon-based therapy.

Irradiation of healthy tissue is inevitable during RT. The radiation-induced toxicity leads to various side effects [13]. It imposes a limitation on the maximum prescribed dose to tumors [14]. Several treatment modalities have been developed to reduce normal tissue damage during RT. Fundamentally, minimization of irradiated volume of normal tissue can lessen the problem. Moreover, normal tissue can tolerate a higher dose and reduce injury if the irradiated volume is small, known

as the dose-volume effect [15, 16]. GRID therapy uses spatially fractionated dose distribution to treat tumors and may also reduce normal tissue complications [17]. The idea of utilizing non-uniform doses to enhance normal tissue tolerance was first reported over a century ago by Alban Köhler [18]. With reduced adverse effects on the normal tissue, this modality permits an elevated tumor dose.

Considering severe post-radiation effects, tumor regression, and local control rates with reduced toxicity, GRID irradiation has proven its potential to supplement conventional homogeneous dose distribution in several clinical experiments [19]. ProGRID [20] studies the effects of a highly inhomogeneous dose on tumors and the corresponding immunogenic response when using proton beams [21]. With small distinct spots of high dose, immunogenic cell death may be induced at the unirradiated points of a tumor. Bystander effects explain this observation [22]. A narrow beam capable of producing high doses at small spots is essential to utilize its advantages.

In addition to GRID RT, a small transverse beam size is also crucial for proton-based microbeam radiotherapy (MRT) [23], minibeam radiotherapy (MBRT) [24], and lattice radiotherapy [25]. It can precisely irradiate a small tumor or metastasis with an enhanced normal tissue sparing. Moreover, it has the potential to treat noncancer diseases like epilepsy [26]. The main objective of this work is to develop suitable beam shaping techniques to generate precise proton beams capable of producing distinct spots at the tumor, and reducing the dose to neighbouring tissues. In addition, we propose a novel irradiation pattern using focused proton beams of conventional (70 MeV to 250 MeV) and higher energy. The techniques are based on well-known accelerator physics from the high energy physics field, applied in an innovative way for proton beam therapy.

Chapter 2

Theory

Radiotherapy (RT) is a multidisciplinary field. It involves several domains of science, including cell biology, radiation physics, radiation biology, and accelerator physics. A clear understanding of all these aspects of RT is a prerequisite to develop and administrate a treatment modality. This chapter introduces the basic principle of RT with a brief review of the components which are essential to our discussions in later chapters. The necessary accelerator physics theory needed to develop advanced beam shaping techniques is also presented.

2.1 Radiation physics

Ionization is the process of acquiring charges in atoms or molecules. Gaining or losing electrons results in an imbalance between the number of protons and electrons of an atom, giving it a net charge. The term ionizing radiation refers to the types of radiation that has the ability to liberate one or more electrons from an atom. The amount of energy needed to break down the bond between a nucleus and the bound electrons is known as the electron binding energy (E_b), commonly called ionization energy. Ionization occurs if the radiation can provide energy equal or more than the E_b of the interacting material. Absorption of smaller energy quanta (less than E_b) can cause excitation of an atom where an electron moves from a lower to a higher energy level

The process of ionization can be classified as direct ionization or indirect ionization [27]. When energetic charged particles of ionizing radiation interacts with an atom through Coulombic forces resulting in emission of an electron, it is denoted direct ionization. In contrast, uncharged particles like photons and neutrons can not directly interact by electrostatic force. However, they can release charged particles through various interactions like photoelectric emission by photons or inelastic scattering of neutrons. These secondary charged particles can initiate further ionization events by Coulombic interactions; this called indirect ionization.

The energy transfer between the radiation and the traversed material depends on various factors, including the charge, mass, and energy of the particles (only energy for photon). The processes

of energy transfer are crucial for RT and dosimetry. The following sections will introduce a brief description of the main processes of interactions between ionizing radiations and materials.

2.1.1 Interaction of photons with matter

The photon is the quanta of energy of electromagnetic (EM) waves. X-rays, as well as γ-rays, are part of the EM spectrum. Thus, their characteristics in a material can be explained using photons' interaction. Even though both are EM waves, they are classified depending on their origin. X-rays can be produced through transitions of orbiting electrons from a higher energy level to a lower energy level. Furthermore, accelerating charged particles can produce x-rays known as Bremsstrahlung x-rays during their period of speed reduction. On the other hand, γ-rays are produced through nuclear de-excitation and annihilations of particle-antiparticle pairs. Independent of their origin, photons interact with matter through the following processes.

Photoelectric effect

In photoelectric emission, photons are absorbed by the atoms of the irradiated target and cause the emission of electrons known as photoelectrons. A part of the photon's energy ($E = h\nu$) is used to break down the bond between the nucleus and bound electron, which is equal to the binding energy (E_b) of the material, and the remaining energy is converted to the kinetic energy (T) of the photoelectrons. According to Einstein's equation of photoelectric emission [28]

$$T = E - E_b. \tag{2.1.1}$$

The ejection of an electron from an inner energy level produces a vacancy that subsequently is occupied by a higher level electron and consequently emits the characteristic x-rays or Auger electrons. The probability of this interaction is directly proportional to the atomic number (Z^4) of the material and inversely proportional to the photon's energy (E^{-3}) [27].

Compton scattering

Within the therapeutic energy range, the Compton scattering is the most frequent interaction experienced by photons in water [29]. Incoming photons interact with atomic electrons as though they were free [30]. To satisfy this condition, the energy of photons must be much larger than the E_b of the material. The interacting photons deliver a fraction of their energy to the electrons. Consequently, their wavelength increases following the interactions. The direction of emitted electrons and secondary photons is governed by the law of conservation of momentum and energy. The cross-section of Compton scattering increases linearly with the electron density of the material.

Pair production

Pair production is a unique process of producing particle-antiparticle pairs (such as electron-positron) from photons. It occurs in an electromagnetic field, commonly close to a nucleus. The

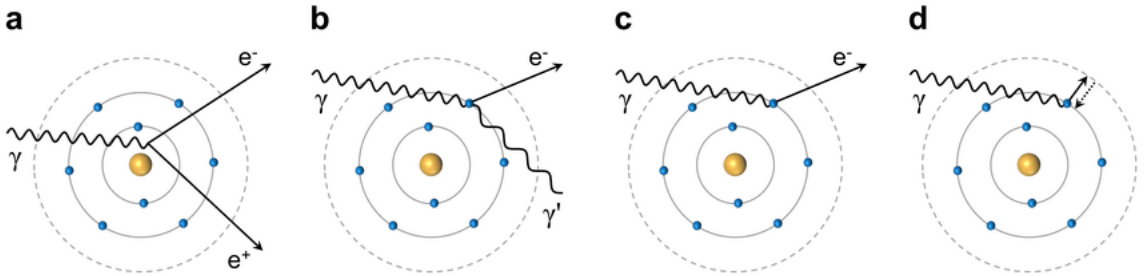

Figure 2.1.1: Interaction processes of photons with matter: Pair production (a), Compton scattering (b), photoelectric effect (c), electronic excitation and de-excitation (d). The figure is taken from Soliman [31].

entire energy of a photon is delivered to create the mass of the pairs and their kinetic energies. Following conservation of energy

$$h\nu = 2m_0c^2 + T_{particle} + T_{antiparticle}, \tag{2.1.2}$$

where m_0 is the mass of the particle (and antiparticle), $T_{particle}$ and $T_{antiparticle}$ are the kinetic energy of the particle and the corresponding antiparticle, respectively [27]. Pair production occurs if the photon's energy is larger than the threshold value, which is equal to $2m_0c^2$. The threshold energy for the electron-positron pair is 1.022 MeV. The kinetic energy of the produced particle and antiparticle can be different. The direction of the particles is governed by the momentum of the photon. If $h\nu \gg 2m_0c^2$, they are emitted with a small opening angle.

Figure 2.1.1 shows the main processes of photon interactions with traversed material. Apart from these, photons can interact through coherent scattering and photonuclear interaction. Atoms as a whole deflect photons in coherent scatterings. This is an elastic interaction and the energy deposited by the photons is negligible. They are deflected at a minimal angle, and the atoms receive sufficient energy to keep the momentum conserved. It is not relevant for radiotherapy since the interaction process does not deliver energy to the surrounding materials.

In the photonuclear interactions, energetic photons interact with nuclei to emit nucleons (e.g. (γ, p), (γ, n)). The produced protons contribute to the dose through direct ionization. However, the amount of energy delivered by these protons is negligible compared to the competing pair production process. In contrast, neutrons are important in radiation protection as they have higher LET with an extended penetration depth.

2.1.2 Interaction of charged particles with matter

Unlike photons, charged particles can interact with electrons and nuclei of the traversed material through Coulombic forces. These interactions have two distinct impacts on the particles. Firstly, the energy of the particles decreases through collisions. The lost energy is transferred to the surrounding materials. Secondly, the collisions can deflect the particles from their initial direction of

propagation, causing random scattering of the particles.

In a passage through a material, charged particles can interact with the orbiting electrons. These inelastic collisions are mostly responsible for the energy loss. They also interact elastically with the atomic nuclei. These collisions lead to the scattering of the particles. As the mass of the nuclei is usually very large compared to the projectile charged particles, the amount of energy loss through the Coulombic interactions with nuclei is insignificant.

Additionally, charged particles also experience nuclear reactions and radiative energy loss. Even though the radiative losses like Bremsstrahlung and Cherenkov radiation are possible modes of energy loss, they are very unlikely within the therapeutic energy range for protons [32, 33].

Inelastic Coulombic scattering

The inelastic Coulombic scattering is the most frequent interaction process of charged particles in a material. These interactions with orbiting electrons can transfer energy to the surrounding material, leading to ionization and excitation of the atoms. The amount of energy delivered through a collision is very small; however, the large electron density causes many collisions producing a significant cumulative energy loss. As a consequence of these interactions, the kinetic energy of the particles decreases, which can be considered a quasi-continuous process. In addition to energy loss, these collisions can cause deflection of the charged particles from their original direction of propagation. However, due to the larger mass of protons (approximately 1832 times of electron mass), the deflection is negligible, and they follow almost a straight path. Contrarily, electrons are scattered prominently, which impacts their depth-dose profile.

Considering the interactions' impact parameter, the distance of closest approach for the projectile following its initial trajectory, inelastic scatterings can be classified into two groups: Soft- and hard collisions. If the impact parameter of charged particles is considerably larger than the radius of the atom, they usually interact with the atom as an entity. This interaction is called soft collision, which leads to atomic excitation or ejection of valence electrons. In contrast, an impact parameter smaller than the atomic radius leads to hard collisions. The charged particles interact with individual orbiting electrons and cause ionization through their ejection. These ejected electrons, known as delta rays (δ-ray), carry away a considerable amount of energy from the interaction point. They have the potential to causes further ionization and excitation through Coulombic interactions. The path of energy dissipation of a δ-ray is different than the path of the primary charged particle from hence it originated. The largest possible energy transfer to a stationary electron by a charged particle can be expressed as

$$E_{\delta}^{max} = 2m_e c^2 \frac{\beta^2}{1-\beta^2}\left[1 + 2\frac{m_e}{M}\frac{1}{\sqrt{1-\beta^2}} + \left(\frac{m_e}{M}\right)^2\right], \tag{2.1.3}$$

where m_e and M are the mass of an electron and charged particle, respectively, and β is the speed

of the charged particle in units of the speed of light (c) [32]. For a proton of energy E_p, it can be approximated as

$$E_{\delta}^{max} \approx \frac{E_p}{500}. \tag{2.1.4}$$

Following equation 2.1.4, the maximum energy of electrons produced by a 250 MeV proton beam is about 500 keV, and the corresponding range of δ-ray from a proton track is about 2.5 mm. Usually, most of the electrons have energy far below 300 keV, with a range of less than 1 mm [34]. This information is crucial for determining the "production cut" (discussed in chapter 3) and the accuracy of the spatial dose distribution of a proton beam.

Multiple Coulomb scattering

In their passage through a material, charged particles like protons also interact with the atomic nuclei. As we mentioned before, these Coulombic interactions cause deflection of the particles from their initial direction of propagation. The observed angular dispersion of the particles can be explained using the cumulative effect of several interactions. This is known as Multiple Coulomb scattering (MCS).

The positive charge of protons and the nuclei are responsible for the frequent electrostatic repulsive interactions. Each of these interactions causes a slight deflection of charged particles, and the resulting effect can be described in a statistical formulation. For small deflections, the distribution of the scattering angles can be approximated as a Gaussian function. Several theories have been developed to explain and quantify the MCS. Among those, Moliere's theory provides a complete explanation [35]. The Moliere's characteristic multiple scattering angles (θ_M), which is analogous to the mean scattering angle, can be expressed as

$$\theta_M = \frac{1}{\sqrt{2}}(\chi_c\sqrt{B}), \tag{2.1.5}$$

where χ_c is the characteristic single scattering angle and B is the reduced target thickness. The physical interpretation of χ_c is that, on average, a proton suffers exactly one single scatter greater than χ_c in its traversal of the target. For a projectile of charge number z, the characteristic single scattering angle in a target of atomic number Z can be written as

$$\chi_c^2 = c_3 t/(pv)^2, \tag{2.1.6}$$

where p and v represent the momentum and velocity of the charged particle, respectively. The constant c_3 can be expressed as

$$c_3 = 4\pi N_A \left(\frac{e^2}{\hbar c}\right)^2 (\hbar c)^2 \frac{z^2 Z^2}{A}, \tag{2.1.7}$$

where N_A is Avogadro's number, the fine structure constant $e^2/\hbar c \approx 1/137$, and the conversion factor $\hbar c \approx 197 \times 10^{-13}$ MeV [34]. With the reduced angle

$$\theta^{'} = \frac{\theta}{\chi_c \sqrt{B}}, \tag{2.1.8}$$

Molière approximated the angular distribution function $f(\theta)$ of the proton space angle θ by a power series in $1/B$ as

$$f(\theta) = \frac{1}{2\pi\theta_M^2}\frac{1}{2}\left[f^{(0)}(\theta^{'}) + \frac{f^{(1)}(\theta^{'})}{B} + \frac{f^{(2)}(\theta^{'})}{B^2} + \cdots\right], \tag{2.1.9}$$

where

$$f^n(\theta) = \frac{1}{n!}\int_0^\infty y\, dy J_0(\theta^{'} y) e^{\frac{y^2}{4}} \left(\frac{y^2}{4}\ln\frac{y^2}{4}\right)^n. \tag{2.1.10}$$

The function $f^0(\theta^0)$ is a Gaussian

$$f^0(\theta^0) = 2e^{-\theta^{'2}}. \tag{2.1.11}$$

Even though Molière's theory can accurately estimate charged particle scattering, it is mathematically complicated. For many applications, it is sufficient to use Highland's simplified formula [36], which is derived through parameterizing Molière theory. According to Highland's formula, the standard deviation of the angular spread is given by

$$\theta_0 = \frac{14.1 \text{ MeV}}{pv} Z_p \sqrt{\frac{d}{L_R}}\left[1 + \frac{1}{9}\log_{10}\left(\frac{d}{L_R}\right)\right] [\text{rad}], \tag{2.1.12}$$

where d is the distance traversed through the material, and L_R is a constant depending on the material, called radiation length. It is defined as the mean length of a material to reduce the energy of a charged particle by a factor of $1/e$ [37]. The L_R of liquid water is 36.08 g cm^2 or 39.31 cm [38]. The value of θ_0 varies inversely with the velocity (v) of the charged particles. Thus, it gets larger around the end of the range of a beam, where its energy is lower. This feature can be evident in figure 2.1.2. The lateral spread of a beam of heavier particles is less pronounced. Comparing beams with the same range in water, the angular spread of a proton beam is three times larger than a carbon ion beam. The use of heavy ions is thus of clinical relevance for treatments near organs at risk, allowing a safer approach to sensitive structures.

Radiative losses

A charged particle produces Bremsstrahlung x-rays when it is deflected by an electromagnetic field. It also emits similar radiation during its deceleration phase inside an obstacle. As mentioned earlier, the large mass of protons results in less deflection and therefore less Bremsstrahlung radiation. On the other hand, electrons experience large deflection due to smaller mass. It can emit a considerable amount of energy through the radiative loss mechanism.

Moreover, charged particles produce Cherenkov radiation if they travel faster than light in the

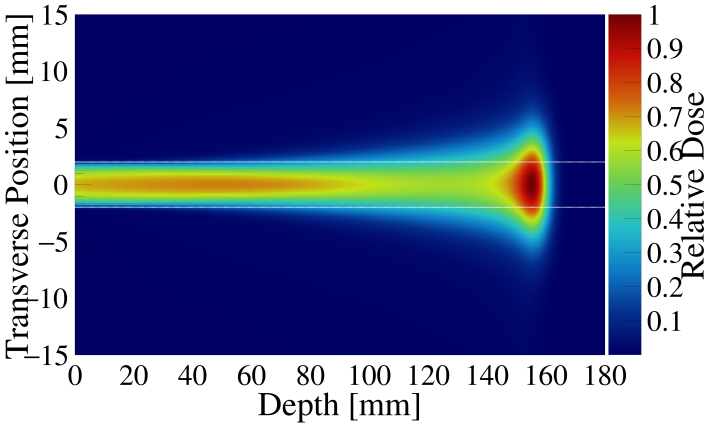

Figure 2.1.2: The two-dimensional dose profile of 150 MeV proton beam shows an enhanced scattering effect and beam broadening at the end of the range. The horizontal white lines shows the initial size (2 mm) of the beam. Dose is normalized to the peak value.

medium [39], such as for electrons in water. In the context of proton RT, it does not have any significant influence.

Nuclear reactions

High energy protons and ions encounter nuclear-nuclear collisions in the traversed material. These interactions have two major impacts. Firstly, it reduces the number of primary particles (defined later in this section). Secondly, they can produce a wide variety of secondary particles, including protons, neutrons, deuterons, tritons, helium nuclei, and heavier ions. These secondaries have a significant contribution to dose deposition and are important to evaluate for radiation protection. The secondary protons in a proton beam therapy contribute around 10% of the total dose, and the total contribution from all other secondaries is not as significant as secondary protons (less than 1%) [32]. Figure 2.1.3 shows the relative contribution of different particles in dose deposition obtained from simulation. In addition, nuclear reactions can produce γ-rays, which can be used for real-time beam monitoring systems [40].

All nuclear reactions can be classified into three groups [34]: elastic reactions, non-elastic reactions, and inelastic reactions. The total kinetic energy of the system remains conserved during the elastic collisions. The target nuclei cause deflection of the projectiles while keeping their internal composition unchanged. In contrast, even though the internal composition of nuclei remains unchanged, inelastic reactions change the total kinetic energy of the system. Non-elastic reactions can lead to the splitting up of interacting nuclei and nuclear excitation. In addition, the particle transfer reaction where the ejectile differs from the projectile ($X(p,q)Y$) is also non-elastic. Total kinetic energy of the system no longer remains conserved. The primaries and secondaries can be classified on the basis of interaction experienced by the particles. The term primary is used to refer to the particles which are part of the original beam. These particles can keep their identity unchanged by taking part in scattering interaction with electrons or elastic interaction with nuclei. However, in-

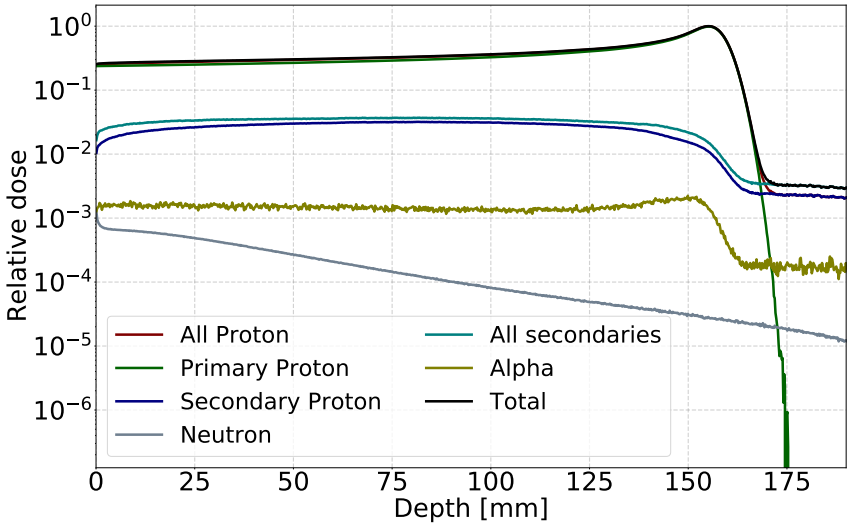

Figure 2.1.3: Depth-dose profile of 150-MeV proton beam in water. The Contribution of all other secondaries except the secondary protons is insignificant. The dose is normalized respect to the maximum value of the total deposited dose.

elastic or non-elastic interaction of particles with nuclei produces secondaries [41]. In the process of these reactions, a compound nucleus is formed before producing the products. Even the compound system ejects a proton by absorbing a primary proton $(X(p,p')X)$; the ejected proton is classified as secondary because it is not possible to distinguish between two protons of a compound system.

Simultaneously, inelastic and non-elastic nuclear interactions reduce the primary beam fluence, as shown in figure 2.1.4a. The initial energy of the beam has an impact on the fluence at the target (end of the range), as shown in figure 2.1.4b. The fragmentation of the projectile is also responsible for the depletion of the primary beam. The production of secondaries increases with depth up to the position of the Bragg peak; afterwards, it decreases [42].

2.1.3 Stopping power

Coulombic interactions are responsible for transferring most of the charged particles' energy to the traversed material, causing the particles to stop eventually. The average energy loss per unit path length through these interactions is defined as electronic stopping power (S). The more commonly used quantity is called mass stopping power (S/ρ), which is defined as the amount of energy loss per unit distance and per unit density of the material. It can be expressed as

$$\frac{S}{\rho} = -\frac{dE}{\rho dx}, \tag{2.1.13}$$

where E is the mean energy loss and x is the distance traveled by the charged particles through a material of density ρ. Here, several mathematical formulae have been developed to calculate (S/ρ) of charged particles. A simplified formula based on Bragg and Kleeman (BK) [43] rule can estimate

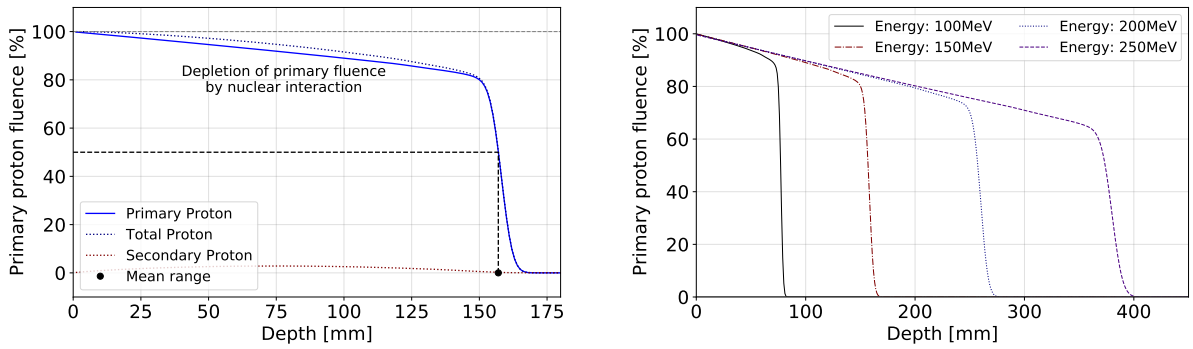

(a) (b)

Figure 2.1.4: The fluence of protons as a function of depth in water. (a) Compares the depletion of total, primary and secondary proton fluence as a function of depth of 150 MeV beam. The mean range corresponds the half of the initial primary fluence of the beam. (b) Compares the primary fluence of different energies as a function of depth.

S/ρ with a significant precision. According to the formula, the mass electronic stopping power is

$$\frac{S}{\rho} = -\frac{E^{1-p}}{\rho \alpha_c p}, \tag{2.1.14}$$

where α_c is a material depending constant and p is a constant depends on the beam energy [32]. This equation can determine S/ρ of proton beam with a high accuracy. The experimental or theoretical data of energy and corresponding ranges of the proton beam in a material can be used to obtain the values of constant[1] α_c and p. These values can also be obtained by fitting the experimental stopping power data of proton beam.

Niels Bohr developed a more physically significant relation based on the impact parameter [44]. He used the classical concept of impulse to formulate the stopping power. Following his classical formula, stopping power can be expressed as

$$-\frac{dE}{dx} = \frac{4\pi z^2 e^4 N_e}{m_e v^2} \ln\left[\frac{\gamma^2 m v^3}{z e^2 \bar{\nu}}\right]. \tag{2.1.15}$$

c:	Speed of light in vaccum	N_e:	Electron density
γ:	$\frac{1}{\sqrt{1-\beta^2}}$	β:	$\frac{v}{c}$ for incoming particle
v:	Velocity of incoming particle	m_e:	Electron mass
$\bar{\nu}$:	mean frequency of electron	ze:	Charge of incoming particle

In this relation, the interacting atomic electrons are considered stationary, and the deflection of charged particles is ignored. These assumptions are valid for high-energy heavy charged particles. Thus, Bohr's equation can explain the stopping power of alpha and heavier charged particles realistically.

Including the quantum mechanical effects of inelastic interactions, Hans Bethe and Felix Bloch

[1]Usually labeled with α, we used α_c to avoid conflict with the Twiss parameter α.

developed a more accurate formula for high-energy charged ions [44]. Instead of the impact parameter, their calculations were based on momentum transfer during the collision, a measurable quantity that can provide a more realistic result. The relation is known as the Bethe-Bloch formula, which describes the mass electronic stopping power of high-energy ions in a material [44] as

$$\frac{S}{\rho} = -\frac{dE}{\rho dx} = 2\pi N_a r_e^2 m_e c^2 \frac{Z}{A}\frac{z^2}{\beta^2}\left[ln\frac{2m_e c^2\gamma^2\beta^2 W_{max}}{I^2} - 2\beta^2 - \delta - 2\frac{C}{Z}\right]. \tag{2.1.16}$$

A:	Atomic weight of matter	N_a:	Avogadro's number
ρ:	Density of matter	r_e:	Classical electron radius
δ:	Density correction	W_{max}:	Maximum energy transfer in a single collision
C:	Shell correction	Z:	Atomic number of matter
I:	Mean excitation potential	z:	Charge of incoming particle in e

Charged particles produce an electric field around their path of propagation, which can polarize the surrounding atoms. As a result, remote electrons are shielded from the actual electric field strength and experience a lower net Coulombic force. At higher energy, distnance collisions are the significant contributors to the stopping power. Thus, the inclusion of the density correction factors δ is crucial for the high-energy beam. Simultaneously, the density of the materials impacts δ since the polarization effect is more significant for dense materials like metals than low-density gases. However, it is not significant within the clinical energy regime of proton beam therapy.

In addition, the speed of the orbiting electrons is insignificant compared to the charged particles of high energy beam. These electrons can be considered stationary. In contrast, at lower energy, particularly near the end of the track of a particle, this assumption is not valid because the speed of the charged particles is equal or less than the orbiting electrons. Consequently, the Bethe-Bloch formula becomes inconsistent with observation. The shell correction C is included to compensate for the inconsistency with experimental data that is seen at lower energy.

As described by the Bethe-Bloch formula, the energy transfer through Coulombic interactions increases with the charge of the projectile (z^2). In addition, energy loss is more significant for high-Z materials (Z), which causes a smaller beam range in the materials of higher atomic number. Moreover, S/ρ of incident particles varies with velocity following inverse square law. Consequently, energy loss increases at a lower velocity. This feature of the Bethe-Bloch equation explains the unique property of the depth dose profile of hadrons called the Bragg peak, which we will discuss later in this chapter.

The mean excitation potential (I) is a material-dependent quantity, a key parameter of the Bethe-Bloch equation. It is defined as the product of the average orbital frequency of the electrons and Planck's constant ($h\bar{\nu}$). It determines the uncertainty in the range of clinical proton beams. Theoretically, it is a logarithmic average of ν weighted oscillator strength of the atomic levels. The

unknown value of the oscillator strength makes it difficult to calculate I with sufficient precision. Usually, its value is estimated by fitting experimental data for S.

Range straggling

As illustrated in figure 2.1.4, the fluence of primary protons decrease with increasing depth. Following the Bethe-Bloch equation, the stopping power of a beam of charged particles gradually increases with depth because the particles' energy (velocity) decreases. Consequently, it deposits a large amount of energy close to its stopping point.

A beam is a collection of a large number of particles. All these particles do not interact with matter identically. Due to the statistical fluctuations of their interactions, they stop at different depths. The range of a particle beam designates the depth where the number of primary charged particles drops to half of its initial value. It is also known as the mean projected range [32], as shown in figure 2.1.4a. The range is a characteristic of a beam, not the individual particles. Usually, nuclear interactions cause slow depletion of primary particles, which is ignored in the range estimation. Alternatively, in clinical applications, the range is commonly defined as the depth of the distal point of the Bragg peak (see section 2.1.4) where the dose drops to 80% of the peak value and is labeled by R80 [45]. Because of their large mass, protons follow an almost straight line through material, and the average path length is approximately equal to the range. Based on this assumption, the range of proton beams can be calculated from their stopping power as

$$R(E) = \int_0^E \left(\frac{dE'}{dx}\right)^{-1} dE', \tag{2.1.17}$$

where $R(E)$ is called the continuous-slowing-down approximation (CSDA) range of the proton beam with initial kinetic energy E. The Bragg-Kleeman rule (equation 2.1.14) leads to a simple equation [45, 46] to estimate the range of proton beams in material with significant precision.

$$R(E) = \alpha_c E^p. \tag{2.1.18}$$

Figure 2.1.5 demonstrates a good agreement between range-energy relation in equation 2.1.18 and a simulated result. The accuracy of range estimation can be enhanced by tuning the parameters (α_c and p) for different energy ranges.

Usually, charged particles follow random zig-zag paths in a physical medium as a result of various interactions. Thus, the mean projected depth of a beam is slightly smaller than the CSDA range. The ratio of these two ranges is called the detour factor [47]. Its value is close to one for protons and other ions [47, 48]. The statistical fluctuation of the interaction probability of a charged particle with electrons leads to a Gaussian distribution in energy loss. It is known as energy straggling, which leads to different penetration depths of particles, causing range straggling. It impacts the shape of the Bragg peak. With the penetration depth, particles experience more

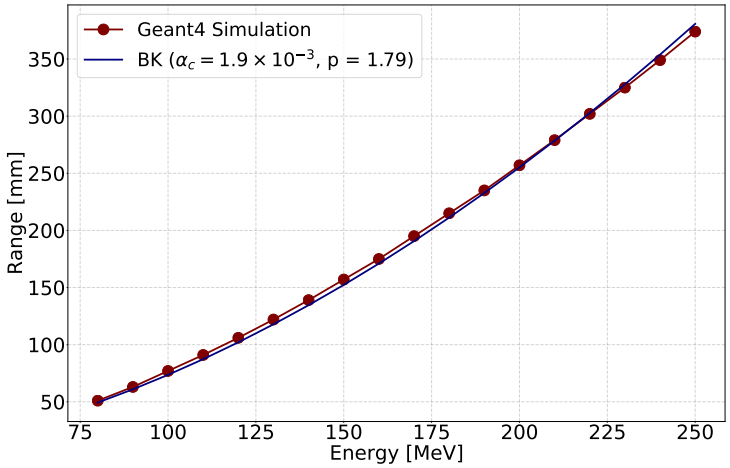

Figure 2.1.5: Comparison of range-energy relation for protons in water obtained using Bragg-Kleemann (BK) rule and Monte Carlo simulation.

numerous interactions, leading to a more significant straggling. Consequently, it extends the width of the Bragg peak at higher energies, as shown in figure 2.1.6b. However, particles with larger mass experience a smaller straggling. The straggling width σ_R is used to quantify the effect. The ratio of the σ_R and R can be expressed as

$$\frac{\sigma_R}{R} = \frac{1}{\sqrt{m}} f\left(\frac{E}{mc^2}\right), \tag{2.1.19}$$

where m is mass of the particle mass and E is the energy of the particle [49]. The function f depends on the material.

2.1.4 Dosimetric quantities

Dose

Dosimetry is the field of study that deals with measuring the absorbed dose deposited by ionizing radiations in tumors, organs, or the whole body. As we have discussed in the previous section, ionizing radiations deliver energy through different interaction processes. A clear understanding and quantification of this energy distribution are essential to implement these radiations in clinical applications. The absorbed dose or dose (D) is the most crucial quantity in this context. It relates the ionization radiation with the associated biological effect. The dose is expressed as

$$D = \frac{d\varepsilon}{dm}, \tag{2.1.20}$$

where ε represents a stochastic quantity called energy imparted by the ionizing radiation. It is defined as

$$\varepsilon = (R_{in})_u - (R_{out})_u + (R_{in})_c - (R_{out})_c + \sum Q, \tag{2.1.21}$$

where $(R_{in})_u$ and $(R_{out})_u$ are radiant energy of incoming and outgoing uncharged particles, $(R_{in})_c$ and $(R_{out})_c$ represent radiant energy of incoming and outgoing charged particles, and $\sum Q$ denotes

the energy converted from mass [27]. The dose is expressed in grays (Gy), equivalent to J/kg and defined as the expectation value of the energy imparted to per unit mass at a point of the traversed material [27]. The integral dose ($D_{integral}$) is the product of the average dose and mass of the irradiated volume. It is expressed in units of joules and denoted as

$$D_{integral} = \bar{D}m, \tag{2.1.22}$$

where $\bar{D}$ is the average value of absorbed dose in mass m.

The fluence (Φ) is defined as the number of protons crossing through per unit area of a surface normal to the direction of propagation. It can be expressed as

$$\Phi = \frac{dN}{dA}, \tag{2.1.23}$$

where dN is the number of particles incident on a sphere of cross-sectional area dA [50]. Fluence is expressed in m^{-2}. Dose can be defined using fluence and mass stopping power and expressed as

$$D = \Phi\frac{S}{\rho}. \tag{2.1.24}$$

Dose rate ($\dot{D}$) can be defined using the time derivative of equation 2.1.24. It can be expressed as

$$\dot{D} = \frac{i_p}{a}\frac{S}{\rho}, \tag{2.1.25}$$

where i_p/a is the proton current density. The beam curent thus plays plays a crucial role in achieving a high dose rate.

Depth-dose graph

The ionizing radiations deposit energy through the interaction processes discussed earlier in this chapter. The dose distribution depends on the type of radiation, energy, charge, material, etc. As illustrated in figure 2.1.6a, the longitudinal dose profile of protons, electrons, photons, and neutrons have very distinct features. The dose of uncharged particles (neutrons and photons) rises sharply at the entrance, known as the buildup region. They liberate electrons at the surface of the target. These short-ranged electrons deposit their energy within a few millimeters and produce the maximum dose. Another consequence of the interaction is absorption (or complete stop) of primary particles. Thus the fluence of the primary beam decreases. In addition, particles are also scattered out from the initial transverse size of the primary beam, causing a drop in the fluence of primary particles. Reduced primary fluence is responsible for the exponential decrement of the dose beyond the peak. It can be understood from equation 2.1.24.

In contrast, the dose profile of the proton beam is unique. It has a low entry dose and a sharp

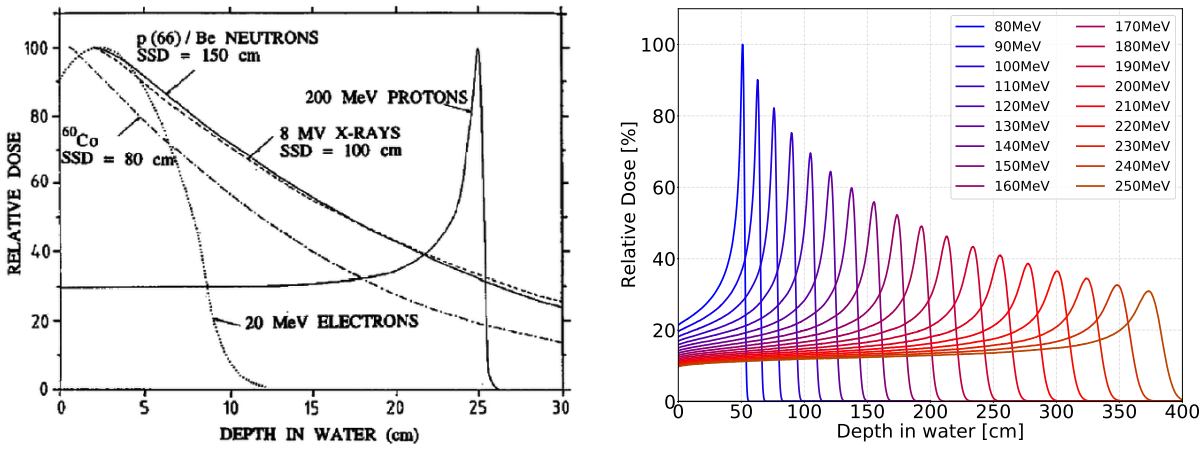

(a) (b)

Figure 2.1.6: (a) Percentage depth dose (PDD) curves of the electron, photon, neutron, and proton beams [51]. (b) Depth-dose curves of proton compare the impact of beam energy on the dose profile. The dose is normalized to the number of simulated protons and peak dose deposited by the 80 MeV beam.

peak near the end of the track. This peak dose of the proton beam (and other hadrons) is known as the Bragg peak [52]. The dose increases rapidly at the proximal edge of the dose curve, followed by a sharp falloff at the distal edge. The Bragg peak of a proton depth dose curve can be explained using the Bethe-Bloch formula given in equation 2.1.16. As a consequence of the gradual reduction of beam energy with depth, protons travel slower. At lower speeds, higher stopping power is responsible for an increased dose at the proximal edge. Beyond the Bragg peak, the fluence of the primary proton drops to zero, leading to a sharp distal falloff. Due to the stochastic nature of the interaction, all protons do not stop exactly at the same point. The width of the Bragg peak depends on the distribution of beam energy and energy straggling. A beam with higher initial energy travels further into the target. Thus the particles encounter more interactions. Consequently, the Bragg peak becomes wider as shown in figure 2.1.6b. The Bragg peak of a proton beam can improve the conformity of treatment. The dose profile of the electron beam is different even though it has an equal charge as protons. Electrons are scattered frequently due to their small mass. Thus, the length of the actual path traveled by the electron differs from its projected range.

Linear energy transfer

Ionizing radiation deposit energy within the vicinity of its path of propagation. It causes ionization by ejecting electrons. These electrons carry energy away from the primary track. The computation of the stopping power includes the total energy imparted by the particles, regardless of the point of energy deposition.In contrast, the linear energy transfer (LET) only considers the locally imparted energy, which should be specified by using a predefined maximum distance from the track of the primary particle or maximum energy of the secondary particle beyond the which the energy deposition is not considered as local. It is also described as restricted linear electronic

stopping power and defined as

$$LET_{\Delta} = \frac{dE_{\Delta}}{dl}, \tag{2.1.26}$$

where dE_{Δ} is the mean energy lost by the charged particles through electronic interactions with surrounding material minus the mean sum of the kinetic energies in excess of Δ of all the electrons released by the charged particles in traversing a distance dl [50]. LET describes the density of energy deposition in a particle track and usually expressed with a unit of $\mathrm{keV\mu m^{-1}}$. It depends on the type of radiation, energy, and traversed material. High LET radiations like a beam of alpha particles ($> 10\mathrm{keV\mu m^{-1}}$) deposit energy with small separation, enhancing the probability of double strand breaks of DNA. Clinical proton beams are considered low LET radiation. However, the value of LET increases with decreasing kinetic energy of proton beams around the end of their track.

The expression of LET given in equation 2.1.26 is applicable for a monoenergetic beam. However, in practice, particles in a beam have a range of energy, and often, multiple energies are used to produce a uniform longitudinal dose. Thus an average value is used to quantify LET. Two different approaches are commonly used to calculate the average LET. These are called dose-averaged LET (LET_d) and track-averaged LET (LET_t). The LET_d includes the relative dose contribution of each individual energy deposition event as the weighting factor. It is quantified as

$$LET_d = \frac{\int_0^{\infty} S_{el}(E) D(E,z) dE}{\int_0^{\infty} D(E,z) dE}, \tag{2.1.27}$$

where $S_{el}(E)$ is the electronic stopping power of primary charged particles with kinetic energy E and $D(E,z)$ is the absorbed dose contributed by primary charged particles with kinetic energy E at location z [53]. For n number of charged particles, LET_d can be calculated from the following expression

$$LET_d = \frac{\sum_{i=1}^{n} \frac{\varepsilon_i^2}{l_i}}{\sum_{i=1}^{n} \varepsilon_i}, \tag{2.1.28}$$

where ε_i is the energy deposition by the i-th charged particle and l_i is step length.

In contrast, LET_t relies on the arithmetic mean value of the fluence spectrum of LET and also known as fluence-averaged LET. If $\Phi(E,z)$ represents the fluence of primary charged particles with kinetic energy E at position z, LET_t can be expressed as

$$LET_t = \frac{\int_0^{\infty} S_{el}(E) \Phi(E,z) dE}{\int_0^{\infty} \Phi(E,z) dE}. \tag{2.1.29}$$

We will only use LET_d for further studies of radiation qualities in this thesis.

2.2 Radiation biology

Radiobiology is an essential component of radiotherapy. This complex field of science studies the impact of ionizing radiation on living bodies. An irradiated biological system experiences a multi-level (molecular, cellular, tissue) consequences. The effects can be observed within 10^{-18} seconds to few years after irradiation. The time scale of different radiation effects is illustrated in figure 2.2.1a.

DNA (Deoxyribonucleic acid) is the most radiation sensitive and vital component that governs most cellular activities. Radiation-induced DNA damage can be crucial for cells [54]. Ionizing radiation can produce several types of lesions in DNA molecules like base damage, single-strand break (SSB), double-strand break (DSB). Usually, healthy cells can repair damaged DNA correctly. If a cell fails to repair DNA damage, it can cause cell death. On the other hand, an incorrect repair can lead to cell mutation, and possibly eventually cancer. These cellular-level effects are usually noticed within few hours of irradiation. At the tissue level, acute effects like inflammation, bleeding, or oedema can be evident, and possibly with a short time after radiation exposure. In contrast, chronic symptoms like fibrosis, atrophy, and even cancer can be expressed after several months to years.

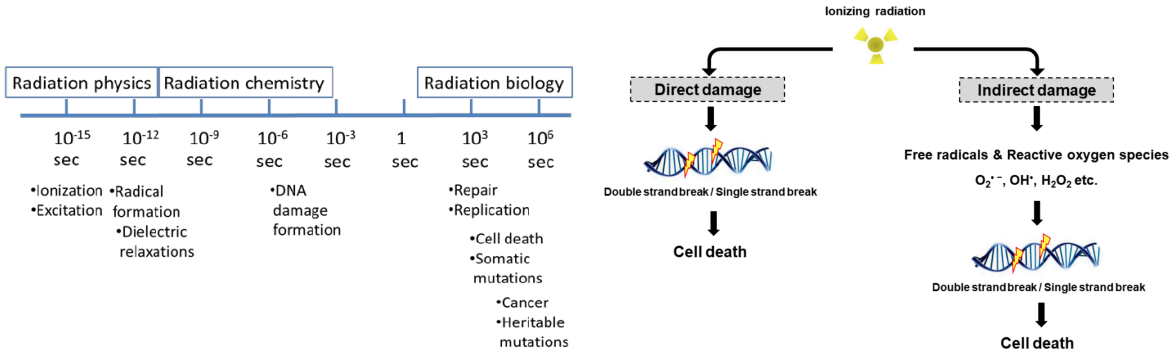

(a) (b)

Figure 2.2.1: (a) The time scales of radiation-induced biological events [55]. (b) Two distinct pathways to introduce radiation-induced cell death [56].

Ionizing radiation can damage a cell directly through ionization or excitation of DNA molecules, called direct effect. In addition, they can also produce reactive oxygen species (ROS) through the radiolysis of cellular molecules, mainly water. These highly reactive products can induce cell damage by reacting chemically with DNA molecules [57]. It is known as the indirect effect of radiation which is responsible for most of the radiation-induced damage. Figure 2.2.1b shows two distinct pathways to activate radiation-induced cell death. With an identical absorbed dose, different radiation qualities produce various levels of biological consequence. The biological effectiveness of radiation qualities is quantified using relative biological effectiveness (RBE). It is defined as the ratio of absorbed dose of a reference beam of photons to the actual absorbed dose of the radiation

under consideration, to achieve the same biological endpoint [58]. It can is denoted as

$$\mathrm{RBE} = \frac{D_{ref}}{D_{con}}, \tag{2.2.1}$$

where D_{ref} and D_{con} are the dose of reference radiation and dose of the radiation under consideration. A range of physical and biological parameters govern the RBE of proton beams. Several phenomenological RBE models based linear quadratic (LQ) model [59] have been reviewed by Rørvik et al. [60]. The RBE value can be estimated from the equation

$$\mathrm{RBE}\big(D_p, (\alpha/\beta)_x, \mathrm{RBE}_{max}, \mathrm{RBE}_{min}\big) = \frac{1}{2D_p}\Big(\sqrt{\big(\frac{\alpha}{\beta}\big)_x^2 + 4D_p\big(\frac{\alpha}{\beta}\big)_x + 4D_p^2\mathrm{RBE}_{min}^2} - \big(\frac{\alpha}{\beta}\big)_x\Big), \tag{2.2.2}$$

where D_p is the physical dose deposited by protons per fraction. α_x and β_x are the LQ-model parameters [59] for the reference photon radiation [61]. The parameters RBE_{max} and RBE_{min} are given as

$$\mathrm{RBE}_{max}(LET_d) = 0.892 + 0.179(\mathrm{keV}/\mu\mathrm{m})^{-1} LET_d,$$
$$\mathrm{RBE}_{min} = 1.$$

The points of energy deposition of higher LET radiation are close to each other. Thus, it enhances the probability of DSBs and subsequent cell inactivation. Higher LET thus leads to an elevated RBE, as illustrated in figure 2.2.2. However, RBE reaches its peak value for LET $\approx 100\ \mathrm{keV}\mu\mathrm{m}^{-1}$. Beyond this value, RBE decreases with increasing LET, known as the overkill effect.

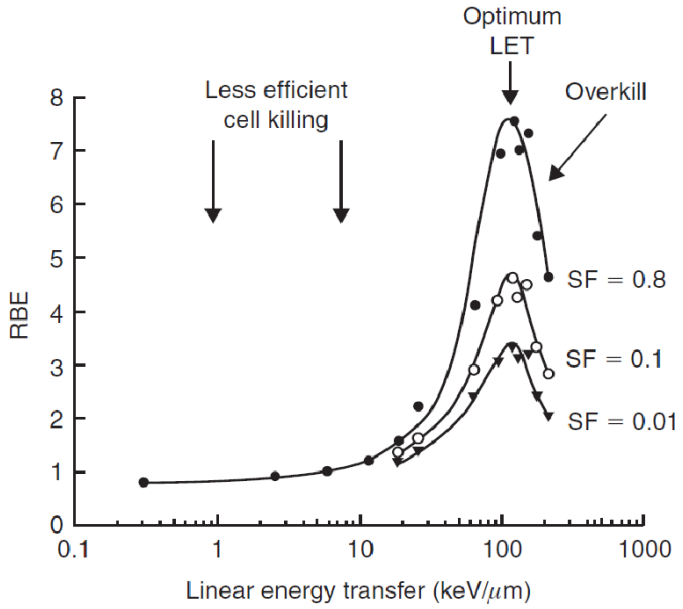

Figure 2.2.2: Evolution of relative biological effectiveness of proton beam as a function of LET [62]. Graphs for three Surviving fraction (SF) are compared.

2.3 Radiotherapy

Radiotherapy (RT) uses ionizing radiations to treat cancer. Ionizing radiation can damage a biological system by inducing cell death mechanisms. It mostly relies on DNA strands break to initiate irreversible damage of cancerous cells. Simultaneous impact of ionizing radiation on healthy tissue is inevitable; however, the better repair mechanisms of normal cells give us the opportunity to implement RT in treatment [62, 63]. The efficacy of RT depends on the optimization of tumor control probability (TCP) and normal tissue complication probability (NTCP) [64]. The TCP increases with radiation dose following the sigmoid function up to its peak value. The NTCP also follows a similar trend as a function of dose, as shown in figure 2.3.1. At a very high value of dose, change in TCP and NTCP is insignificant. A similar pattern also can be seen at a very low dose region; in between, the dose-response changes sharply. Even though they follow the same pattern, NTCP catches TCP at a slightly higher dose. It leads to a dose interval, called the therapeutic window, where TCP is significantly higher than the NTCP. RT can be used within the therapeutic window to treat a tumor, producing minimum damage to the healthy tissue. The spread of the therapeutic window depends on various factors, including cell type. A wider window is suitable to treat tumors effectively with a reduced side effect. If TCP and NTCP curves are very close to each other, the therapeutic window becomes very narrow. It restricts the maximum achievable dose at the tumor to produce a curative effect. A wider therapeutic window can be produced by enhancing the radiation effect on tumors, like adding sensitizers or increasing the normal tissue tolerance to shift the NTCP curve toward the higher dose [62].

The therapeutic index (TI) is a quantitative measure to determine the safety level of RT. It is defined as the ratio of dose to achieve two distinct biological endpoints. In general, a ratio of dose corresponding to the 50% of the NTCP curve (TD_{50}) and 50% of the TCP curve (ED_{50}) is used to obtain the therapeutic index of RT as

$$TI = \frac{TD_{50}}{ED_{50}}. \tag{2.3.1}$$

Depending on its implementation process, RT can be classified as brachytherapy (BT), radiometabolic therapy (RMT), intraoperative RT (IORT) and external beam RT (EBRT). In this thesis, we have studied the characteristics of proton beams for EBRT.

EBRT is also known as teletherapy, where the source of ionizing radiation is placed outside of the patient's body. It is the most frequently employed treatment modality that accounts for about 90% of total RT. Megavoltage x-ray and electron are most commonly used for EBRT. In addition, hadrons like protons, neutrons, carbon ions have been getting popular for the last few decades. A few exotic particles such as muon, anti-proton has also proven their potential to be employed for EBRT. Particle accelerators, usually compact size linear accelerators (linacs), are used for megavoltage x-ray generation used for EBRT. At the initial stage, an electron gun produces a beam of electrons. These

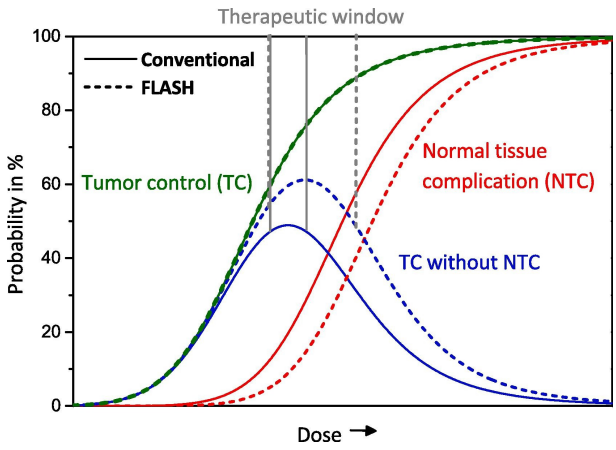

Figure 2.3.1: Comparison of the therapeutic window of conventional RT and FLASH RT [65].

electrons are accelerated using a high-frequency electromagnetic wave. High-energy electrons decelerate rapidly in a collision against a stationary metal target of high atomic number. Thus, they produce Bremsstrahlung x-rays. It is a suitable form of radiation to treat deep-seated tumor. On the other hand, an electron beams also can be employed directly to treat superficial tumors due to its suitable dose fall-off within few millimeters.

The large mass of hadrons makes a beam magnetically stiff and challenging to accelerate. A hadron therapy system is comparatively challenging to built and costly. However, a sharp fall-off of dose behind the target makes it an attractive candidate for RT. This feature of hadrons can ensure a localized conformal dose. Among all hadrons, the proton beam is most widely used, followed by the carbon ion beam. Further details of proton beam therapy will be discussed in the following section.

2.3.1 Proton beam therapy

In the context of RT, the unique dose profile of the proton beam is its primary advantage over x-rays and electron beams. As the proton beam completely stops at the end of its range, it deposits a negligible dose beyond the target. In addition, the Bragg peak of a proton beam deposits a large dose at tumors, sparing normal tissue. This enhances the dose conformity; however, a pristine Bragg peak can not deposit a homogeneous dose over a longitudinally extended tumor. This limitation can be overcome by superimposing multiple Bragg peaks as shown in figure 2.3.2. The peak homogeneous dose over an extended longitudinal space is called spread-out Bragg peak (SOBP). Furthermore, the lateral dose profile of a proton beam has an attractive characteristic of a smaller penumbra. Following the equation 2.1.12, the larger mass of proton reduces its scattering angle, leading to a smaller lateral spread of the beam. This feature of the proton beam facilitates us to spare adjacent sensitive organs like the spinal cord. Within the therapeutic energy range, the proton beam is considered low-LET radiation, similar to x-rays. However, at the end of the track where beam energy is low, the LET of proton beams has been found to be very high [53, 66]. Consequently, it can produce denser ionization in the target and enhance the probability of cell death by forming

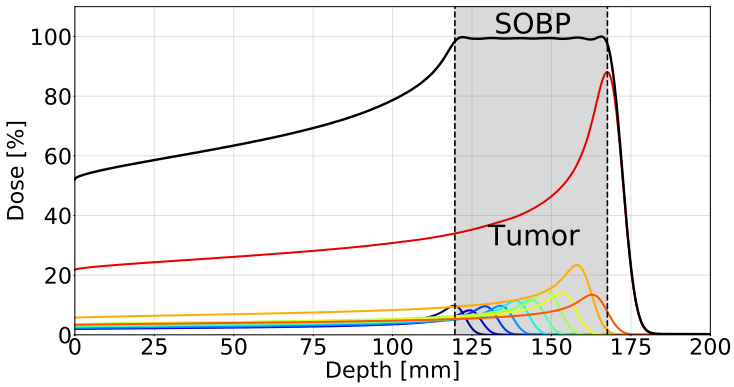

Figure 2.3.2: Spread-out Bragg peak of proton beam.

a cluster of DNA damage [67]. Conventionally, an RBE value of 1.1 is used for clinical treatment planning, and it increases with the value of LET_d [61]; however, its value depends on several factors, including cell type and total dose. In recent years, several new approaches to RT have been studied using proton beams. Among those, spatially fractionated radiation therapy (SFRT) using GRID irradiation and FLASH radiotherapy have demonstrated their superiority to reduce normal tissue damage.

The complex proton therapy system consists of a particle accelerator to produce high-energy beams, the beam transport section with an energy selector, and a treatment delivery system that includes the gantry, nozzle, snout, and patient positioning system [68]. The basic principle of particle accelerators is discussed in sectiom 2.4.1. The accelerated proton beam is transported to the treatment room through a vacuum pipeline consisting of a collection of dipole and quadrupole for beam manipulation. The details of beam focusing is included in section 2.4.2. The gantry is the largest component of the treatment delivery system. It allows the projection of beam from several directions through its full ($360°$) or limited (0-$220°$) rotation. Finally, the beam is delivered to a patient using the nozzle that is installed in the gantry. Two alternative designs are used for the nozzle to deliver beams to treat tumors.

A passive scattering system contains scatterers, range modulators, dose monitoring chamber, patient-specific beam-shaping collimators, and compensators. A narrow beam delivered by the transportation system is scattered to obtain a large field size. It is shaped by patient-specific collimators to irradiate the tumor. The longitudinal position of dose delivery is tuned using a range compensator.

In contrast, an active scanning system uses a narrow beam of protons to irradiate a tumor spot by spot. It uses two orthogonal dipole magnetic fields to steer the beam in the horizontal and vertical directions and deliver the dose at a desired point in the tumor. The energy of the beam is tuned to manage the longitudinal position of the spot.

In the following chapters we will discuss the advanced way of beam delivery system.

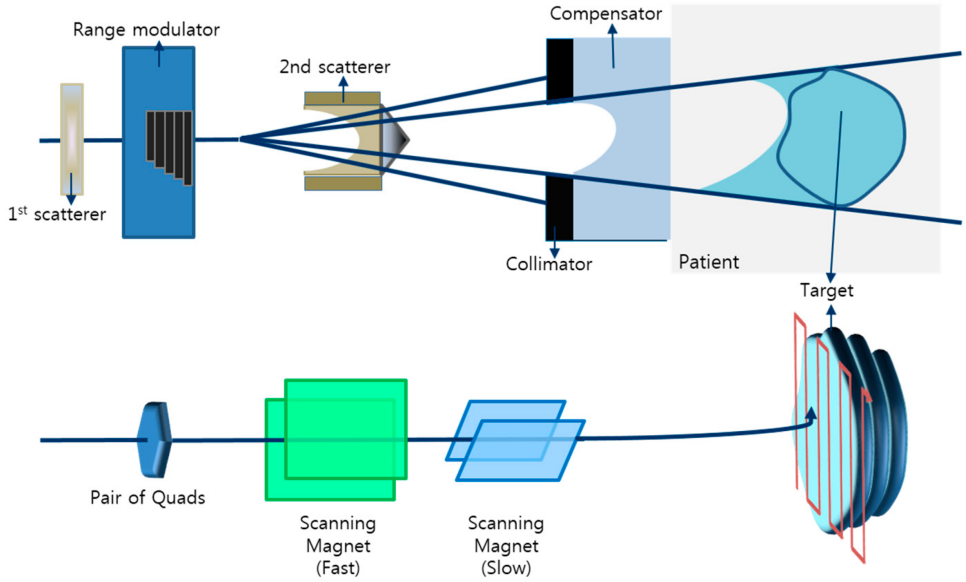

Figure 2.3.3: Active scattering (top) and Passive scanning (bottom) system of proton beam delivery system [69].

Spatially fractionated radiation therapy (SFRT)

The principle of SFRT is to produce a highly inhomogeneous dose distribution to reduce the normal tissue exposure. As illustrated in figure 2.3.4, the total field of irradiation is split into high-dose and low-dose regions. The high-dose area is called the peak, and the low-dose area is labeled as the valley. The most crucial parameter for SFRT is the peak-to-valley-dose ratio (PVDR). In addition to a high PVDR, a lower valley dose is essential to achieve the goal of SFRT [23]. The PVDR quantifies the dose contrast between peaks and valleys and can be expressed as

$$\mathrm{PVDR} = \frac{D_{Peak}}{D_{Valley}}, \tag{2.3.2}$$

where D_{Peak} and D_{Valley} are dose at the peak and valley region of the inhomogeneous distribution, respectively. The D_{Peak} and D_{Valley} are usually measured at the center of the peak and valley region indicated by the blue and green lines in figure 2.3.4. The PVDR depends on various factors, including beam energy, divergence, and centre-to-centre (c-t-c) distance. In practice, SFRT can be implemented using several beam-shaping techniques. GRID irradiation is the most widely studied. Besides, microbeam radiotherapy (MRT) and minibeam radiotherapy (MBRT) can produce dose contrast.

GRID irradiation creates an inhomogeneous dose pattern by regulating radiation exposure. Usually, valleys are shielded to ensure a very low dose (preferably zero). A wide variety of metal collimators have been studied to obtained desired dose profile [70]. High dose contrast in normal tissue is a prerequisite for GRID irradiation. However, in a tumor, two different approaches of irradiation can be effective for treatments. Firstly, a homogeneous dose, as shown in figure 2.3.4a,

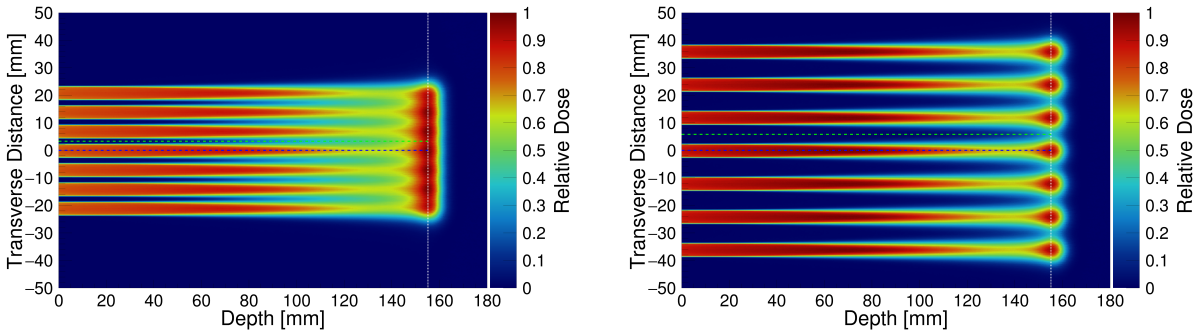

(a) (b)

Figure 2.3.4: The inhomogeneous dose distribution of SFRT produces a sharp contrast between the peaks and valleys. The dose distributions are produced for c-t-c = 5 mm (a) and c-t-c = 12 mm (b). The dose is normalized to the peak value.

can induce a cell death mechanism in tumors. Secondly, a highly heterogeneous dose distribution depicted in figure 2.3.4b can effectively treat tumors [71, 72]. The radiation-induced bystander effects can initiate a cell death mechanism close to the irradiation field where cells are not directly exposed to radiation [22, 73, 74]. Extensive studies are required to determine the most effective clinical dose pattern at the target.

The underlying radiobiological mechanisms to explain the SFRT is an active field of study. The dose-volume effect, radiation-induced bystander effects, microvascular alterations, and immunomodulation are known for their potential role in SFRT [25]. It reduces the risk of normal tissue complications by irradiating a smaller volume. Moreover, the repair mechanism is stimulated due to the migration of healthy cells from the unexposed part of the tissue to the high dose area [16].

FLASH radiotherapy

FLASH radiotherapy uses ultra-high dose rates, that are orders of magnitude compared to conventional RT, for a very short irradiation period [75]. The impact of ultra-high dose rate to reduce the normal tissue damage without impacting the tumor control probability is known as FLASH effect [76]. Compared to $\sim$5 Gy/minute dose rate of conventional proton beam therapy, the FLASH effect has been observed beyond 40 Gy/second [75, 77]. One hypothesis for the mechanism of action is that a very high dose rate causes a depletion of oxygen at the irradiated volume, leading to a hypoxic environment in the tissue. This hypoxic condition reduces the radiosensitivity of the cell and enhances normal tissue tolerance [76]. Consequently, it expands the therapeutic window as shown in figure 2.3.1. The clinical implementation of FLASH is complicated for several technical challenges like high beam current, faster energy adjustment, rapid pencil beam scanning, and accurate dosimetric measurements within a short time period [78].

2.4 Accelerator and Beam optics

2.4.1 Accelerator

Particle accelerators are complex machines designed to produce high-energy charged particle beams for various applications, ranging from basic science research to cancer treatment. In principle, charged particles are accelerated using electromagnetic force, where electric fields are employed to change the kinetic energy, and magnetic fields are used to alter the direction of velocity. Change in kinetic energy (ΔE_K) of q charge in an Electric field can be formulated as

$$\Delta E_K = q \int E ds, \tag{2.4.1}$$

where s is the distance traveled through the electric field and field strength $E = V/d$. E is also known as electric potential gradient. Following equation 2.4.1, higher kinetic energy can be achieved using a larger field gradient. However, it is limited to $\lesssim$ 100 MV/m due to electric breakdown effects. Alternatively, a longer accelerating section can increase the energy. It is achievable using a series of linear accelerating elements (single-pass scheme) or by passing the charged particles through the same field multiple times (multi-pass scheme). For the application of radiotherapy, linear and circular accelerators are used depending on the choice of the ionizing beam. Usually, x-ray and electron beam therapy are implemented using linear accelerators. In contrast, proton and ion beam therapy systems are designed based on cyclotrons and synchrotrons.

Linear accelerators

The linear accelerator, commonly known as a linac, was developed by Wideröe in 1928. He used high-frequency alternating voltage to accelerate charged particles in a linear path. There are several methods to implement this principle of linear acceleration to produce high-energy charged particle beams. In one type of linear accelerator, the charged particles travel through a series of drift tubes connected to the radio frequency (RF) sources known as Alvarez structure. It is commonly used to accelerate protons. In this structure, the charged particles travel through the drift tube during the half-time period of the RF source, where they are shielded from the external field and maintain a constant speed. They accelerate in the gap between two drift tubes. With increased energy, charged particles move faster and travel a larger distance within a given time. For adequate acceleration, the period of RF frequency must be synchronized with the path length that can be achieved using the increasing length of the drift tubes. This condition can be satisfied by adjusting the length of the i-th tube following the equation

$$l_i = \frac{v_i \tau_{RF}}{2}, \tag{2.4.2}$$

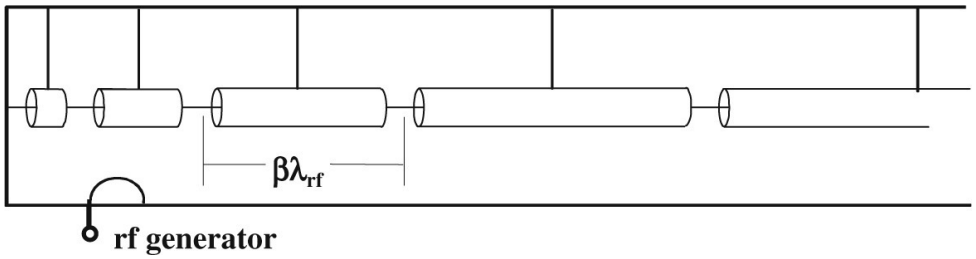

Figure 2.4.1: Conceptual structure of a linear accelerator (Alvarez structure) [79].

where v_i is the velocity at the i-th tube, and τ_{RT} is the time period. In modern accelerators, drift tubes are replaced by drift spaces between RF cavities, where charged particles are accelerated by electric field. In addition, standing or traveling microwave oscillations are used to accelerate charged particles. In principle, charged particles can reach arbitrarily high energy using a higher potential gradient or a larger number of drift tubes. However, the maximum achievable potential gradient is limited by the corona formation and electric discharge. Furthermore, space constraints impose a limitation on the maximum number of drift tubes.

Cyclotron

In a cyclotron, charged particles are accelerated in a circular path to generates a continuous beam of constant energy. It was first developed by the American physicists Ernest Orlando Lawrence and M. Stanley Livingston [80]. The main structure of a cyclotron is consist of a hollow chamber enclosed by two semicircular metal electrodes called “dee” (shape similar to “D”). These electrodes are placed with a small gap as illustrated in figure 2.4.2a. The entire system is placed in a uniform magnetic field perpendicular to the plane of the electrodes.

The charged particles are injected at the center of the cyclotron. An alternating electric field is generated at the narrow gap between two dees to apply force on the particles along the direction of their motion. The Lorentz force produced by the magnetic field acts in perpendicular to the velocity of the changed particles and deflect to move in a circular path. The polarity of the electric field is altered synchronously to ensure continuous acceleration of particles in the gap. The frequency of the alternating voltage to satisfy this condition is called cyclotron frequency and expressed as

$$f_c = \frac{Bq}{2\pi m}, \tag{2.4.3}$$

where q and m are the charge and mass of the accelerating particles, respectively, and B represents the magnetic field strength [34]. Usually cyclotrons are driven by RF (Radio frequency) generator with a voltage between 30 kV to 100 kV and a frequency between 50 MHz to 100 MHz [34]. With the increasing speed of the particles, they follow an outward spiral path. At a relativistic speed, effective mass of the particles increases. It is compensated with reduced frequency or increased magnetic field.

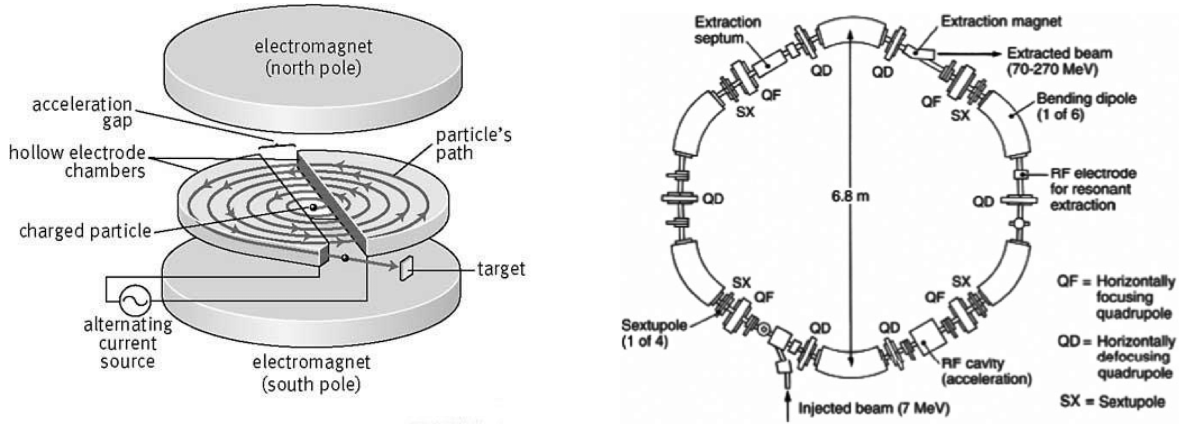

(a) (b)

Figure 2.4.2: (a) Principle of high energy beam production using a cyclotron [81]. (b) Schematic diagram of a synchrotron [82].

Synchrotron

In a synchrotron, a beam of charged particles is accelerated in a circular evacuated ring-like arrangement. It contains bending magnets to deflect the charged particles in a circular path. In addition, quadrupole and sextupole magnets are employed for beam focusing and correction of chromatic aberrations, respectively. One or more acceleration cavities raise the beam energy using electric fields. The final energy of the pulsed beam produced by a synchrotron can be tuned, which is an advantage for medical applications. The components of a synchrotron is illustrated in figure 2.4.2b.

A pre-accelerated (by a cyclotron or linac) beam of charged particles is injected into a synchrotron. The beam continuously circulate in the ring and gain energy each time it passes through the acceleration cavity. The magnetic field is elevated to keep the beam moving in the same path with higher energy.

2.4.2 Charged particle beam optics

A beam is a collection of moving particles. For accelerator physics, their collective behavior is more crucial than the properties of individual particles. In the following sections we will give a brief review of relevant beam optics concepts, including coordinate system, beam optics, transfer matrix formalism, and focusing principle. We will however not treat collective effects such as space charge and wake-fields.

Beam focusing

A charged particle interacts with electric fields, which do not depend on its state of motion. In contrast, only moving charged particles experience force inside magnetic fields. The interaction of charged particles with an electromagnetic field can be described using the Lorentz force

$$F = q(E + v \times B), \tag{2.4.4}$$

where E and B represent electric and magnetic field respectively. F is the force on a particle with q charge when it moves at a velocity of v. Force exerted by the electric field acts in parallel to the direction of the field; however, the magnetic field applies force in perpendicular to the direction of field and velocity of the charged particle. It can cause centripetal acceleration of the particle following equation

$$\frac{mv^2}{R} = qvB, \tag{2.4.5}$$

where R is the radius of curvature of the charged particle's path.

In particle accelerators, dipoles are commonly used for bending, and quadrupoles are employed for beam focusing. Besides, higher-order multipoles are also used for specific purposes. Chromatic aberrations can be corrected using sextupole. Octupoles are sometimes used to to compensate field errors.

One of the primary goals of this thesis is to evaluate suitable techniques to generate small spots at the tumor using a proton beam. Focusing a beam at the desired point can be a solution. Magnetic lenses in the form of quadrupole magnets (see Figure 2.4.3) are extensively used for beam focusing where Lorentz force deflects the charged particles towards the focal point. The angle of deflection of the charged particle depends on its initial velocity, distance d from the focal point, and focal length f. If the entrance velocity of the particle at the lens is parallel to the designed orbit (discussed later in section 2.4.2), the angle of deflection to focus the beam at focal point, $\theta = \arctan(d/f)$. This condition is true for a laminar beam where beam emittance is zero. In this case, all the particles have identical transverse velocity, which is proportional to the displacement from the reference orbit. Theoretically, an ideal lens can focus a beam to a point of zero dimension provided that it is laminar. However, actual particle beams have non-zero emittance, as discussed in the next section, and the particles move in various directions with a range of transverse velocity. It is impossible to focus all these particles at a common point with a specific lens; instead, it can change the average motion of the beam's particles. Thus beam emittance impacts the spot size at the target. A lower emittance is advantageous to produce smaller precise spots. However, there is a fundamental limitation of the spot size at the focal point.

An azimuthal magnetic field (B_ϕ) can also provide a suitable force for beam focusing. The deflection of the charged particle produce by a magnetic field can be described by

$$\theta = -\frac{qc}{\beta E} B_\phi l, \tag{2.4.6}$$

where c is the speed of light and l is the length of the field [79]. If the length l is not very short compared to the focal length, $B_\phi l$ should be replaced by $\int B_\phi dl$. A conductor with uniform current density is capable of producing an azimuthal magnetic field that can provide focusing force. However, it is not a practical solution in the context of particle accelerator and beam focusing. The

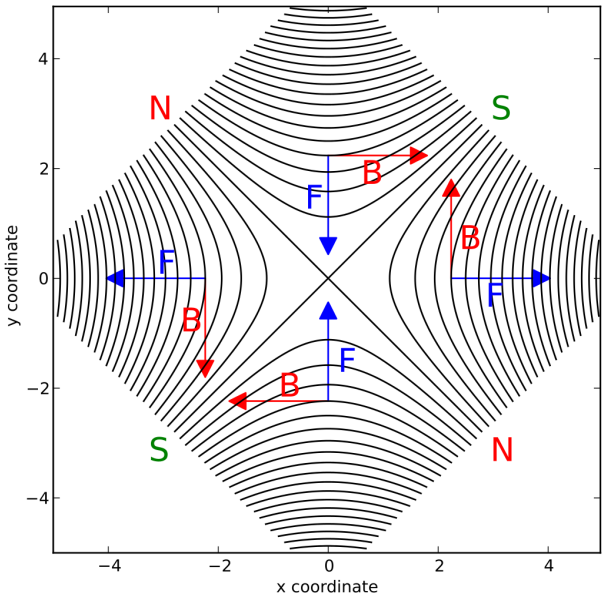

Figure 2.4.3: The magnetic field inside a quadrupole [83]. Red arrows represent the direction of magnetic field (black curve lines), and blue arrows represent the direction of Lorentz force on the charged particles. The effective force is inward (focusing) in the vertical direction and outward (defocusing) in the horizontal direction. The strength of the force grows linearly with the distance from the origin.

quadrupole is the most suitable device that can ensure material free aperture with a suitable magnetic field configuration for beam focusing. Its magnetic field, $B = (gy, gx, 0)$ where field gradient $g = \frac{\partial B_x}{\partial y} = \frac{\partial B_y}{\partial x}$. The focusing strength of a quadrupole is defined as

$$k\ (\mathrm{m}^{-2}) \approx 0.2998 \frac{g\ (\mathrm{T/m})}{\beta E\ (\mathrm{GeV})}, \tag{2.4.7}$$

and the focal length of the quadrupole is

$$f = \frac{1}{kl}. \tag{2.4.8}$$

Figure 2.4.3 shows the magnetic field of a quadrupole. An individual quadrupole causes focusing in a transverse direction and defocusing in the perpendicular direction. An overall focusing effect can be obtained using an appropriate combination of quadrupoles.

Coordinate system

A curvilinear coordinate system can be used to describe the motion of the constituent particles of a beam in an accelerating system [84]. Usually, accelerators are designed to produce particles with predefined energy at a particular point of the system. However, the energy of all the particles of a beam are not exactly equal to the design value. The reference trajectory, also known as design trajectory, is described as the trajectory followed by the ideal particles having the central

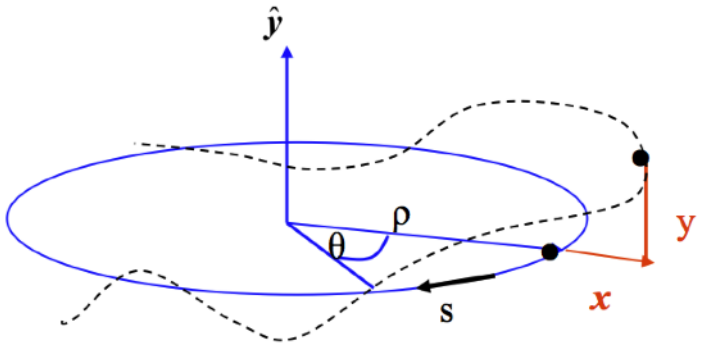

Figure 2.4.4: The motion of charged particles in an accelerator is described using a curvilinear coordinate system [85].

design momentum of the accelerator [84]. In circular accelerators, it is called design orbit. It is usually consists of a series of straight segments and circular arcs. Particle motion is conventionally described in a coordinate system moving along with the ideal particle. As depicted in figure 2.4.4, the co-moving Cartesian coordinate system is centered at the design trajectory. Usually, the x-axis and y-axis represent two transverse directions, and the z-axis is used to represent the longitudinal direction. The position of a particle along the design trajectory is described using the s-axis. The tangent to the s-axis gives the instantaneous direction of motion of ideal particles.

The evolution of particle beams phase space is described using three pairs of variables, each corresponding to one 2D Cartesian coordinate system given by (x, x'), (y, y'), and $(z, \Delta p)$. The deviations of the particles' position from the design trajectory are given by x, y, and z. The quantities x' and y' represent the derivative of x and y with respect to s ($x' = \frac{dx}{ds}, y' = \frac{dy}{ds}$). Δp represents the deviation of the momentum from the design value. The ideal particle has a momemtum $p = [0, 0, p]$, while in general the particle momentum is given by $[p_x, p_y, p_z]$. Often it is convenient to use the transverse momenta p_x and p_y instead of the angular variables x' and y' with $x' = \frac{p_x}{p}, y' = \frac{p_x}{p}$. The transverse momenta (p_x and p_x) are assumed to be small compared to the longitudinal momentum. Total momentum is thus

$$p = \sqrt{p_x^2 + p_y^2 + p_z^2} \approx p_z. \tag{2.4.9}$$

The angles of deviation in horizontal and vertical direction can be expressed as

$$\begin{aligned} \frac{p_x}{p_z} &= \tan\theta_x \approx \theta_x \approx x', \\ \frac{p_y}{p_z} &= \tan\theta_y \approx \theta_y \approx y'. \end{aligned} \tag{2.4.10}$$

The derivative x' and y' represent the horizontal and vertical slope of particle trajectory consecutively and usually stated with a unit of angle, commonly mrad and μrad.

Equations of motion

Magnetic fields are used to deflect particles with transverse offsets back towards the the design trajectory, causing an oscillatory motion around the reference orbit. In a single plane (x or y), this motion can be described using Hill's equation [86]

$$u'' + K_u u = 0 \quad (u = x, y), \tag{2.4.11}$$

where K_u represents the focusing effect on the particle due to the dipole (bending) and quadrupole (focusing/defocusing) magnets. The solution of Hill's equation can be written as,

$$u(s) = \sqrt{\epsilon}\sqrt{\beta(s)}\cos(\psi(s) + \phi), \tag{2.4.12}$$

where ϵ is called single particle emittance. Equation 2.4.12 describes the transverse oscillation of a particle respect to the reference orbit, known as betatron oscillation. The amplitude is proportional to the single particle emittance, and is proportional to the phase space area of a particle at a point in its trajectory (ϵ = Area/π). Derivative of $u(s)$ can be expressed as

$$u'(s) = -\frac{\sqrt{\epsilon}}{\sqrt{\beta(s)}}\left[\alpha(s)\cos(\psi(s) + \phi) + \sin(\psi(s) + \phi)\right]. \tag{2.4.13}$$

Using the Twiss parameters β, α, and γ, the equation of the phase space ellipse can be expressed as

$$\gamma u'^2(s) + 2\alpha(s)u(s)u'(s) + \beta(s)u^2(s) = \epsilon, \tag{2.4.14}$$

where, $\beta(s)$ represents the amplitude function that depends on the focusing elements of the lattice. $\alpha(s)$ describes the orientation of the phase space ellipse and defined as $\alpha(s) = \frac{\beta'(s)}{2}$. $\gamma(s)$ depends on the two other Twiss parameters following the relation

$$\gamma(s) = \frac{1 + \alpha^2(s)}{\beta(s)}. \tag{2.4.15}$$

Transfer matrices

A point of its phase space describes the particle's trajectory of a beam. The motion of each constituent particle can be calculated using a transfer matrix, transforming particle coordinates from an initial to a final position. The coordinate transformation can be written as

$$\begin{bmatrix} u_f \\ u'_f \end{bmatrix} = \begin{bmatrix} m_{11} & m_{12} \\ m_{21} & m_{22} \end{bmatrix} \begin{bmatrix} u_i \\ u'_i \end{bmatrix}, \tag{2.4.16}$$

where m_{ij} are the components of the transfer matrix M. An accelerator has several components, such as drift sections, focusing magnets, bending magnets. The transfer matrices for these elements

are different. Particles remain undeflected in the drift section; thus, the transfer of particles can be expressed using a simple matrix

$$M_{Drift} = \begin{bmatrix} 1 & L \\ 0 & 1 \end{bmatrix}, \tag{2.4.17}$$

where L is the length of the drift section. The transfer matrix for quadrupoles can be represented as

$$M_{Focusing} = \begin{bmatrix} \cos(\sqrt{K}l) & \frac{1}{\sqrt{K}}\sin(\sqrt{K}l) \\ -\sqrt{K}\sin(\sqrt{K}l) & \cos(\sqrt{K}l) \end{bmatrix}, \tag{2.4.18}$$

$$M_{Defocusing} = \begin{bmatrix} \cosh(\sqrt{K}l) & \frac{1}{\sqrt{K}}\sinh(\sqrt{K}l) \\ \sqrt{K}\sinh(\sqrt{K}l) & \cosh(\sqrt{K}l) \end{bmatrix}, \tag{2.4.19}$$

where l is the length of the quadrupole. All transfer matrices have a fundamental property of unit determinant (det(M) = 1). If particles travel through several elements between their initial and final point, the total composite transfer matrix is described by the product of multiple matrices

$$M = M_n M_{n-1} M_{n-2} \ldots\ldots M_3 M_2 M_1. \tag{2.4.20}$$

Representing a beam of particles

An ensemble of moving particles is usually described using statistical parameters. It is common to describe the transverse phase spaces, (x, x') and (y, y') as bivariate Gaussian distributions. The statistical parameters (first and second order moments) of distribution of position and slope of particle trajectories can describe the size and divergence of beams. The Twiss parameters can be expressed using the second moments of the beam distribution [86]:

$$\begin{aligned} \langle u^2 \rangle &= \epsilon_{rms}\beta_u(s) \\ \langle uu' \rangle &= -\epsilon_{rms}\alpha_u(s) \\ \langle u'^2 \rangle &= \epsilon_{rms}\gamma_u(s) \end{aligned} \tag{2.4.21}$$

Here ϵ_{rms} is called geometric emittance of the beam, and is proportional to area of the transverse phase space. Following Liouville's theorem, the phase space area, and therefore the geometric emittance of the beam, is constant as the particles undergoes betatron oscillations. The standard deviation σ_x and σ_y represent the beam's transverse size

$$\sigma_u(s) = \sqrt{\langle u^2 \rangle - \langle u \rangle^2} = \sqrt{\langle u^2 \rangle} = \sqrt{\epsilon_{rms}\beta_u(s)}. \tag{2.4.22}$$

Similarly, transverse divergences are given by $\sigma_{x'}$ and $\sigma_{y'}$

$$\sigma_{u'}(s) = \sqrt{\epsilon_{rms}\gamma_u(s)}. \tag{2.4.23}$$

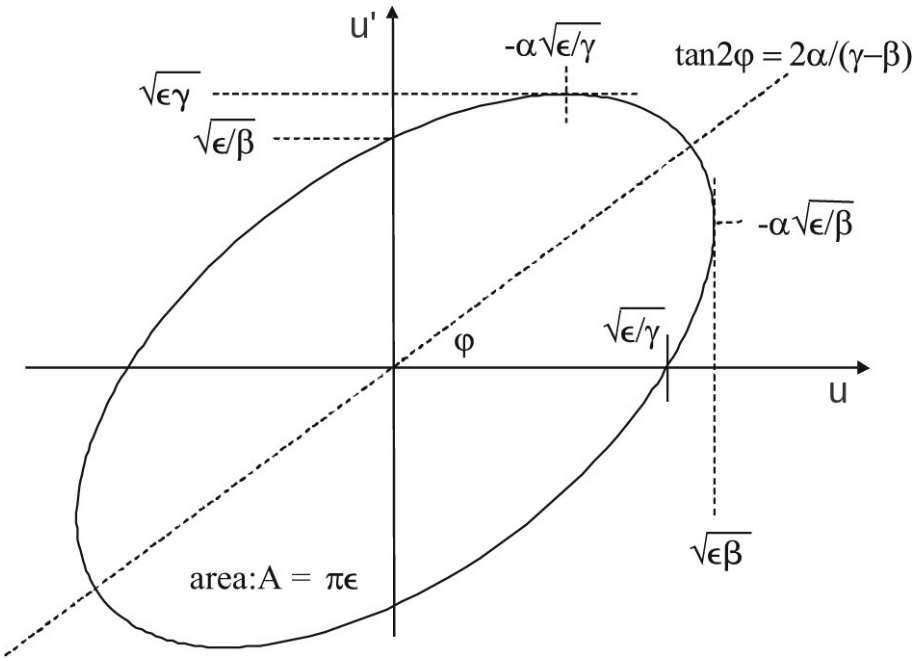

Figure 2.4.5: The phase space ellipse describes the particles motion in (u, u') plane [79]. With constant emittance, the area of the ellipse remains constant. The shape of the ellipse changes along the trajectory of the particles.

Instead of tracking individual beam particles, which is computationally expensive, it is often convenient to track only the moments of the beam distribution, since they give its size and divergence. The covariance matrix (Σ), which is also known as beam matrix or sigma matrix, can represent this information in a simplified way. It satisfies the relation, $\Sigma = U\Sigma U^T$. In matrix form, it can be described as

$$\Sigma = \begin{bmatrix} \langle u^2 \rangle & \langle uu' \rangle \\ \langle u'u \rangle & \langle u'^2 \rangle \end{bmatrix} = \epsilon_{rms} \begin{bmatrix} \beta_u & -\alpha_u \\ -\alpha_u & \gamma_u \end{bmatrix} \tag{2.4.24}$$

The determinant of the sigma matrix gives the square of the geometrical emittance.

$$\epsilon_{rms}^2 = \det(\Sigma). \tag{2.4.25}$$

The geometrical emittance (ϵ_{rms}) of a beam, defined in equation 2.4.25, changes with energy. It is convenient to use normalized emittance (ϵ_N), which is invariant under acceleration.

$$\epsilon_N = \beta\gamma\epsilon_{rms}. \tag{2.4.26}$$

where $\gamma = E/m_0c^2$ is the Lorentz factor and $\beta = v/c$ is the relativistic velocity.

Transformation of Twiss parameters

A beam can be parameterized using its emittance, and its Twiss parameters. The Twiss parameters evolve as the beam propagates along the accelerator. This evolution can be calculated using

the single-particle transfer matrices [86], as

$$\begin{bmatrix} \beta \\ \alpha \\ \gamma \end{bmatrix} = \begin{bmatrix} m_{11}^2 & -2m_{11}m_{12} & m_{12}^2 \\ -m_{11}m_{21} & m_{11}m_{22} + m_{12}m_{21} & -m_{12}m_{22} \\ m_{21}^2 & -2m_{21}m_{22} & m_{22}^2 \end{bmatrix} \begin{bmatrix} \beta_0 \\ \alpha_0 \\ \gamma_0 \end{bmatrix}. \tag{2.4.27}$$

There is no focusing effect in a drift space. Thus, the transformation of the Twiss parameters can be obtained from equation 2.4.27.

$$\begin{bmatrix} \beta \\ \alpha \\ \gamma \end{bmatrix} = \begin{bmatrix} 1 & -2s & s^2 \\ 0 & 1 & -s \\ 0 & 0 & 1 \end{bmatrix} \begin{bmatrix} \beta_0 \\ \alpha_0 \\ \gamma_0 \end{bmatrix}. \tag{2.4.28}$$

The matrix relation in equation 2.4.28 can be described as

$$\beta = \beta_0 - 2\alpha_0 s + \gamma_0 s^2, \tag{2.4.29}$$

$$\alpha = \alpha_0 - \gamma_0 s, \tag{2.4.30}$$

$$\gamma = \gamma_0. \tag{2.4.31}$$

In any linear optics section, beam emittance remains constant provided that there is no energy spread. According to equation 2.4.22, β determines the sigma of the beam at any point of a drift section. Thus, we can characterize the beam waist as a point with the smallest β. At this point (waist), the rate of change of β with respect to s ($d\beta/ds$) must be zero. Using this argument, equation 2.4.29 leads to the distance of the beam waist from the reference point (where the Twiss parameters are β_0, α_0, and γ_0)

$$s_w = \frac{\alpha_0 \beta_0}{1 + \alpha_0^2}. \tag{2.4.32}$$

Matching

In a beam transport system, the initial values of the Twiss parameters are usually preset, which depends on the design of the experimental requirements and pre-acceleration conditions such as particle source. These parameters evolve along the beamline and deviate from their initial values at different points of the system, which can be calculated using the transfer matrix. Moreover, various applications and experiments have specific requirements of optical functions. A suitable combination of quadrupoles and drift space can modify the Twiss parameters from their initial value to the desired value, known as matching.

In figure 2.4.6, a magnetic structure is employed for matching beam optics. The transfer matrix for each constituent quadrupole can be constructed using their strength (K). Following equation 2.4.20, the product of the transfer matrices of the quadrupoles and drift spaces provides the ulti-

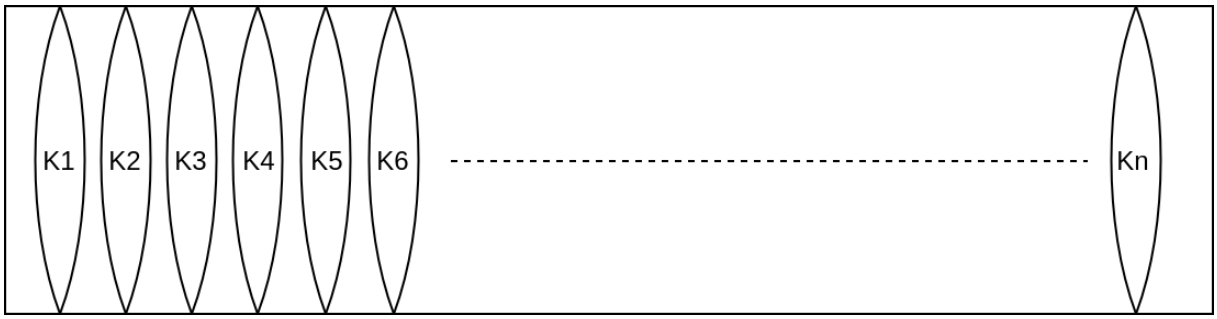

Figure 2.4.6: Combination of quadrupoles used for beam focusing and matching.

mate single particle transfer matrix between the initial to a final point.

Equation 2.4.27 shows the relation between the initial and the final Twiss parameters, which is non-linear. Conventional analytical methods can not determine the absolute solution of this equation. However, a numerical iteration method can obtain one of the approximate solutions to match the beam optics.

The alteration of quadrupole strength changes all Twiss parameters, thus a simultaneous matching is essential in both transverse directions. Their dependence on the quadrupole strength can be expressed as

$$F_i = f_i(K_1, K_2, K_3, ...K_n), \tag{2.4.33}$$

where F_i represents the Twiss parameter. After one iteration difference between the difference between the ideal value (F_{ideal}) of the Twiss parameters and the current value (F_0) can be written as

$$F_{ideal} - F_0 = A(K - K_0), \tag{2.4.34}$$

where A is known as the response matrix. K_0 is the arbitrary starting values of the quadrupols and K is the modified values [86]. The iterative relation can be describe as

$$K_{i+1} = K_i + A_i^{-1}(F_{ideal} - F_i). \tag{2.4.35}$$

The most effective match can be obtained with the equal number variables (quadrupole strengths and drift spaces) and Twiss parameters. However, different algorithms are available to match any number of constraints and optical functions. We will use a tool, MADX [87], to obtain matching conditions numerically. For example, MADX can calculate the incoming beam parameters needed to reach a specific beam condition at a point (like at the boundary of a water phantom), as discussed in chapter 7. A brief description of MADX is given in chapter 3.

Chapter 3

Simulation methods

Monte-Carlo (MC) simulation is a popular tool to study the microscopic world without complex experiments. It is widely used to investigate the interactions of radiations with matters and evaluate dose distribution. We used MC simulation to examine the proton beams' interactions in a water phantom. This chapter introduces the basics of the MC method and Geant4 simulation, including the basic setup used in our studies. It describes the algorithms used to produce the SOBP and calculate dose-averaged LET from the simulated data. In addition, it gives a brief description of MAD-X, a comprehensive tool to track particles in an accelerator.

3.1 Monte-Carlo Simulation

3.1.1 Monte-Carlo method

The MC method is used to obtain a numerical solution to a problem by random sampling from a known probability distribution based on theoretical considerations [88, 89]. It can be an alternative tool to study a microscopic system's behavior in the event that the analytical solution is complicated to obtain. In principle, it can mimic a complex procedure when an experimental assessment is impractical to conduct or costly. This idea was first adopted in the Manhattan Project during the second world war, where it played a prominant role in developing nuclear weapons. John von Neumann and Stanislaw Ulam recommended its inclusion to examine the properties of neutron diffusion through the fissionable materials [90]. It was named after the Monte Carlo Casino in Monaco to attribute the underlying concept of utilizing random numbers.

The principle of MC method for radiation transport is to simulate a large number of particles and record their properties of interest along their trajectories. In this process, a source generates primary particles and assigns initial values of specific properties like position, momentum, energy, etc., depending on the simulation's objective. These initial properties are selected randomly from a defined distribution. A geometry is implemented to transport the particles and study their interactions. The materials and dimensions of the geometry are defined depending on the goal of the

research. Simulated particles encounter a range of interactions along their path of propagation that can cause energy deposition. The mode of interaction and distance between any two consecutive interaction points are determined using several probability distributions that depend on the physics model. It also allows producing secondary or higher-order particles and and transporting them through the defined volume. During the interactions, properties like the energy of the particles are updated based on the physics principle. These particles are continuously transported as long they remain inside the volume of interest. Simulation of a particle is also terminated if it is absorbed by the interaction process like photoelectric absorption of a photon or its energy drops below a predefined threshold value.

The interaction probabilities per unit length govern a charged particle's transportation through a traversed material [91]. The random sampling of interactions and their outcomes at each step of the simulation can provide information equivalent to the Boltzmann particle transport equation [34]. However, MC simulation's advantage is that it is easier to implement with the same physics model. In practice, particle transport equation is implemented in MC simulation following three algorithms: track structure, condensed history, and mixed simulation.

The track structure algorithm can provide a detailed description of particle interactions and is capable of producing an exact solution of the transport equation. Thus an accurate reproduction of particle-matter interactions is possible [92]. It is a very useful feature of MC simulation for microdosimetric and nanodosimetric studies. However, it is computationally expensive and time-consuming, especially for higher energy particles [93]. Furthermore, these precise details of the track structure algorithm are not interesting for many studies.

In contrast, the condensed history algorithm analyzes the cumulative impact of a large number of collisions. At each step, the random selection of energy loss and angular deflection relies on the multiple scattering theories to diffuse the particle spatially through the material [94]. Since this algorithm is computationally inexpensive and more efficient, it is a natural choice to deal with high-energy particles. Due to its convenient implementation and sufficient degree of accuracy, the condensed history algorithm established itself as a reference method in clinical dosimetry of macroscopic scale [95].

On the other hand, the mixed algorithm uses track structure and condensed history simultaneously in the same simulation with an energy threshold to optimize the process. The energy loss by a collision above the threshold value is defined as hard or catastrophic is considered one individual event and simulated using the track structure algorithm. In contrast, soft collisions with energy-loss below the threshold value are grouped together, and their cumulative effect is studied using the condensed history algorithm. It can enhance the time efficiency and accuracy of the simulation. Several authors have extensively studied the comparison between the track structure and condensed history algorithm [96, 97, 98].

In general, the probability distributions are given by physics models, and gives the mode of in-

teraction in a given step of MC simulation.A large number of particles should be simulated to obtain a realistic result with physical significance. The uncertainty of the simulated outcome depends on the number of histories (n) taken. With an increasing n, the uncertainty (e) decreases following the relation, $e \approx 1/\sqrt{n}$.

3.1.2 Applications of MC simulation

With the increasing complexity of a stochastic problem, MC becomes preferable over the analytical approach due to its computational speed [99]. It has the potential to solve a wide range of problems [100]. It has already been adopted in various fields, including different branches of physics and biology, engineering, and finances [101, 102, 103, 104].

Implementing MC simulation in medical physics and particle transport has been increasing since the fourth quarter of the last century [105, 106]. Random sampling plays the central role in MC simulation. Advancement in modern computer algorithms can provide a long sequence of random numbers without repeating the period and offer an opportunity to use MC simulation to probe complex problems.

The continuous growth in computation power and memory in the past few decades [107, 108] has enhanced its adaptation of MC simulation. Due to technological advancement, the MC method has been proved beneficial in studying a wide range of features of radiation therapy, including dose estimation, beam delivery systems, nuclear imaging, and treatment planning [34, 99, 109, 110, 111]. Due to its ever-growing popularity, many MC simulation codes have been developed over the last few decades. Some of these codes are designed to implement track structure algorithm such as Geant4-DNA, NOREC, KURBUC, etc. [112, 113, 114]. Simultaneously a wide range of codes are available to implement the condensed history algorithm; among those, perhaps the most frequently used codes are Geant4, MCNP, FLUKA, EGS, and PENELOPE [115, 116, 117, 118, 119]. In this thesis, we have used Geant4 extensively to simulate proton beam's interaction in water.

3.1.3 Geant4

Geant4 (GEometry ANd Tracking 4) is a general-purpose MC simulation toolkit to study the trajectories and interactions of particles in the traversed material with an energy of a few eV to 10 PeV [120]. It was developed at CERN with a primary intention to simulate events at high-energy physics experiments. Large group researchers, engineers, and programmers from all over the world collaborate to maintain this C++ based toolkit. They are also responsible for the validation of new versions of the toolkit [121]. Its modular design facilitates the user with the flexibility to customize based on their research requirements. It is widely used in various research fields, including nuclear and particle physics, accelerator physics, astrophysics and space science, medical physics, and radiation protection. A large variety of particles can be studied using the Geant4 toolkit. It can simulate a number of interaction processes using a wide range of physics models with corresponding parame-

ters and cross-sections. Moreover, passage of particles through an electric and magnetic field can be simulated. The code allows multi-threading, which can significantly reduce the computation time of the simulation.

Geant4 offers a rich code library on which a user can build simulation tools. A user-defined geometry is one of the prerequisites for a simulation. The entire geometry is constructed in a three-dimensional space called the world volume. All other geometrical structures (daughters) are placed inside the world volume. It also enables importing a geometrical configuration from an external software like CAD (computer-aided design). Users essentially specify the materials for the geometrical components used for the simulation. These materials can be chosen from a predefined Geant4 database. Alternatingly, the user can construct self-defined materials specifying their chemical and physical properties like density, temperature, constituent elements, isotope, and their ratios.

Furthermore, the inclusion of a particle source and the desired physics list is essential. In a simulation, the particle source defines the primary particles' properties, such as their initial energy, momentum, position, direction, etc. The physics list describes the available particles and their interaction processes for the simulation. A set of predefined reference physics lists are available for inclusion in the simulation. Additionally, it allows the user to construct a custom physics list using a combination of models. In general, the physics list should be constructed based on the research interest, particles, and energy range. For a given number of histories, the computation time is determined by the physics list. Thus, an optimization between accuracy and execution time of a simulation should be carefully tuned by choosing an appropriate physics list. The validation studies and benchmarking of these physics lists have been performed for several applications of medical physics [122, 123, 124, 125, 126, 127, 128, 129, 130].

3.1.4 Simulation physics

In Geant4, the processes are used to implement the physical interactions between particles and the traversing material. All the processes provided by Geant4 can be classified into seven main categories: electromagnetic, hadronic, decay, photolepton-hadron, optical, parameterization, and transportation. Simultaneously, Geant4 provides a range of models to simulate various processes. One specific model cannot simulate all possible interactions of various particles within the entire energy range. Usually, the models are valid for particular particles within their associated energy range. A suitable model for a given energy range can be incorporated from a collection of competing models. The experimentally obtained cross-section can describe the interactions most realistically. However, experimental data are not available for all interactions over the entire energy range. Thus, a model is a combination of theory-driven results, parameterizations, and experimental data [131]. Several models might need to be deployed to cover the energy range of interest. The selection of models depends on the interacting particles and energy range. Besides, the user needs

to balance the accuracy and computation efficiency of the simulation. An appropriate combination of multiple models and processes can portray realistic interaction behavior. It can be implemented through a physics list that defines the primary and secondary particles of simulation, physics models and processes, production cut, step size, etc. These are the essential ingredient to execute an accurate and precise simulation of a microscopic world. Depending on the study's objective, the desired physics list is incorporated through a mandatory user class called "G4VUserPhysicsList".

In this work, the interaction of protons with water is the most crucial process to study the dose profile of a proton beam. A comprehensive list of proton interactions with the material has been discussed in chapter 2. These interactions can be classified as electromagnetic, elastic scattering, inelastic scattering of protons and neutrons, and inelastic scattering of heavier hadrons. Incorporation of a hadronic model is necessary to simulate nucleus-nucleus and particle-nucleus interactions. On the other hand, the electromagnetic model deals with the interactions that take place through electromagnetic force. Thus, hadronic and electromagnetic physics models are essential components of the physics list to study a therapeutic proton beam's behavior. Because of a small variety of options, electromagnetic interactions can be implemented conveniently. In contrast, a wide variety of exit channels makes the implementation of hadronic interaction challenging.

Geant4 offers two models to simulate electromagnetic energy loss of hadrons. These are the default model and low-energy parameterized model. The default model relies on the analytical description of electromagnetic interaction of all charged particles and chargeless photons down to 1 keV. The Bethe-Bloch equation is used to calculate the energy loss of hadrons with energy larger than 2 MeV. Below this limit, a stopping power-based parameterized formula of ICRU is used to obtain hadronic energy loss. Electromagnetic energy loss of electron and photon can be obtained down to 250 eV using the model's parameterization-driven low energy extension.

A physics list can be constructed by the user, which is the most flexible way of Geant4 simulation. However, it is comparatively tricky and error-prone. For each particle type, physics models must be specified with an effective energy range for every variant of interactions. Depending on the application, the user needs to select the appropriate physics models because Geant4 simulates the interactions registered explicitly in the physics lists. As a convenient alternative, Geant4 provides a number of precompiled physics lists called the reference list. The incorporation of these prebuild physics lists is simple and effective. Four physics lists could be used for effective simulation of medical physics studies. These are:

- QGSP_BIC_EM (EM Option0)
- QGSP_BIC_EMY (EM Option3)
- QGSP_BIC_EMZ (EM Option4)
- QGSP_BIC_HP_EMZ (EM Option4)

These physics lists combine different sets of models different models for electromagnetic and

hadronic processes. To study proton beam therapy's clinical aspects with a high level of accuracy, QGSP_BIC_EMY is strongly recommended [132]. It activates G4EMStandardPhysics_Option3 and the Urban multiple scattering model for simulation of particle interactions. QGSP stands for "Quark Gluon String Precompound" that initiates hadronic models to simulate the interactions of nucleons. It can imitate high energy nuclear excitation and subsequent de-excitation. BIC refers "Binary Ion Cascade" that activates the models to simulate inelastic interactions of ions. It is a suitable model to simulate the intranuclear cascade [133, 134]. The electromagnetic interactions of all particles are defined in EMY, which stands for ElectroMagnetic Y, particularly designed for medical applications.

Detailed comparison among the aforementioned reference physics lists has been published [134]. The EMZ option can produce the most accurate result; however, it is computationally expensive [134, 135]. To optimize simulation time and precision of results, we have therefore used QGSP_BIC_EMY for all simulations of this work.

3.1.5 Range cut and step size

The simulation transport parameters like range cut and step size impact the outcomes of proton beam studies such as LET and Dose. The range cut represents the production threshold of secondary particles [136]. In Geant4, secondary particles are produced by various physical processes. Continuous tracking of these particles is performed until they run out of total energy. Thus the range of a particle depends on its initial energy. The range cut production threshold is assigned as a distance using SetCut() method of G4UserPhysicsList(). It is internally converted to an energy for each combination of the simulated materials. If secondary particles' energy is less than this threshold value, their production is aborted, and the equivalent energy is deposited locally.

Moreover, the execution time increases exponentially at lower energy. For the optimum simulation time, a predefined minimum energy is needed to terminate simulation. After termination tracking of a particle, the remaining energy is deposited locally.

The step size limits the distance between two consecutive interactions. The accuracy of a simulation also depends on the step size. It is assumed that the energy of a particle remains constant during a step. The cross-section of interaction is energy-dependent; thus, a smaller step size can ensure a negligible change in energy, providing a more reliable cross-section for the entire step. On the other hand, it significantly impacts the simulation time; thus, a balance between time and accuracy is essential. We examined several step sizes to observe their impacts on dose profile and preferred to use the 0.2 mm step length for the studies. The maximum range of secondary electrons (see section 2.1.2) explains our preference of step length.

3.2 Dose and fluence calculation

A cylindrical water phantom was modeled to analyse the proton beam's dose deposition. The geometrical configuration of the target (water phantom) is given in figure 3.2.1. The entire target was divided into cylindrical slices of 0.2 mm thickness each. The slice shown in figure 3.2.1B was divided into 2000 concentric cylindrical elements (rings) with a radial thickness of 0.1 mm.

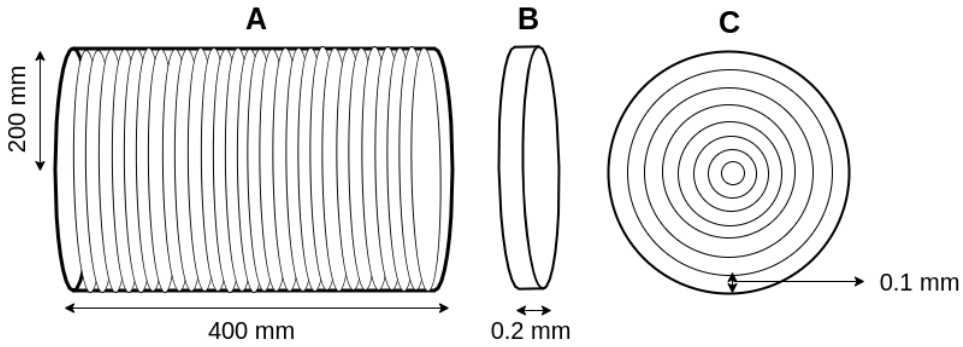

Figure 3.2.1: Cylindrical configuration implemented in MC simulations to obtain dose profile. Water phantom was modeled to study the effects of proton irradiation in a tissue-equivalent environment.

The energy deposited by the simulated particles at a volume element was accumulated. The dose was calculated as

$$D = \frac{\Delta E}{\Delta m}, \tag{3.2.1}$$

where ΔE is the amount of energy imparted and Δm is the mass of the volume element that is calculated as

$$\Delta m = \pi(r_2^2 - r_1^2)\rho t. \tag{3.2.2}$$

The density of water is $\rho = 997\ \mathrm{kgm}^{-3}$, t represents the thickness, and $r_2 - r_1 = 0.1\ \mathrm{mm}$ for a ring. The dose for any cylindrical configuration (wide or narrow) can be obtained using $r_1 = 0$ and $r_2 = r$.

The (r, z) coordinate was used to obtain the radial dose distribution as shown in figure 3.2.2. Due to the azimuthal symmetry of dose distribution, this configuration could provide an realistic dose map. The (r, z) dose distribution can be used to obtain longitudinal and transverse dose profiles of cylindrical configurations of any radius.

In parallel, a three-dimensional Cartesian grid was also employed to determine the dose deposition pattern. The dimension of each 3D voxel was $0.2\ \mathrm{mm} \times 0.2\ \mathrm{mm} \times 0.2\ \mathrm{mm}$. The amount of energy deposited by any particle at point (x, y, z) is recorded using ROOT histograms by registring it into the corresponding voxel. The radial distance r of point (x, y, z) from the beam's central axis is $\sqrt{(x^2 + y^2)}$, where z is the direction of propagation of the beam. Individual histograms were constructed for primary protons, secondary protons, neutrons, electrons, photons and alpha particles.

Simultaneously, the particle fluence was calculated along the depth at an interval of 1.0 mm. The number of particles (N) passing through a predefined circular area around at the central axis

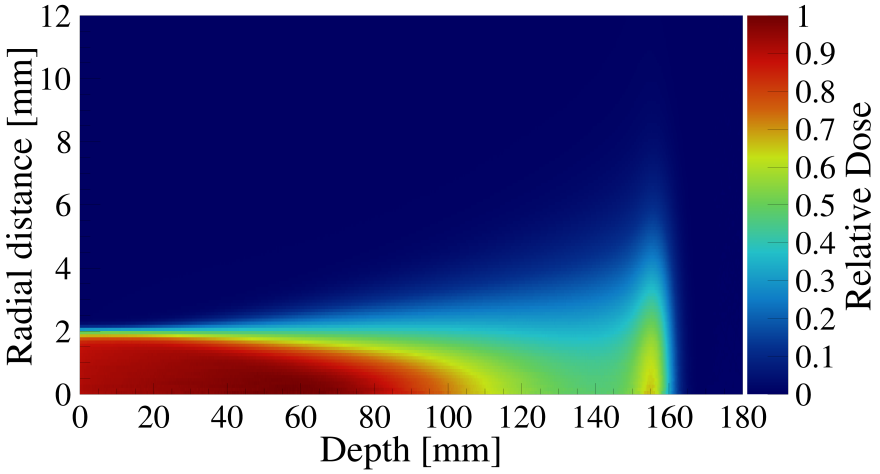

Figure 3.2.2: Two-dimensional (r-z) dose profile of 150 MeV proton beam in water. The dose is normalized to the peak value.

of the beam was recorded. The average fluence was calculated as

$$\phi = \frac{N}{\pi r^2}, \tag{3.2.3}$$

where r is the radius of the assessed area. Fluence was calculated for a range of circular areas of radius 1.0 to 25.0 mm, and also of 200 mm, which is the radius of the simulated water phantom..

3.3 LET calculation

The dose-averaged LET (LET_d) was calculated as a function of depth in the modeled water phantom. The energy deposited by protons (ε) and their step lengths (l) were determined by simulating the interaction of a proton beam with water. The value of ε^2/l at each longitudinal bin of size 0.2 mm was accumulated. Simultaneously, the energy deposited by the protons was recorded to determine $\sum_{i=1}^{n} \varepsilon_i$ at each bin. These quantities were used to calculate LET_d at a given depth using equation 2.1.28.

3.4 SOBP algorithm

The SOBP is constructed by superimposing multiple pristine Bragg peaks to produce a uniform dose over an extended longitudinal space (see figure 2.3.2). The relative intensity (fluence) of the constituent beams is modified to achieve the goal. Bortfeld and Schlegel developed a simple analytical method to determine the weighting factors for beam's intensity [137]. Numerical methods can be employed to determine the accurate weighting factors. We used the method of least squares [138] to determine optimum weighting factors to produce uniform dose in an extended range. The lenght (longitudinal spread) of an SOBP was split into $(n-1)$ segments by n equispaced points. The unmodulated dose of m beams (of different energies) was determined at these points.

The optimum weighting factors were determined from the numerical solution of equation

$$Ax = B, \tag{3.4.1}$$

where the matrix A gives the magnitude of doses at the target without modulation of the beams, the matrix B contains desired doses at the target and the matrix x represents the relative fluences of the beams. The matrices A, x, and B can be expressed as

$$A = \begin{bmatrix} a_{11} & a_{12} & \cdots & a_{1m} \\ \vdots & \vdots & \ddots & \vdots \\ a_{n1} & a_{n2} & \cdots & a_{nm} \end{bmatrix}, \quad x = \begin{bmatrix} f_1 \\ \vdots \\ f_m \end{bmatrix}, \quad B = \begin{bmatrix} b_1 \\ \vdots \\ b_n \end{bmatrix}, \tag{3.4.2}$$

where a_{ij} is the unmodulated dose of beam number j at point number i, b_i is the desired dose at point number i and f_j is the relative intensity of beam number j to produce the desired dose. If equation 3.4.1 does not have any absolution solution, the error can be expressed as

$$\epsilon = B - Ax. \tag{3.4.3}$$

The optimum solution can be found through the minimization of ϵ. It can be simply done by solving $A^T Ax = A^T B$, where A^T is the transpose of A. To avoid negative weighting factors, which does not have any physical interpretation, we used the "optimize.nnls" function of Scipy [139] package of Python, which determines an optimum solution for non-negative values of the weighting factors.

3.5 MAD-X

MAD (Methodical Accelerator Design) is developed at CERN for accelerators design and beam optics analysis over many years. It is a widely used tool for tracking particles in accelerators and lattices. The most recent version, known as MAD-X, was introduced in 2002 [87]. Currently, it is maintained by a dedicated group of people. It can be used using interactive mode through a command line. Besides, MAD-X can also be executed in batch mode, where all the commands can be provided through a file.

We used MAD-X exclusively for matching (discussed in section 2.4.2), an effective optimization tool to determine magnet strengths to tune beam optics. It relies on the optimum solution of a system of non-linear equations. Because of several local minima, it is often tricky to obtain the global solution. The initial value of variables has an impact on the final solutions. Manual tuning of initial values helps to find an optimum global solution.

The MATCH command can produce an optimum magnetic configuration based on the user-defined constraints and ranges. MAD-X offers several matching algorithms. LMDIF and SIMPLEX are the most commonly used algorithms, which are computationally less expensive than the JA-

COBIAN algorithm. Even though LMDIF is the fastest algorithm, its implementation is limited with the number of variables is less or equal to the number of constraints. Moreover, differentiable constraints are a prerequisite for its implementation. On the other hand, an effective solution to a set of non-differentiable constraints can be obtained using SIMPLEX. The JACOBIAN algorithm is suitable for a system with an arbitrary number of constraints and variables. It is more effective when the variables are very close to the solutions. To execute the match operation, the user needs to define at least one sequence which includes all components and their positions along the beamline.

Chapter 4

Collimated beams

A very narrow beam of ionizing radiation is a crucial element to treat small tumors. It has the potential to reduce side effects of treatment by decreasing normal tissue exposure [140]. It is also an essential component to implement several proton-based treatment modalities, particularly proton microbeam radiotherapy, proton minibeam radiotherapy, and proton GRID therapy. A metal collimator of a suitable material is naturally the first preference to produce a narrow beam due to its simple construction and convenient implementation. The geometry and material of the collimator have a significant influence on the dose distribution [70]. It also determines the number of secondary particles generated, including neutrons [70]. Implementation of the collimator in proton therapy systems needs a detailed understanding of the dose profile of the collimated beam (CB). This chapter explores the properties of CB through simulation.

4.1 Collimated beam generation

In principle, a collimator produces a narrow beam from its initial broader parent by chopping off a fraction of initial particles based on its aperture. We have imitated the procedure in our simulations, in order to produce circular proton beams of various radii between 0.5 mm to 6.0 mm. The length of the collimators was 200 mm, which we optimized by reducing the length until a significant fraction of 250 MeV primary protons were not stopped. The simulations modeled cylindrical lead (Pb) collimators with an outer radius of 200 mm. The inner radius (R) was varied to obtain beams of desired widths. If not mentioned otherwise, collimator radius refers to the inner radius (radius of the hollow section).

In the simulations, the proton beam was introduced at 800 mm away from the water phantom using Geant4 particle source. The collimators were placed between the primary source and the cylindrical water phantom to modify the beam's shape before reaching the circular entrance surface of the modeled phantom. As shown in figure 4.1.1, the center of the primary Gaussian source was placed at the central axis of the phantom and the collimator. The direction of propagation of the

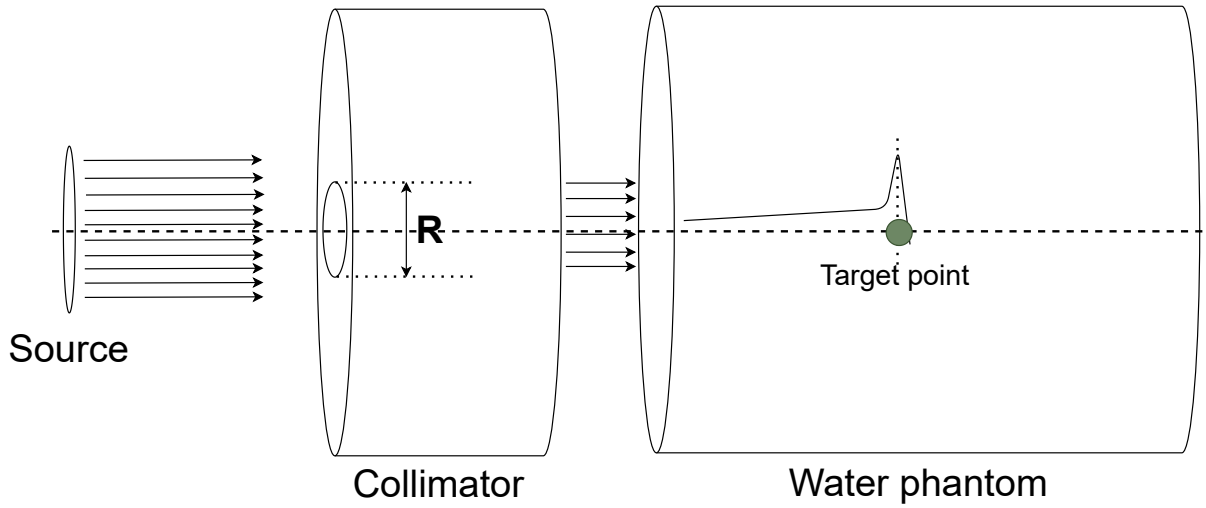

Figure 4.1.1: Principle of CB generation scheme using lead collimator of length 200 mm and outer radius 200 mm. The primary beam is circular Gaussian. The standard deviation of the energy distribution of the primary beam is 1% of the beam energy. The inner radius was varied to produce a beam of the desired size.

beam is parallel to the length of the phantom.

The Geant4 particle source generates particles based on the preset parameters. Besides particle type and energy, the initial position and direction of each particle are essential elements of the beam generation algorithm. The initial beam was designed to be a circular Gaussian of size[1] (σ_u) 6.0 mm. The values of the Twiss parameters, α and β, were given as inputs. The emittance was calculated for each set of variables, and the covariance matrix was constructed for both transverse planes. The initial transverse phase space of the primary beam was generated using bivariate Gaussian distribution based on the covariance matrix. The desired beam was produced by sampling from the transverse phase space distribution. This method of beam generation was designed by following the open-source Geant4 wrapper MiniScatter [141]. The spatial and angular distribution of the beam depends on the Twiss parameters. The initial value of α and β were 0 and 18.8 m, respectively, for all simulations of CB. Impacts of kinetic energy were studied by simulating proton beams of various energies. The initial beam energy at the source had a Gaussian distribution where the standard deviation of the distribution was 1% of the beam energy.

4.2 Longitudinal Dose Profile

In the simulations, the CB entered the water phantom through the circular surface. It deposited energy within the vicinity of its path. The desired beam should be composed of primary protons exclusively. However, the presence of a metal collimator can be a reason for beam contamination. A counter was incorporated at the entrance to record the number of different particles. As expected, the major constituent of the CB was primary protons. However, the counter also identified sec-

[1]We use σ_u in general to represent circular beam's transverse size, where $\sigma_u = \sigma_x = \sigma_y$.

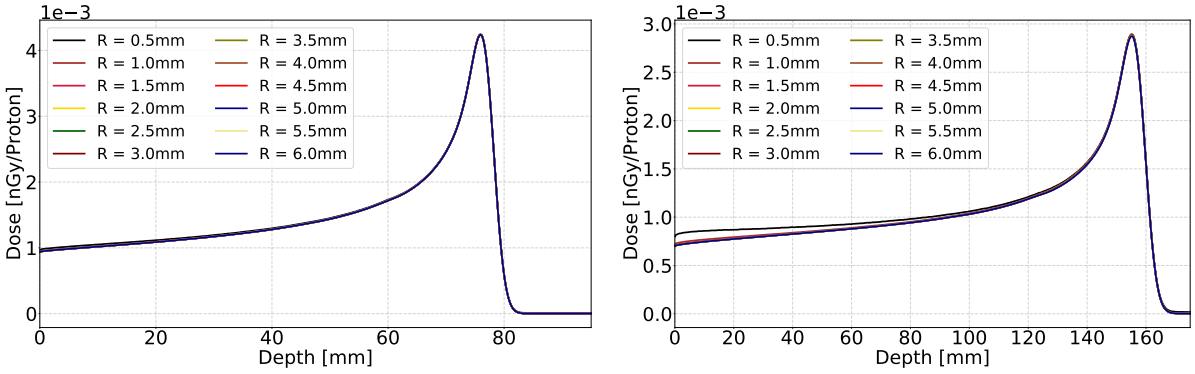

(a) (b)

Figure 4.2.1: Comparison of the depth-dose curves of proton beam of various collimator radius obtained with beam energy (a) 100 MeV and (b) 150 MeV. The dose is calculated using cylindrical elements of radius 200 mm and length 0.2 mm. The contribution of all protons (primary and secondary) is considered for dose calculation.

ondary proton, neutron, alpha, and a small number of other particles. The relative numbers of different particles were observed to vary with beam energy and collimator size. A similar impact of collimators has been noticed by Guardiola et al. [70].

We calculated dose as a function of the depth. The details of the dose calculation method have been discussed in section 3.2. The dose obtained with a wide geometrical configuration provides an average impact of energy deposition, which we labeled “average dose”. In contrast, the locally deposited radiation energy has been quantified using the “central axis dose”, which was calculated for cylindrical elements with a very small radius around the beam center.

4.2.1 Average dose

The average dose along the longitudinal direction was calculated using equation 3.2.1. We considered cylindrical volume elements of radius 200 mm (equal to the radius of the water phantom) and length of 0.2 mm for dose calculation. Figure 4.2.1 shows the dose-depth curve of proton in water for 100 MeV (a) and 150 MeV (b) energy. For each energy, the radius of the collimator was varied between 0.5 mm to 6.0mm. We accumulated the energy imparted by all protons (primary and secondary) within the volume element for the dose calculation.

The depth-dose curves of proton beams (both primary and secondary) in figure 4.2.1 are similar for all values of the collimator radius and beam energy. For a given energy, the Bragg peak (BP) position can be predicted from the range-energy relation given in equation 2.1.18, and it is independent of the collimator radius, which explains the coincidence of BPs. In figure 4.2.1 the depth of BP is 76.0 mm and 155.2 mm for 100 MeV and 150 MeV beams, respectively. In general, the surface dose (D_{Sur}) of the 100 MeV proton beam is larger than the 150 MeV beam. For a 1 mm collimator, the D_{Sur} of 100 MeV and 150 MeV proton beam are 9.46×10^{-4} nGy/proton and 7.21×10^{-4} nGy/proton, respectively. The higher stopping power at smaller energy is responsible for the enhanced D_{Sur} of lower energy beam (see equation 2.1.16). In addition, the Bragg peak

dose (D_{BP}) of 100 MeV proton beam is 50% higher than the 150 MeV beam.The range straggling, which becomes more significant with increased range, explains this difference along with the more notable drop of primary fluence of a higher energy beam (see figure 2.1.4b).

It is also remarkable that the D_{Sur} slightly varies with the collimator radius in spite of identical energy. It is 8.01×10^{-4} nGy/proton for 0.5 mm proton beam with 150 MeV initial energy, which is 10.1% higher than the 1.0 mm beam of identical energy. In contrast, smaller discrimination in D_{Sur} among various collimator sizes can be observed for the 100 MeV energy. It decreases from 9.70×10^{-4} nGy/proton to 9.46×10^{-4} nGy/proton when collimator radius increases from 0.5 mm to 1.0 mm. Overall, D_{Sur} of a narrow beam is higher than a wider one of the same energy, and the difference among various collimator radius is more prominent for the higher energy (150 MeV) proton beam. However, for both energies, the discrepancy in D_{Sur} disappears at larger R (>2.0 mm).

The discrimination of D_{Sur} among different collimators can be explained using the concept of slit scattering and secondary particle dose. The slit scattered protons are produced if the degradation of the proton's energy through the interactions with the collimator is insufficient to stop it completely [142]. These protons can be classified into "inners" and "outers" categories. A proton is considered to be in the prior category if it enters through a collimator's opening and grazes through the far corner. In contrast, a proton from the outers category enters outside the nominal radius but managed to back into the collimator's hollow space through multiple scattering. Protons from both these categories contaminate the beam with lower energy particles. As a consequence of their reduced energy, the slit scattered protons have a smaller range than their non-interacting counterpart. A collimator with a smaller opening is likely to produce more slit-scattered protons (larger fraction of the total number of protons). The lower energy slit scattered protons deposit their energy within a small depth of water, caused an enhanced D_{Sur}. It can also be a reason for the different D_{Sur} of collimated and non-collimated beams we observed in simulations. The D_{Sur} of 150 MeV proton beam was 7.21×10^{-4} nGy/proton for the 1.0 mm collimator, which was 4.6% higher than the non-collimated beam of identical energy.

The probability of slit scattering increases as the collimator gets narrower. In addition, the initial beam energy can influence the number of slit scattered protons. At higher energy, protons are more likely to survive without being stopped by the interactions. This energy effect can be noticed in figure 4.2.1, where the 150 MeV proton beam has a higher D_{Sur} dose enhancement for smaller collimator radius.

In addition, a significant number of secondary particles produced by the collimator were recorded through simulations. The number of secondaries was observed to increase for narrow collimators and higher beam energy. These secondaries can contribute in D_{Sur}. However, the depth-dose curves produced using exclusively the energy deposits from protons exclude exclude the contribution from other particles. According to the definition of secondary proton discussed in section 2.1.2, the slit scattered protons are in this category. Their effect can be excluded by considering primary proton

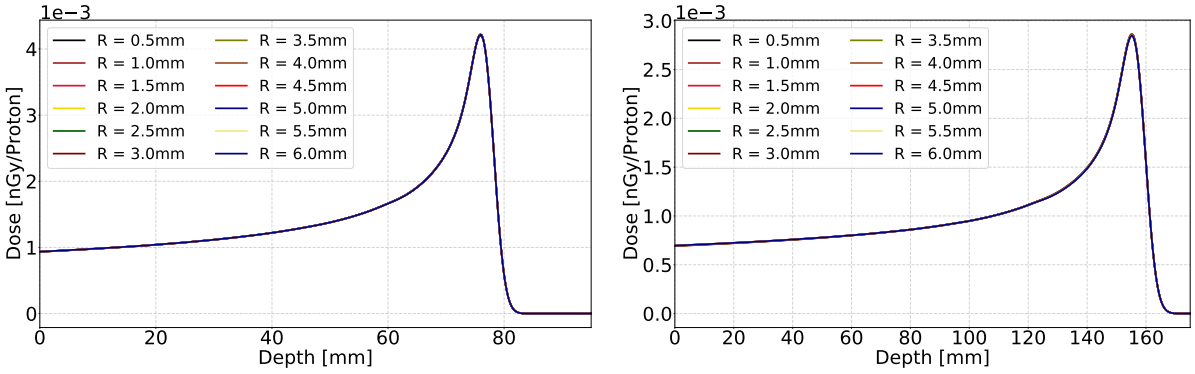

(a) (b)

Figure 4.2.2: Comparison of the depth-dose curves of proton beam of various collimator radius obtained with beam energy (a) 100 MeV and (b) 150 MeV. The dose is calculated using cylindrical elements of radius 200 mm and length 0.2 mm. The contribution of the primary protons is considered for dose calculation.

exclusively for dose calculation. The identical depth-dose curves of primary protons in figure 4.2.2 are in good agreement with our reasoning.

4.2.2 Central axis dose

The evaluation of the central axis dose reveals interesting features of CB. We used cylindrical volume elements of 0.5 mm radius and 0.2 mm length at the beam's central axis to determine the local dose deposition. The depth-dose curves for 100 MeV and 150 MeV proton beam are depicted in figure 4.2.3. A sharp contrast between the average dose and the central axis dose can be noticed from their longitudinal dose profile. The D_{Sur} of 100 MeV proton beam is higher than the Bragg peak dose (D_{BP}) for 0.5 mm and 1.0 mm collimators. It is also true for 150 MeV proton beam. In addition to 0.5 mm and 1.0 mm, it exhibits a higher D_{Sur} for 1.5 mm and 2.0 mm collimators. The central axis depth-dose curve approaches the characteristic proton depth-dose curve (with a higher value of D_{BP}) as the collimator radius increases. However, it simultaneously reduces the magnitude of the dose at the beam's center. The depletion of proton fluence at the center of a beam can explain the unusual pattern of the central axis depth-dose curves produced with a narrow collimator [32].

The proton fluence at the central axis was determined in the simulations, and the result is shown in figure 4.2.4. A circular area of radius 1.0 mm around the central axis was considered for fluence quantification using equation 3.2.3. The number of incident protons within this predefined area was recorded. Both primary and secondary protons were considered in the fluence calculations. As we have discussed in section 2.1.2, inelastic nuclear interactions reduce fluence, as it can cause depletion of primary protons. The cross-section of nuclear interactions within the therapeutic range can not explain the sharp drop of central axis proton fluence observed for narrow collimators as shown in figure 4.2.4. This rapid drop of fluence was produced because of scattering out of proton from the center of the primary beam. Considering a narrow beam, the fraction of primary protons moving out along the transverse direction is very large, leading to a drastic drop of the center

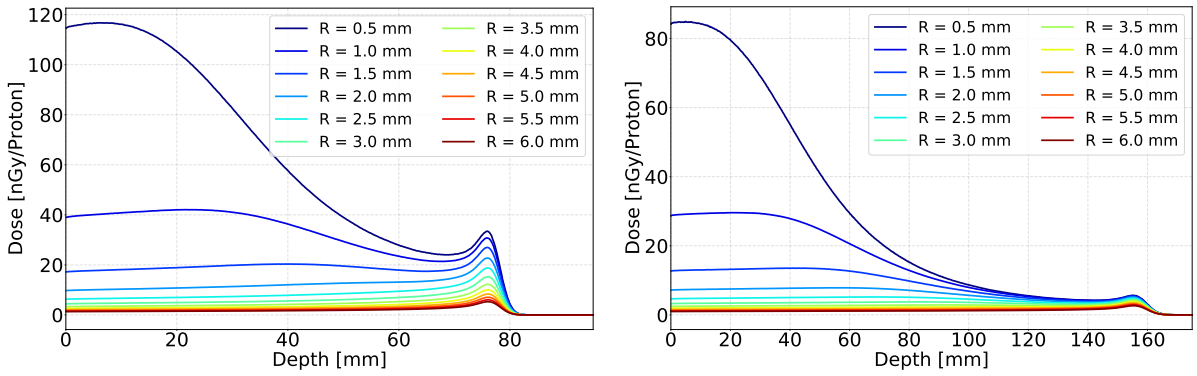

(a) (b)

Figure 4.2.3: Comparison of the central axis depth-dose curves of proton beam of various collimator radius obtained with beam energy (a) 100 MeV and (b) 150 MeV. The dose is calculated using cylindrical elements of radius 0.5 mm and length 0.2 mm.

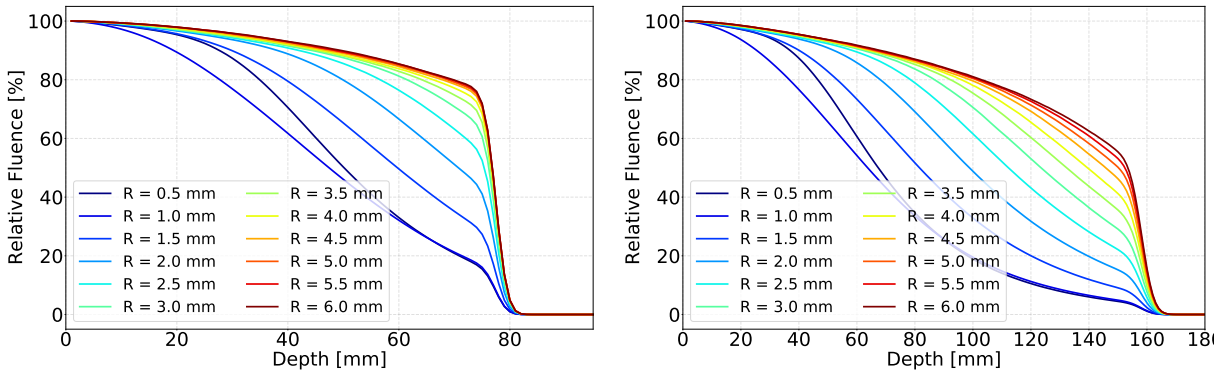

(a) (b)

Figure 4.2.4: Evolution of the central axis proton fluence obtained for (a) 100 MeV and (b) 150 MeV proton beam as a function of depth in the water phantom. The impact of the collimator radius is compared for both of the energies. The fluence is calculated for a circular area of radius 1.0 mm.

axis fluence. Consequently, the central axis dose decreases following equation 2.1.24. A broader beam experiences a smaller drop of fluence at the central axis. The simultaneous inward scattering of protons from the periphery of the beam balances the outward scattering, leading to a lateral equilibrium at the beam's center. The most prominent drop can be noticed if the fluence is calculated for an area equal to the collimator's aperture.

As illustrated in figure 4.2.5, both D_{Sur} and D_{BP} of a proton beam at the central axis decrease as a function the collimator radius. The drop in D_{BP} is prominent for 100 MeV beam. It decreases from 33.5 nGy/proton to 5.3 nGy/proton while the radius increases from 0.5 mm to 6.0 mm. Within the same range of collimator radius, the D_{BP} of 150 MeV proton beam decreases from 5.6 nGy/proton to 2.7 nGy/proton. In contrast, D_{Sur} varies within a larger range, from 114.7 nGy/proton to 1.3 nGy/proton for 100 MeV and 84.2 nGy/proton to 0.96 nGy/proton for 150 MeV beam energy. As the fluence changes reciprocally with the area (πR^2 for a circular beam), it drops at the surface of the water phantom as a function of radius. Consequently, the dose at the surface decreases with R following the inverse square law ($1/R^2$).

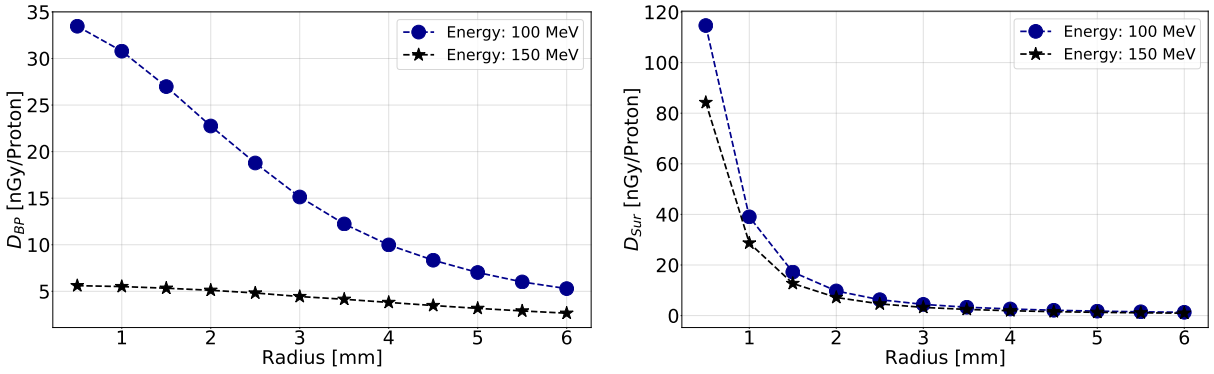

(a) (b)

Figure 4.2.5: Evaluation of (a) D_{BP} and (b) D_{Sur} of proton beam (calculated at the central axis) as a function of collimator radius. Impact of initial beam energy is compared using 100 MeV and 150 MeV beams.

Even though both D_{BP} and D_{Sur} decrease with the collimator radius, the rate of reduction of D_{Sur} is more prominent than the D_{BP}. Consequently, the Bragg peak to surface dose ratio (D_{BP}/D_{Sur}) at the central axis of the proton beam increases with the collimator radius as illustrated in figure 4.2.6a. The gradient of graphs decreases after an initial rise. A larger value of D_{BP}/D_{Sur} is desirable, at least greater than 1, which implies a larger dose at the target point than the surface. The D_{BP}/D_{Sur} of the 100 MeV proton beam is 0.292 for 0.5 mm collimator. It is saturated at around 4 beyond 5.0 mm collimator, whereas 150 MeV proton beam starts with 0.0665, which is approximately 23% of 100 MeV. Within the assessed range of the collimator radius, it (150 MeV beam) does not reach its saturation. The value of D_{BP}/D_{Sur} is 2.75 for 6.0 mm collimator. It is around 70% of 100 MeV proton beam of an identical collimator. A higher D_{BP}/D_{Sur} can be achieved with a wider beam. In contrast, a narrow beam geometry deposit several folds larger surface dose than the Bragg peak dose that can be a potential limitation of its (CB) practical implementation.

Figure 4.2.6b shows the ratio of dose of 100 MeV and 150 MeV (D_{100}/D_{150}) proton beam as function of collimator radius. The ratio of D_{Sur} of these two energies remains constant for all collimators. In contrast, the ratio of the D_{BP} drops significantly. It provides a piece of crucial information to determine the CB's suitability at the treatment system. With lower beam energy, a smaller radius of the collimator can provide a several times higher peak dose than a higher energy beam. Thus, a narrow collimator can be preferred to produce a small high dose spot in a shallow region. By contrast, a higher energy narrow CB is limited by the multiple scattering and can not precisely deliver a large dose at the target point.

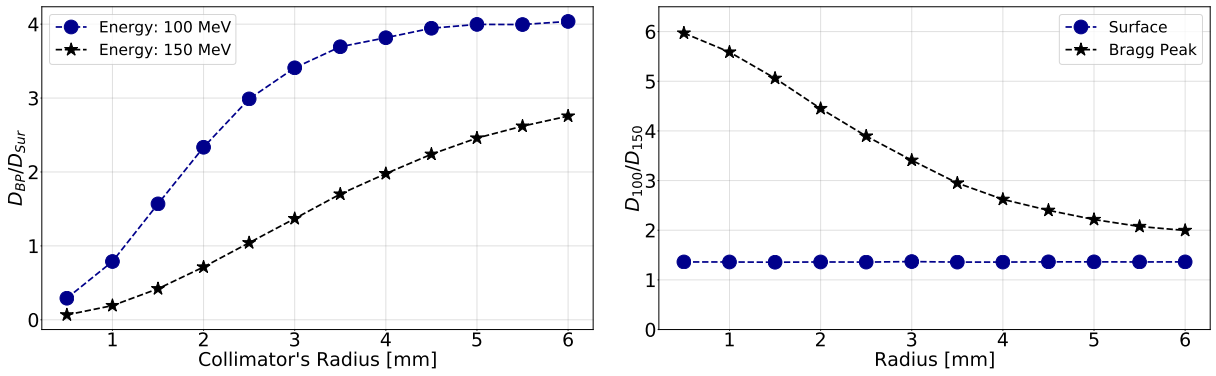

(a) (b)

Figure 4.2.6: (a) Comparison of the D_{BP}/D_{Sur} of 100 MeV and 150 MeV as a function of collimator radius. (b) D_{100}/D_{150} at the Bragg peak and surface of the water phantom.

4.3 Two dimensional dose profile

two-dimensional (x-z) dose profiles of CB are illustrated in figure 4.3.1. We considered the beam's central section (0.2 mm along y-axis) instead of the entire beam's projection on the x-z plane. It can provide a more meaningful impression of 2D dose distribution. The volume of the scoring voxel was $0.2\ \text{mm} \times 0.2\ \text{mm} \times 0.2\ \text{mm}$. Amount of energy deposited by the primary and secondary protons within each voxel was accumulated in the simulations. The ratio of this accumulated energy and mass of the voxel is used to obtain the dose.

The impact of the beam's initial energy and collimator radius on the dose distribution can be evident in the 2D dose profile. As the beam gets narrower, the shallow region's dose becomes significantly higher than the target's dose (BP dose), which we have also noticed in the central axis dose profile. Due to the smaller stopping power at higher energy, the amount of energy deposition by the protons at the entrance is smaller. However, it is confined within a smaller volume of the water phantom and, in consequence, produces a higher dose. With increasing propagation depth, the stopping power gets larger and more energy is deposited at the BP region. The simultaneous lateral expansion increases the volume of the energy deposition and reduces the BP dose of a narrow beam.

In addition, 150 MeV proton beam exhibits a lower dose at BP compare to 100 MeV beam. It can be seen in figure 4.2.1 that the position of Bragg peak of 150 MeV proton beam is more than twice as deep as 100 MeV beam. In its longer passage in water, 150 MeV beam encounters a higher number of MCS and expands more along the lateral direction. Consequently, deposited energy is spread over a larger mass and reduces dose.

The proton beam generated with the 1.0 mm collimator produces a significantly higher dose at the non-target region, especially with 150 MeV initial energy. Thus, it might be challenging to treat a deep-seated small tumor using CB. However, the spot size of a lower energy beam is smaller. It implies that a small tumor near the surface can be effectively irradiated using a narrow CB.

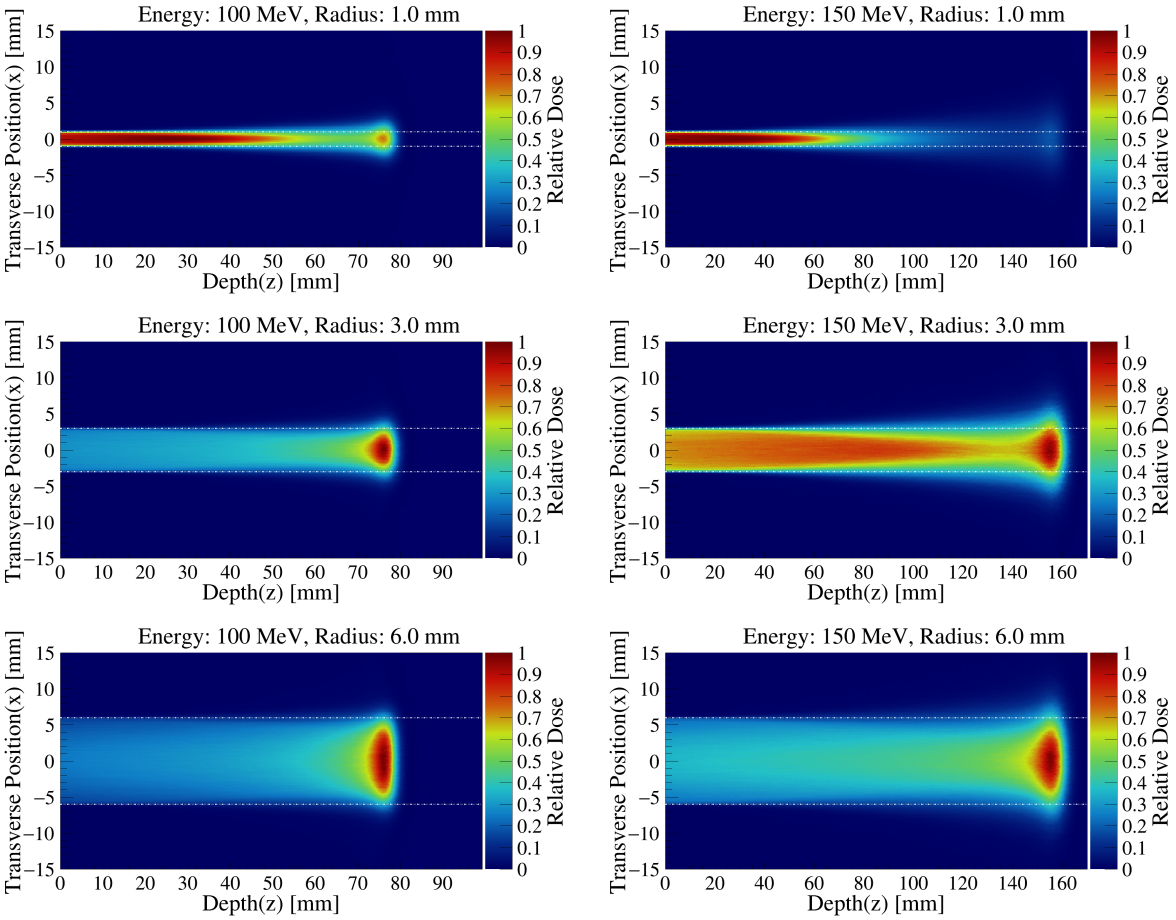

Figure 4.3.1: Two-dimensional physical dose profiles of 100 MeV (left) and 150 MeV (right) proton beams with collimator radius of 1.0 mm, 3.0 mm, and 6.0 mm. The dose is normalized to the peak value and the number of protons entered inside the water phantom.

4.4 Transverse dose profile

As the beam propagates through water, protons experience various interactions, as we have discussed in chapter 2. The MCS causes deflection of particels (see section 2.1.2). Consequently, the beam spreads out, and its transverse profile changes with depth. The beam energy strongly influences the overall effect of the MCS. At higher energy, the scattering angle is very small following Highland's formula given in equation 2.1.12. The energy of the beam decreases as it goes deeper into the water, and the scattering effect becomes more prominent. At the last few mm of its range, the beam experiences the most significant scattering effect, and it expands at the highest rate along the lateral direction.

The cylindrical collimators cut out the initial Gaussian beam's tail and provide a well-defined circular beam at the entrance of the water phantom. The radius of the circular beam at the entrance depends on the collimator's opening. In figure 4.4.1, the two-dimensional (x-y) transverse dose profiles of 150 MeV proton beam at 20.0 mm and 155.2 mm (BP) depth are compared for collimator radius of 1.0 mm, 3.0 mm, and 6.0 mm. Despite their circular shape, the beams have a

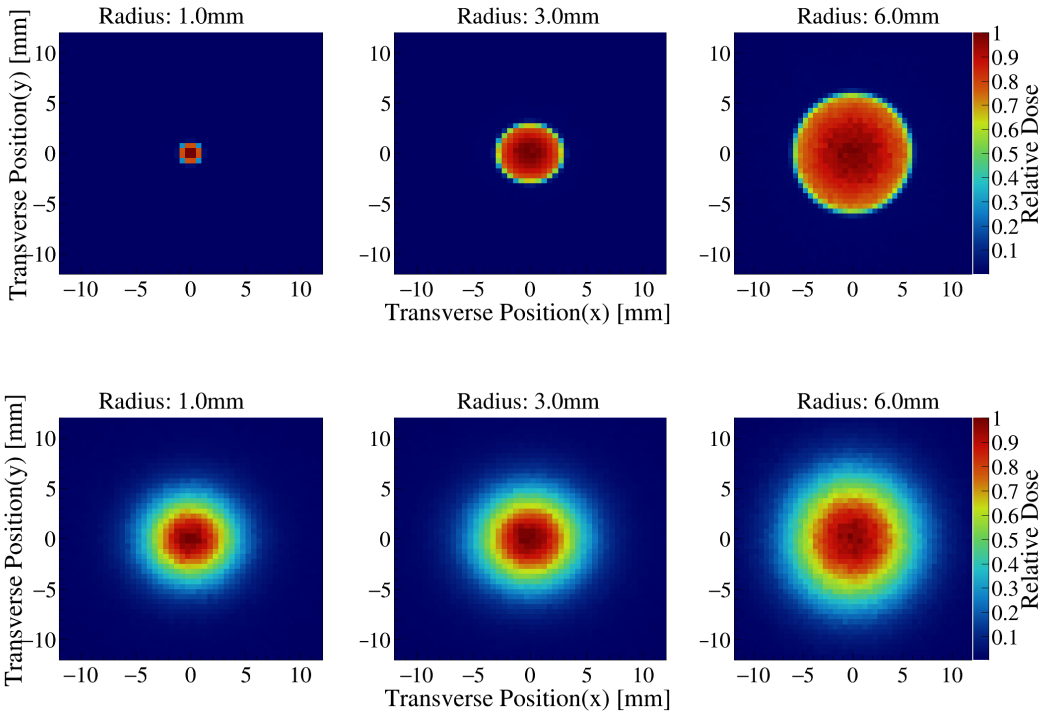

Figure 4.4.1: Two-dimensional transverse dose profile of 150 MeV proton beam at 20 mm (top row) and at Bragg peak (bottom row). The dose profiles are obtained for the collimator radius of 1.0 mm (left), 3.0 mm (middle), and 6.0 mm (right). The dose is normalized to the peak dose value and the number of proton entered into the simulated water phantom.

Gaussian distribution. There is a significant difference in beam dimension at the shallow region governed by the collimator radius. In addition, they have a very sharp edge in this region. As the beams propagate, their transverse size grows. The difference between their transverse size is less pronounced at the BP region, especially among the beams generated by the 1.0 mm and 3.0 mm collimator.

We have quantified the increase of beam's transverse dimension using the standard deviation of the lateral distribution of energy deposition (we will specify it as transverse beam size or beam size (σ)). The Gaussian fit of the simulated data has been obtained using 'fit' function from ROOT. This function provides fit parameters, including the standard deviation of the distribution. The full width at half maximum (FWHM) is another commonly used parameter to quantify the lateral expansion of a beam, and for a Gaussian distribution it is related to σ as

$$\text{FWHM} = 2\sqrt{2\ln 2}\sigma \approx 2.355\sigma. \tag{4.4.1}$$

Figure 4.4.2 shows the expansion of the transverse size of 100 MeV and 150 MeV proton beam as a function of depth. The difference among the beams' size is more significant in the shallow region. This disparity in σ gets compressed as the beam travels deep into the water. All the simulated beams, independent of collimator radius, follow a similar pattern of lateral growth. In a narrow

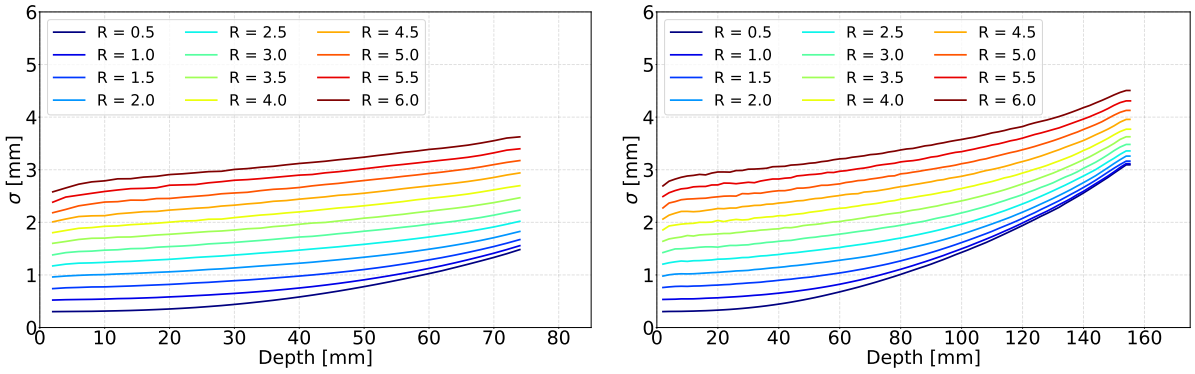

(a) (b)

Figure 4.4.2: Evolution of the transverse size of (a) 100 MeV and (b) 150 MeV proton beam as a function of depth in the water phantom. The impact of collimator radius is compared for both of the energies. The statistical error in σ was found within 2 micrometers.

beam, protons are more likely to scatter out from their primary beam dimension. Thus, the relative spread of the 0.5 mm beam is most notable.

The Bragg peak plays the most crucial role in the treatment using proton RT. The transverse dose profile at this region is an important parameter to evaluate beam performance to treat small tumors preciously, sparing healthy tissue. Figure 4.4.3 illustrates the transverse dose profile of 100 MeV (a) and 150 MeV (b) proton beam at their Bragg peaks. The spread of the distribution is smaller for the lower energy beam. However, it increases faster as a function of collimator radius.

In figure 4.4.4, we have assessed the collimators' efficiency to produce narrow beams at the Bragg peak, which position is generally considered as the target of RT using proton beam. We have calculated transverse beam size at Bragg peak for 100 MeV and 150 MeV proton beam with a range of collimator radius (figure 4.4.4a). As we mentioned before, the 150 MeV proton beam produces the Bragg peak much deeper than the 100 MeV beam. It encounters more scattering interaction; as a result, it has a larger transverse size at BP. A narrower collimator can reduce the transverse beam size, but the effect diminishes for a collimator of a very small radius, as shown in figure 4.4.4a. With a 150 MeV proton beam, the transverse size at BP is not practically impacted below R = 1.5 mm. However, there is an opportunity to slightly reduce the final spot size of 100 MeV proton beam by using a narrower collimator. A collimator of 0.5 mm radius can keep the 100 MeV beam's transverse size below 1.55 mm at the Bragg peak.

In figure 4.4.4b, the growth of transverse beam dimension with depth is quantified using the percentage increase of σ between entrance (10.0 mm) to the BP. The 0.5 mm collimator with 150 MeV energy exhibits the highest growth of 830%. Using an identical collimator with a 100 MeV beam leads to a 409% increase. As the collimator radius gets larger, this growth declines. The 6.0 mm collimator ends up with 67% and 37% change for 150 MeV and 100 MeV proton beam, respectively.

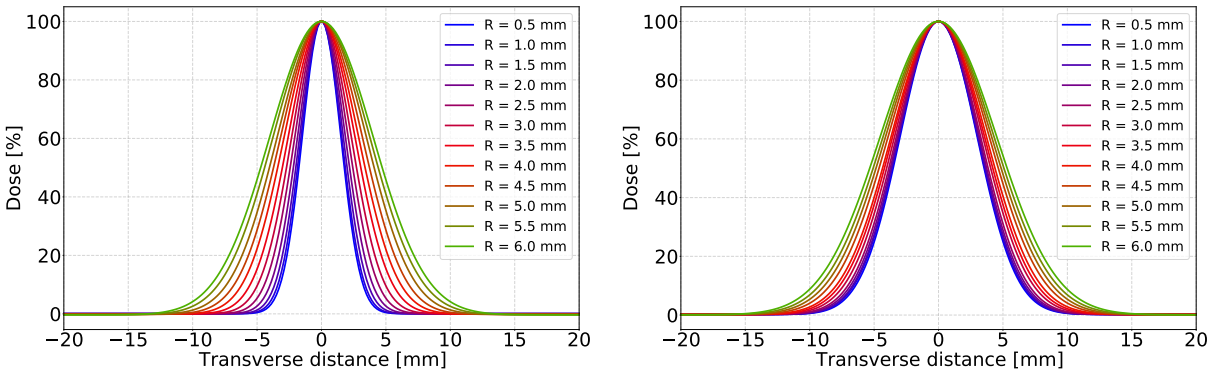

(a) (b)

Figure 4.4.3: Transverse dose distribution of (a) 100 MeV and (b) 150 MeV proton beam at the Bragg peak obtained for a range of collimator radius. The dose is represented as a percentage of the peak value. Graphs are fitted using the Gaussian function.

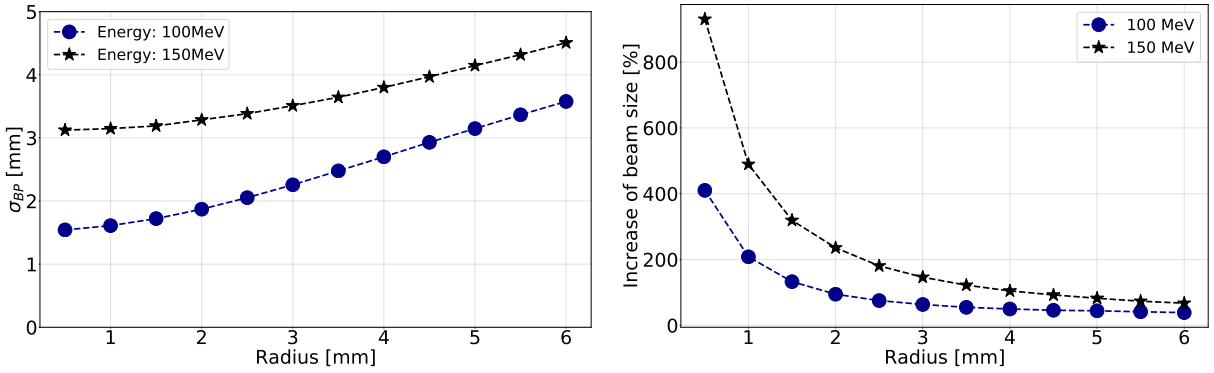

(a) (b)

Figure 4.4.4: (a) Comparison of the beam size of 100 MeV and 150 MeV proton beam at the Bragg peak as a function of collimator radius. The statistical error in σ was found less than 4 μm. (b) The percentage growth in transverse size of 100 MeV and 150 eV proton beams between entrance (10 mm) and the Bragg peak.

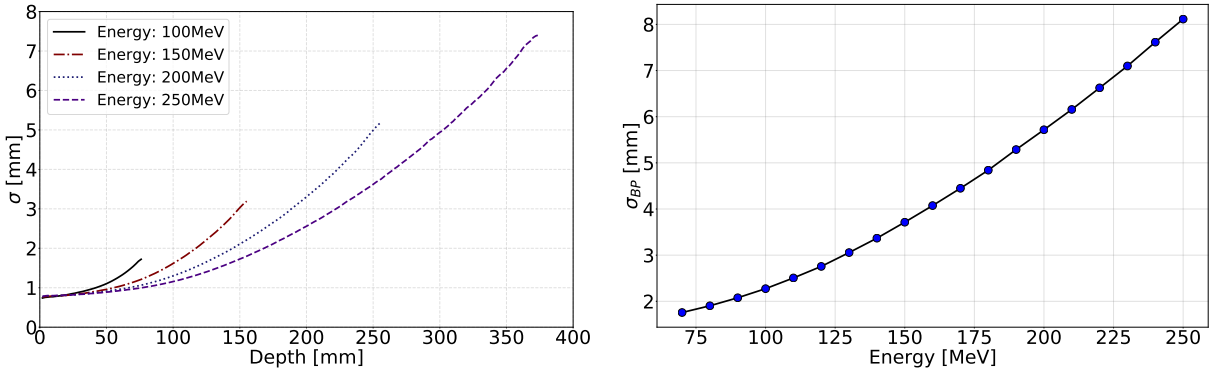

(a) (b)

Figure 4.4.5: (a) Comparison of the evolution of transverse beam size for four different energies as a function of depth. Results are obtained with 1.5 mm collimator. (b) Evolution of beam size (produced with 3.0 mm colliamtor) at the Bragg peak as a function of initial energy.

The increased range of proton beam at higher energy leads to a more extensive lateral expansion of the beam at its Bragg peak. The σ of 100 MeV, 150 MeV, 200 MeV, and 250 MeV proton beam

is determined at various depths in water. Figure 4.4.5a shows a gradual increase in σ for all beam energies. The curve's gradient gets steeper at the end of the range as the beam energy is lower. Less scattering of a higher energy beam is responsible for their slower growth in transverse size. The proton therapy system uses a range of energies to produce the SOBP, which is needed to treat a large field of radiation with a homogeneous dose. The energy variation can create a significant difference in lateral profile between entry and exit surfaces with a particular collimator radius. The transverse beam size at BP depends on initial energy following a non-linear relation, as shown in figure 4.4.5b.

4.5 Linear energy transfer

The method to determine the dose-averaged LET (LET_d) based on the simulation has been discussed in section 3.3. The step-limit (section 3.1.5) has the potential to impact the value of LET_d, which has been reviewed by Fada et al. [53]. We carried out our simulations with a step-limit of 0.2 mm. In terms of the radiobiological impact of the proton beam, the primary and secondary protons are indistinguishable. The energy spectrum of the secondary protons differs from the primary. Thus, the contribution of both primary and secondary protons is considered in the LET_d calculation. Figure 4.5.1 shows the LET_d as a function of depth for 100 MeV and 150 MeV proton beam.

At the entrance, the LET_d is usually smaller for both energies independent of collimator radius (with a few exceptions, which we will discuss later). It increases after the plateau region, and sharp growth can be noticed at the last few centimeters of the beam's range. The increasing stopping power with reduced beam energy (equation 2.1.16) explains this property of LET_d.

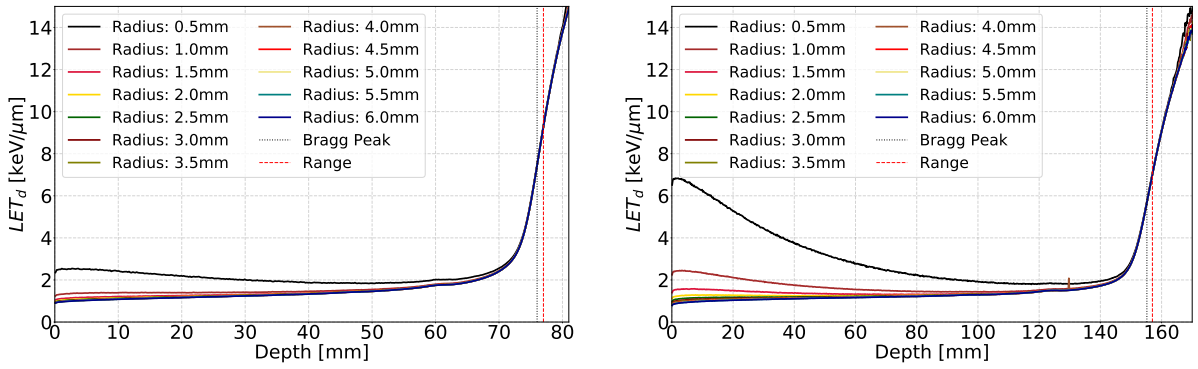

(a) (b)

Figure 4.5.1: Evolution of LET_d as a function of depth obtained for (a) 100 MeV and (b) 150 MeV proton beam. The Bragg peak position and range are obtained from the simulated data. Contribution of both primary and secondary protons are considered.

In addition, an impact of collimator radius on the LET_d can be noticed in figure 4.5.1. It is essentially due to the fact that the fraction of secondary proton at the entrance varies for different collimators, as discussed earlier in this chapter. With 100 MeV initial energy, LET_d at the water entrance (1.0 mm depth) is 2.48 keV/μm for 0.5 mm collimator. However, an identical setup recorded

LET_d of 6.73 keV/µm using a 150 MeV beam. The LET_d at entrance decreases with increasing collimator radius for both energies. The impact is more significant at higher energy because the generation of secondary protons at the collimator is elevated with the increased energy of a beam. In contrast, LET_d at the Bragg peak and beyond is not impacted by the collimator aperture. How-

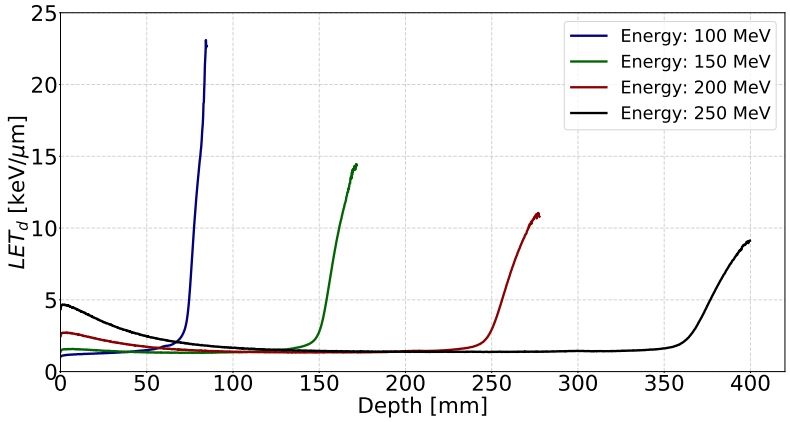

Figure 4.5.2: LET_d of 1.5 mm collimated proton beam as a function of depth. Four energies are compared. At higher energy, the LET_d is significantly lower at the Bragg peak of the beam, opposite is true at entrance

ever, it changes with beam energy. Higher energy beam has a smaller value LET_d at its Bragg peak. As it can be seen in figure 2.1.6 that a lower energy proton beam has a higher dose at the Bragg peak. As a consequence of more prominent range straggling, protons of a high energy beam stop over a larger longitudinal distance and smeared out the Bragg peak. Thus, the fraction of lower energy proton decreases at the Bragg peak and reduces LET_d, as shown in figure 4.5.2.

A very high LET_d can be observed beyond the range of the beams. The major fraction of the primary protons stop before this region. Therefore, the LET_d calculation relies on inadequate data. Moreover, the enhanced LET_d can be explained using the higher fraction of secondary protons in this region.

The LET_d calculated using only primary protons was identical for all collimators with a given energy. The exclusion of secondary protons eliminates the discrepancy of the entrance value of the LET_d. The distinctive contribution of primary and secondary proton in the LET_d has been shown by Romano et al. [143]

We evaluated the impact of primary and secondary protons on the LET_d. The results obtained for a 2.0 mm collimator are depicted in figure 4.5.3. The contribution of the primary (green) and secondary (red) protons are plotted on the same axis. Their combined contribution (blue) represents the LET_d for all protons is consolidated in the same graph. The smaller energy of secondary protons is responsible for their short-range and enhanced LET_d at the entrance.

In addition to the LET_d, figure 4.5.3 also shows the relative fluence of the primary, secondary and total protons as a function of depth. The number of secondary protons at any depth is very small compared to the primary protons. However, independent of the collimator radius, this number

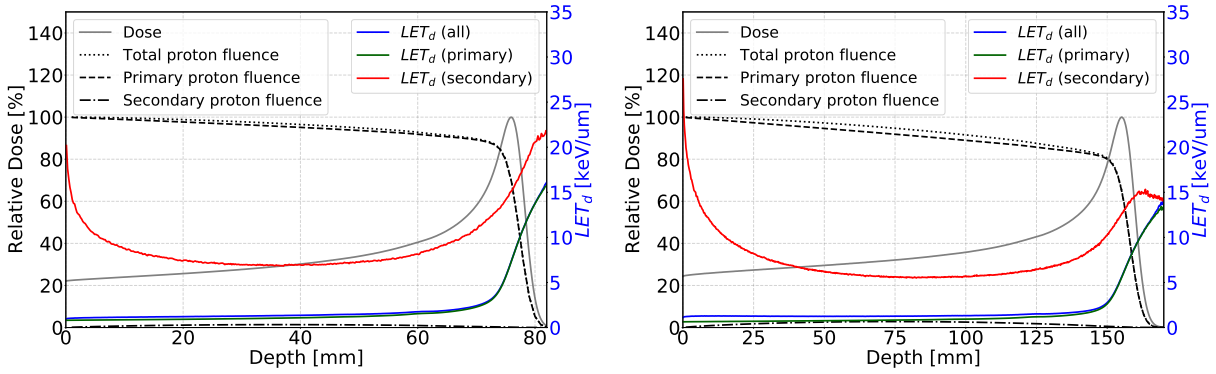

(a) (b)

Figure 4.5.3: Comparison of the LET_d obtained for primary, secondary and all protons. Fluence is measured for the total cross section of the water phantom. The results are obtained for 2.0 mm collimator.

gradually increases to a peak and drops slowly to practically zero beyond the primary proton beam's range. In contrast, the primary proton fluence starts with its largest value and decreases very slowly. Inelastic nuclear interactions cause this slow reduction of primary fluence. Within the Bragg peak's proximity, the primary proton fluence drops to ∼85% and ∼80% for 100 MeV and 150 MeV beam consecutively. With 160 MeV beam energy, a ∼20% drop in primary proton fluence has been reported [41], which is very similar to our result.

4.6 Relative biological effectiveness

The relative biological effectiveness (RBE) is one of the most relevant parameters to quantify the cell-killing efficiency of radiation for a given dose. In addition to the LET and dose, the RBE depends on a few other parameters such as biological endpoint, cell type, cell hypoxic status, and fractionation sensitivity. However, our RBE quantification depends on dose and LET_d. We used equation 2.2.2 to calculate RBE for our simulated dose profile of proton beams.

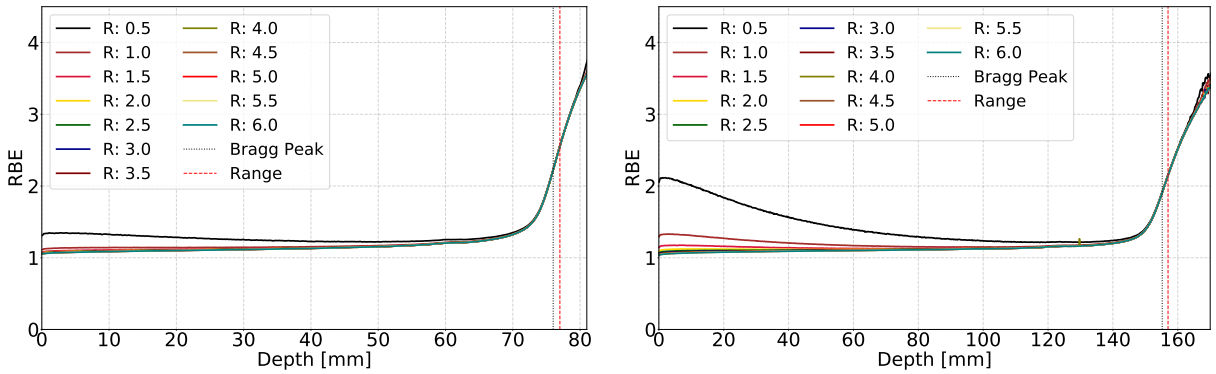

(a) (b)

Figure 4.6.1: Evolution of the RBE of (a) 100 MeV and (b) 150 MeV proton beam as a function of depth. The impact of the collimator radius is more prominent for the higher energy beam at the entrance of the water phantom.

Figure 4.6.1 illustrates how the RBE changes with the propagation of the proton beam into the simulated water phantom. As expected, these graphs follow a similar pattern as LET_d-depth relations shown in figure 4.5.1. The RBE at the entrance is higher for narrow collimators. With a 0.5 mm radius, the RBE at the surface of the water phantom is 1.33 and 2.09 for 100 MeV and 150 MeV beam, respectively. These values drop with increasing radius, and they are saturated at around 1.1, that is the standard value of RBE for proton beam within therapeutic energy range [61]. Following LET_d, with particular beam energy, the RBE at the Bragg peak is independent of the collimator radius. However, the RBE of a narrow beam calculated at the entrance of the water phantom is impacted by the initial beam energy. With a higher beam energy, the RBE is larger due to its higher entrance LET_d as shown in figure 4.5.2.

4.7 Neutron Dose

Neutrons are produced inside the water phantom by nuclear interaction, accompanying other secondaries. In addition, the components of the beam modification system, like the nozzle, can also produce neutrons. The secondary neutrons have a broad energy spectrum, and a fraction of these neutrons has higher energy to penetrate a large distance. Thus, the high LET neutrons can irradiate the whole body of patients.

Figure 4.7.1 compares number neutron generated at the collimator by a 100 MeV and 150 MeV proton beam. It is normalized to the number of entering protons after collimation. A narrow collimator favors a larger number of nuclear interactions before the water phantom, and consequently produces more secondaries. For both 100 MeV and 150 MeV energies, the initial number of neutrons gradually decreases as the collimator radius increases. Despite the fact that the neutron number decreases similarly as a function of collimator radius, the impact of energy is indisputable. A higher energy beam enhances the production of secondary neutrons. The 0.5 mm collimator irradiated with a 150 MeV proton beam delivers about five (4.95) times more neutrons than the number of entering protons. In contrast, it is only about 1.5 times for 100 MeV. The ratio of the initial beam size (before the collimator) and the collimator radius plays the most vital role in modifying the relative number of secondary neutrons.

The impact of beam energy on neutron generation can be seen in figure 4.7.2. The number of initial neutrons increases with beam energy at a steady rate, as shown by the bar chart in figure 4.7.2a. High energy proton beams generate more secondary neutrons by nuclear interactions at the collimator. As they propagate in the water phantom, neutrons are absorbed, and their energy is deposited. Simultaneously, the secondary neutrons are produced by nuclear interactions. The variation of the number of neutrons as a function of depth for four different energies is illustrated in figure 4.7.2b. These can be interpreted as relative fluence of secondary neutrons. All different energies generate a similar pattern of neutron fluence. It increases within the first few centimeters. At

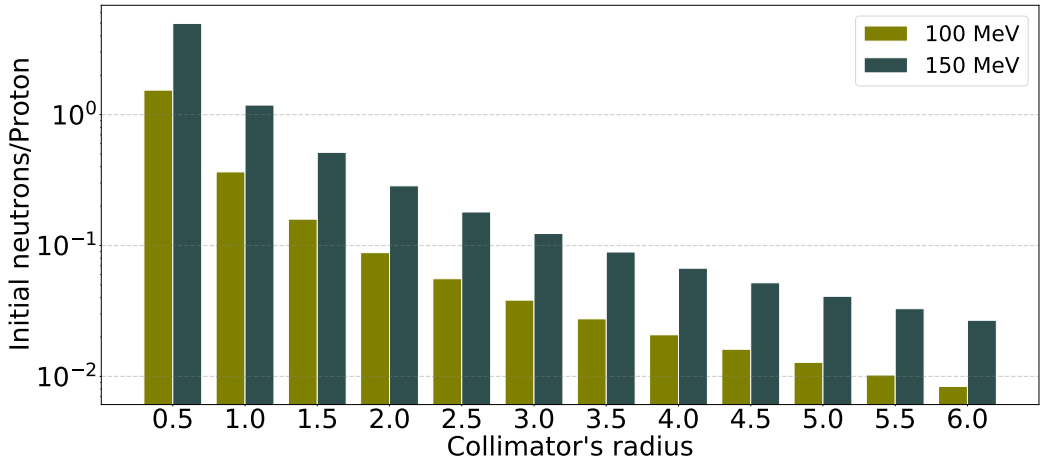

Figure 4.7.1: Comparison of the initial number of neutrons at the surface of the water phantom obtained for 100 MeV and 150 MeV proton beam with various collimator radius.

the end of the build-up region, neutron fluence reaches the peak, where neutrons achieve a longitudinal equilibrium. Afterward, it decreases gradually with depth as the capture process dominates over the generation process. The higher energy of proton beams can generate more relativistic neutrons. These high-energy neutrons are capable of producing more neutrons by participating in nuclear reactions. Consequently, an elevated neutron fluence can be seen for higher energy beams. Moreover, the energy of secondary neutrons produced by protons depends on the kinetic energy of the primary beam. A higher energy beam generates energetic neutrons, which can travel further. Thus the peak neutron fluence of the high-energy proton beam is deeper into water.

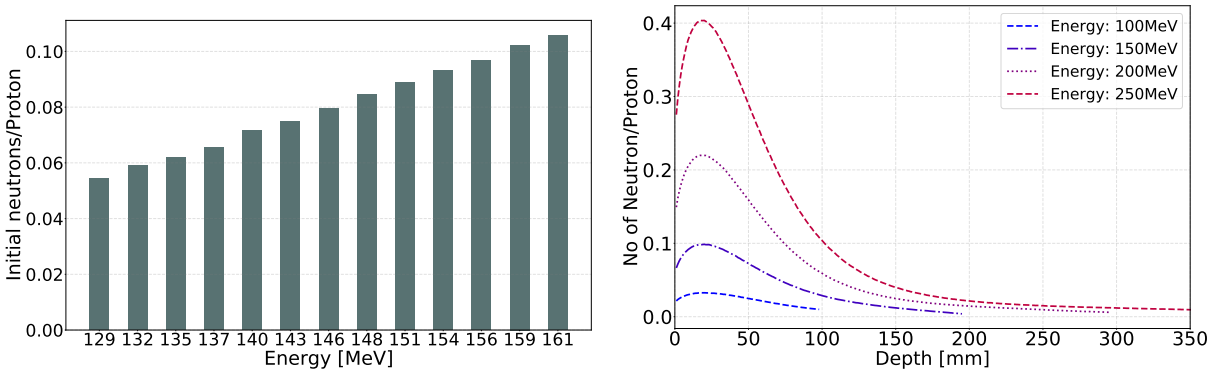

(a) (b)

Figure 4.7.2: (a) Number of neutrons at surface for different energies obtain for 2.0 mm collimator. (b) The number of neutrons as a function of depth for four energies.

The collimator radius also dominates the neutron fluence inside the water phantom. As shown in figure 4.7.3, independent of radius, normalized number of neutrons varies with depth following similar relation. However, its value is larger for a smaller radius throughout the assessed range.

The neutron dose is very small in comparison to the proton's contribution. Following the number of neutrons, the dose contributed by neutrons varies in the same way for all collimators and

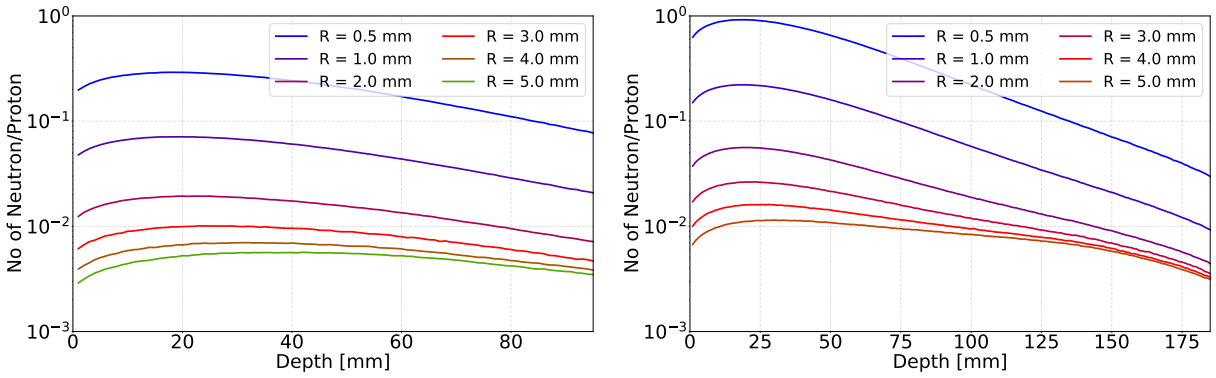

(a) (b)

Figure 4.7.3: Number of neutrons as a function of depth obtained for 100 MeV (a) and 150 MeV (b).

.

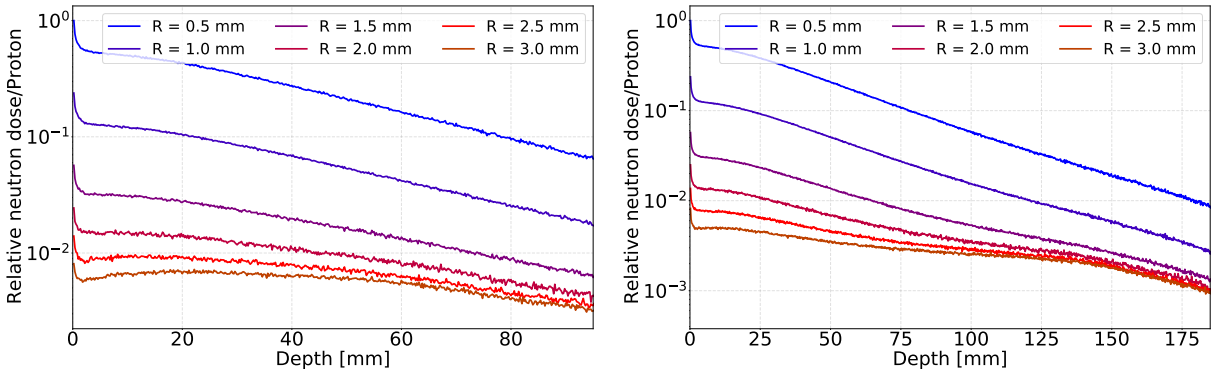

(a) (b)

Figure 4.7.4: Neutron dose as a function of depth obtained for 100 MeV (a) and 150 MeV (b). The dose is normalized to the maximum deposited dose obtained for 0.5 mm collimator.

energies. At the entrance, it is very large, where low energy neutron of the CB deposited their energy within few millimeters. The rapid absorption of these neutrons causes a sharp fall in the entrance neutron dose. Afterward, it decreases slowly with depth. For a low-energy beam with a larger collimator radius, the contribution of neutrons by the primary beam is negligible compare to the number of neutrons produced inside the water phantom. Thus, their neutron dose slightly increases after the initial fall.

4.8 Summary

The metal collimators are capable of effectively reducing the beam size. Concerning the spot size, the CB is limited by the MCS. With a low energy beam, the final spot is located in the shallow region, where the small transverse size of CB can be preserved effectively. Consequently, it can produce a small spot. However, it could not be obtained with high-energy beams where the final spot is deep inside the target. Depending on the initial beam energy, the final spot size was observed to reach a threshold. Further reduction in the collimator radius could not improve the result.

In addition, the surface dose becomes very large for a narrow CB in comparison with the Bragg

peak dose, particularly at high energy. Consequently, it deposited more dose at the nonspecific region than the target. This imposes a crucial limitation on the maximum achievable dose.

Moreover, the collimator eliminates a significant fraction of protons delivered by the accelerator. It reduces the effective beam current, and consequently reduces the maximum achievable dose rate. This reduced efficiency could be very crucial for FLASH modalities. It also reduces the overall efficiency of the system.

Besides reducing efficiency by stopping the protons, CB is contaminated with neutrons. These secondary neutrons can deposit doses at off-target regions inside and outside of the patient's body. However, optimization of the metal collimator can keep the contribution of biological dose of neutrons at a very low level which can not create any potential threat to patients [70].

Chapter 5

Focused beams

Despite the fact that a mechanical collimator can produce the desired narrow beams, it reduces the overall system efficiency by absorbing a large fraction of protons, which is a major obstacle to achieve a high dose rate [144]. Moreover, in addition to the target, it produces a significant number of secondary neutrons. These neutrons have higher penetration range, and contribute an additional unwanted dose to patients. The amount of dose deposited by these neutrons might be small, but it has the potential to cause long-term damage due to its higher RBE [145]. It is possible to mitigate these issues by shaping the beam without using a physical collimator. The use of magnetic fields can be an option to perform beam shaping without mechanical collimators.

Manipulation of charged particles beam using magnetic fields is a common practice in accelerator physics. It has been adopted in nozzle technology to implement active scanning in proton beam therapy. Furthermore, in recent years, several studies have been demonstrated the potential of magnetically shaped proton beams for RT [144, 146]. Usually, quadrupoles are used for focusing and defocusing of charged particle beams. In addition to the quadrupoles' gradient, a range of factors like emittance (ε), transverse beam size (σ_x, σ_y), kinetic energy (E), and Twiss parameters (β and α) determine the degree of focusing by a magnetic field. This chapter evaluates the characteristics of the magnetically focused beam within the conventional therapeutic energy range based on their longitudinal and transverse dose profile.

5.1 Beam Generation

The principle of the proposed focused beam treatment modality using proton beams of conventional energy range is depicted in figure 5.1.1. A beam can be focused at its Bragg peak depth using quadrupole magnets. Thus, it will stop at the focal point, depositing a large amount of the beam's energy. In the simulations of conventional energy focused beam (CEFB), the proton beam was introduced at 0.5 mm away from the water phantom using the Geant4 particle source to mimic magnetically focused beams produced by quadrupoles. The center of the source was modeled at the

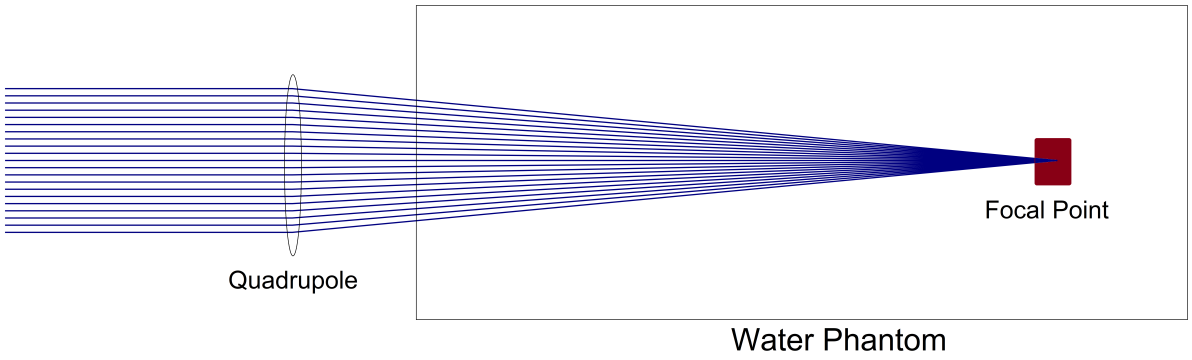

Figure 5.1.1: Focused beam generation configuration. The source is at 0.5 mm away from the surface of the water phantom. The Twiss parameters are tuned to produce the beam waist at the Bragg peak.

central axis of the cylindrical water phantom. The direction of propagation of the beam is parallel to the length of the target. Details of the beam generation using Geant4 particle source have been discussed in section 4.1.

The beam was designed to be a circular Gaussian with a σ_u of 10.0 mm. The Twiss parameters were tuned to modify the degree of focusing of the beam. For each set of Twiss parameters, 10^7 proton histories were simulated in order to minimize the uncertainty in the low-dose areas. The actual number of primary protons that reached the entrance of the target was slightly smaller than the number of particles generated by the source. The difference was observed to increase for higher focusing parameters. The root mean square (rms) of inclination angles (u' = x' or y') of particles is called rms divergence or divergence ($\sigma_{u'}$) of a beam. As listed in table 5.2.1, the $\sigma_{u'}$ of the beam increases with α following a non-linear positive correlation. The initial direction of the particles was assigned from a Gaussian distribution. A beam with higher $\sigma_{u'}$ is more likely to contain protons with large u'. Despite the small distance between the target and the source (0.5 mm), a few particles skip the target for their very large inclination angles, reducing the number of proton entering the target. It was also impacted by the initial beam energy. At higher energy (150 MeV), the number of protons at the entrance was larger than the lower energy (100 MeV) beam. This impact of beam energy can be explained using the initial beam divergence. It can be seen in table 5.2.1 that the $\sigma_{u'}$ of 100 MeV beam is larger than 150 MeV beam for a given α. This beam loss was not significant in the simulations. However, in practice, the source cannot be placed very close to the target, which might cause a noticeable beam loss. Simultaneously, it might be a concern of radiation protection.

5.2 Focusing parameters

The treatment modalities of proton beam therapy rely on the Bragg peak to deposit a higher dose at the target. The objective of the CEFB modality is to focus the proton beams of conventional therapeutic energy range at the corresponding Bragg peak depth to irradiate smaller volumes. In addition to the higher stopping power at the end of the range, the concentrated interaction of CEFB

can potentially enhance the dose at the focal point. Moreover, the focusing effect generated by the magnetic field can reduce the beam broadening caused by MCS, eventually produce a smaller spot.

The initial value of α and β was tuned based on equation 2.4.32 to focus the beam at the desired depth. We have gradually increased α to enhance the focusing effect. There is a corresponding β for each α to focus the beam at a fixed depth. The constant initial σ_u leads to a unique emittance for a set of Twiss parameters. The emittance was calculated from equation 2.4.22, and the covariance matrix was constructed for both transverse planes to produce the desired beam.

A set of simulations was performed with a range of α between 1.0 to 20.0 to evaluate the magnetically modified beams' dose profile. We studied the effects of beam energy and Twiss parameters by simulating 100 MeV and 150 MeV proton beams. The Twiss parameter α was used to quantify the degree of focusing. The relation between the beam's divergence and α can be expressed as

$$\sigma_{u'} = \sqrt{\epsilon_{rms}\left[\frac{1+\alpha_u^2}{\beta_u}\right]}. \tag{5.2.1}$$

Table 5.2.1: Initial beam parameters to focus 100 MeV and 150 MeV proton beam at the Bragg peak.

	100 MeV			150 MeV		
α	β [m]	ϵ [mm-mrad]	$\sigma_{u'}$ [mrad]	β [m]	ϵ [mm-mrad]	$\sigma_{u'}$ $[mrad]$
1.0	0.151	661.02	93.482	0.313	318.60	45.05
3.0	0.252	396.61	125.42	0.523	191.16	60.45
5.0	0.393	254.23	129.63	0.816	122.54	62.48
7.0	0.540	185.08	130.87	1.120	89.20	63.08
9.0	0.689	145.10	131.39	1.429	69.93	63.33
11.0	0.838	119.20	131.66	1.740	57.45	63.45
13.0	0.989	101.09	131.81	2.052	48.72	63.53
15.0	1.139	87.746	131.91	2.364	42.29	63.57
20.0	1.516	65.937	132.03	3.146	31.78	63.64
25.0	1.894	52.797	132.09	3.929	25.44	63.67
30.0	2.271	44.019	132.13	4.713	21.21	63.68

The depth of the Bragg peak of 100 MeV and 150 MeV proton beam was determined using Bragg-Kleeman formula given in equation 2.1.17 and validated using simulated data. The initial Twiss parameter β of focused beam for a given α and focal length is calculated using equation 2.4.32 is listed in table 5.2.1. Figure 5.2.1a shows the beam emittance and β as a function of α to produce the beam waist at the Bragg peak of corresponding energy, with the assumed initial beam size. For a given α, a 150 MeV beam needs a larger initial β and smaller ε to focus the beam at the Bragg peak, which is obviously deeper into water compared to the 100 MeV beam. The evolution of the initial beam divergence as a function of α is depicted in figure 5.2.1b.

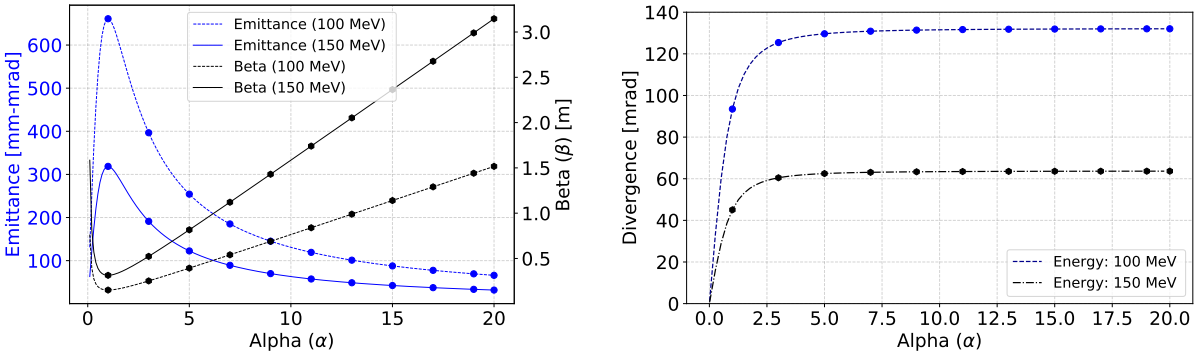

(a) (b)

Figure 5.2.1: (a) Evolution of the initial beam emittance and β as a function of α to produce beam waist at the Bragg peak of 100 MeV and 150 MeV proton beams. (b) Comparison of the initial divergence of 100 MeV and 150 MeV proton beams.

5.3 Longitudinal Dose Profile

5.3.1 Average dose

The average dose of 100 MeV and 150 MeV proton beams as a function of depth is shown in figure 5.3.1. As we have discussed in section 3.2, cylindrical volume elements of 0.2 mm length and 200 mm radius were implemented to quantify the average dose. There is no significant difference in dose profile between the collimated and focused beams of identical energy regarding the shape of their dose profile. Both of these beam shaping techniques produce the usual depth-dose graph of proton beams. However, a detailed study of focused beams' curves revealed a discrepancy in the Bragg peak position and peak dose. The location of the Bragg peak produced by the collimated beams (parallel beam) is slightly deeper than the focused beams of an identical energy. For example, the Bragg peak of 100 MeV collimated beam is located at 76.0 mm, whereas it can be observed between 74.6 mm to 75.4 mm (depends on α) for the focused beams of the same energy. The peak dose is slightly higher for collimated beams than the focused beams, and the difference increases for larger α. The focused beam's peak dose is less them 4×10^{-3} nGy/proton except for the beam with $\alpha = 1$. While on the contrary, a collimated beam of an identical energy deposited 4.24×10^{-3} nGy/proton dose, which is 6% higher than the focused beam.

It can be seen in figure 5.3.1 that the magnitude of the Bragg peak doses and their positions are not identical for all focused beams of the same energy. The simulations with 100 MeV proton beam exhibit a more significant difference in dose profile between $\alpha = 1$ and $\alpha = 3$. The Bragg peaks at lower alphas are slightly deeper into the water; with $\alpha = 1$, it is located at 75.4 mm that is 0.8% to 1.1% deeper than the other focused beams. This discrepancy in the average longitudinal dose profile diminishes among the larger values of α (table 5.3.1. The smaller growth of beam divergence at larger α explains their insignificant difference.

As shown in figure 5.2.1b, the proton beam's divergence gets larger with α at a decreasing

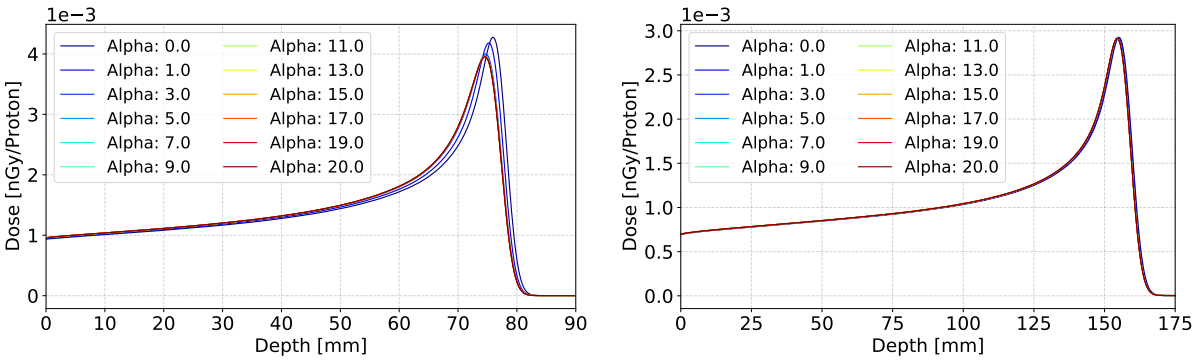

(a) (b)

Figure 5.3.1: Depth-dose curves of (a) 100 MeV and (b) 150 MeV proton beams. Initial beam size is 10.0mm. The value of α varies between 0.0 to 20.0. Beam emittance and β are modified to keep the beam waist at the Bragg peak.

Table 5.3.1: Bragg peak depth and dose in water.

	100 MeV		150 MeV	
Alpha	BP depth [mm]	BP dose [nGy/proton]	BP depth [mm]	BP dose [nGy/proton]
1.0	75.4	0.004183	155.0	0.002926
3.0	74.8	0.004001	154.6	0.002916
5.0	74.8	0.003969	154.6	0.002914
7.0	74.6	0.003960	154.6	0.002916
9.0	74.8	0.003958	154.4	0.002914
11.0	74.6	0.003956	154.6	0.002915
13.0	74.6	0.003954	154.6	0.002914
15.0	74.6	0.003954	154.6	0.002914
17.0	74.6	0.003953	154.6	0.002915
19.0	74.6	0.003954	154.6	0.002913
20.0	74.6	0.003954	154.6	0.002915

rate. The change in beam divergence is largest between α = 1 and α = 3. Due to the non-zero beam divergence, the protons' path makes an angle with the longitudinal direction. The Bragg peak depth along the beam's longitudinal direction is equal to the projection of the actual distance traveled by the particles. As a consequence, the Bragg peak of focused beams is observed at a depth slightly smaller than the actual location estimated for a parallel beam. The difference between projected depth and actual depth of the peak dose increases at decreasing rate with α.

Following the Bragg-Kleeman formula given in equation 2.1.17, the range of the 100 MeV proton beam in water is about 76 mm. The divergence of the beam to be focused at the Bragg peak with $\alpha = 1$ and $\alpha = 3$ are 0.093 rad and 0.125 rad, respectively. The difference between the projected Bragg peak depth corresponding to these divergences is approximately 0.3 mm. The simulated result gives a difference of 0.6 mm. These two values are mostly consistent within the limit of simulation resolution of 0.2 mm. The penetration depth of the proton beam at higher energy increases. With an identical set of focusing parameters, the angle between the protons' path and the longitudinal direction becomes smaller with increasing depth, reducing the discrepancy between the depth

dose curve for different values of α as observed for 150 MeV proton beam (see table 5.3.1). Simultaneously, the fraction of protons stopping before the Bragg peak of a focused beam increase due to energy straggling. Consequently, the number of protons at the Bragg peak becomes lower, leading to a reduced peak dose.

5.3.2 Central axis dose

The central axis depth-dose curves of focused beams illustrated in figure 5.3.2 is completely different than the pattern we observed for collimated beams discussed in the previous chapter. A focused beam's peak dose (D_{BP}) is higher than its surface dose (D_{Sur}); however, the opposite is true for the collimated beams with small openings. It also varies immensely with increased focusing strength. The D_{BP} for both energies gradually increases with α. In addition, the initial beam energy influences the D_{BP} of the focused beams. The 100 MeV proton beam can deliver a higher D_{BP} than 150 MeV beam. The lower energy beam expands less as they encounters smaller number of MCS. As a result, it deposits more energy within a short distance from the center of the beam and enhances the D_{BP}. For 100 MeV proton beam, the D_{BP} increases from 0.82 nGy/proton for $\alpha = 0$ to 28.75 nGy/proton for $\alpha = 20$. The 150 MeV proton beam followed the same pattern with a lower dose throughout the range of α. Within the same interval, value of its D_{BP} increases from 0.49 MeV/proton to 5.61 nGy/proton.

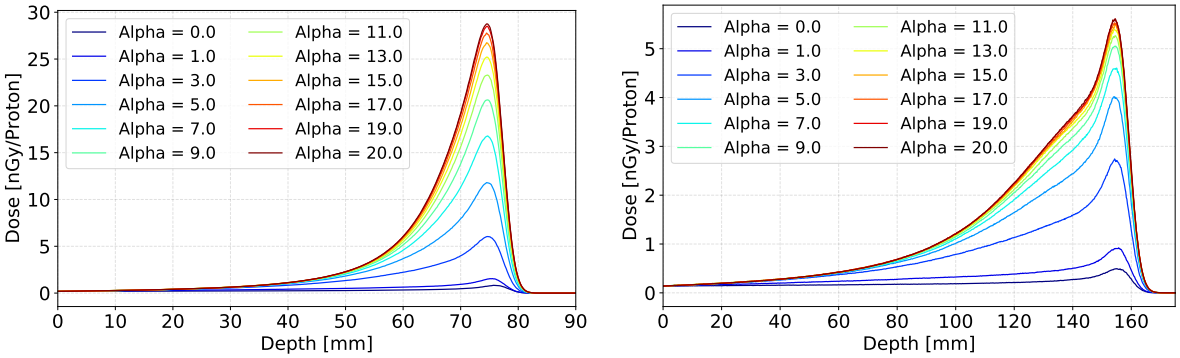

(a) (b)

Figure 5.3.2: Central axis depth-dose curve of (a) 100 MeV and (b) 150 MeV proton beams. Initial beam size is 10.0 mm. α varies between 0 to 20. Beam emittance and β are modified to keep the beam waist at the Bragg peak. The dose is calculated for cylindrical volume elements of radius 0.5 mm and length 0.2 mm.

Figure 5.3.3a shows the D_{Sur} at the central axis of 100 MeV and 150 MeV proton beams as a function of α. For a given energy, the D_{Sur} is almost constant because the beam has not traveled any significant distance to achieve different transverse sizes depending on α (see equation 2.4.29). However, the impact of energy can be noticed; the lower energy beam produces a higher D_{Sur}. The D_{Sur} obtained from the simulations is 0.19 nGy/proton and 0.14 nGy/proton for the 100 MeV and 150 MeV proton beam, respectively. The lower stopping power at higher energy causes this dose difference [147].

In contrast, independent of beam energy, the D_{BP} at the central axis increases with α as shown in figure 5.3.3b. With $\alpha = 0$, there is no focusing effect and the beam waist is at the entrance of the water phantom. Thus, the proton beam start to expand laterally as it propagates into the water. The smallest D_{BP} can be observed without beam focusing. The beam energy causes a discrepancy at D_{BP} because of the larger transverse expansion of high energy beam at its Bragg peak. In addition, the 150 MeV proton beam encounters more scattering interactions than 100 MeV beam. As we have discussed in chapter 4, a higher energy beam experiences more prominent range straggling and produces a wider Bragg peak. It also leads to a smaller amplitude of D_{BP} as fewer protons ends up at the Bragg peak position. With increasing α, the D_{BP} of 100 MeV proton beam grows at a higher rate and reaches to around 28 nGy/proton for $\alpha = 20$. In contrast, 150 MeV proton beam's D_{BP} not only increase slowly but also saturates around 5.5 nGy/proton at much smaller α.

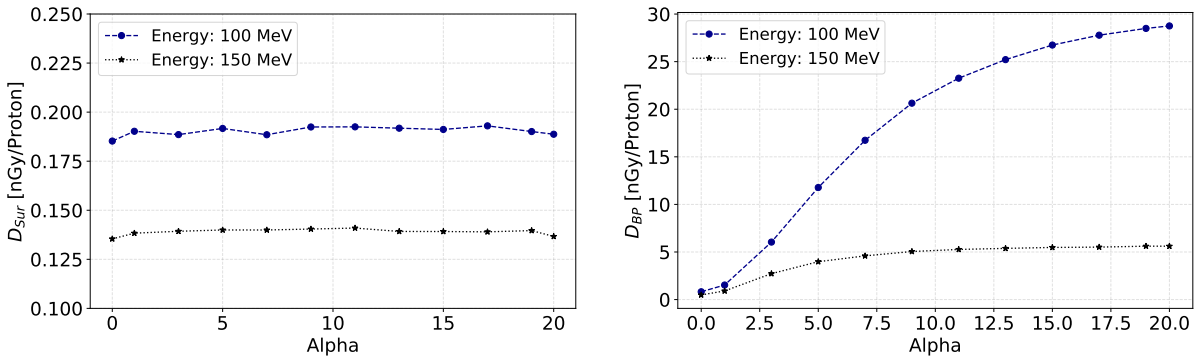

(a) (b)

Figure 5.3.3: Evolution of (a) D_{Sur} and (b) D_{BP} of focused proton beams (calculated at the central axis) as a function of α. Proton beams of 100 MeV and 150 MeV are compared.

The variation of peak to surface dose ratio (D_{BP}/D_{Sur}) as a function of α is shown in figure 5.3.4a. At α = 1, D_{BP}/D_{Sur} of 100 MeV proton beam is 68% higher than 150 MeV. The difference in D_{BP}/D_{Sur} between these two energies gradually increases with focusing strength. Beyond $\alpha = 15$, D_{BP}/D_{Sur} is almost constant around 40 for a 150 MeV beam, however, a 100 MeV proton beam has a noticeable growth throughout the assessed range of α. With lower beam energy, it is possible to achieve a higher D_{BP}/D_{Sur} by increasing α. In contrast, at higher energy, the focusing effect is limited by multiple scattering. Overall, focused beams have large D_{BP}/D_{Sur}, which allow them to deliver a higher dose at the desired point compared to the non-specific entrance region. It is undoubtedly an advantage of CEFB in the context of RT.

In Addition, we have calculated the ratio of dose of 100 MeV and 150 MeV proton beam at the surface and the Bragg peak position using our simulated data. The result is illustrated in figure 5.3.4b. The ratio of their D_{Sur} remains constant; however, at the Bragg peak ratio of their dose increases with a decreasing rate. Thus, the D_{BP} of a lower energy beam (in a shallow region) can be enhanced at a larger scale by utilizing the focused beam modality.

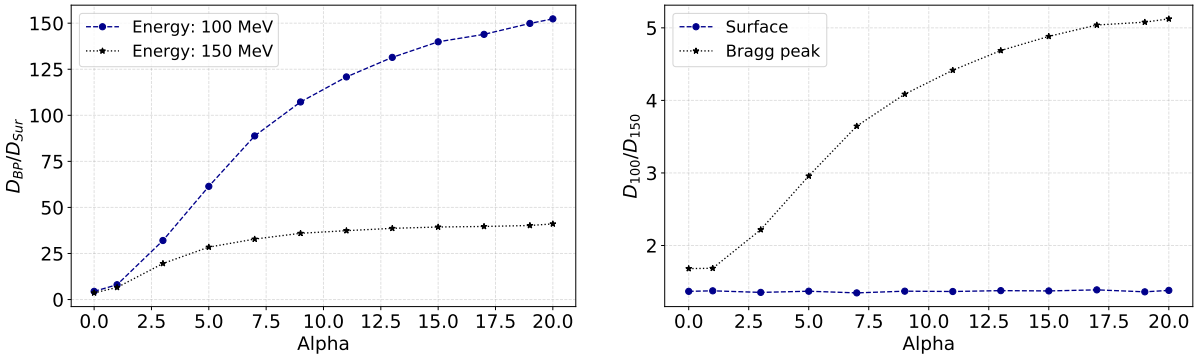

(a) (b)

Figure 5.3.4: (a) Comparison of the D_{BP}/D_{Sur} of 100 MeV and 150 MeV focused proton beams as a function of α. (b) D_{100}/D_{150} at the Bragg peak and surface of the water phantom.

5.4 Two dimensional dose profile

Figure 5.4.1 compares the two-dimensional (x-z) dose profiles of 100 MeV (left) and 150 MeV (right) proton beams for α equal to 1, 5 and, 11. As we have mentioned in chapter 4, the projection of the entire beam on the x-z plane shows an enhanced dose at the central part of the beam compared to the edge. To avoid this impractical overestimation of dose, we have taken 0.2 mm of the central part of the beam along the y-axis. Rectangular cuboids are used for dose calculation. The size of each voxel is $0.2\ \text{mm} \times 0.2\ \text{mm} \times 0.2\ \text{mm}$. The horizontal white lines represent the initial σ of the beam.

The impact of the beam focusing on dose distribution is evident in the figure. It can be seen that α = 1 offers a weak beam focusing, and spot sizes are similar for both energies. At a larger value of α, a stronger focusing effect can be noticed. The spot size is smaller for the 100 MeV proton beam, and it is observed to decrease with depth up to the Bragg peak. With identical Twiss parameters, the 150 MeV proton beam ends up with a larger spot size, and the transverse beam size appears to increase at the last centimeter after the initial lateral contraction. As we have mentioned earlier, this broadening of lateral dimension is produced due to MSC. The rms value of the scattering angle is inversely proportional to the momentum (equation 2.1.12). At the end of the track, lower energy protons are deflected most. Moreover, in the traversed material, rms value of the scattering angle builds up gradually with depth. The range of 100 MeV proton beam is 48.6% of the 150 MeV. It is therefore likely to encounter a smaller number of scattering interactions. Its scattering angle can not grow enough to produce a significant lateral expansion before it stops completely.

5.5 Spot size

A small spot is needed to irradiate tiny tumors with better normal tissue sparing. Moreover, it can be implemented for proton GRID therapy. A magnetically focused beam has the potential to produce a small spot at the Bragg peak with an enhanced dose at the focal point. Figure 5.5.1 shows

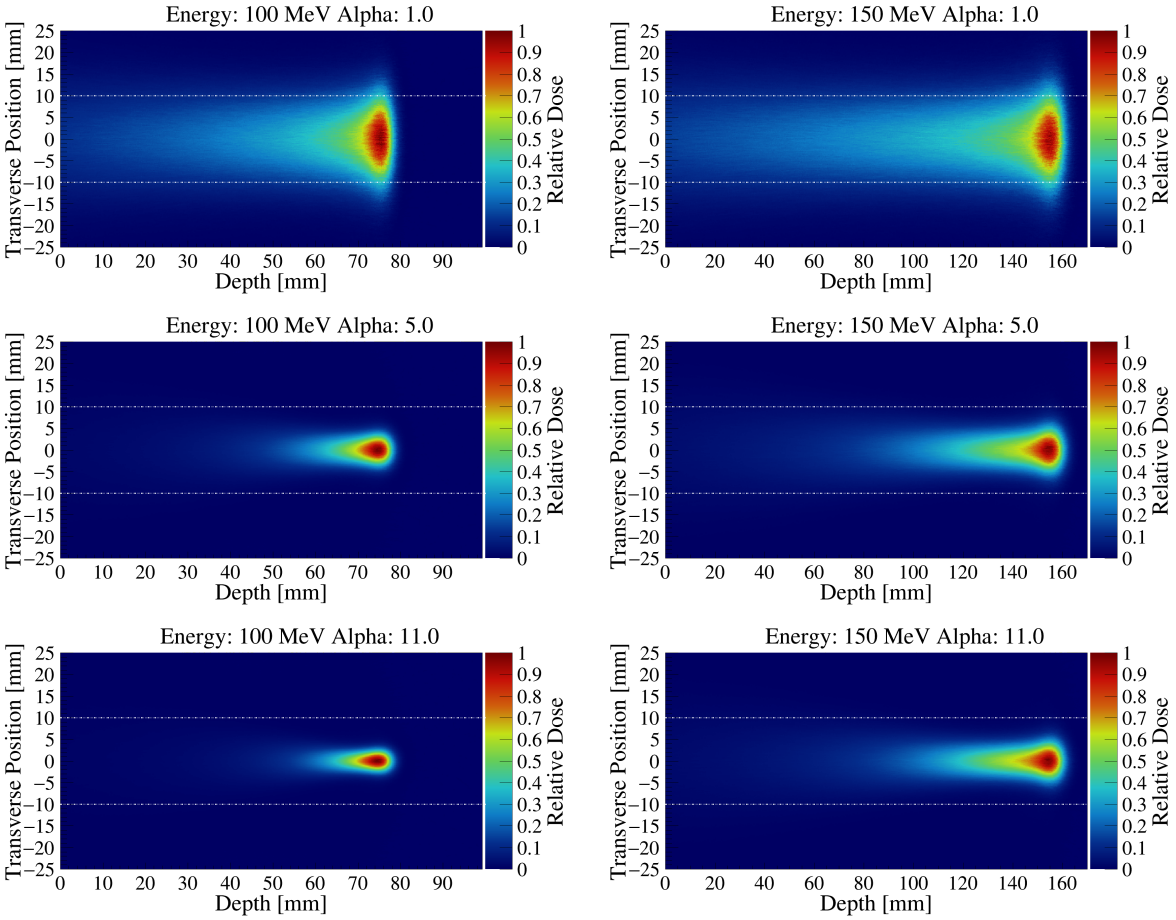

Figure 5.4.1: Two-dimensional physical dose profiles of 100 MeV (left) and 150 MeV (right) proton beam. The initial σ of the beam is shown by two dotted horizontal lines. The dose is normalized to the peak value.

the variation of the transverse size of focused beams at the Bragg peak (σ_{BP}) as a function of α. The beam size has been determined from the Gaussian fit of the transverse distribution of energy. For both energies (100 MeV and 150 MeV), the σ_{BP} decreases with α following a similar pattern. The smaller beam size of the lower energy beam has been explained earlier as a result of a reduced number of scattering interactions. A sharp change in transverse beam size can be noticed as the value of α increases from 0.0 to 5.0. Beyond this range, it reduces slowly. It can be explained using the corresponding divergence of the beam. The growth of divergence of the beam is not significant at larger α. The largest α to achieve reasonable enhancement in beam focusing for 150 MeV beam is around 7. A slightly larger α value appeared to be advantageous for lower energy to achieve a narrower beam at the Bragg peak.

The study of the transverse beam size along the longitudinal direction indicates a natural limitation of the focused beam at a higher energy spectrum. Figure 5.5.2 compares the evolution of transverse size (σ) of two proton beams of different energies. The σ of 100 MeV proton beam decreases with depth for all values of α, as shown in figure 5.5.2a. The analytical value of the beam size in vacuum is plotted on the same axis. As it can be seen that the transverse size of the proton

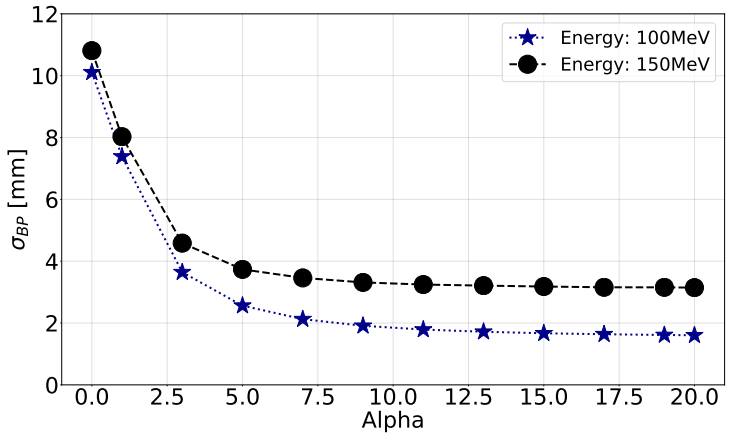

Figure 5.5.1: Comparison of simulated beam size at the Bragg peak of 100 MeV and 150 MeV focused proton beams as a function of α. The largest statistical error was less than 2.0 µm.

beam in water evolves in the same way as the analytical relation. However, the beam size in water obtained from simulation is always larger than the analytical value. The difference between the analytical values and simulated results increases for larger α. In addition, the simulated beam waist is flattened out by MCS and observed slightly before the analytical depth.

The 150 MeV proton beam in figure 5.5.2b follows a similar trend as 100 MeV at the shallow region of water. However, the transverse beam size expands at the last couple of centimeters. Additionally, the difference between the simulated results and analytical values is more pronounced. The 150 MeV beam was focused deeper into the water to produce beam waist at its Bragg peak. To satisfy the condition in equation 2.4.32, a larger β was required for the 150 MeV proton beam with an identical α (figure 5.2.1a). The larger value of β generates a beam where the directions of the protons are more parallel. This parallel nature of the beam makes it more sensitive to scattering interactions. Moreover, the 150 MeV proton beam travels deeper due to its high energy and encounters more MCS. The combined effect of larger beta and an extended number of scattering reduces the focusing effect. Consequently, the high-energy beams begins to expand before it stops.

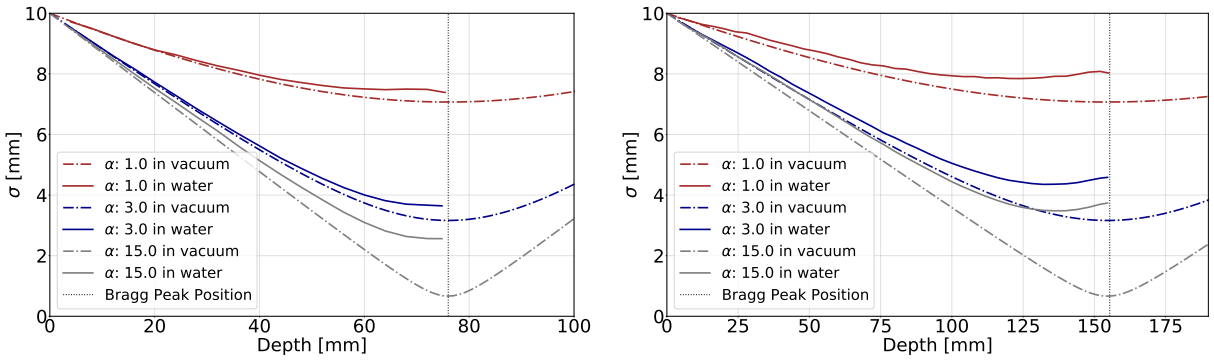

(a) 100 MeV Energy

(b) 150 MeV

Figure 5.5.2: Evolution of the transverse size of (a) 100 MeV and (b) 150 MeV focused proton beams as a function of depth in the water phantom.

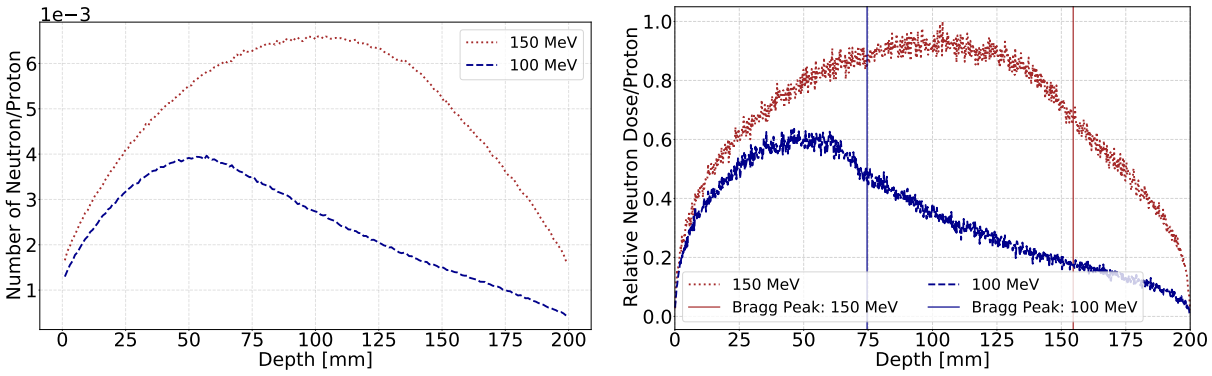

(a) (b)

Figure 5.6.1: Evolution of the number of neutrons (a) and dose deposited by neutrons (b) as a function of depth in water. The dose is normalized to the maximum deposited dose by the 150 MeV proton beam and the number of protons entered inside the water phantom.

5.6 Neutron dose

In our simulation of focused beams we did not insert any component of the proton beam therapy system that could contribute neutron to the target. However, as we have discussed in chapter 2, the primary protons can produce secondary neutrons by nuclear interactions inside the target. The neutron fluence of the focused beam as a function of depth was recorded for 100 MeV and 150 Mev proton beam. There was no impact of beam focusing on the neutron fluence as the interaction cross-section solely determines the production of secondaries. Figure 5.6.1a shows the influence of beam energy on neutron fluence. It can be explained using the energy of the secondary neutrons.

The simulated focused beam was exclusively composed of protons. Entering the target, they produce secondary neutrons. As we have discussed in chapter 4, the energy of these secondary neutrons depends on the primary proton. With high-energy proton beam, secondary neutrons have a larger range, and longitudinal equilibrium is achieved at a deeper point (further away from the entrance). Besides, they (high energy secondary neutrons) are also capable of producing further neutrons by nuclear interactions to enhanced the peak fluence. The dose contribution of neutron shown in figure 5.6.1b follows a similar trend as the number of neutrons.

5.7 Summary

Magnetically focused beams can produce a small spot at the target. Particularly, a lower energy proton beam that corresponds to a smaller depth can be focused more effectively. Simultaneously, it has a very high value of D_{BP}/D_{Sur}. This is advantageous in the context of RT because a higher dose can be deposited at the target as well it reduces the normal tissue (entrance) dose. However, for a deep-seated target, the focused beam starts to expand at the vicinity of the Bragg peak. The enhanced effect of MCS at lower energy along with the long projected range of high energy beams is responsible for this limitation. This can be overcome using high-energy focused beams, which we

will discuss in the next chapter.

Chapter 6

High energy focused beams

Within the conventional therapeutic energy range (70 MeV to 250 MeV), focused proton beams can be used to irradiate small volumes while sparing surrounding healthy tissue. The beam stops at the end of its range and deposits a negligible dose beyond the target. However, as the beam gets slower with depth, it becomes more sensitive to scattering interaction. Consequently, a small spot is difficult to achieve, especially at a deep-seated target.

In contrast, a high-energy proton beam is less affected by MCS, and the lateral expansion of the beam is much smaller. This feature of the high-energy beam makes it a promising candidate for treating small deep-seated tumors. However, while it is less scattered, irradiation with a high-energy parallel beam can not produce a significant dose contrast between the target and the healthy tissue because of an insufficient growth in stopping power. Nevertheless, a focused beam can produce a prominent dose difference between its focal point (waist) and surroundings. The effect of focusing of very high energy electron (VHEE) beams has been studied extensively through simulation and experiment [148, 149]. Adaptation of this concept in proton beam therapy has a primary drawback. The Bragg peak dose cannot be incorporated into the treatment plan, which is considered one of the most attractive features of proton beams for therapeutic applications. But, the higher RBE of the proton beam compared to the x-ray and electron is a clear advantage that can enhance the treatment's efficacy. This chapter evaluates the characteristics of high-energy focused beams (HEFB) based on their dose profile.

6.1 Beam Generation

The principle of high energy beam focusing is illustrated in Figure 6.1.1. The objective of this beam shaping modality is to produce a converging high energy proton beam (larger than the conventional therapeutic energy range). The initial energy should be sufficient to ensure the escape of the beam from the patient's body without any significant drop of the beam's energy. Consequently, it can guarantee a large distance of the Bragg peak from the target. In our HEFB studies, we sim-

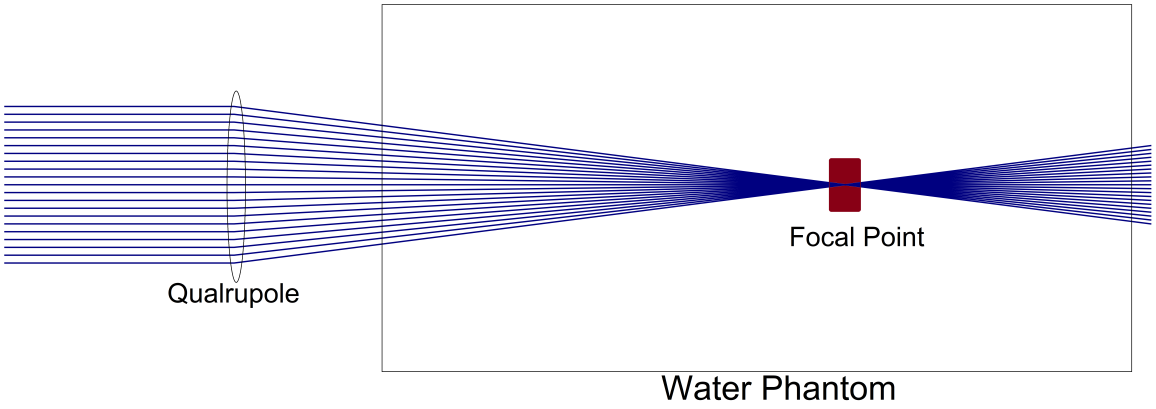

Figure 6.1.1: Principle of high energy focused beam radiotherapy.

ulated 350 MeV proton beam with 1% energy spread. With this initial kinetic energy, the projected range of proton beam in water is $66.21\ \mathrm{g\ cm^{-2}} (\approx 662.80\ \mathrm{mm})$ [150]. This range is sufficient in most cases to satisfy the aforementioned requirements of HEFB.

The principle of beam generation is identical to CEFB discussed in section 5.1. In a similar way, the Geant4 particle source is employed at 0.5 mm away from the entrance of the modeled water phantom with a desire to produce a circular Gaussian beam. The initial beam size ($sigma_u$) was 15.0 mm. As discussed in section 5.2, the Twiss parameters govern the depth and width of the beam waist at the focal point. The initial emittance and β for different values of α to focus the high energy beam at 50 mm and 100 mm are compared in figure 6.1.2a. The initial divergence for 50 mm focal length showed in figure 6.1.2b is twice of 100 mm beam. In principle, with a reduced transverse size, a beam can deposit a higher dose at the focal point. The frequent interactions of protons in a smaller volume can explain this enhanced dose. Consequently, it can generate a desired dose discrepancy between the target (focal point) and surroundings. Unlike conventional proton beam therapy, HEPB deposits a non-zero dose in the region beyond the target. However, the exit dose is reduced by the divergence of the beam after the focal point.

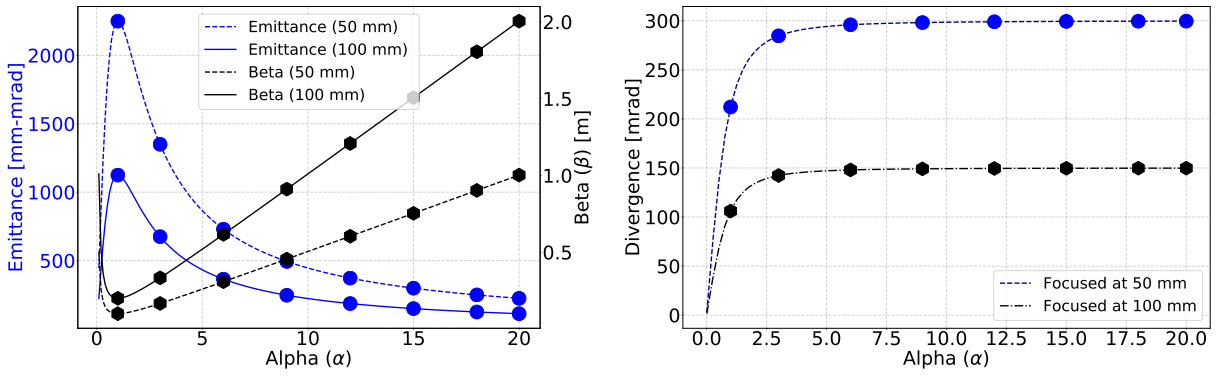

(a) (b)

Figure 6.1.2: (a) Evolution beam emittance and β as a function of α to focus a 350 MeV proton beam at 50 mm and 100 mm depth. (b) Growth of the initial divergence of the beams.

6.2 Longitudinal dose

The longitudinal dose profile of HEFB was evaluated using two different configurations (average and central axis) as we have used to study the CB (Chapter 4) and CEFB (Chapter 5). Certainty, the average dose profile was not interesting because it could not reveal HEFB's exciting properties crucial for RT. In contrast, the central axis dose profile exhibited several interesting features of HEFB.

6.2.1 Central axis dose

The central axis dose of HEFB was calculated using an identical geometrical configuration as described in chapter 4. We have considered narrow cylindrical volume elements (described in section 3.2) to determine the local dose at beam's center. The initial Twiss parameters were tuned to focus the beam at 50 mm and 100 mm. In addition, the focusing strength of the beam was gradually increased for each depth.

It can be seen in figure 6.2.1 that the dose approaches a peak value at the focal points (50 mm and 100 mm) of the beams. A sharp change of dose around these points for higher values of α is noticeable. The dose of a HEFB drops after its peak value. The dose distribution follows a approximately symmetric pattern about the focal point. Since the Bragg peak is way beyond the target, it does not contribute to the peak dose of a HEFB, like the conventional proton therapy, and the beam does not stop inside the target. Instead, the transverse size gradually of the beam decreases till the focal point, and it expands afterward following the principle of beam dynamics described by equation 2.4.29. The variation of fluence of primary protons at the beam's central axis, shown in figure 6.2.2, explains this unique dose profile. As the beam gets narrower, the interaction points (points of energy deposition) become concentrated within a predefined small target volume; hence, the central axis dose increases. The gradual spreading out of the beam's particles after the focal point causes the systematic dose reduction.

In addition, figure 6.2.1 also reveals crucial relations between the focal length and the attributes of the peak dose. With an identical α, the longitudinal distribution of the peak dose at a shallow point is sharper than a longer focal length. This feature can be explained using the basic principle of beam focusing. Following the equation 2.4.32, two beams with an identical initial α and σ can produce their beam waist at different depths if their initial β is modified. A larger β is needed to construct the beam waist at a deeper point. As a consequence, the beam waist becomes flat, and the transverse beam size evolves slowly around the focal point for a deep-seated target. This also reduces the amplitude of the peak dose by spreading out the deposited energy longitudinally.

The surface dose (D_{Sur}) and peak dose (D_{BP}) at the central axis of HEFB are illustrated in figure 6.2.3. Their variation as a function of α is similar for different focal lengths. The D_{sur} in figure 6.2.3a is almost independent of focusing parameters and remains constant around 0.0037 nGy/pro-

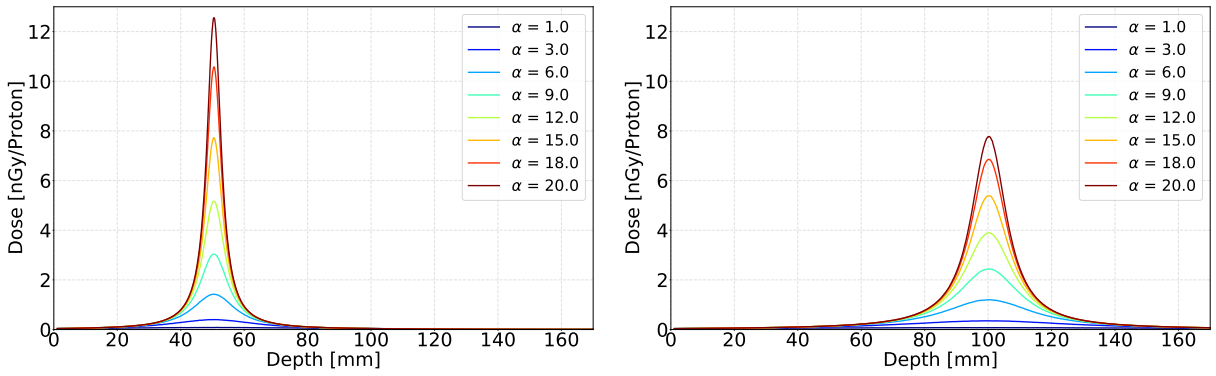

(a) (b)

Figure 6.2.1: Central axis depth-dose curve for 350 MeV proton beams focused at 50 mm (a) and 100 mm (b). Initial beam size is 15.0mm. The value of α varies between 1.0 to 20.0. The beam emittance and β are modified to keep the beam waist at the focused point. The dose is calculated for cylindrical volume elements of radius 0.5 mm and lenght 2.0 mm. It is normalized to the number of initial primary protons entered the water phantom.

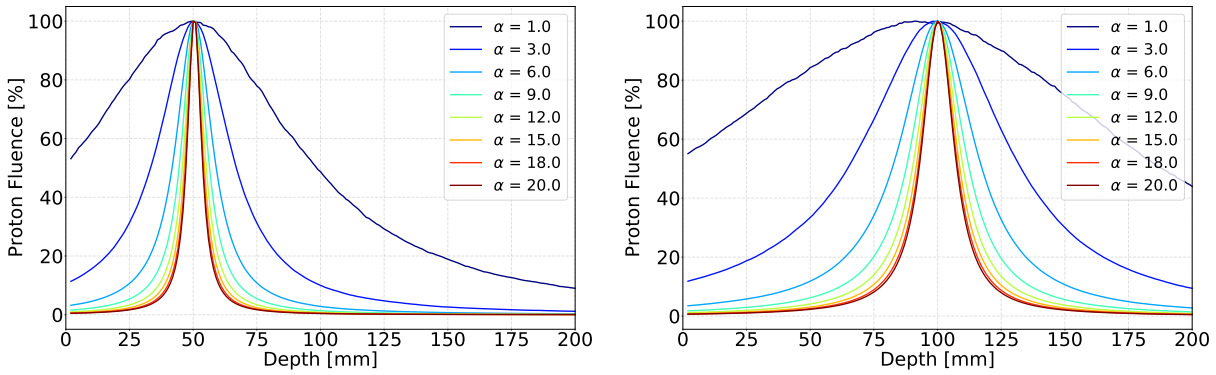

(a) (b)

Figure 6.2.2: Central axis fluence of primary protons of 350 MeV beams focused at 50 mm (a) and 100 mm (b). The fluence is calculated for a circular area of 1 mm radius at the central axis of the beams.

ton. In the context of RT, this low D_{sur} is very desirable.

All simulated HEFBs, independent of the initial Twiss parameters, have identical sizes at the source. They propagates 0.5 mm through a vacuum space between the source and the target. This region acts like a drift space where the beam evolved without any scattering interaction. For a given focal length, the initial divergence of the beam does not differ much to produce a noticeable difference in the transverse size of the beam within the small drift space. Consequently, all the beams have almost equal size at the entrance, leading to an even surface dose. It is also true for different focal points with smaller longitudinal separation. However, a larger distance between the focal points is reflected in the initial divergence of a beam. For a shorter focal length, it is significantly larger, as shown in figure 6.1.2b. Consequently, its lateral contraction is slightly more than the beam with a longer focal length. It explains the slightly elevated D_{sur} of the beam with 50 mm focal length in figure 6.2.3a.

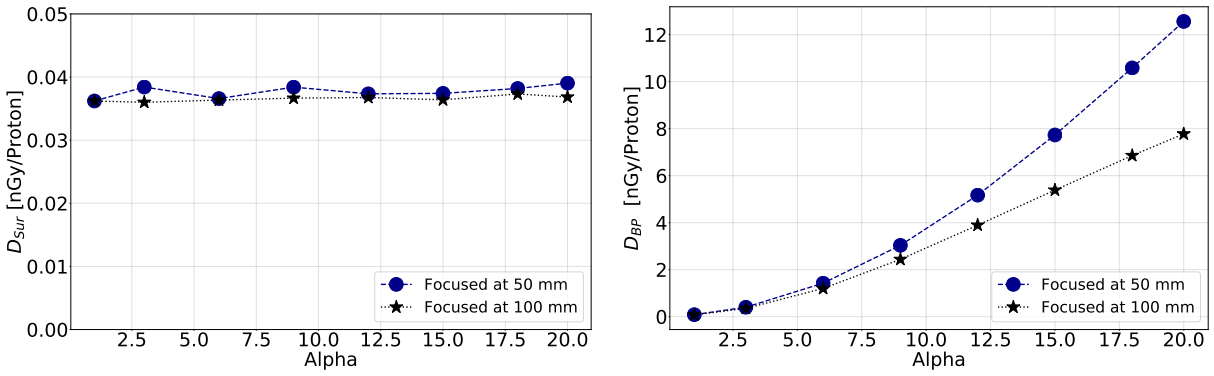

(a) (b)

Figure 6.2.3: (a) D_{Sur} obtained from the simulation of 350 MeV proton beam focused at 50 mm and 100 mm with various focusing strength. (b) Evolution of peak dose (D_{BP}) at 50 mm and 100 mm depths as a function of α.

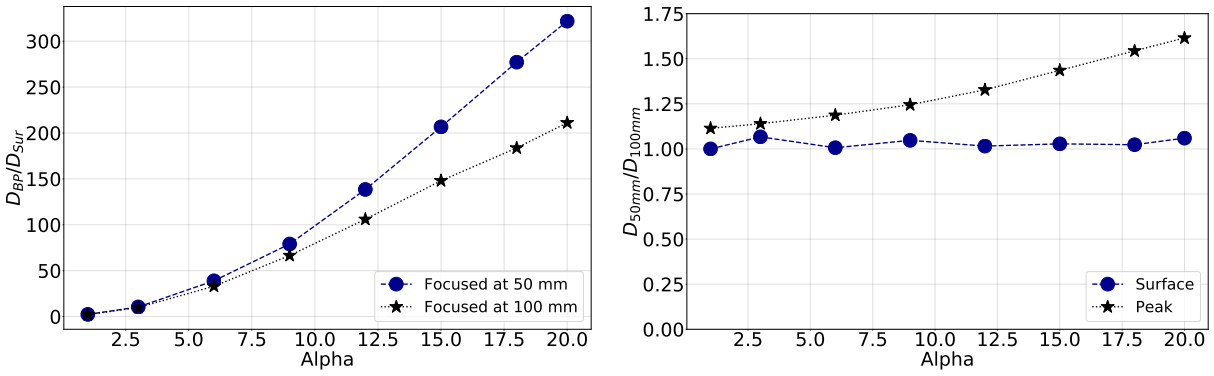

(a) (b)

Figure 6.2.4: (a) D_{BP}/D_{Sur} of 350 MeV HEFB as a function of α. (b) Ratio of D_{BP} and D_{Sur} obtained for 50 mm and 100 mm focal length.

In contrast, the peak dose[1] (D_{BP}) at the central axis of HEFB shown in figure 6.2.3b increases with α for both focal lengths. A larger rate of increase for the beam with a smaller focal length can be evident. The sharper longitudinal peak for shorter focal length in figure 6.2.1 can explain the higher growth rate. With an increased α and corresponding β, the beam waist gets narrower and produces a higher peak dose. At the least focusing strength, $\alpha = 1$, the peak dose is 0.0849 nGy/proton and 0.0762 nGy/proton for 50 mm and 100 mm focal points, respectively. Their difference is about 10% that gradually grows with increasing α. Eventually, the peak dose raises to 12.563 nGy/proton (at 50 mm) and 7.778 nGy/proton (at 100 mm) for $\alpha = 20$ with a difference of 62%.

The peak to surface dose ratio (D_{BP}/D_{Sur}) of two beams, focused at 50 mm and 100 mm, are compared in figure 6.2.4a. They have followed a similar pattern with increased values of α. At a lower value of α, the beams were not very converging. Since the beam's energy do not degrade significantly from its initial value, the stopping power remains almost constant throughout the target. Thus, the difference between the entrance dose and peak dose is not large, leading to a lower D_{BP}/D_{Sur} at smaller α. With increased focusing strength, the peak dose at the focal point

[1]For HEFB, the peak dose is not located at BP, but labeled by D_{BP} for consistency.

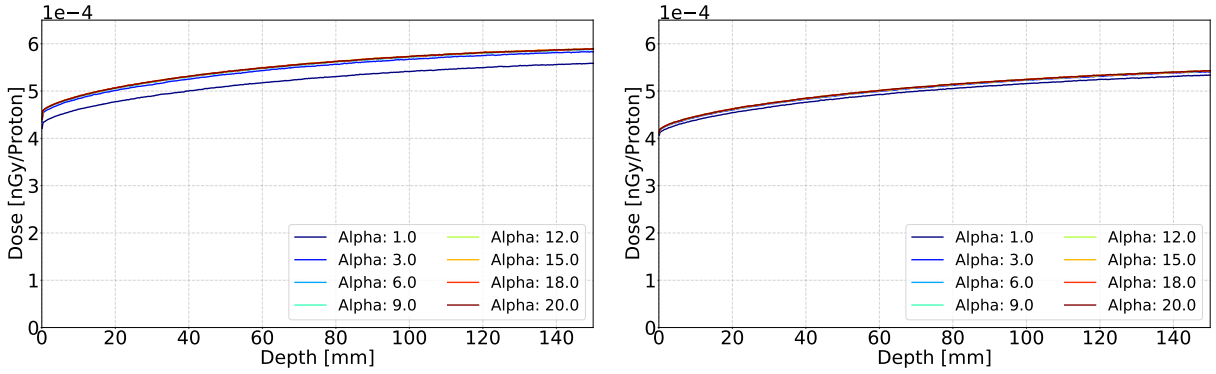

(a) (b)

Figure 6.2.5: Longitudinal depth-dose curves obtained by simulating 350 MeV proton beams focused at (a) 50 mm and (b) 100 mm. Initial beam size is 15.0 mm. The value of α varies between 1.0 to 20.0. The beam emittance and β are modified to keep the beam waist at the focal point.

increases, keeping the surface dose constant. Consequently, the D_{BP}/D_{Sur} gets larger. This is a crucial feature for therapeutic applications. A higher D_{BP}/D_{Sur} provides an opportunity to deposit a larger dose at the tumor, sparing the skin and superficial tissue.

The impact of the focusing depth was assessed using the ratio of D_{Sur} and D_{BP} obtained for two focal points. At the surface, the ratio of their dose is about 1 with a little fluctuation as depicted in figure 6.2.4b. The insignificant difference between their D_{Sur}, shown in figure 6.2.3a, explains this observation. On the contrary, the D_{BP} dose at a shallow focal point grows at a higher rate with α, enhances the value of D_{50mm}/D_{100mm}.

6.2.2 Average dose

The average dose for the broad beam geometry was calculated using an identical configuration as described in the two previous chapters. The result obtained from the simulation of HEFB is shown in figure 6.2.5. The graphs do not look like a conventional depth-dose curve of proton beam as we did not include data up to the Bragg peak position, which was deliberately produced far away from the water phantom. Despite the identical initial energy, there is an inconsistency among the curves of different Twiss parameters. Moreover, the impact of focusing strength and focal point on the dose distribution can be noticed from the graphs.

With the increasing α, the average dose at each depth rises. A similar pattern was observed for CEFB in chapter 5. As we have discussed, the difference between the actual distance traveled by the proton and the projected depth along the longitudinal direction can explain their inconsistency. For a given depth, the growth of the dose is more prominent at the lower range of α. The figure shows that the difference in the deposited dose of two beams with unique focusing parameters remains almost constant through the range of depth with a slightly smaller separation at the shallow region.

6.3 Two dimensional dose profile

Figure 6.3.1 describes the impact of beam focusing on dose distribution schematically. The spot size gets smaller at 50 mm (left) and 100 mm (right) depth with increased focusing strength. The transverse distribution of peak dose varied similarly for both of these focal lengths. However, a difference in longitudinal distribution can be noticed. As we have mentioned earlier in this chapter, the rate of change of transverse beam size with depth at shallow focusing point is larger. In addition, it produces a deep beam waist. Thus the beam can produce a confined high dose region (small volume) for a smaller focal length. On the other hand, σ changes slowly at 100 mm and lead to a flat beam waist. The extended longitudinal high dose region produces a slightly elongated spot. Overall, the spot size at the target can be reduced by tuning the beam parameters, and a fundamental limitation arises given the depth of the focal point and the initial size.

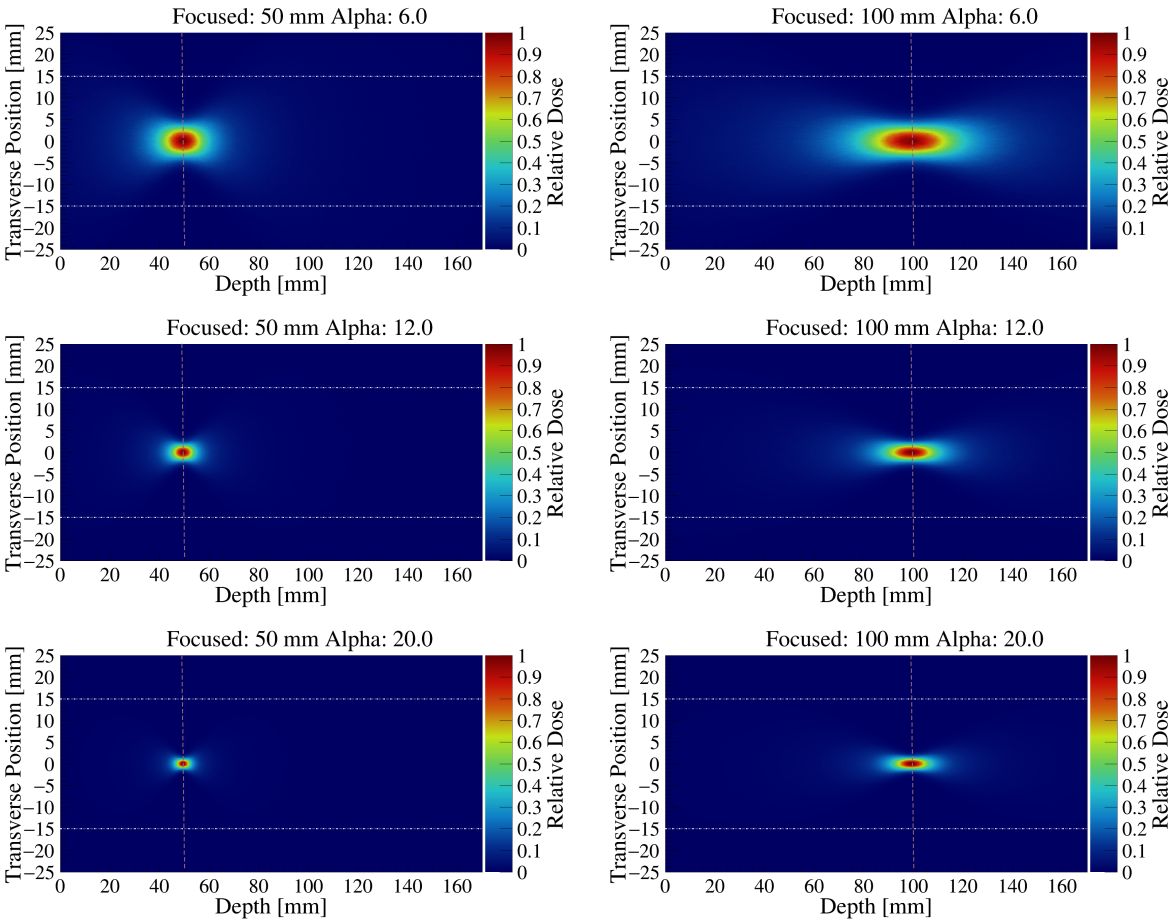

Figure 6.3.1: Two-dimensional physical dose profiles obtained with 350 MeV proton beam focused at 50 mm (left) and 100 mm (right). The initial beam size is given by dotted horizontal lines. The vertical dotted lines represent the position of the focal point. The dose is normalized to the peak dose value and the number of proton entered into the water phantom.

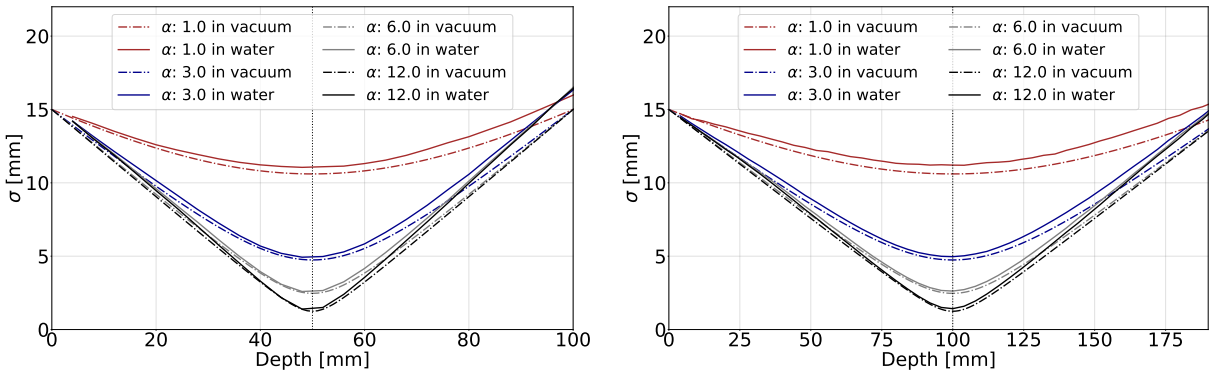

(a) (b)

Figure 6.4.1: Comparison of the simulated (in water) and analytical (in vacuum) beam size obtained by simulating 350 MeV proton beams focused at 50 mm (a) and 100 mm (b).

6.4 Transverse dose profile

As we have discussed in section 2.1.2, ignoring the long tail, the distribution of scattering angles of beam particles in a traversed media can be approximated as a Gaussian. For a transverse dose distribution, a Gaussian is not the most accurate but a reasonable assumption [151]. We used the standard deviation of the distribution to quantify the transverse dose profile of high energy beam as have also done for the two other beam modalities assessed in this thesis. Using the simulated data, we calculated the transverse beam size (σ) at several depths of the water phantom. Simultaneously, we calculated the analytical value of σ in a vacuum as a function of depth. The simulated results and the analytical values for four focusing configurations ($\alpha = 1, 3, 6, 12$) are compared in figure 6.4.1. Independent of the focal length, the simulated beam's size in water gradually gets smaller until its waist. Afterward, it starts to expand following the natural characteristic of focused beam.

Figure 6.4.1 also exhibits a useful feature of the high-energy focused beam that is worthy of mentioning here. It follows a similar lateral expansion in water and vacuum, which means the analytical formula strongly coincides with MC simulation. This feature offers a handy way to estimate beam profiles without executing MC simulations, which is a time-consuming and computationally expensive method. It might be functional for a treatment planning system, where it is challenging to adopt MC simulation due to its slow execution speed.

Despite having a similar pattern, there is a disagreement between simulated outcomes and analytical values. Their difference became less pronounced with increasing α. As shown in figure 6.1.2b, a lower α signifies a smaller divergence and higher β of the focused beams of a given focal length. Thus, the parallel beam becomes more sensitive to scattering. In addition, a more significant deviation of simulated results from the analytical assumption can be seen beyond the beam waist could be a result of MCS. The diverging beam (beyond the waist) is more impacted by scattering interaction.

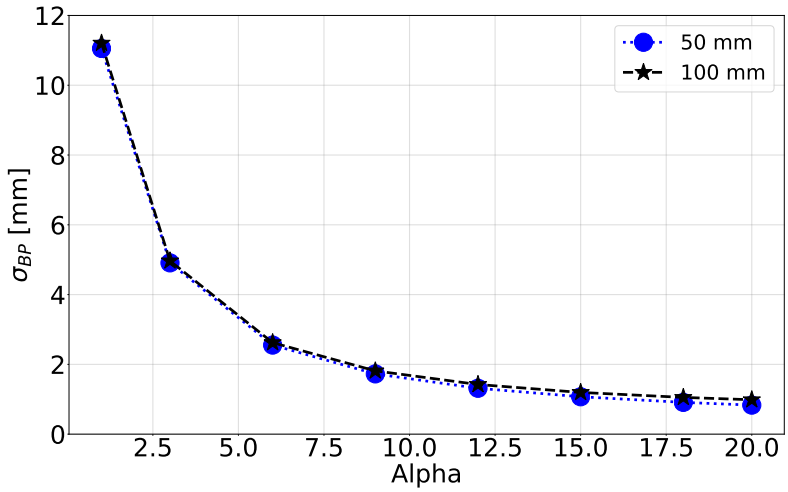

Figure 6.4.2: Evolution of the beam size at focal points (50 mm and 100 mm in water) as a function of α. The maximum statistical error in σ_{BP} is few micrometers. Here, σ_{BP} represents beam size at the focal point, not at the Bragg peak. The notation is used to keep it consistent with the previous chapters.

The transverse beam size at the focal point (50 mm and 100 mm)[2] (σ_{BP}) is compared for a range of focusing strength in figure 6.4.2. The values of σ_{BP} were determined from the Gaussian fitted transverse dose profile at the focal point, as discussed in chapter 4. Independent of focusing depth, the beam size at the waist decreases as a function of α. The results obtained for 50 mm and 100 mm focal lengths are identical at smaller values of α. However, as the α grows, the beam waist at 50 mm becomes relatively smaller. Two factors can cause this difference. Firstly, as a beam travels deep into the water, it encounters more scattering interactions. Even though their influence is less significant at higher energy, it has the potential to cause lateral expansion of the beam, leading to a larger σ_BP at 100 mm depth. Secondly, the beam energy degrades with depth. Thus, the energy of a beam at 100 mm depth in water is lower compared to 50 mm. At lower energy, the beam becomes more sensitive to scattering, which can cause more significant lateral expansion at a longer focal length. However, this minor difference is not likely to impact practical applications. In addition, this discrepancy can be overcome using a higher energy beam.

The divergence of a focused beam is smallest for $\alpha = 1$, and it produces the least focusing effect. As a consequence, the transverse beam size drops slightly from its initial value of 15 mm to 12.08 mm and 12.20 mm at 50 mm and 100 mm depth, respectively. In addition, figure 6.4.2 shows a nonlinear reciprocal relation between σ_{BP} and α. Beyond an optimum value of α, around 12, the transverse beam size changes a little at its focal point. This effect can be understood from the divergence-α relation depicted in figure 6.1.2b. The change in beam divergence is very small for larger values of $alpha$. Initially, σ_{BP} drops sharply with α and reaches around 1.75 mm at $\alpha = 9$. Further increase in α provides a slower drop of σ_{BP}. The simulated data shows a sub-millimeter beam size as the α approaches to 20. It is 0.83 mm and 0.98 mm for 50 mm and 100 mm focal length,

[2]For HEFB, the peak dose is not located at BP, but we labeled σ_{BP} for consistency.

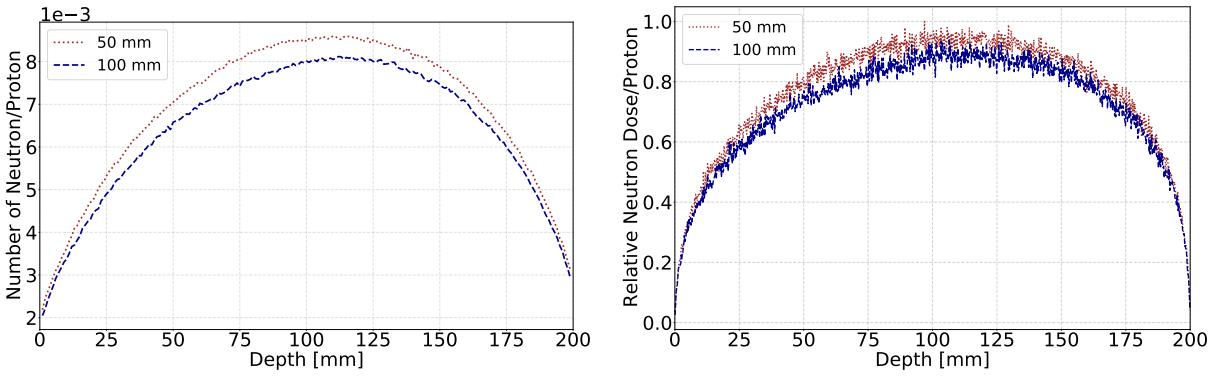

(a) (b)

Figure 6.5.1: (a) Evolution of number of neutrons as a function of depth in the water phantom. The number is normalized to the number of initial protons. (b) Comparison of neutron dose deposited by HEFB of focal length 50 mm and 100 mm. The dose is normalized to the peak dose deposited by the beam focused at 50 mm. The graphs in (a) and (b) are obtained for 350 MeV proton beam with $\alpha = 20$.

respectively. This small lateral beam size can be used to irradiate small tumors, even metastasis, with improved precision.

6.5 Neutron Dose

The HEFB configuration used in the simulations does not contain any external source of neutron like a collimator in the case of CB. However, nuclear interactions inside the water phantom generate neutrons. Figure 6.5.1a shows how the number of neutrons changes with depth inside the phantom. The assessed beams were simulated to focus at 50 mm and 100 mm. The initial Twiss parameters and emittance were tuned for α = 20. The number of neutrons gradually increases until the peak value, where a longitudinal equilibrium is reached. The shape of the curve is explained in chapter 5.

The neutron dose-depth curves of HEFB illustrated in figure 6.5.1b follow a similar trend as the number of neutrons shown in figure 6.5.1a. It increases with depth at a decreasing rate and reaches the maximum at around 120 mm, where a longitudinal equilibrium is achieved. Afterward, it starts to decrease as a function depth.

Despite the same initial kinetic energy, there is a clear difference between two focal lenghts (50 mm and 100 mm) in the context of neutron-induced properties. Both quantities are higher for 50 mm focal length. The initial divergence of a beam with shorter focal length is higher. As the beam converges, the difference between the actual distance traveled by the protons and the projected distance increases. Thus, protons of a beam with increased divergence have a higher probability of interact due to their larger traversed distance. These interactions can produce more neutrons, consequently enhanced neutron dose.

6.6 Summary

HEFB has the potential to produce a very small spot at the target. Its energy spectrum is suitable to mitigate the lateral expansion caused by the MCS. The large value of D_{BP}/D_{Sur} offers an exclusive opportunity to deposit an extended dose at target with minimum skin damage. The longitudinal spread of the focal point increases with depth, which can be advantageous because a spread-out peak can be produced using fewer beams. Besides, the beam properties can be estimated with higher accuracy by utilizing time-efficient analytical methods.

This beam shaping technique can not utilize the benefits of the high dose produced by the Bragg peak. However, it can create a significant contrast in dose between the target and surroundings. This feature can be utilized to achieve the goal of external beam therapy. The higher LET of low energy Bragg peak region can not be incorporated in the treatment plan as the energy degradation of HEFC is less pronounced. Further radiobiological studies are needed to understand the efficacy of treatment using HEFB.

The simulation of the 250 MeV proton beam showed a similar result as the 350 MeV beam. The conventional proton beam therapy centers are likely to produce 250 MeV beams. Thus, the experimental studies can be carried out in existing proton beam therapy centers with an additional focusing device or nozzle modification. The next chapter will discuss a possible solution to generate a focused proton beam for experimental purposes based on the conventional proton beam therapy center's beamline.

Chapter 7

Magnetic optics

A focused proton beam can produce a small spot at the tumor, as we have discussed in two previous chapters. Simultaneously, its unique dose profile can reduce the entrance dose. The ability to produce distinct spots makes the focused beam a competent candidate to perform Grid therapy. However, its implementation in practical applications needs experimental assessment, which is not covered in this thesis. This chapter will discuss the feasible techniques based on a conventional proton therapy center to validate our proposed focused beam modalities.

7.1 Principle of focusing

In general, magnetic lenses like quadrupoles are used to produce converging and diverging beams. The principle of beam focusing has been discussed in section 2.4.2. Proton beam therapy centers employ the active or passive scanning technique to irradiate tumors. Usually, a conventional treatment system does not require a strongly focused beam. However, several quadrupoles are employed in proton therapy beamlines for beam manipulation. In principle, a suitable combination of a few quadrupoles can produce a highly focused beam from a traditional proton therapy beamline. In the below, we assume that we add magnetic components to an existing proton therapy beamline, for example, at Oslo proton therapy center, which is currently under construction, to produce a focused beam. Since the exact beam parameters for the center are not yet available, we base our calculations on the measurements of the beam parameters from the DCPT (Danish center for proton therapy) [152]. The parameters for 150 MeV is listed in table 7.1.1 [153].

Figure 7.1.1 shows the conceptual diagram of our intended component to produce a focused proton beam using a conventional proton therapy beamline. It should be placed in between the target and the nozzle of a traditional therapy center. With perfect alignment, the overall shape of a beam changes in a predictable way during its passage through a combination of quadrupoles. The strength and separation of these quadrupoles should be tuned to produce a beam with the desired characteristics. The basic principle of beam optics matching has been discussed in section 2.4.2.

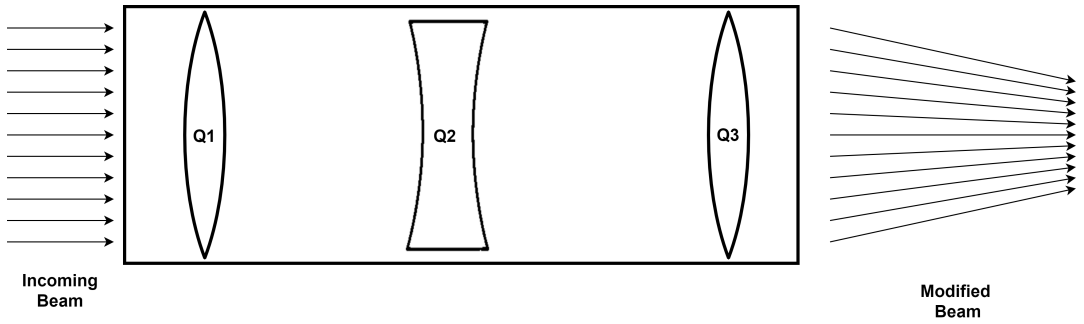

Figure 7.1.1: Principle of beam matching to generate desired focused beam using a conventional proton therapy beamline.

MADX is a comprehensive tool for beam optics simulation, which we have used extensively for our studies in this chapter. A detail of the MADX simulation method has been discussed in section 3.5.

A beam with a circular cross-section is preferred for our proposed focused beam modalities discussed in chapter 5 and chapter 6. Fundamentally, the magnetic field of a quadrupole converges (focus) a beam along one transverse direction and diverges (defocus) in another, making it difficult to achieve a circular beam configuration. Even though an overall converging effect can be produced in both transverse directions using multiple quadrupoles, their focusing strengths are usually not identical. As a consequence, without proper tuning a combination of quadrupoles produce an elliptical beam. Mathematically, the area of an ellipse, $A = \pi ab$, a and b are the lengths of the major and minor axis. An optimum value of quadrupoles' strength and configuration can be developed to minimize the cross-section of a beam at the focal point. The transverse sizes σ_x and σ_y can be used to quantify the area:

$$A = \pi \sigma_x \sigma_y. \tag{7.1.1}$$

The parameters of a proton beam change as it propagates through various components of a proton therapy system. The values of these parameters at the nozzle and the isocenter are crucial for our studies. The mechanical isocenter refers to the center of rotation of the gantry of a proton beam therapy center. On the other hand, the radiation isocenter is the point in space where the center of radiation of a rotating gantry intersects. It is characterized by the locus of the perpendicular distances of the beam center from the mechanical isocenter [154]. The nozzle is located in the gantry, where the protons come out of the machine to irradiate a target placed at the isocenter. A set of a typical values of proton therapy beamline are listed in table 7.1.1. The values at the isocenter were taken from the DCPT. The approximate values of the Twiss parameters at the nozzle were calculated through back-projection of the beam using equation 2.4.29, 2.4.30, and 2.4.31. The estimated distance between the isocenter and the nozzle was 1.5 m.

The focusing effect on a narrow beam is not significant to distinguish its dose profile from the narrow collimated beam as compared in appendix C. With its smaller initial size, the converging effect generated by the quadrupole is shortly balanced by the diverging effect due to MCS. In fact,

Table 7.1.1: Parameters of conventional proton therapy beamline for 150 MeV beam.

Parameters (x-plane)	**Standard value at isocenter**	**Standard value at nozzle**
Emittance (mm-mrad)	13.59	13.59
Beta (m)	1.112	2.94
Alpha	-0.066	1.29
Gamma (m^{-1})	0.90	0.90
Sigma (mm)	3.89	6.32
Divergence (mrad)	3.50	3.50
Parameters (y-plane)	**Standard value at isocenter**	**Standard value at nozzle**
Emittance (mm-mrad)	5.36	5.36
Beta (m)	1.14	8.41
Alpha	1.46	3.50
Gamma (m^{-1})	1.57	1.57
Sigma (mm)	2.80	6.71
Divergence (mrad)	2.90	2.90

it (MCS) surpasses the converging effect at the end of the range of a beam, especially at high initial energy, causing lateral expansion. In contrast, a larger initial beam size can enhance the effect from focusing. We simulated the CEFB with an initial size of 10 mm. However, a significant focusing effect in their dose profile was observed for narrower focused beams, however these results are not included in this thesis.

We have assessed two distinct focusing schemes. Firstly, we tried to produce the desired beam using the existing emittance of the conventional proton beam therapy center. We found it challenging within the limitations of the quadrupole gradient and length of the focusing device. In the second scheme, we have attempted to improve the matching performance using an increased emittance. Even though it is very unconventional from the context of accelerator physics, we found interesting outcomes.

7.2 Focusing with constant emittance

It can be seen in table 7.1.1 that the conventional estimated beam size at the nozzle is smaller than 10 mm at 150 MeV energy. The proposed beam shaping modality using conventional energy proton beam prefers an increased initial beam size to produce effective focusing. Assuming the initial emittances from Table 7.1.1 and requiring a beam size (σ_u) of 10 mm at the entrance of the simulated water phantom, leads to specific values of the Twiss parameter β following equation 2.4.22. For a 150 MeV beam, values of β were found 7.361 m and 18.658 m in the transverse x and y directions. We designed our CEFB irradiation modality to produce the waist (focal point) at the BP of the beam. As we have discussed in section 2.1.3, the depth of the BP solely depends on the beam energy for a given material. From the simulation, we found the depth of the BP of 150 MeV proton beam is around 155.2 mm. A set of Twiss parameters determines the depth of the focal point (beam waist) following equation 2.4.32. With constant depth of the focal point and β, this second-degree equation has two solutions of $\alpha = 46.88$ and $\alpha = 0.0213$ for x-direction. The

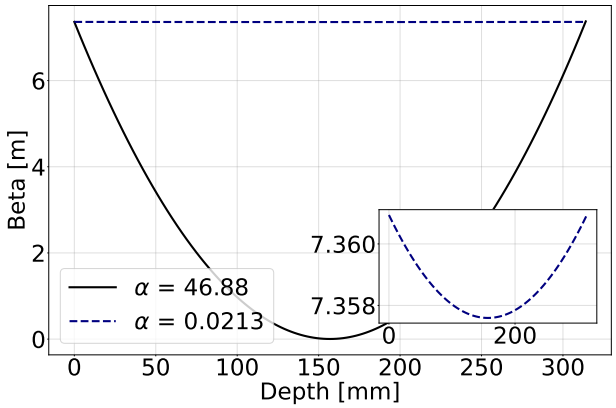

Figure 7.2.1: Evolution of the analytical value of β as a function of distance obtained for $\alpha = 46.88$ and $\alpha = 0.0213$. The change in β is insignificant for the smaller α.

smaller value of α corresponds to an almost parallel beam. Thus, the larger value of α among the two solutions of equation 2.4.32 is desirable for beam focusing. In fact, the smaller α could not produce any significant focusing to converge the beam as shown in figure 7.2.1. Both graphs have hyperbolic shape; however, the change in β with depth is negligible with the smaller α. Similarly, in transverse y-direction, $\alpha = 118.9$ produced desired focusing effect.

In order to produce the desired beam, we simulated quadrupole assemblies. The number of quadrupoles was gradually increased to optimize the matching. The results using up to three quadrupoles were not promising. The inclusion of the fourth quadrupole within a length of 1.6 m in the matching algorithm produced a significantly improved result. In the model used for the matching, the entrance of the water phantom was designed as being 0.2 m away from the exit of the final quadrupole. We tuned quadrupole strength and their separation to obtain the intended beam. The maximum quadrupoles gradient was limited to 30 T/m with an aperture of 30.0 mm radius. These limiting parameters were set considering the commercially available options of quadrupoles [155]. However, a custom-made quadrupole can have a higher gradient. The four quadrupoles configuration with associated limitations could not provide us an exact match. Nonetheless, the obtained result was promising, as shown in table 7.2.1. A large difference between intended and obtained Twiss parameters has two consequences. Firstly, the beam waist cannot be focused on the target, reducing the effective dose at the tumor. Secondly, there might be another position inside the patient's body where the beam has a smaller transverse dimension resulting enhanced dose at the healthy tissue. Moreover, the β function, which determines the size of the beam, was large inside the quadrupoles assembly, which can be seen in figure 7.2.2a. The limitation of the aperture of quadruple might cause a beam loss which is not desired. In addition, beams with a larger β function experience a bigger phase shift in their passage through quadrupoles with higher strength, known as the chromatic effect [86]. As a consequence, all protons of a beam with energy spread can not be focused at the same point. It can increase the spot size and reduce the peak dose. This effect

can be minimized by inserting sextupole magnets in the beamline, which is beyond the scope of this thesis.

Table 7.2.1: Matching results obtained using four quadrupoles.

Parameters	Intended values	Obtained values	Difference [%]
Beta (x)	7.36	10.74	45.9
Alpha (x)	46.88	28.49	39.3
Beta (y)	18.65	22.81	22.3
Alpha (y)	118.88	111.00	6.6

Table 7.2.2: Matching results obtained using five quadrupoles.

Parameters	Intended values	Obtained values	Difference [%]
Beta (x)	7.36	7.36	0.0
Alpha (x)	46.88	46.88	0.0
Beta (y)	18.65	18.65	0.0
Alpha (y)	118.88	118.88	0.0

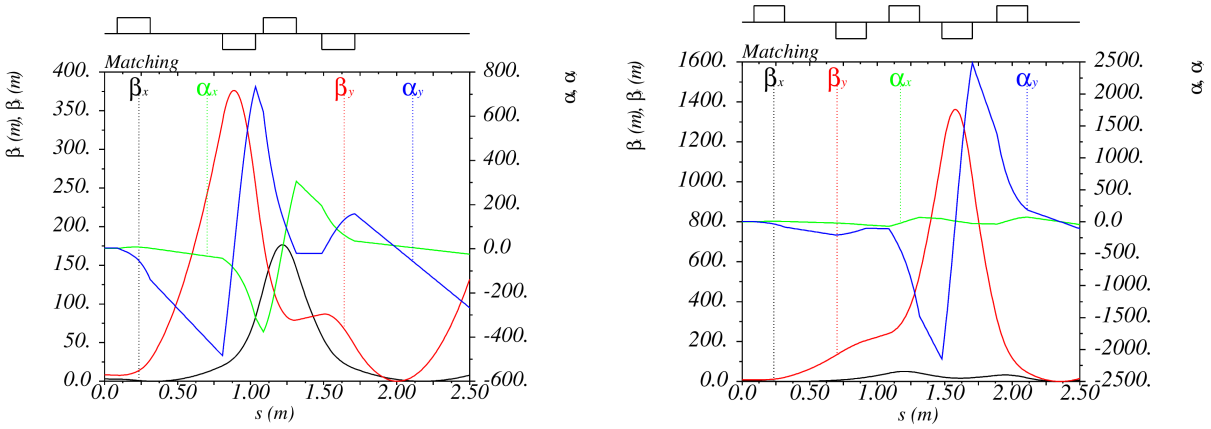

(a) (b)

Figure 7.2.2: Evolution of the Twiss parameters through four (a) and five (b) quadrupoles assembly. The positions of the quadrupoles are shown at the top bar. Desired α of the focused beam is 7.0 and β is 1.12 m. The quadrupoles strengths are tuned to match the beam at 1.8 m (a) and 2.2 m (b).

Conversely, an array of five quadrupoles of 2.0 m length can produce a perfect match of beam optics. The results are listed in table 7.2.2. The evolution of the beam's optical parameters for the assembly is shown in figure 7.2.2b. The β function in one transverse direction is very large at some points inside the focusing device. It can reduce the beam current due to the large transverse size of the beam.

The method of implementing existing emittance has another crucial limitation. As we have seen in the earlier chapters, the degree of focusing depends on the combination of the Twiss parameters. A fixed β can generate a certain focusing at the beam waist, which can not be tuned further.

7.3 Focusing with increased emittance

A focused beam produces large dose contrast between surface and target due to the difference in transverse beam size, which gets narrower with depth. It can enhance the Bragg peak to surface dose ratio, a desirable feature for RT. A large divergence ($\sigma_{u'}$) of a converging beam reduces the transverse size more prominently. The Twiss parameters and emittance determine the divergence of a beam (see equation 2.4.23). A higher α reflects a more potent focusing effect. For a fixed focal point, increasing α must be compensated with a corresponding increase of β following equation 2.4.32. The emittance must be modified to achieve a particular β-function with a constant beam size (σ_u) of 10 mm. This method also facilitates us with an opportunity to alter the degree of beam focusing. The beam emittance of a conventional proton therapy center is lower than our designed value. Implementing our proposed treatment modalities requires a larger emittance, which is possible to achieve by means of a scattering device. A sample calculation based on gold scattering foil has been included in appendix A. The scatterer also modifies the Twiss parameters and increases the energy spread of the beam. However, we have ignored these effects for our estimation of the focusing device.

Matching results obtained for different focusing strength (quantified by α) using three quadrupoles can be seen in figure 7.3.1. The solid black lines in figure 7.3.1a and 7.3.1b represent the perfect match where the obtained values are equal to the desired values. The three quadrupoles combination can produce a suitable match in both transverse directions for smaller focusing. However, it can not produce a reasonable configuration to generate a highly focused beam. In addition, the field gradient of the third quadrupole shown in figure 7.3.1c was above 40 T/m, which is a bit high for conventional quadrupoles. A sample evolution of beam parameters (to obtain $\alpha = 7$) in the quadrupoles array is illustrated in figure 7.3.3a.

In our estimation of beam parameters, we assumed a non-zero initial α at the nozzle. It is likely possible to make close to zero by changing the strength of the final quadrupoles in the beamline. With $\alpha = 0$, the initial beam becomes parallel. We observed better matching results with a zero initial α as shown in figure 7.3.2. The evolution of the Twiss parameters to obtain $\alpha = 7$ with this initial beam configuration is shown in figure 7.3.3a.

As depicted in figure 7.3.4, an assembly of four quadrupoles extended our limit of the perfect match. It matches α in both transverse directions with 100% accuracy up to 12. However, the obtained β can be observed to deviate from the desired value beyond $\alpha = 10$. In addition, the quadrupoles' strength (except the fourth quadrupole) increased as a function of focusing strength. Looking into the figure 7.3.4c, we can identify the maximum field gradient around 35 T/m, lower than the three quadrupoles assembly. This is a reasonable gradient. The evolution of the Twiss parameters for four quadrupole assembly is depicted in figure 7.3.6a. The largest $beta$ is within moderate range.

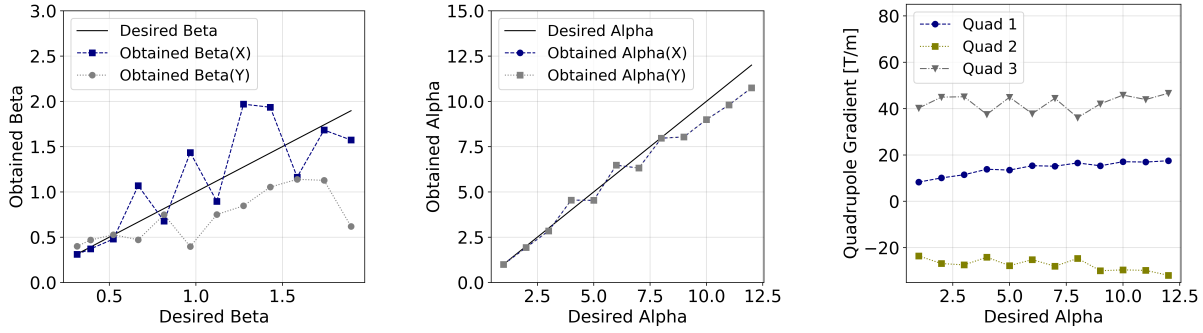

(a) (b) (c)

Figure 7.3.1: (a) Obtained β as a function of required β when matching the Twiss parameter using three quadrupoles. (b) Obtained α as a function of required α when matching the Twiss parameter using three quadrupoles. (c) Required quadrupole gradients as a function of α to produce an optimum match. Results are obtained for non-zero initial α.

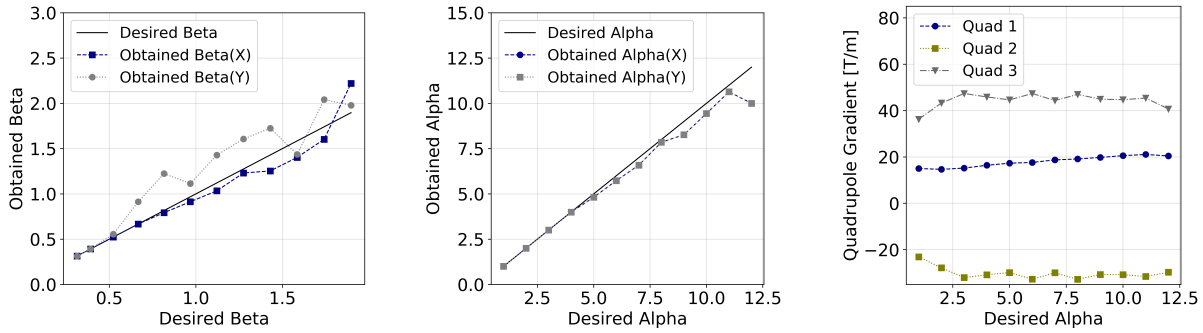

(a) (b) (c)

Figure 7.3.2: (a) Obtained β as a function of required β when matching the Twiss parameter using three quadrupoles. (b) Obtained α as a function of required α when matching the Twiss parameter using three quadrupoles. (c) Required quadrupole gradients as a function of α to produce an optimum match. Results are obtained for initial $\alpha = 0$.

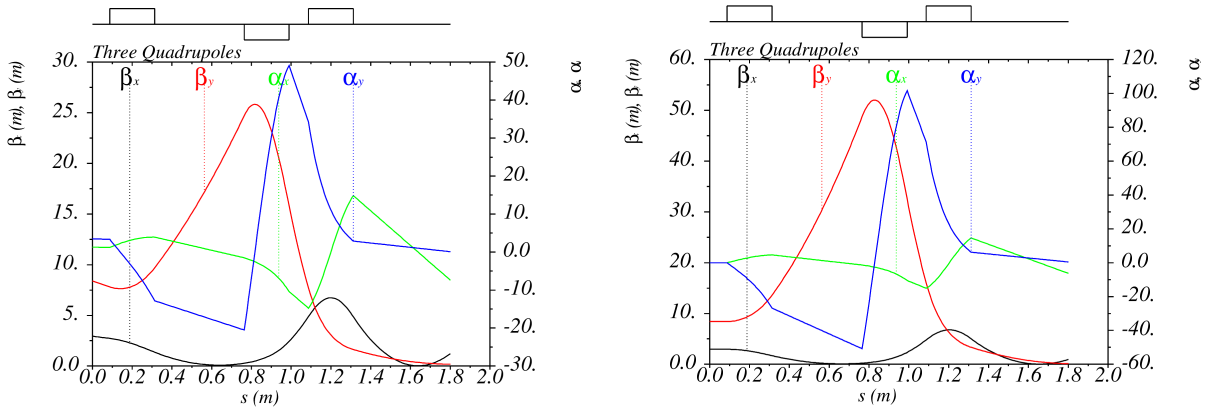

(a) (b)

Figure 7.3.3: Evolution of Twiss parameters through three quadrupoles assembly with initial non-zero α (a) and zero α (b). Desired α of the focused beam is 7.0 and β is 1.12 m.

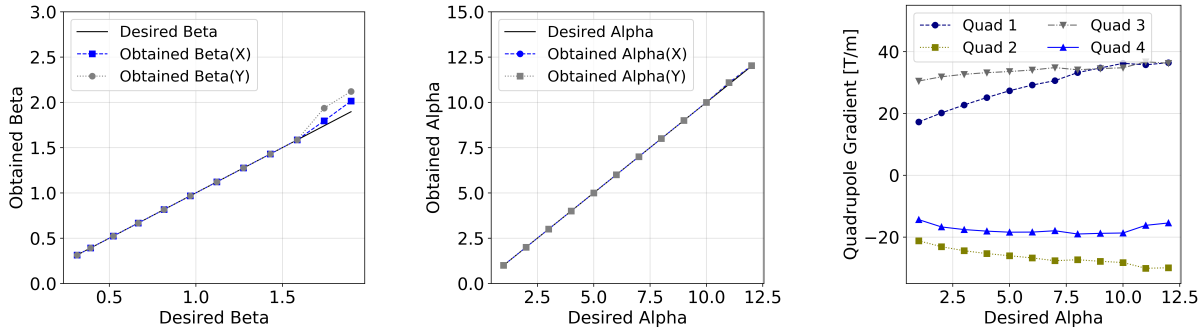

(a) (b) (c)

Figure 7.3.4: (a) Obtained β as a function of required β when matching the Twiss parameter using four quadrupoles. (b) Obtained α as a function of required α when matching the Twiss parameter using four quadrupoles. (c) Required quadrupole gradients as a function of α to produce an optimum match. Results are obtained for non-zero initial α.

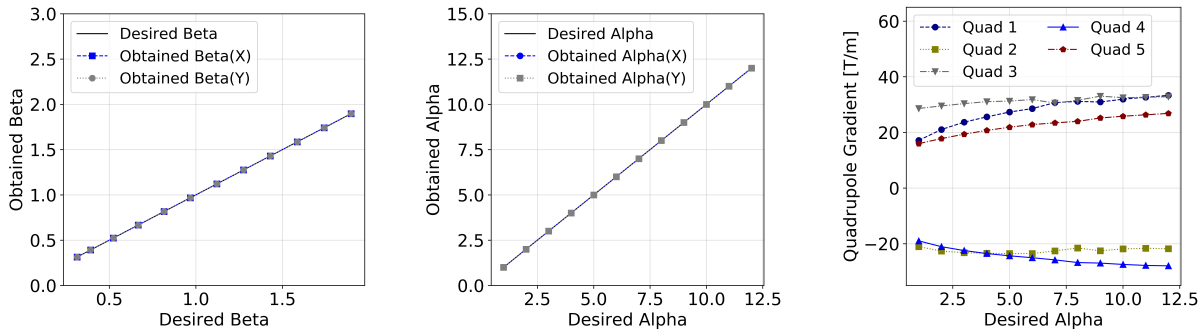

(a) (b) (c)

Figure 7.3.5: (a) Obtained β as a function of required β when matching the Twiss parameter using five quadrupoles. (b) Obtained α as a function of required α when matching the Twiss parameter using five quadrupoles. (c) Required quadrupole gradients as a function of α to produce an optimum match. Results are obtained for non-zero initial α.

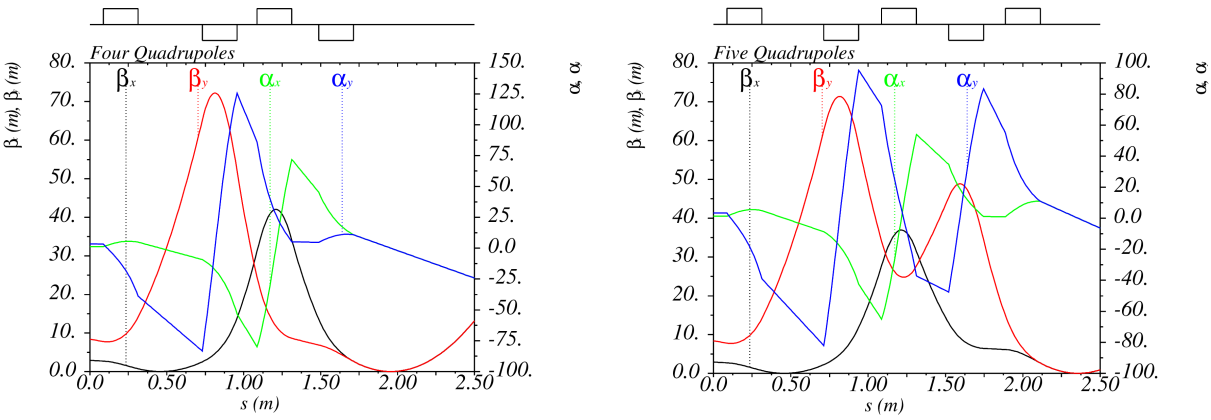

(a) (b)

Figure 7.3.6: Evolution of Twiss parameters through four (a) and five (b) quadrupoles assembly with initial non-zero α. Desired α of the focused beam is 7.0 and β is 1.12 m.

Within the assessed range of α, With a combination of five quadrupoles we could determine a perfect match in both transverse directions. The results are compiled in figure 7.3.5. The maximum field gradient was found less than 35 T/m. With reasonable quadrupole gradient and moderate β (in figure 7.3.6a), this configuration can deliver the desired focused beam.

7.4 Summary

In the chapter, we have developed an approximate design for beam focusing based on conventional proton therapy beamline. The results are based on several estimations. A perfect match using a beam with existing emittance is challenging to achieve by using a limited number of quadrupoles with a restricted gradient. However, the results are promising. On the other hand, the unconventional method of increased emittance can deliver a better result.

The beam emittance can be increased using metal scatterer. This will also introduce a spread in the beam energy. As we have mentioned earlier, it can cause a chromatic effect inside strong quadrupoles. Chromatic effects have not been studied here, and deserves further investigations. However, the overall result shows a reasonable quadrupole configuration that can be constructed to produce desired beams to validate the biological effects of our proposed beam shaping techniques. The matching algorithm does not depend on the beam energy. For high energies, matching is possible with an elevated quadrupole gradient. Thus, we did not examine high-energy beams individually. Experimental validation of HEFB can be carried out using a 250 MeV proton beam, usually produced by most of the existing proton therapy centers.

Chapter 8

Comparison and Discussion

We have assessed three different beam shaping techniques specified as Collimated beam (CB), Conventional-energy focused beam (CEFB), and High-energy focused beam (HEFB). The generation of CB using metal collimators is very convenient and well established. Its dosimetric properties have been discussed exclusively in chapter 4. In principle, a focused proton beam can be produced by employing quadrupoles in the beamline. The degree of focusing depends on the quadrupoles strength as well as the initial beam parameters. The feasibility of producing CEFB and HEFB based on existing proton beam therapy facilities has been assessed in chapter 7. We have noticed several distinct features of CEFB and HEFB in chapter 5 and chapter 6, respectively. This chapter draws a comparison among different beam shaping techniques based on their pristine Bragg peak, spread out Bragg peak (SOBP), and proton GRID configuration. Simultaneously, it assesses potential medical applications of different beam shaping techniques depending on their dose profile.

8.1 Pristine Bragg peak

The depth-dose curve of a quasi-monoenergetic proton beam, generated by an accelerator, usually produces a sharp peak near the end of its range, often called the pristine Bragg peak. As we have seen, the largest fraction of the beam's energy is deposited at its Bragg peak (BP), which is the basis of the proton-based treatment modalities. Additionally, this feature enables high conformity to the tumors.

A comparison among proton depth-dose curves and corresponding BPs generated by CB, CEFB, and HEFB was conducted through simulations. The CB was simulated by implementing a natural lead (Pb) collimator with a circular opening of radius 2.0 mm. The detailed procedure has been given in section 4.1. Despite the fact that a submillimetric collimator is capable of producing a narrower beam, this 2.0 mm collimator is used for comparison because it can deposit a moderate dose at the Bragg peak, which changes reciprocally with the collimator radius (Section 4.3). The energy of the CB was 150 MeV with a 1% spread. The CEFB of 150 MeV and HEFB of 350 MeV

were simulated with the same relative energy spread as CB. The initial beam size (σ_x and σ_y) of HEFB was 15.0 mm which was 50% larger than the CEFB's size of 10.0 mm. The beam parameters were tuned for $\alpha = 20$ to produce the peak dose[1] (D_{BP}) at the same depth as the BP of 150 MeV proton beams in water (approximately 155 mm). The comparison of the dose profiles of these beams, illustrated in figure 8.1.1, reveals several distinct features of different beam shaping techniques.

The two-dimensional dose profile of CB, CEFB, and HEFB are compared in the left column of figure 8.1.1. It shows the depth dose curves of these proton beams in the right column. The longitudinal dose has been calculated for cylindrical volume elements of radius (r) 0.5 mm, 2.0 mm, and 5.0 mm. The horizontal lines in the two-dimensional dose profile represent the outline of the volume around the beam's central axis where dose calculations have been performed (green for 0.5 mm, white for 2.0 mm, and red for 5.0 mm). The 2.0 mm cylindrical configuration appears to be the most appropriate dimension to quantify dose as it includes the highest dose region of the beams reasonably. A further reduction in radius did not change the peak dose of the CB and CEFB effectively, even though a small dose enhancement at the focal point of the HEFB can be noticed in figure 8.1.1d. In contrast, a larger radius starts to reduce the peak dose significantly. We have assessed the longitudinal dose profile using 0.5 mm (figure 8.1.1d) and 5.0 mm (figure 8.1.1f) radius to compare the effects of very narrow and wide geometrical configurations on different beam shaping modalities.

At the entrance, the beam energy is largest, reducing the effect of multiple Coulomb scattering (MCS) experienced by protons. Thus, most of the primary protons of CB remain inside the initial transverse size of the beam and deposit their energy within a 2.0 mm range around the central axis (figure 8.1.1a). As the beam propagates deeper into the simulated water phantom, it spreads laterally, carrying energy out of its initial transverse size. In contrast, CEFB and HEFB are focused on a point, which is located at the BP depth of a 150 MeV proton beam. Because of their converging nature, the density of energy deposition was concentrated around the focal point.

Figure 8.1.1e compares the average dose within the cylindrical volume of 2.0 mm radius around the beam's central axis. The dose has been normalized to the number of protons entering the water phantom for all different beam shaping methods to ensure a reliable comparison. The D_{BP} of the CB is a result of the higher stopping power of the proton beam at its lower energy [150]. In contrast, the focusing of the CEFB enhance the dose at its BP along with the higher stopping power. According to the simulated data, the D_{BP} of the CEFB is 4.77 nGy/proton, which is almost equal to the CB's D_{BP} of 4.65 nGy/proton. It can be explained from the similar transverse dose distribution of CB and CEFB at the BP. Nearly equal fractions of protons were encapsulated within a 2.0 mm radius for both beam shaping modalities. The small difference of 2.5% between their D_{BP} might not significantly impact the treatment procedure. However, a clear difference between

[1]For HEFB, the peak dose is not located at BP, but we labeled D_{BP} for consistency and avoid conflict with "Peak Region Dose" of GRID configuration.

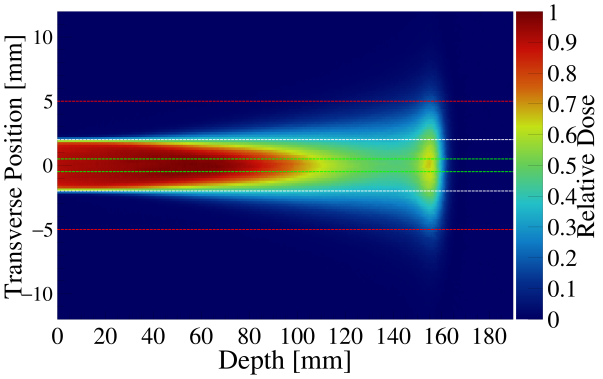

(a) 2D dose profile of 150 MeV CB

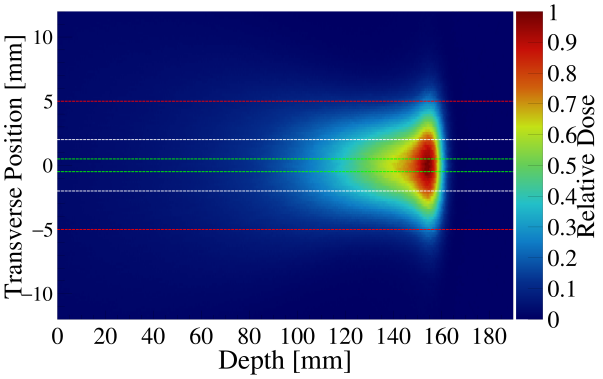

(b) 2D dose profile of 150 MeV CEFB

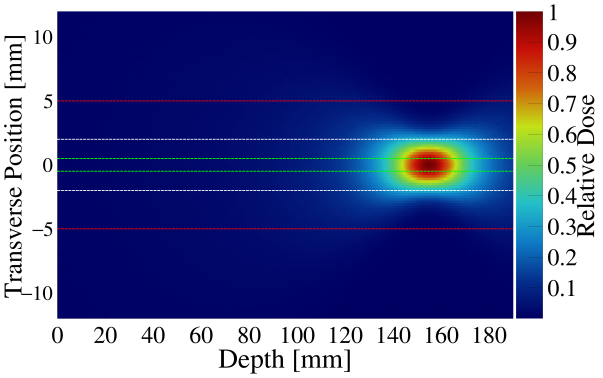

(c) 2D dose profile of 350 MeV HEFB

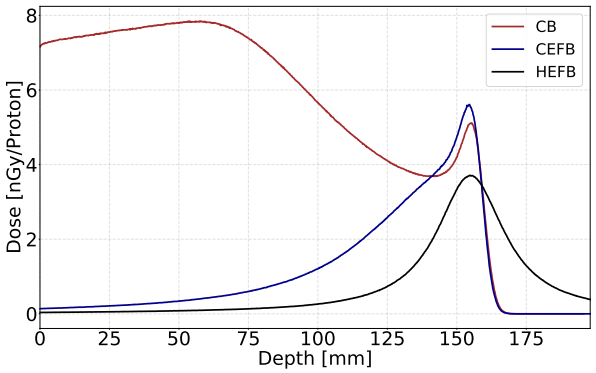

(d) Depth-dose curves, r = 0.5 mm

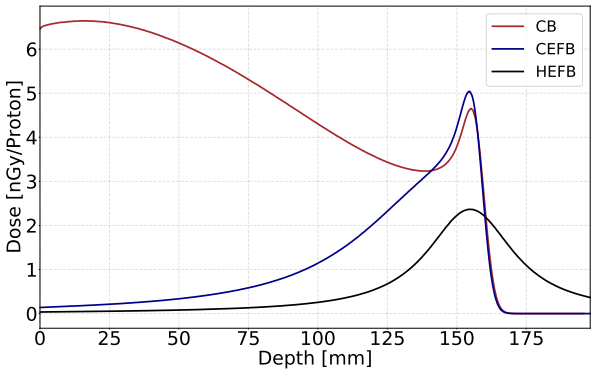

(e) Depth-dose curves, r = 2.0 mm

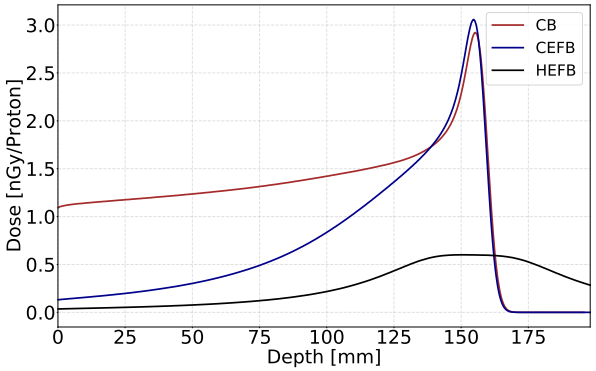

(f) Depth-dose curves, r = 5.0 mm.

Figure 8.1.1: Left: Comparison of two-dimensional dose profile of CB (a), CEFB (b), and HEFB (c) with an identical peak dose position. CB was simulated with a 2.0 mm collimator. Focused beams were produced for $\alpha = 20$. The horizontal lines show the outline of volume included for dose calculation (green for 0.5, white for 2.0 mm, and red for 5.0 mm). The dose is normalized to the peak value. Right: Comparison of depth-dose curves obtained for CB, CEFB, and HEFB measured at the central axis of the beams. The curves are produced for cylindrical configuration of radius (r) 0.5 mm (d), 2.0 mm (e), and 5.0 mm (f) to compare the longitudinal dose profile of three beam shaping modalities. The longitudinal dose profile looks similar, particularly for 0.5 mm and 2.0 mm collimator radius. However, the magnitude of the dose is significantly different.

their surface doses (D_{Sur}) can be noticed in figure 8.1.1e, which can impact the healthy tissue with a different degree of severity. The higher D_{Sur} of CB has the potential to damage skin and superficial tissue. Nevertheless, the adverse effect of high D_{Sur} can be ameliorated by employing submillimetric proton beams (commonly known as microbeam and minibeam), which can exploit the dose-volume effect, essentially requiring a small irradiation volume [156]. Even though a narrow beam can enhance the normal tissue tolerance, it diminishes the D_{BP} as we have discussed in chapter 4. Consequently, it reduces the Bragg peak to surface dose ratio (D_{BP}/D_{Sur}) and overall efficiency of the irradiation process is lower than for the focused beam.

On the other hand, the magnetically modified CEFB can reduce the D_{Sur} substantially compared to the CB. We determined a D_{Sur} of 6.46 nGy/Proton with a D_{BP}/D_{Sur} of 0.74 of the CB. This lower value of D_{BP}/D_{Sur} (less than 1) implies that the dose deposited at the non-target region (entrance) is higher than at the tumor. In contrast, the CEFB deposited 0.14 nGy/Proton at the entrance, which is around 2% of the collimated beam's D_{Sur}. Additionally, the higher D_{BP}/D_{Sur} of 34.5 obtained for the CEFB signifies the reduced possibility of biological damage to the surface tissue than the tumor by depositing a larger dose at the BP.

Table 8.1.1: Comparison of the D_{Sur}, D_{Bp}, D_{BP}/D_{Sur}, and Bragg peak depth (d_{BP}) obtained for CB, CEFB, and HEFB. D_{Sur} and D_{BP} are given in nGy/proton and d_{BP} in mm

	r = 0.5 mm			r = 2.0 mm			r = 5.0 mm		
	CB	**CEFB**	**HEFB**	**CB**	**CEFB**	**HEFB**	**CB**	**CEFB**	**HEFB**
D_{Sur}	7.16	0.141	0.036	6.46	0.138	0.036	1.09	0.131	0.035
D_{BP}	5.11	5.26	3.71	4.65	4.77	2.37	2.92	2.97	0.60
d_{BP}	155.0	154.4	154.6	155.0	154.4	154.4	155.2	154.4	150.8
D_{BP}/D_{Sur}	0.71	37.3	104.0	0.72	34.5	66.2	2.67	22.6	17.2

The D_{BP} and D_{Sur} of the HEFB are lower than two other beams compared in figure 8.1.1e. However, it has the highest D_{BP}/D_{Sur}. In contrast to the two other beams, the D_{BP} of HEFB is not a consequence of the higher stopping power. The highly converged beam increases the number of interactions around the central axis at the focal point, leading to an elevated dose. Beyond the focal point, the beam naturally diverges and reduces the dose gradually as a function of depth in the water phantom. The large D_{BP}/D_{Sur}, small D_{Sur}, and reduced dose beyond the target establish the potential of HEFB to be implemented in treatment. However, it is worthy of mentioning that the 2.0 mm radius around the central axis of the HEFB enclosing a part of the lower dose region, which is clear from figure 8.1.1c. A smaller radius can provide a more accurate approximation of the D_{BP} of the simulated HEFB. Conversely, a larger radius reduces the dose at all depths, as depicted in figure 8.1.1f. The inclusion of a larger volume with a lower energy deposition diminishes the D_{BP} of HEFB most prominently. The geometrical configuration of dose assessment has a significant impact on the dose quantification, independent of beam shaping techniques, which is clearly evident in the depth-dose curves in figure 8.1.1e, 8.1.1d and 8.1.1f.

The positions of the BP of CB and CEFB are slightly different even though they have identical beam energy. We have explained this discrepancy in chapter 5. The difference is tiny and unlikely to create any problems in the treatment planning system, as it can be estimated with sufficient accuracy and can be compensated. On the other hand, the position of peak dose is not an issue for HEFB because the BP position does not impose any spatial restriction. Its peak position can be easily varied by tuning the initial Twiss parameters.

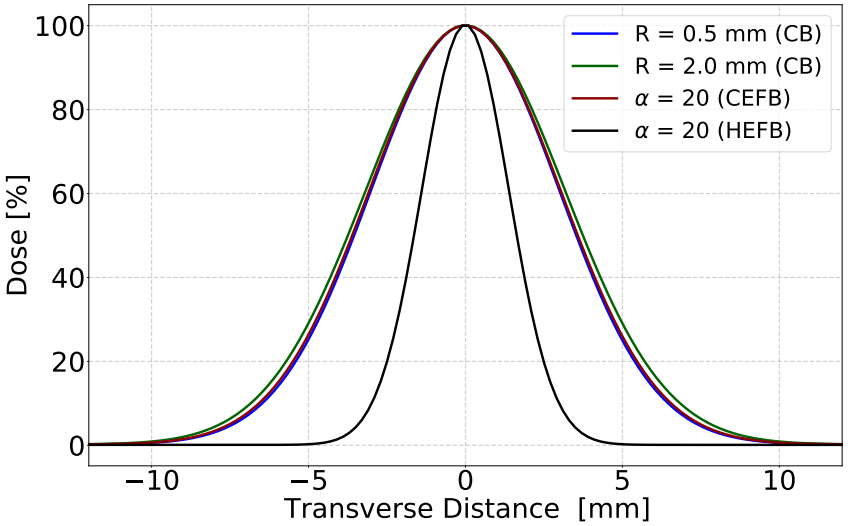

Figure 8.1.2: Comparison of the transverse dose profile of CB (0.5 mm and 2.0 mm), CEFB and HEFB at BP (focal point). The dose is normalized to the peak value ($D_{max} = 100\%$) of the distribution and the curves are plotted using Gaussian fit.

Table 8.1.2: Transverse beam parameters of CB, CEFB, and HEFB at the BP (or focal point).

Beam	Penumbra (80% to 20%)	FWHM	σ
CB (R = 0.5 mm)	3.6 mm	7.35 mm	3.12 mm
CB (R = 2.0 mm)	3.7 mm	7.70 mm	3.27 mm
CEFB (α = 20)	3.6 mm	7.42 mm	3.15 mm
HEFB (α = 20)	1.4 mm	3.32 mm	1.41 mm

One of the primary objectives of this work is to develop an optimum technique to produce a minimal spot size at the target to treat small tumors or metastasis with reduced toxicity at the surrounding healthy tissue. The beam penumbra (80% to 20%) or σ (or FWHM) are the most suitable and commonly used parameters to quantify the transverse size of a beam [157, 158, 159, 160]. The term penumbra generally describes the region at the edge of a beam where the dose drops rapidly as a function of radial distance from its central axis [161]. Table 8.1.2 compares the beam penumbra of the assessed beam shaping methods at their BP (focal point). Figure 8.1.2 shows the relative dose of the proton beams as a function of transverse distance from the central axis. The CBs have almost identical lateral spread at the Bragg peak in spite of their different size. The penumbra of the beams shaped by 0.5 mm and 2.0 mm collimators is 3.6 mm and 3.7 mm, respectively. Further reduction of the beam's initial width using a narrower collimator could not reduce lateral spread

significantly at the BP. As it can be seen, the CEFB has an almost equal spread as the CB produced by a 0.5 mm collimator. In contrast, the HEFB has a very narrow spread at the focal point. The penumbra is 1.4 mm, which is less than half of the 0.5 mm CB. This characteristic of HEFB shows its potential to irradiate a small radiation field, sparing surrounding healthy tissue.

Moreover, the overall efficiency of the magnetically focused beams is higher than the CB as it utilizes all the protons delivered by the system. It has the potential to be used for FLASH irradiation. Introducing the FLASH effect demands to escalate the dose rate 1000 times than the standard proton beam therapy, faces several technical challenges including high beam current (100 to 1000 nA) at treatment area [75, 77]. Due to the efficient beam delivery system, magnetically shaped beams can therefore more conveniently reach an ultra-high dose rate. In contrast, eliminating a large fraction of the protons by a metal collimator makes it challenging for a CB to deliver a higher dose rate.

Additionally, the normal tissue tolerance [162, 163] limits the maximum dose that can be delivered to tumors without toxic effects on healthy tissue. The irradiation time (Dose/Dose rate) is very short at an ultra-high dose rate, and is crucial in order to introduce the FLASH effect. With a dose-averaged dose rate (DADR) of 40 Gy/second, the entire dose should be delivered within 100 ms [78]. This time structure is challenging because a uniform dose distribution over the whole tumor needs a time-consuming energy modification of the beam. The unique dose profile of HEFB can be utilized to introduce a novel treatment modality. The elongated uniform longitudinal dose at the target region offers a rare opportunity to deposit homogeneous dose over an extended length using a single or smaller number of beams. Therefore, a reduced number of beams can meet up the temporal profile of the FLASH irradiation.

The neutron dose is another issue that makes focused beams more attractive over the CB. Figure 8.1.3a shows the relative neutron dose as a function of depth. Neutrons are produced by nuclear interactions with the proton beam in the collimator and inside the water phantom. In contrast, CEFB and HEFB were assumed to be pure proton beams (which is not true for a complete beamline), and nuclear interaction inside the water phantom was their only neutron source (a simplified prediction for comparison). The simulation showed that the CB deposited approximately 670 and 540 larger neutron doses at the entrance than CEFB and HEFB, respectively.

The relative neutron fluence of the CB depicted in figure 8.1.3b has distinct features compared to focused beams, due to the secondary neutrons produced by the collimator. The number of neutrons of the CB is higher than two other beams and can be observed to increase sharply within the first few centimeters. Afterward, it gradually decreases with depth. In contrast, CEFB and HEFB follow a similar trend with a slightly larger fluence of HEFB at any depth in the water phantom. The difference between their fluence gradually increases with depth. The large difference between their kinetic energy explains this feature, as we have discussed in chapter 5.

Although a HEFB has several properties that are advantageous for RT, it has a prominent

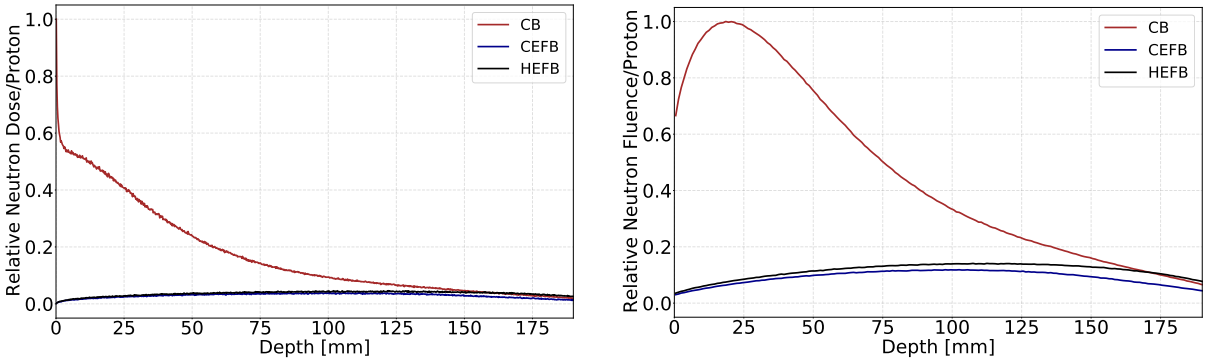

(a) (b)

Figure 8.1.3: Comparison of the relative neutron dose (a) and normalized fluence (b) among different beam shaping modalities. The dose is quantified in relative to the peak dose of the CB ($D_{max(CB)} = 1$), and fluence is normalized to the peak value ($\Phi_{max(CB)} = 1$) of the CB.

drawback of having a smaller LET at the target point. As the energy of the beam used for this modality changes by a small fraction, it can not reach the high LET range, as observed at the BP of CB and CEFB. In appendix B, we have illustrated a comparison among LET obtained for CB, CEFB, and HEFB.

8.2 Spread Out Bragg Peak (SOBP)

The longitudinal spread of a BP is usually smaller than the size of a typical tumor. Therefore, a mono-energetic proton beam cannot deliver a uniform longitudinal dose. However, a homogeneous dose over an extended longitudinal range of a tumor can be deposited by stacking up multiple quasi-monoenergetic beams with suitable weighting factors, as discussed in section 2.3.1, known as SOBP. We have utilized eleven equispaced BPs, shown in figure 8.2.1a, to assess the SOBP using CBs. All these beams were simulated with an identical collimator of radius 2.0 mm. The dose has been calculated using a wide cylindrical configuration of radius 200 mm, which was equal to the radius of the cylindrical water phantom implemented in the simulations. The peaks are located between 120 mm to 170 mm. A uniform dose within this range was produced with optimum weighting factors following the algorithm described in section 3.4. Figure 8.2.1b shows the SOBP accompanying its constituent pristine BPs representing relative contribution (weighting factors) of the modulated beams. It shows that a longitudinal homogeneity of dose in the target with minimal fluctuations can be achieved using CBs.

Figure 8.2.2a shows the two-dimensional dose profile of the SOBP of collimated proton beams. The total dose between 120 mm to 170 mm is almost constant (figure 8.2.1b) for a wide cylindrical configuration of a 200 mm radius, which we have found valid for any radius a few times larger than the beam's dimension. We calculated the central axis dose of the collimated SOBP using various cylindrical configurations (r =1.0 mm to r=15.0 mm). The results obtained from the simulated data is shown in figure 8.2.2b. It revealed a crucial feature of the SOBP of narrow collimated beams.

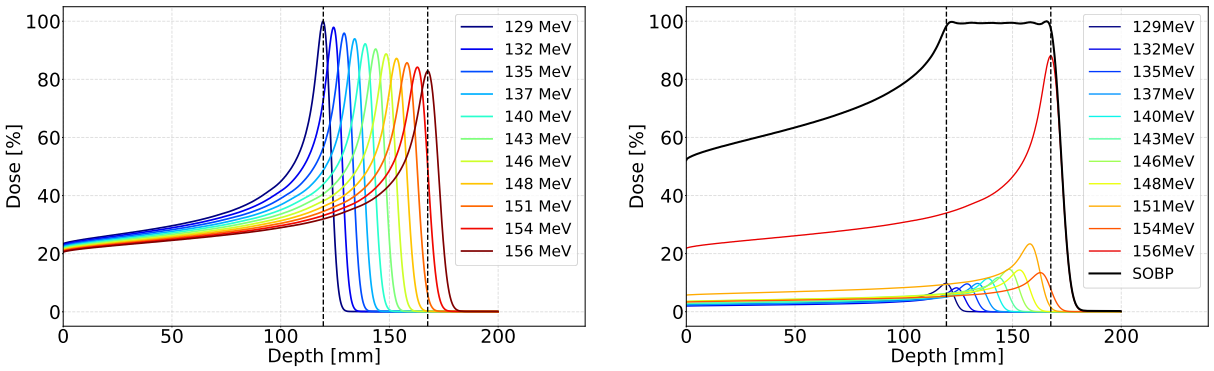

(a) (b)

Figure 8.2.1: (a) The unmodulated pristine Bragg peaks of CB to produce a uniform dose over 50 mm between 120 mm to 170 mm in the water phantom. Dose is calculated for r = 200 mm. These curves are equivalent to the integral depth dose curves (IDD). (b) The percentage depth dose (PDD) of the SOBP and the modulated pristine Bragg peaks. The relative fluence of the modulated beams is optimized through the method of least squares.

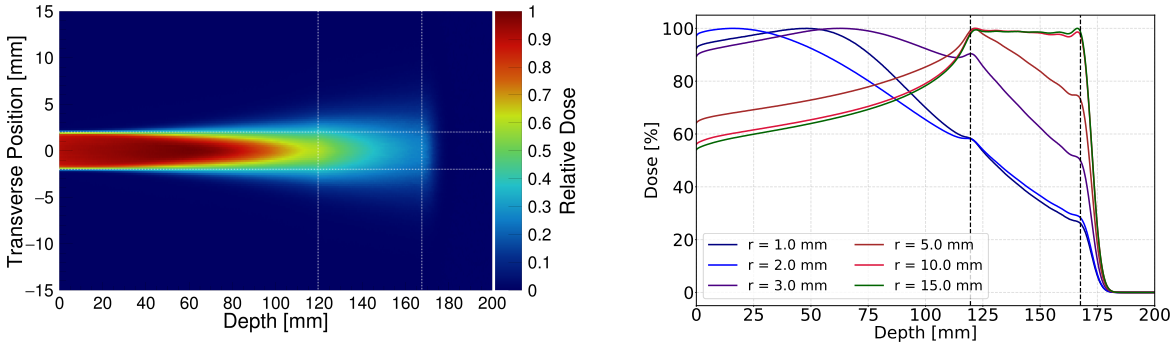

(a) (b)

Figure 8.2.2: (a) Two-dimensional dose profile of SOBP between 120 mm to 170 mm. The dose is normalized to the peak value. (b) PDD curves of the SOBP using various radius of the cylindrical volume element around the beam's central axis. The discrepancy between two ends of the SOBP increases for smaller values of r.

Even though the uniform average dose was achieved for a wide geometrical configuration, it could not ensure a uniform localized dose around the beam's central axis. The higher energy beams travel further into the water phantom, causing more scattering of protons. Consequently, the fraction of protons escaping out from the initial transverse beam size increases, leading to a lower central axis dose at the distal edge of the SOBP. This phenomenon does not impact a wide beam as severely because the fraction of protons that move away of the center of the beam is negligible. Moreover, a wide beam reaches lateral equilibrium near the central axis as explained in section 4.2.2.

Magnetically shaped CEFB and HEFB are also capable of producing SOBP following the identical algorithm implemented for the CB. However, the focused beams demonstrated several distinct features. Their ability to deliver a higher dose at the target region relative to the surroundings can be evident in figure 8.2.3a and figure 8.2.3b. In contrast, the highest dose region of a narrow CB was found at the non-target region (entrance).

The dose of CEFB (figure 8.2.3c) and HEFB (figure 8.2.3d) has been calculated for 2.0 mm radius. The CEFB is capable of producing uniform SOBP. Its distal falloff is similar to the CB. The initial energy of a proton beam determines its penetration depth in a physical medium. Therefore, using conventional energy range with magnetic focusing (CEFB) can assure sparing healthy tissue beyond the tumor during radiation therapy. Furthermore, its dose contribution to the entrance is much smaller than the narrow CBs. As it can be seen in figure 8.2.2b, the D_{Sur} of CB is more than 50% of its D_{BP}. It is commonly observed for the SOBP of conventional proton beam therapy [164, 165]. In contrast, the D_{Sur} of the CEFB is less than 10% of its SOBP dose (figure 8.2.3c). Implication of CEFB in treatment will widen the path to escalate the dose per fraction with reduced toxicity at normal tissue.

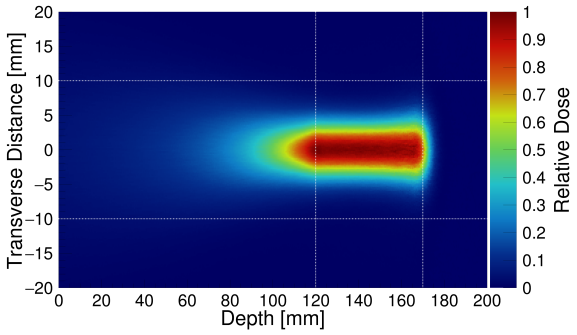

(a) SOBP dose profile of CEFB.

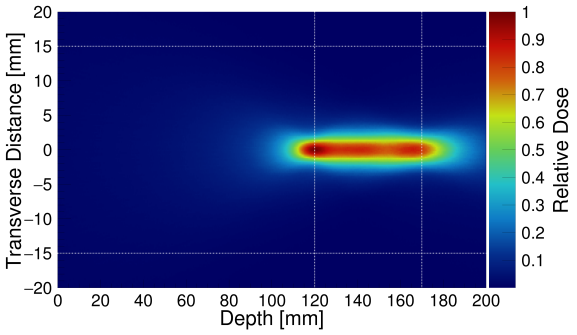

(b) SOBP dose profile of HEFB.

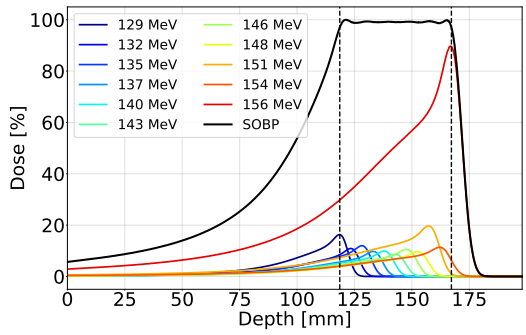

(c) PDD of SOBP using CEFB.

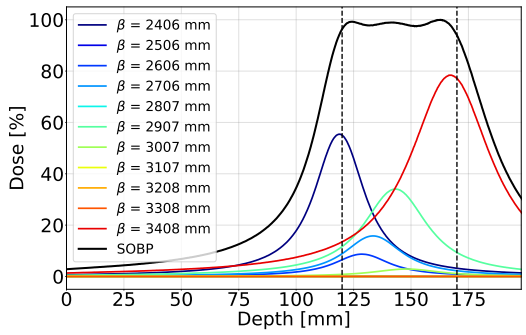

(d) PDD of SOBP using HEFB.

Figure 8.2.3: Top row: Two-dimensional dose profile of SOBP between 120 mm to 170 mm using CEFB (a) and HEFB (b) demonstrate a higher dose at target than the entrance. The dose is normalized to the peak value. Bottom row: PDD curves of SOBP produced by the CEFB (c) and HEFB (b). A Uniform dose between 120 mm to 170 mm is deposited by CEFB with sharp distal falloff. The SOBP of HEFB deposits dose beyond the target. The dose in (c) and (d) is calculated for a cylindrical geometrical configuration of radius 2 mm and normalized to the peak dose of the SOBP ($D_{Max(SOBP)} = 100\%$).

The SOBP produced by HEFB, following the identical algorithm, was less uniform than CB and CEFB. Inclusion of more points in the calculation of weighting factors (see section 3.4) might produce a smoother and more uniform dose in the target region. Moreover, only seven beams (four beams in figure 8.2.3d have zero weighting factor) produced the SOBP of HEFB in contrast to eleven

beams for CB and CEFB. The beam modification period depends on the accelerator and beam delivery system, which is an essential parameter that determines total treatment time [34]. With a reduced number of beams, the HEFB can deliver a sufficient dose within a shorter time, making the patient's movement less problematic. Additionally, the protons of HEFB are less deflected by MCS due to their higher energy. Thus, the beam focusing is almost independent of the traversing materials (anatomical structure of patient). It can enhance the precision of the treatment. In addition, the smallest D_{Sur} is an attractive feature of the HEFB, and it deposited the least fraction of the D_{BP} before the target region. The slow distal falloff of HEFB is appeared to be its prime disadvantage, which irradiates the tissue beyond the tumor. However, it can be modified using appropriate focusing and beam size. Moreover, the non-specific dose produced by conventional SOBP is higher than HEFB. Thus, proper treatment planning might incorporate the HEFB in medical applications even it has a nonzero exit dose.

8.3 GRID configuration

The basic principle of GRID therapy, which is a method to implement spatially fractionated radiation therapy (SFRT), is to create a highly inhomogeneous dose pattern at healthy tissue, as discussed in section 2.3.1. A smaller transverse beam size is more appropriate to utilize the most benefits of the dose-volume effect. The MCS limits the smallest functional size of the CB for proton GRID therapy [17]. A very narrow (submillimetric) beam can deliver only a small dose at a deep-seated target, as demonstrated in chapter 4. We have studied several circular collimators of radius 0.5 mm to 3.0 mm to evaluate their feasibility for proton GRID therapy. The GRID was simulated by inserting a lead collimator in the beamline. The results obtained for a proton GRID irradiation with circular openings of radius 2.0 mm have been compiled in figure 8.3.1. We used one-dimensional array of beams to study the properties of GRID irradiation. In the simulations, 150 MeV proton beam was modeled with a 1% energy spread, and GRID assessment considered the properties of a pristine BP instead of the SOBP.

The two-dimensional (x-z) dose profile of proton GRID irradiation using metal collimator of c-t-c 6.0 mm and 10.0 mm is shown in figures 8.3.1a and 8.3.1b, respectively. A sharp contrast between peak dose (D_{Peak}) and valley dose (D_{Valley}) at the shallow region is clearly evident. Alternatively, the difference between the D_{Peak} and D_{Valley} gradually decreases as a function of depth. It is not even distinguishable in the vicinity of the BP for c-t-c = 6.0 mm. This feature of proton GRID irradiation can be explained by the scattering interaction of protons which causes lateral spreading of a beam. A similar pattern of proton GRID irradiation of collimated beam has been observed in several experimental and theoretical (simulation) studies [24, 140, 159, 166, 167]. The uniform dose in the non-target region is a barrier in achieving the proton GRID therapy's primary goal.

Conversely, GRIDs with a larger c-t-c can maintain transverse inhomogeneous dose distribution

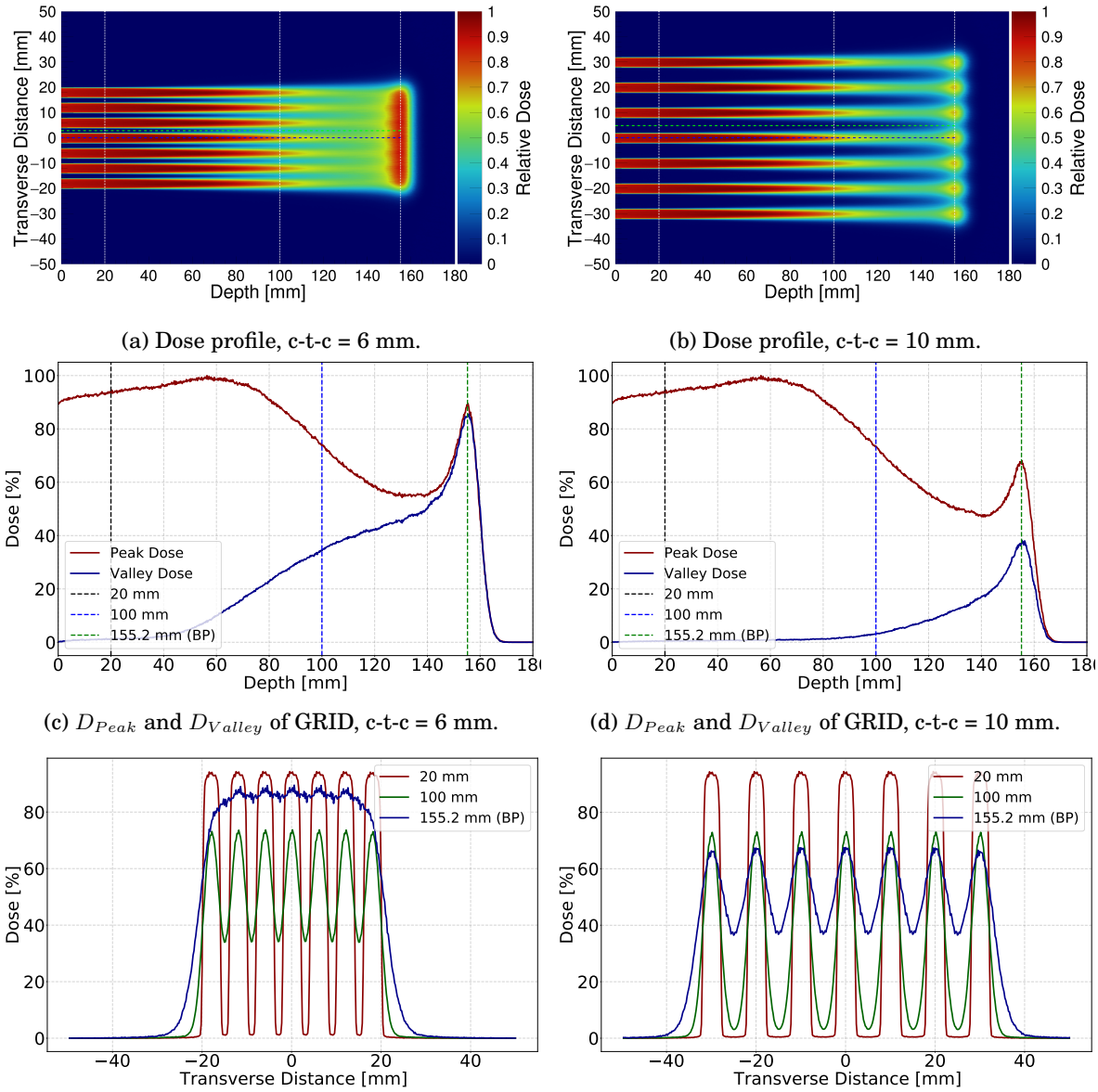

(a) Dose profile, c-t-c = 6 mm.

(b) Dose profile, c-t-c = 10 mm.

(c) D_{Peak} and D_{Valley} of GRID, c-t-c = 6 mm.

(d) D_{Peak} and D_{Valley} of GRID, c-t-c = 10 mm.

(e) Transverse dose profile at BP, c-t-c = 6 mm.

(f) Transverse dose profile at BP, c-t-c = 10 mm.

Figure 8.3.1: Dose profile of collimated beam GRID irradiation obtained with c-t-c = 6 mm (left column) and c-t-c = 10 mm (right column). **Top row:** Two-dimensional dose profile with c-t-c = 6 mm (a) and c-t-c = 10 mm (b). The dose is normalized to the peak value. **Middle row:** Comparison of the evolution of D_{Peak} and D_{Valley} as a function of depth. **Bottom row:** Transverse dose profile at the BP obtained for c-t-c = 6 mm (e) and c-t-c = 10 mm (f) are similar at surface with a larger separation between peaks at (f).

deeper into the water. However, it might cause an inhomogeneous dose distribution at the target, which is not desirable for several treatment modalities. The position of the tumor (target) is crucial for the GRID design. The higher energy beam is essential to treat a deep-seated tumor, which allows a larger lateral spread of a beam. Besides, the metallic collimators introduce secondary neutrons, which have the potential to deposit dose far away from the primary beam. A new approach of beam shaping using magnetic fields has been studied, which replaces metal collimators to reduce the number of secondary particles with additional advantages [144, 168].

Figure 8.3.1c and 8.3.1d show the D_{Peak} and D_{Valley} of proton GRID irradiation as a function of depth. The dose is calculated using voxels of size $0.2\ \mathrm{mm}\times0.2\ \mathrm{mm}\times0.2\ \mathrm{mm}$ at the center of the central peak region and the adjacent valley region. As described in chapter 4, a narrow collimated proton beam cannot achieve lateral equilibrium at its center. Consequently, the D_{Peak} curve is distinctive from the standard depth-dose curves of the proton beam. The low energy protons (scattered and secondary) produced in the collimator could be responsible for the slight increase in peak dose at the first few centimeters. Afterward, the D_{Peak} gradually drops to its minimum value as the protons are escaping out laterally from the original beam volume. Eventually, the D_{Peak} increases sharply due to the escalated stopping power at lower energy and reaches its maximum at the BP. In contrast, the D_{Valley} is practically zero at the entrance because the region is conceptually shielded out from the radiation source. However, slit scattered protons, secondaries, and scattered primaries can reach the valley at the shallow region for a small c-t-c, raising the D_{Valley}. With the increasing depth, it starts to grow as the protons from the proximate peaks enter this unexposed region. The enhanced scattering at the lower energy encourages the lateral migration of protons, leading to a higher increasing rate of the D_{Valley} near the BP.

The transverse dose profile of the proton GRID irradiation has been depicted in figures 8.3.1e and 8.3.1f. An alternating dose pattern indicates a contrast between the D_{Peak} and D_{Valley} of the GRID irradiation. Transverse dose profiles were evaluated at three (20 mm, 100 mm and, Bragg peak) positions in the direction of the beam propagation. A similar dose pattern can be identified at the shallow (20 mm) region for 6.0 mm and 10.0 mm c-t-c. As expected, the larger c-t-c produced a wider valley. However, all peaks have identical transverse sizes at 20 mm, independent of the c-t-c of multi-slit collimators. At 100 mm, the contrast between peak and valley dose drastically reduced for the smaller (6.0 mm) c-t-c. In contrast, the larger (10.0 mm) c-t-c could preserve a notable peak-valley distinction despite a significant reduction of D_{Peak}. Considering the BP, there is no noticeable difference D_{Peak} and D_{Valley} for 6.0 mm c-t-c, whereas the larger c-t-c produces a transverse dose contrast. The two-dimensional (x-y) transverse dose profile at the BP of GRID irradiation in figure 8.3.2 illustrates the impact of c-t-c. Its value needs to be tuned for each beam energy and collimator radius to produce a laterally separated spot at the target.

The peak to valley dose ratio (PVDR) is one of the most crucial parameters to quantify the efficacy of the beam delivery system using GRID configuration. A larger value of PVDR with lower D_{Valley} can spare healthy tissue without reducing tumor control probability [169]. Therefore, enhanced PVDR with $D_{Valley} = 0$ is the ultimate goal of collimator design. Several parameters including beam energy, energy spread, beam size, beam divergence, c-t-c, etc. can potentially influence the value of PVDR.

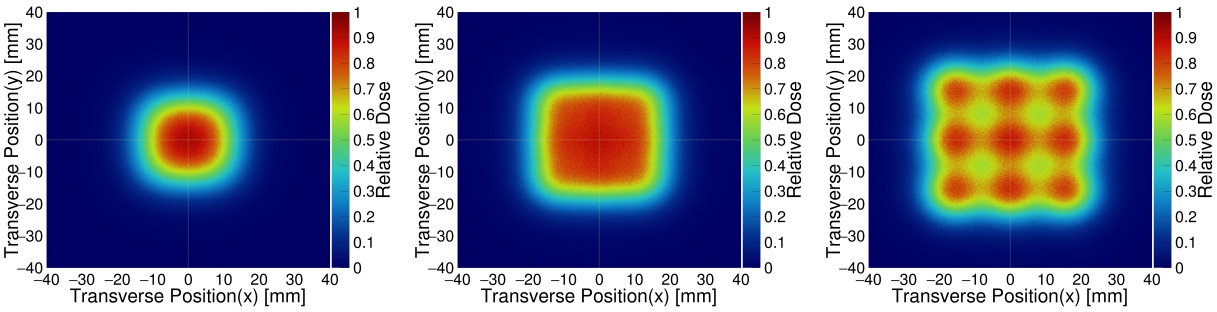

Figure 8.3.2: Transverse two-dimensional dose profile of at the BP of GRID irradiation obtained for CB with c-t-c = 4.0 mm (left), c-t-c = 6.0 mm (middle) and c-t-c = 8.0 mm (right). The beam energy is 150 MeV and collimator radius is 2.0 mm. The dose is normalized to the peak value.

8.3.1 Impact of beam size

Although the smallest possible beam size is the most desirable configuration of the GRID therapy, it is not always practically possible to use the narrowest beam. The initial beam size is determined by the collimator. If it is placed very close to the target, the size of the beam remains approximately equal to the collimator's opening at the entrance of the target. An air-filled larger distance between the edge of the collimator and target causes a slight beam broadening through MCS. In addition, it can modify the beam divergence. However, these impacts are insignificant due to the very low density of air. We have simulated GRID irradiation with a 2.0 cm separation between the surface of the modeled water phantom and the source. Moreover, in the simulations, the gap is assumed to be in a vacuum.

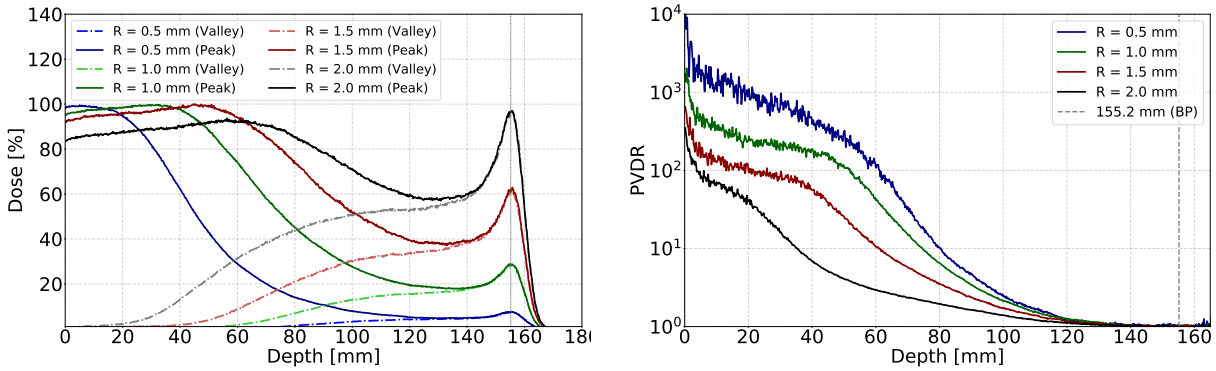

(a) (b)

Figure 8.3.3: Impact of collimator radius (R) on the collimated beam GRID irradiation: (a) Evolution of D_{Peak} and D_{Valley} as a function of depth in the water phantom obtained for R = 0.5, 1.0, 1.5 mm, and 2.0 mm. The dose is plotted in percentage of the maximum value of the D_{Peak}. (b) Comparison of the corresponding PVDR of CB. The results are obtained by simulating 150 MeV proton beams with c-t-c of 5.0 mm.

The impact of the beam size was assessed using collimators of radius 0.5 mm, 1.0 mm, 1.5 mm, and 2.0 mm. The PDD curves at peak and valley of these beams are shown in Figure 8.3.3a and corresponding PVDRs as a function of depth is depicted in figure 8.3.3b. An identical c-t-c of 5.0 mm was used for all four beam sizes. The difference between D_{Peak} and D_{Valley} is largest for the nar-

rowest beam at the shallow region, leading to the highest PVDR. However, the dose deposited by the narrowest beam is least at the target. In contrast, a wider beam can deliver a significantly larger dose at the target with an overall reduced PVDR. A fluctuation in PVDR can be noticed at the entrance, especially for the narrowest beam. In this region, only a few protons or secondaries can reach the center of the valley. However, the trend of the PVDR is clear, which is similar to the result observed by Guardiola et al.[70]

Additionally, the PVDR drops to about one, a few centimeters before the target, indicating a homogeneous dose distribution at normal tissue. This uniform dose at healthy tissue is not desirable for conventional GRID therapy. A treatment planning system based on GRID therapy should consider this feature to reduce normal tissue toxicity, particularly for the deep-seated targets with smaller values of c-t-c.

8.3.2 Impact of c-t-c

Minimizing D_{Valley} is essential to reduce normal tissue toxicity. The c-t-c of the GRID configuration determines the D_{Valley} together with beam energy and transverse size. In figure 8.3.4a, impacts of c-t-c on the D_{Peak} and D_{Valley} of collimated (R = 1.0 mm) proton beam is illustrated. The D_{Peak} is independent of c-t-c at the first few centimeters of the target. However, the D_{Valley} starts to differ within 2.0 cm, where the scattering effect rises, increasing the transverse size of a beam. The smaller c-t-c can not preserve inhomogeneous dose distribution among peaks and valleys till the Bragg peak. The PVDR as a function of depth depicted in figure 8.3.4b shows a non-uniform dose distribution of 9.0 mm c-t-c within the entire range of the beam despite the reduced D_{BP}. Moreover, very large c-t-c might cause inhomogeneous dose at the target, which might be undesirable in several treatment procedures. Thus, an optimum value of c-t-c should be employed in GRID therapy to balance the D_{BP} and PVDR.

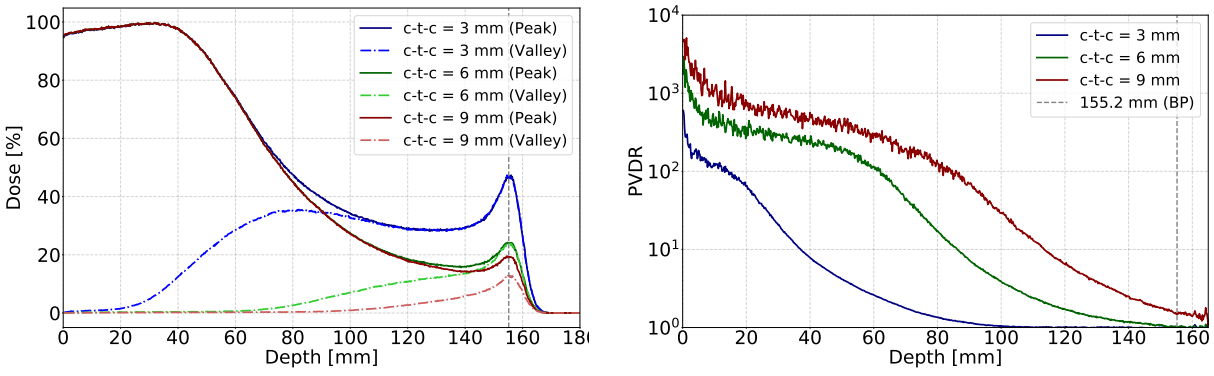

(a) (b)

Figure 8.3.4: Impact of the centre-to-centre (c-t-c) distance on the collimated beam GRID irradiation: (a) Evolution of D_{Peak} and D_{Valley} as a function of depth in the water phantom obtained for c-t-c = 3, 6, and 9 mm. (b) Comparison of the corresponding PVDR of CB. The dose is plotted in the percentage of the maximum of D_{Peak}. The results are obtained by simulating a 150 MeV proton beam with a 1.0 mm collimator radius.

8.3.3 Impact of beam energy

The initial beam energy solely determines the range of a proton beam in a given material. As we have discussed in chapter 4, the transverse size of a collimated beam increases with depth. Consequently, the migration of protons from the proximal proton beams to a valley region rises. Figure 8.3.5a shows the D_{Peak} and D_{Valley} of four beam energies as a function of depth. All the beams were simulated with a 1.5 mm radius and 5.0 mm c-t-c. The PVDR of higher energy beams drops to 1 far before the Bragg peak (target) position. As the dose becomes homogeneous, in principle, GRID irradiation cannot prevent normal tissue toxicity by exploiting the dose-volume effect. It makes the implementation of CB to treat deep-seated tumors more challenging using GRID irradiation.

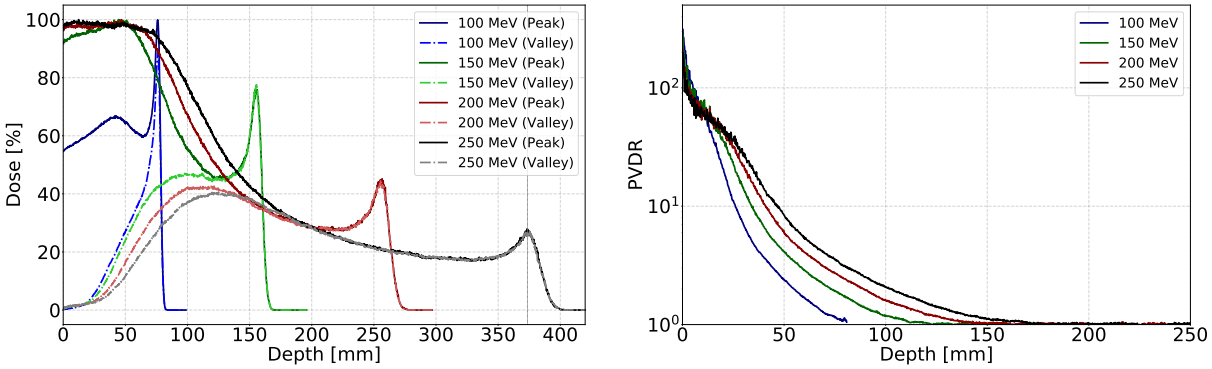

(a) (b)

Figure 8.3.5: Impact of beam energy on the collimated beam GRID irradiation: (a) Evolution of D_{Peak} and D_{Valley} as a function of depth in the water phantom obtained for 100, 150, 200, and 250 MeV proton beams. (b) Comparison of the corresponding PVDR. The dose is plotted in percentage of the maximum value of D_{Peak}. The results are obtained by simulating collimated beams of radius 1.5 mm and c-t-c of 5.0 mm.

8.4 Spatially Fractionated Focused Beam Therapy

The magnetically shaped beam with a small initial transverse size can be used to produce conventional GRID irradiation [144]. We have studied this feature of the focused beams, and the results are compared against GRID irradiation of CB in appendix C. In the context of dose distribution, a narrow CEFB is equivalent to a CB with a reduced number of secondary neutrons and higher irradiation efficiency. However, it can not elevate the Bragg peak to surface dose ratio. Similarly, the HEFB can be employed to produce conventional GRID irradiation. As the peak dose relies on the lateral contraction, the initial size of the HEFB can not be as small as two other beam shaping techniques. Consequently, a sharp contrast between peaks and valleys in the shallow region is difficult to achieve despite the fact that it can offer a sharper contrast in the focal point. Moreover, it is also possible to produce a very narrow beam at the surface of the target using appropriate focusing, which will expand inside the traversed material in a similar way as the CB. The elimination of

mechanical collimators can offer various advantages, as mentioned earlier.

In this work we have studied the focused beams with a larger initial size. As a consequence of their unique dose profile (low at the entrance and high at BP), these beams are not suitable for conventional GRID irradiation with a high dose homogeneity at the entrance. However, it is possible to produce a GRID-like dose distribution in the vicinity of a target using focused beams with a very low uniform dose at the entrance. We have studied this novel irradiation modality using CEFB and HEFB by simulating one-dimensional array of focused beams.

8.4.1 SFRT of CEFB

The two-dimensional (x-z) dose profile of the spatially fractionated irradiation of 100 MeV and 150 MeV CEFB is shown in figures 8.4.1a and 8.4.1e, respectively. We have evaluated D_{Peak} (white) and D_{Valley} (green) along the horizontal lines. The simulation was carried with c-t-c = 15.0 mm. The Twiss parameters were tuned for $\alpha = 15$ to focus the beam at the corresponding BP. The distinct spots can be noticed at the target with a sharp contrast between peaks and valleys for both energies. However, there is no noticeable dose contrast at the entrance of the target.

The homogeneity of the dose distribution might not enable us to spare healthy tissue at the entrance by exploiting the dose-volume effect; however, the dose at the entrance and shallow region can be kept very low to cause any significant damage to the skin and superficial tissue. The inhomogeneity in dose distribution grows with depth, and distinct peak regions can be noticed. The PDD curves of D_{Peak} and D_{Valley} follow the same trend for two different energies as shown in figures 8.4.1b and 8.4.1f. The D_{Valley} is slightly larger for higher (150 MeV) energy. It can be explained from the fact that a high-energy beam traveled deep inside the water, and the migration of protons to the valley is more probable by MCS at its lower energy (end of the range).

The PVDR of fractionated CEFB of 100 MeV and 150 MeV are given in figure 8.4.1c and 8.4.1g, respectively. Independent of energy, the value of PVDR is 1 with little fluctuation at the entrance and shallow region. It starts to increase slowly with depth as the beam approaches the focal point (BP). In the proximity of the BP, the PVDR grows rapidly and reaches the maximum at the BP position. The PVDR of 100 MeV proton beam at the BP is larger due to its lower D_{Valley}, which is a consequence of reduced deflection of beam's particles within its smaller range in water.

The higher PVDR observed in the simulation of the CEFB might satisfy the conditions of GRID irradiation near the target. Simultaneously, a reduced volume of irradiation must be achieved to obtain the full benefits of GRID therapy. As discussed in chapter 5, the CEFB produces its smallest transverse size slightly before the BP because, at the end of the track, the slowest protons of the higher range beam are very sensitive to MCS, causing rapid lateral expansion within few millimeters. In principle, effective focusing can reduce the transverse size to achieve the dose-volume effect before the tumor. This irradiation modality shows a potential to spare radiation-sensitive organs/tissue before the target.

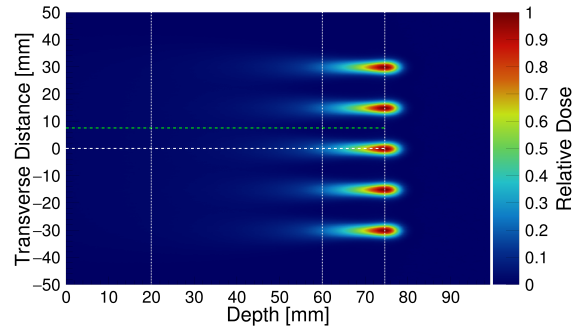

(a) 2D dose profile of 100 MeV CEFB, c-t-c = 15 mm.

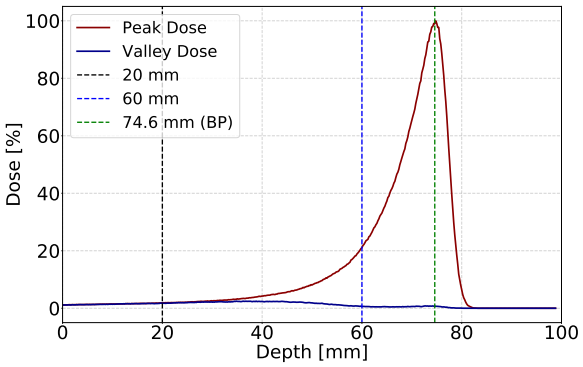

(b) PDD curves of 100 MeV CEFB.

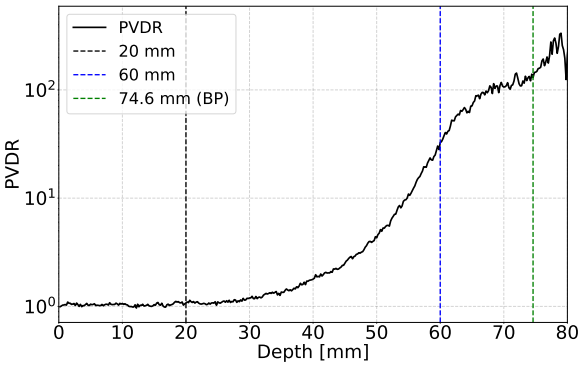

(c) PVDR of 100 MeV CEFB.

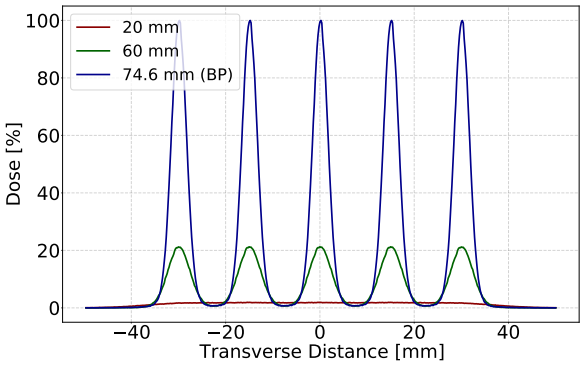

(d) Transverse depth-dose curves of 100 MeV CEFB.

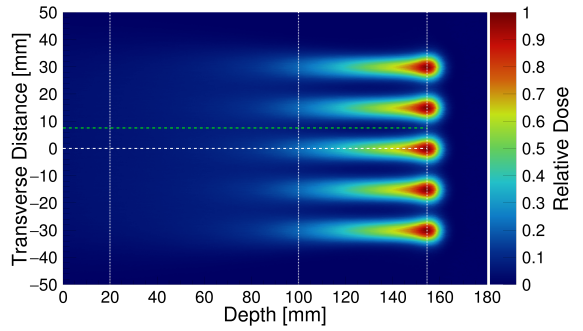

(e) 2D dose profile of 150 MeV CEFB, c-t-c = 15 mm.

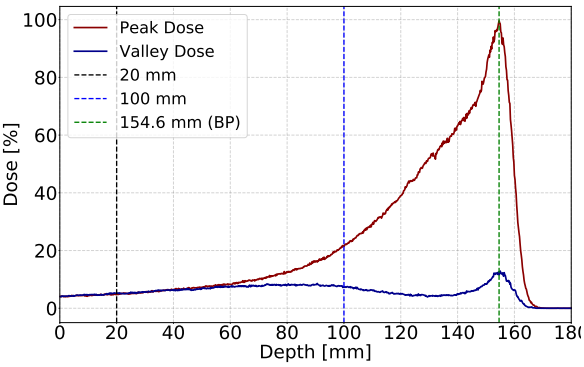

(f) PDD curves of 150 MeV CEFB.

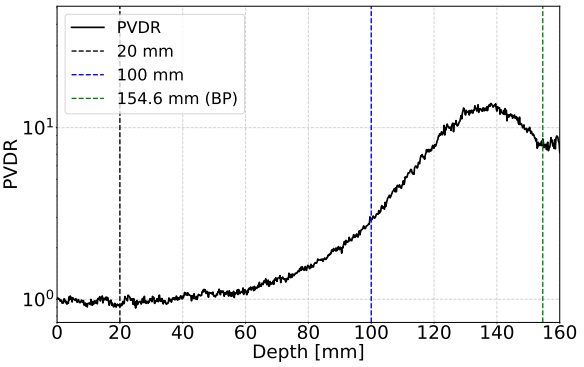

(g) PVDR of 150 MeV CEFB

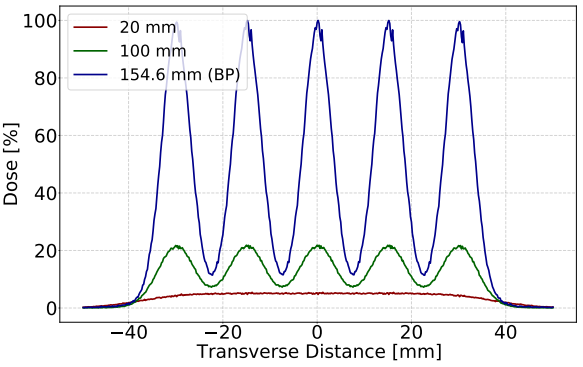

(h) Transverse depth-dose curves of 150 MeV CEFB.

Figure 8.4.1: Dose profile of fractionated irradiation obtained with CEFB of 100 MeV (left column) and 150 MeV (right column) proton beams. **Top row:** Two-dimensional dose profile obtained with c-t-c = 15 mm. The dose is normalized to the peak value. **Second row:** Comparison of the evolution of D_{Peak} and D_{Valley} as a function of depth. **Third row:** Evolution of PVDR of 100 MeV and 150 MeV proton beam as a function of depth in the water phantom. **Bottom row:** Transverse dose profile at the BP.

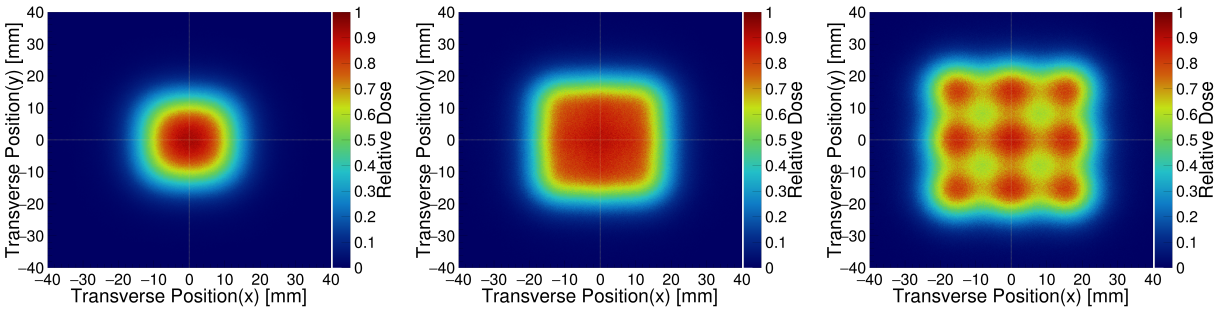

Figure 8.4.2: Transverse two-dimensional dose profile of CEFB GRID irradiation with c-t-c = 4.0 mm (left), c-t-c = 6.0 mm (middle) and c-t-c = 8.0 mm (right). The beam energy is 150 MeV.

The transverse dose distribution at multiple positions along the beam propagation illustrated in figure 8.4.1d and 8.4.1h supports our aforementioned arguments. Distinct peaks at BP position can be identified with a small uniform dose at the shallow region. However, the penumbra of the high-energy beam is clearly larger than its low-energy counterpart. As a consequence, it is challenging to produce distinct spots at the deep-seated tumor.

Figure 8.4.2 shows the transverse two-dimensional dose distribution at the BP of the GRID irradiation using CEFB. The transverse inhomogeneity develops at a large c-t-c, similar to the collimated beam shown in figure 8.3.2. However, the advantage of the CEFB is its larger dose contrast before the target besides the low entrance dose.

8.4.2 SFRT of HEFB

The two-dimensional (x-z) dose profile of the spatially fractionated irradiation of HEFB in figures 8.4.3a and 8.4.3e showed several similar features as CEFB. The beam parameters are tuned for $\alpha = 20$ to produce the focal point at 100 mm and 154.6 mm in the water simulated phantom. However, few distinct features of HEFB might be crucial to SFRT. Firstly, the higher energy of the beam offers an exclusive opportunity to significantly reduce the deflection beam's particles in a physical medium caused by MCS. Thus, the spot size at the target can be further diminished. Consequently, it produces a high PVDR, the most desired feature for GRID irradiation. Secondly, it deposits a small dose beyond the tumor which is unusual for conventional proton beam therapy.

The PDD curves of D_{Peak} and D_{Valley} illustrated in figure 8.4.3b and 8.4.3f are symmetric about the focal point. A very low dose is deposited both in the valley and peak region all over the depth except in the vicinity of the target, where a sharp dose contrast is produced. Consequently, the PVDR has a large bump at the target and almost one at other regions (see figure 8.4.3c and 8.4.3g). Considering conventional proton beam therapy, the dose in the non-target region (8.2.2b) is significantly higher [164, 165] than the dose we found for HEFB (also beyond the focal point). Thus, we can expect to keep the normal tissue dose within a safe level. Similar to the CEFB, it can not produce inhomogeneity in dose distribution at the entrance. However, the entrance dose is very low, reducing the probability of radiation-induced damage at the surface. In addition, a very high PTVD

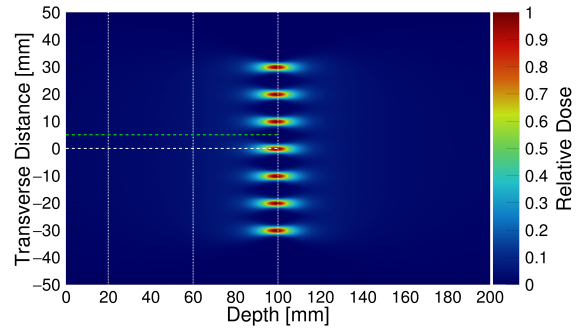

(a) 2D dose profile (100 mm) of SFRT using HEFB

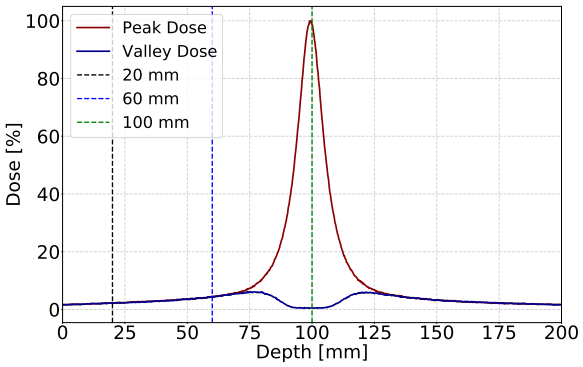

(b) PDD curves of HEFB (100 mm)

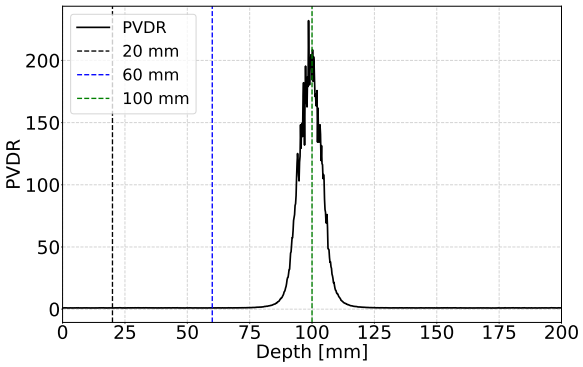

(c) PVDR of HEFB (154.6 mm)

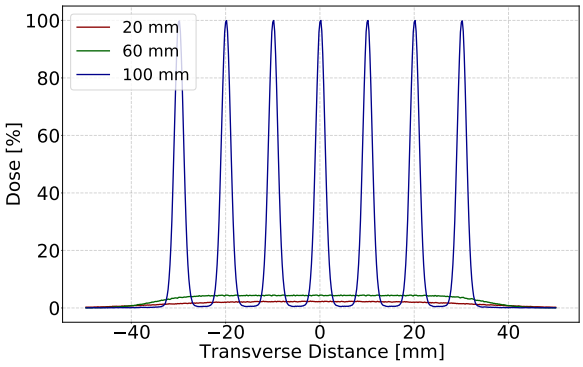

(d) Transverse depth-dose curves of HEFB (100 mm)

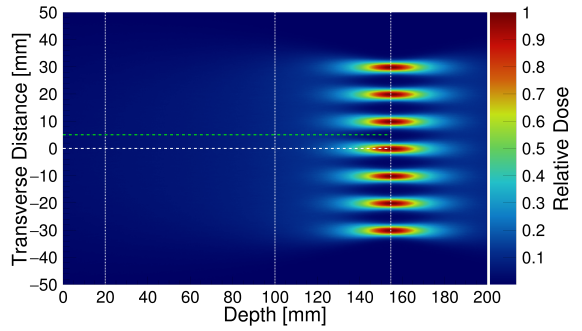

(e) 2D dose profile (154.6 mm) of SFRT using HEFB

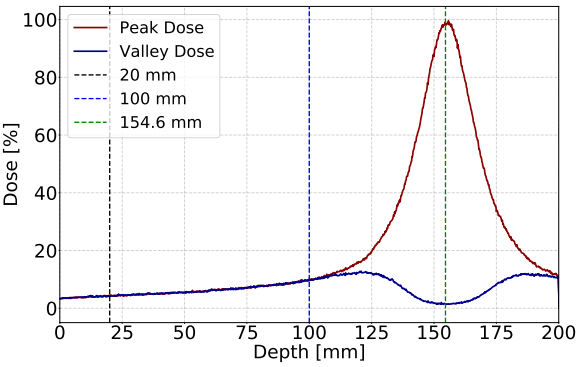

(f) PDD curves of HEFB (154.6 mm)

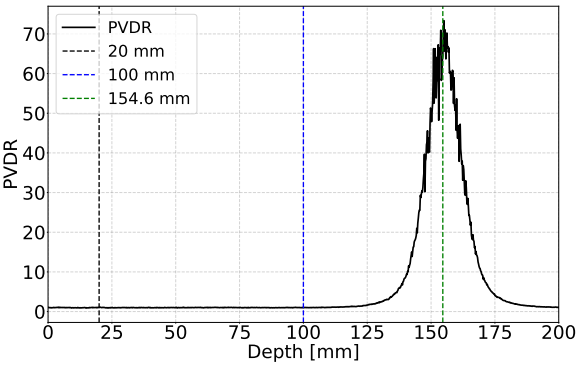

(g) PVDR of HEFB (154.6 mm)

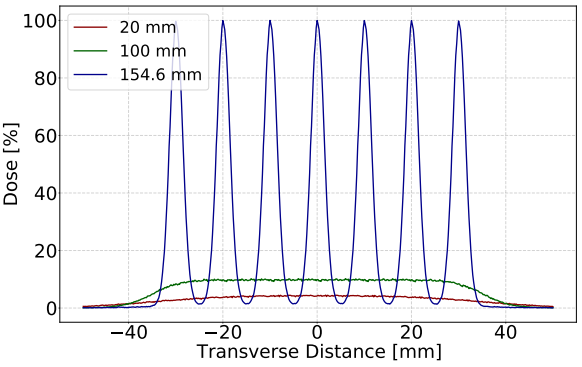

(h) Transverse depth-dose curves of HEFB (154.6 mm)

Figure 8.4.3: Dose profile of fractionated irradiation obtained with 350 MeV HEFB of focal length of 100 mm (left column) and 154.6 mm (right column). **Top row:** Two-dimensional dose profile obtained with c-t-c = 10 mm. The dose is normalized to the peak value. **Second row:** Comparison of the evolution of D_{Peak} and D_{Valley} as a function of depth. **Third row:** Evolution of PVDR as a function of depth in the water phantom. **Bottom row:** Transverse dose profile at the focal points.

and small irradiation field might be sufficient to spare healthy tissue around the tumor.

The transverse dose profile of the HEFB in figure 8.4.3d and 8.4.3h demonstrates a homogeneous low dose at the entrance in contrast to the inhomogeneous high dose of the focal point. Thus, the HEFB beam shaping modality can produce a sharp contrast and small distinct spots at the target to implement GRID irradiation. Its two-dimensional (x-y) transverse dose profile depicted in figure 8.4.4 exhibits its superiority over CB and HEFB in producing small spots at the target.

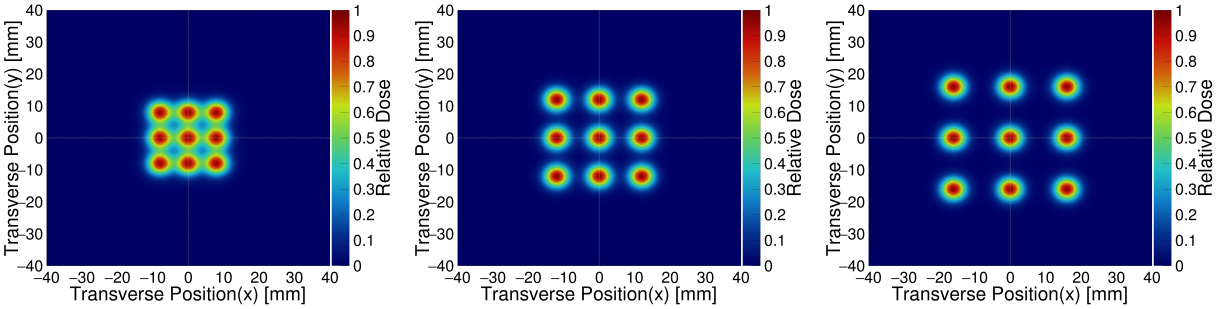

Figure 8.4.4: Transverse two-dimensional dose profile of HEFB GRID irradiation with c-t-c = 4.0 mm (left), c-t-c = 6.0 mm (middle) and c-t-c = 8.0 mm (right). The beam energy is 350 MeV and the focal length is 154.6 mm.

8.5 Summary

We have performed an extensive comparison among three different beam shaping techniques. Their properties are assessed both quantitatively and qualitatively to evaluate their feasibilities in several treatment modalities, including proton GRID therapy.

Collimated beams can be used for GRID irradiation. However, distinct spots at deep-seated targets are limited by MCS. It could hinder the way to implementing collimator in GRID irradiation to treat deep-seated tumors because the dose inhomogeneity was found to disappear some distance before the target.

Moreover, low efficiency and reduced beam current at the treatment room could limit its incorporation with FLASH modalities. However, this problem can be reduced by incorporating pencil beam scanning with metal collimators [144, 170]. Instead of a wide beam irradiating the entire multi-slit collimator as once, magnetically scanning across the collimator using a pencil beam can enhance efficiency. Simultaneously, it can also reduce secondary neutron production.

We have demonstrated novel irradiation modalities using focused beams of conventional energy (CEFB) as well as high energy (HEFB). With their very high value of D_{BP}/D_{Sur} and large PVDR at deep-seated target, these new irradiation modalities demonstrated their potential to treat bulky tumors with an inhomogeneous dose. Focused beams produce several-fold lower secondary neutrons in comparison to CB. A similar observation has been reported by Schneide et al. [144]. Their high efficiency is suitable to deliver the ultra-high dose rate required for FLASH irradiation.

Chapter 9

Conclusions and Outlook

9.1 Conclusion

A narrow beam with a small spot is a crucial tool to obtain a precise dose delivery system with higher treatment efficacy. This research was carried out in order to develop optimum techniques to produce such a beam to deposit large doses at distinct points of a tumor. Generating narrow proton beams using a metal collimator is the most convenient and well-established strategy. This beam shaping approach has been implemented in several proton therapy facilities particularly for passive scattering. It can produce a very narrow beam to spare healthy tissue by exploiting the dose-volume effects. However, it exhibits certain weaknesses, as we have discussed in chapter 4. The MCS limits the smallest obtainable spot size of a CB, and it reaches a plateau with decreasing collimator radius. Further improvement in spot size beyond this extent is impossible to achieve by using CB. At a shallow point, the performance of CB in producing small spots is convincing. However, at a deep-seated target, it can not always satisfy the requirements. In addition, the Bragg peak to surface dose ratio of a high-energy proton beam is very small, which limits the maximum achievable dose at the target. The low efficiency and high neutron production of CB can limit its application.

The advantage of GRID irradiation using x-rays and proton beams has been reported in many studies based on experiment and simulation [71, 171, 172, 173]. One of the primary objectives of this work is to develop an optimum beam shaping technique capable of producing the desired GRID irradiation pattern with protons. Mechanical collimators can deliver an inhomogeneous dose at the entrance to create high peak to valley dose ratio (PVDR). Deflection of protons caused by slit scattering and secondary particles produced in the collimator by nuclear interaction can enhance the valley dose, reducing the PVDR. Moreover, the higher surface dose has the potential to cause damage to the radiosensitive skin and the superficial tissue, limiting the maximum dose per fraction, as mentioned earlier. Consequently, a patient needs to go through several treatment sessions to deliver the total prescribed dose. The movement of patients is very crucial for GRID irradiation

using narrow beams. If the patient cannot be identically placed for each session, the peak and valley regions may be overlapped, reducing the effectiveness of GRID irradiation.

As we have shown in chapters 5 and 6, magnetic beam focusing can be employed to overcome some of the aforementioned drawbacks of collimated beams. The conventional-energy focused beam (CEFB) of given energy can produce almost identical spots at the Bragg peak as a CB, with a large Bragg peak to surface dose ratio. This feature of CEFB can reduce the geometrical sparing factor (GSF), which is defined as the ratio of effective normal tissue dose to the effective tumor dose [174]. It widens the "window of opportunity" and escalates the maximum achievable dose per fraction, sparing healthy tissue [175]. This characteristic has a more significant impact on the SOBP compare to a pristine Bragg peak. Moreover, CEFB stops inside the target, same as CB, and deposit practically zero doses beyond the target. In contrast, a HEFB deposits a small dose beyond the target, decreasing with distance. A 350 MeV proton beam with suitable focusing can produce a submillimetre transverse beam size (σ) at 155 mm depth in water; in contrast, CB and CEFB can not reduce the transverse beam size less 1.5 mm at the same depth. The small σ of HEFB makes it possible to use as a precision scalpel to treat both cancerous and other diseases. An extra advantage here is that the focal point can be changed only by acting on the beamline magnets without changing the beam energy. However, the elongated longitudinal spot of a high-energy focused beam (HEFB) has two contradicting impacts. It can be used to produce a SOBP with a smaller number of beam modifications. In contrast, it will be problematic to irradiate a target with a shorter longitudinal dimension. Also, continious irradiation of larger targets are problematic, due to the overlapping of the entrance doses. Moreover, a HEFB cannot utilize the advantages of high LET observed at lower energy (at Bragg peak).

Magnetically focused beams with a small initial size can be used to produce an inhomogeneous dose profile to implement GRID irradiation. We have included such a distribution in appendix C, which is similar to a narrow collimated beam. However, it can enhance the GRID performance by increasing PVDR through the elimination of slit scattering effects. Moreover, it can improve the efficiency of irradiation by focusing all the protons of the beamline, whereas a collimator reduces the beam fluence at the treatment room. It also reduces the production of neutrons significantly. The details of this beam shaping technique for grid irradiation have been studied by Schneider et al. [144].

This thesis proposes a novel irradiation modality using a focused proton beam following the conventional GRID therapy. They can produce distinct spots at the tumor with a reduced surface dose. In contrast to the conventional GRID irradiation, it produces a homogeneous dose at the entrance and cannot exploit the dose-volume effect to spare normal tissue. However, it can deliver a high dose at the specific spots of a tumor. This beam can be implemented to study bystander effects of radiation. It will enable us to treat a tumor with an inhomogeneous dose distribution and escalate the dose per fraction.

Another major advantage of the focused beams is their high efficiency, creating opportunities to pursue dose rates. FLASH therapy has proven its superiority in normal tissue sparing, relying on the ultra-high dose rate. The lower efficiency of the collimated beam with its higher surface dose limits its implementation in FLASH therapy. In contrast, the focused beam increases the dose rate and enhances the maximum delivered dose to a tumor. Its high dose rate is also preferable for conventional radiotherapy as it makes the movement of patients and/or organs less problematic.

9.2 Outlook

Experimental validation of new beam shaping modalities is essential. In chapter 7, we demonstrated promising results to produce focused beams based on the existing proton therapy center with an additional component consisting of quadrupole magnets. However, we did not consider the impact of energy spread on the beam focusing. If not corrected, this may enlarge the spot size at the target. In addition, the studies are based on the approximate values of different parameters, e.g., the distance between the nozzle head and the isocenter, and the phase-space distribution of the beam from the nozzle (i.e. the Twiss parameters). A detailed further study based on the actual parameters is needed before the construction of a prototype. These extensive studies could be useful to improve the nozzle technology for proton beam therapy.

Moreover, the dose of the spot becomes lower as the beam gets narrower. The Bragg peak to surface dose ratio of 150 MeV proton beam is found less than 1 for any beam of less than 2.0 mm radius. The optimum beam size as a function of energy needs to be determined to ensure normal tissue sparing, and simultaneously deposit a sufficient dose at the target.

In order to understand the feasibility of the new beam shaping techniques and inhomogeneous irradiation modalities, biological studies should be carried out. It will simultaneously help us to understand the bystander effect more fundamentally. The most suitable irradiation pattern (homogeneous or inhomogeneous) to treat a tumor is not clear yet. Further biological studies of distinct high-dose spots using focus beams can answer this question, potentially introducing a novel and powerful tool for cancer treatment.

Appendix A

Emittance growth

A.1 Emittance growth by MCS

The particles of a beam are scattered in their passage through a physical medium. As the slope (u') of the particles increases, the MCS increases the emittance of the beam [176]. In a foil, the emittance growth depends depends on the initial Twiss parameters and the (foil) thickness. For any arbitrary thickness, the change in emittance can be expressed as

$$\Delta\epsilon = \frac{1}{2}\langle\theta^2\rangle\left[\beta_0 + L\alpha_0 + \frac{L^2}{3}\gamma_0\right], \tag{A.1.1}$$

where the rms scattering angle (equation 2.1.12) is $\theta_0 = \sqrt{\langle\theta^2\rangle}$ [177]. The thickness of the foil is L. α_0, β_0, and γ_0 are the initial Twiss parameters at the entrance surface of the scattering foil. The final emittance at the exit surface of the foil

$$\epsilon = \epsilon_0 + \Delta\epsilon, \tag{A.1.2}$$

where ϵ_0 is the initial emittance.

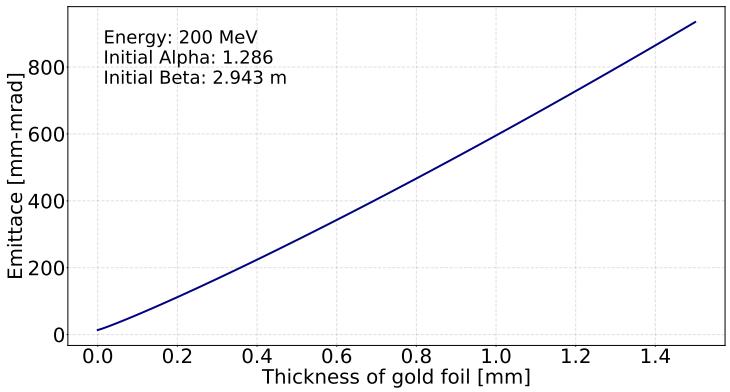

Figure A.1.1: Growth of emittance of 200 MeV proton beam as a function of thickness L of a gold foil. $\alpha_0 = 1.28$, $\beta_0 = 2.94$ m, and $\epsilon_0 = 13.585$ mm-mrad.

A.2 Impact of MSC on Twiss parameters

A scatterer also changes the Twiss parameters as [177]

$$\alpha = \frac{\epsilon_0 \alpha_0 - \frac{L}{2}\langle\theta^2\rangle}{\epsilon_0 + \Delta\epsilon} \tag{A.2.1}$$

$$\beta = \frac{\epsilon_0 \beta_0 + \frac{L^2}{3}\langle\theta^2\rangle}{\epsilon_0 + \Delta\epsilon} \tag{A.2.2}$$

$$\gamma = \frac{\epsilon_0 \gamma_0 + \langle\theta^2\rangle}{\epsilon_0 + \Delta\epsilon} \tag{A.2.3}$$

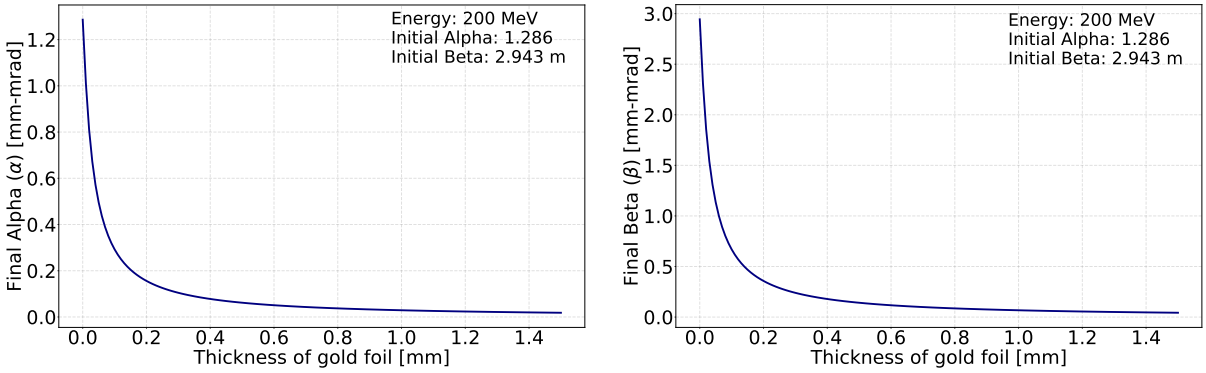

(a) (b)

Figure A.2.1: Evolution of α (a) and β (b) of 200 MeV proton beam as a function of the thickness of gold foil. $\alpha_0 = 1.28$, $\beta_0 = 2.94$ m, and $\epsilon_0 = 13.585$ mm-mrad.

Appendix B

Linear energy transfer

The linear energy transfer (LET) of a beam is one of the most crucial parameters that quantitatively describes the radiation quality. For a given dose, the biological outcome (RBE) changes with the value of LET of ionizing radiations. For a proton beam, the LET increases at the end of the range when beam energy is smaller. In figure B.1 we have compared the dose-averaged LET (LET_d) of a collimated beam (CB), conventional energy focused beam (CEFB) and high energy focused beam (HEFB).

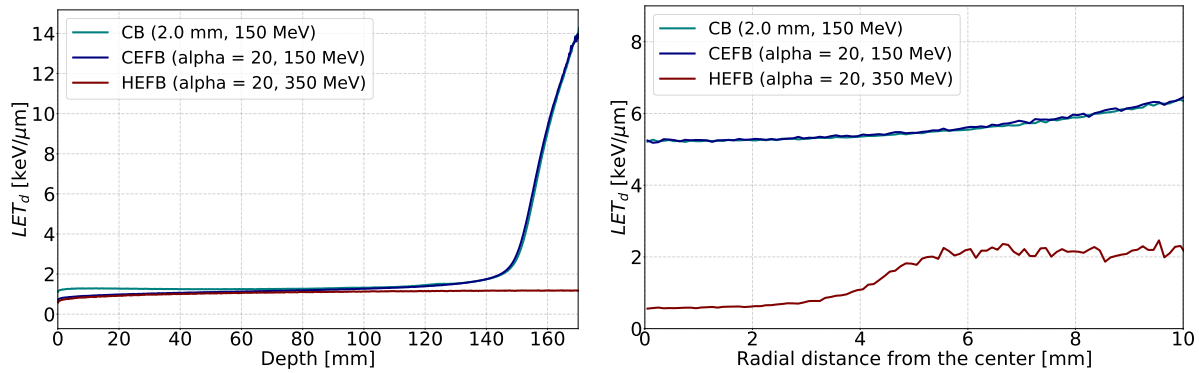

(a) (b)

Figure B.1: Comparison of the evolution of LET_d of CB, CEFB, and HEFB as a function of depth in water (a) and as a function of radial distance from the central axis of the beam (b).

Figure B.1a compares the LET_d of three different beam shaping techniques as a function of depth in the water phantom. The LET_d of CB and CEFB are almost identical except at the entrance, where it is slightly higher for the CB. The incoming secondaries and slit scattered proton explain this difference. On the other hand, the LET_d of HEFB is almost constant as its energy remains very high within the assessed depth in water.

In figure B.1b, the LET_d of CB and CEFB change identically with the radial distance from the center of the beam at their Bragg peak. It increases slowly as the proportion of low-energy protons and secondaries becomes larger at a point away from the center. The LET_d of HEFB is steady at the

center of the beam at the position of its focal point. It increases at a higher rate beyond 3.0 mm.

Appendix C

GRID irradiation

GRID irradiation produces an inhomogeneous dose distribution at the healthy tissue. A conventional energy focused beam (CEFB) can produce similar GRID irradiation as a collimated beam (CB). The features of their GRID irradiation obtained with an identical initial energy of 150 MeV are compared in figures C.1 and C.2. The CB was produced by simulating a collimator radius of 0.5 mm. On the other hand, the CEFB was simulated with the initial σ of 0.5 mm, and it was focused at its Bragg peak by tuning beam parameters for $\alpha = 15$. The CB produces sharp edges of the peak region at the entrance because the collimator removes its Gaussian tail. In contrast, the Gaussian distribution of CEFB produces blurred edges of the peak regions. The dose at the peak region (D_{Peak}) of CEFB increases in the first few centimeters, followed by a gradual drop as a function of depth. However, CB has its maximum D_{Peak} at its surface. In all other aspects, their GRID irradiation patterns are almost identical.

The features of GRID irradiation using high energy focused beam (HEFB) shown in figure C.3 are distinctive from its two counterparts. The high dose at its focal point relies on the transverse contraction of a HEFB, limiting the beam's initial transverse size. The GRID irradiation was simulated with the initial $\sigma = 3.0\ \mathrm{mm}$. It has its highest PVDR at its focal point and least at the surface. The longitudinal elongated high-dose region is noticeable.

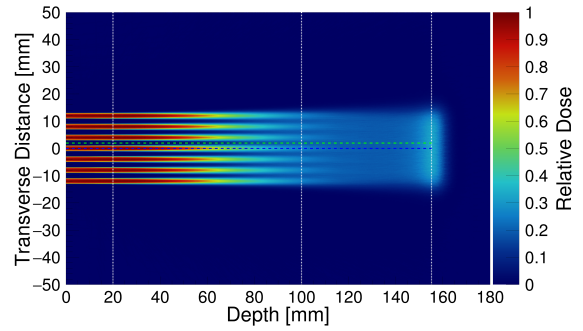

(a) 2D dose profile, c-t-c = 4 mm.

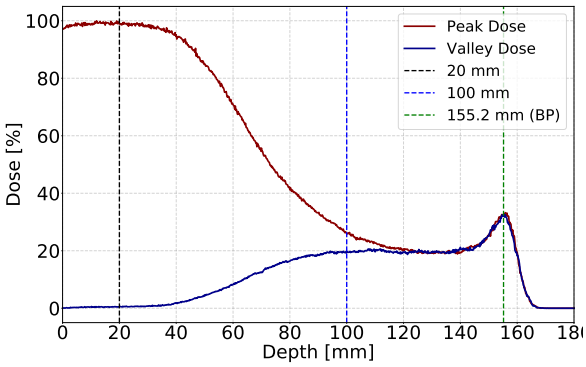

(b) PDD curves of CB, c-t-c = 4 mm.

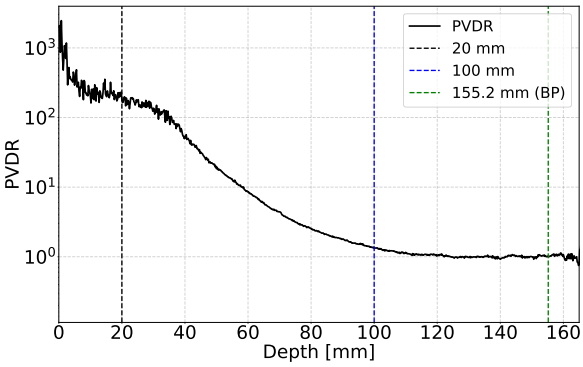

(c) PVDR of CB, c-t-c = 4 mm.

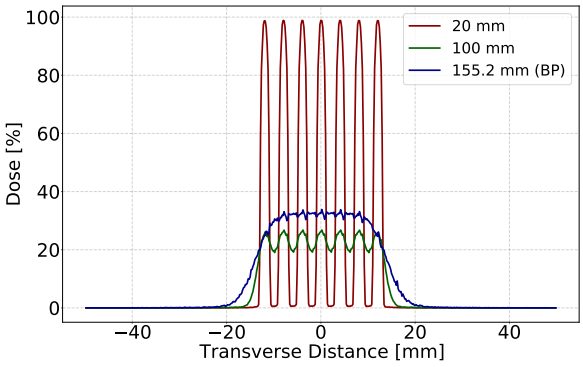

(d) Transverse dose profile, c-t-c = 4 mm.

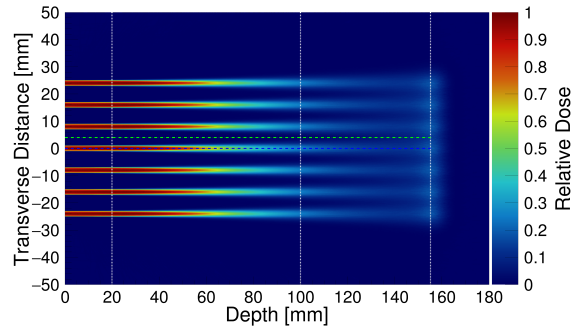

(e) 2D dose profile, c-t-c = 8 mm.

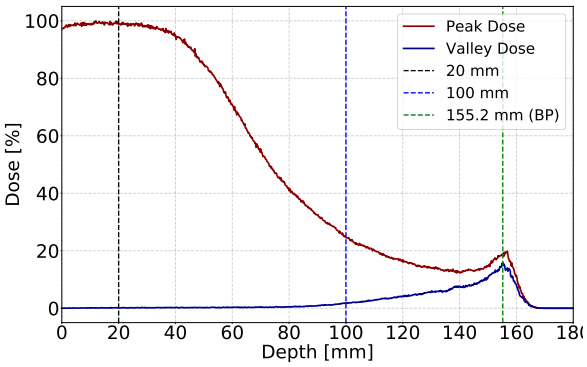

(f) PDD curves of CEFB, c-t-c = 8 mm.

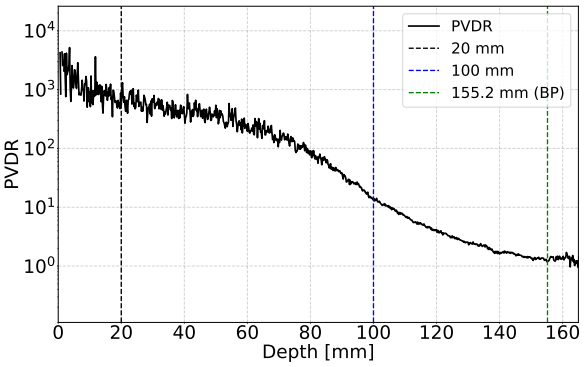

(g) PVDR of CB, c-t-c = 4 mm.

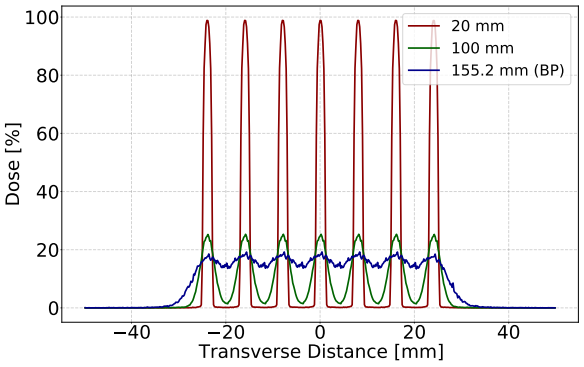

(h) Transverse dose profile, c-t-c = 4 mm.

Figure C.1: **GRID irradiation of CB:** Dose profile of GRID irradiation of 150 MeV CB obtained with c-t-c = 4 mm (left column) and c-t-c = 8 mm (right column). The collimator radius is 1.0 mm. **Top row:** Two-dimensional dose profile. The dose is normalized to the peak value. **Second row:** Comparison of the evolution of D_{Peak} and D_{Valley} as a function of depth. **Third row:** Evolution of PVDR of as a function of depth in the water phantom. **Bottom row:** Transverse dose profile at at 20 mm, 100 mm and 155.2 mm (BP).

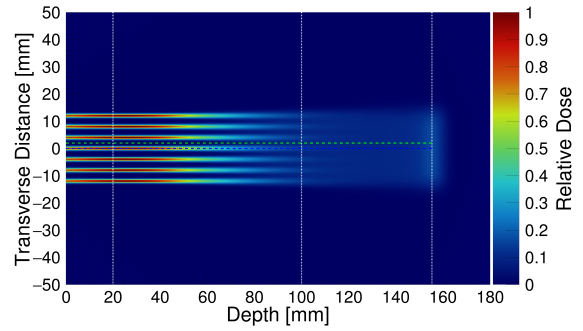

(a) 2D dose profile, c-t-c = 4 mm.

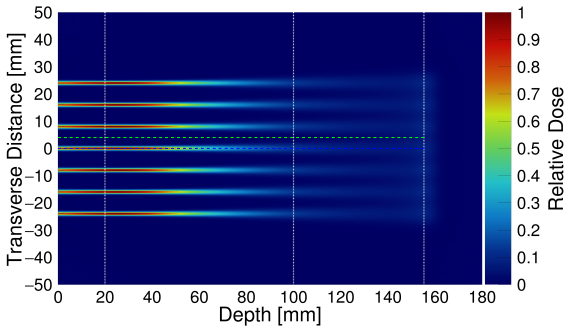

(e) 2D dose profile, c-t-c = 8 mm.

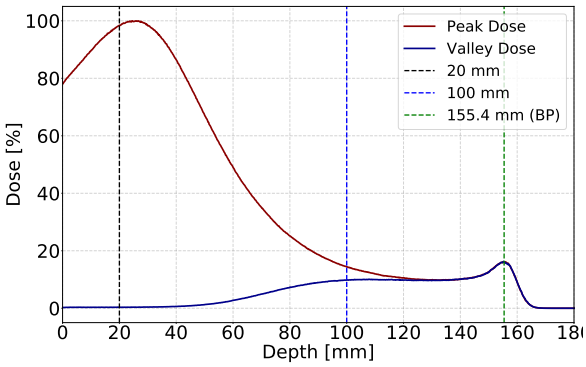

(b) PDD curves of CEFB, c-t-c = 4 mm.

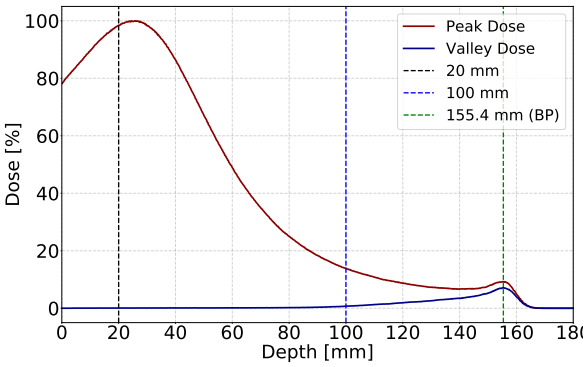

(f) PDD curves of CEFB, c-t-c = 8 mm.

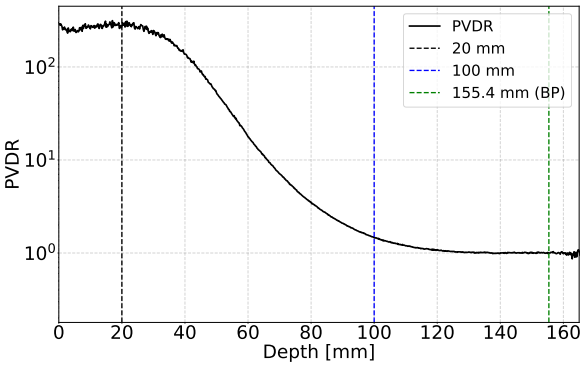

(c) PVDR of CEFB, c-t-c = 4 mm.

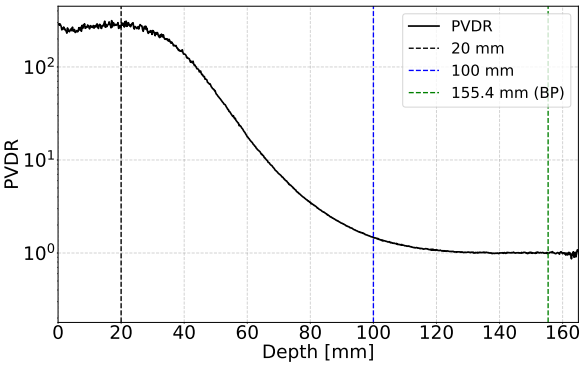

(g) PVDR of CEFB, c-t-c = 8 mm.

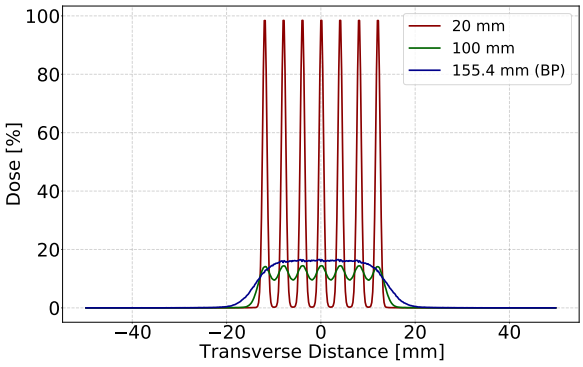

(d) Transverse dose profile, c-t-c = 4 mm.

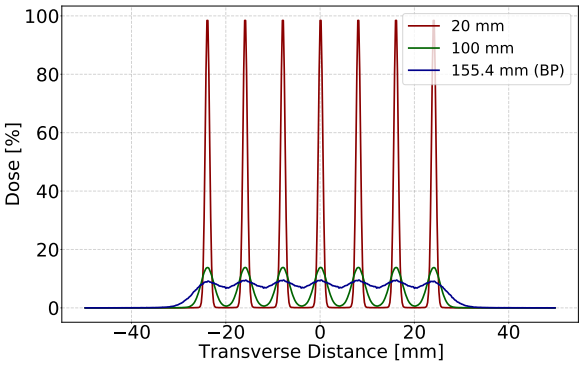

(h) Transverse dose profile, c-t-c = 8 mm.

Figure C.2: **GRID irradiation of CEFB:** Dose profile of fractionated irradiation of 150 MeV CEFB obtained with c-t-c = 4 mm (left column) and c-t-c = 8 mm (right column). Initial beam size (σ) is 0.5 mm. **Top row:** Two-dimensional dose profile. The dose is normalized to the peak value. **Second row:** Comparison of the evolution of D_{Peak} and D_{Valley} as a function of depth. **Third row:** Evolution of PVDR of as a function of depth in the water phantom. **Bottom row:** Transverse dose profile at at 20 mm, 100 mm and 155.4 mm (BP).

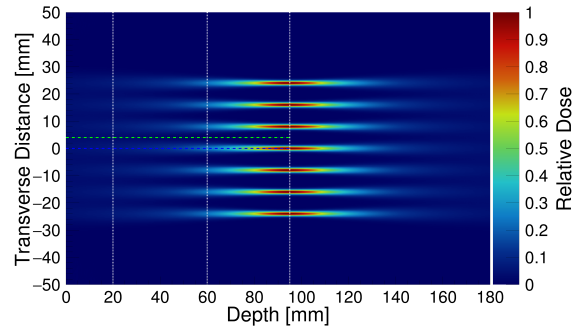

(a) 2D dose profile, c-t-c = 8 mm.

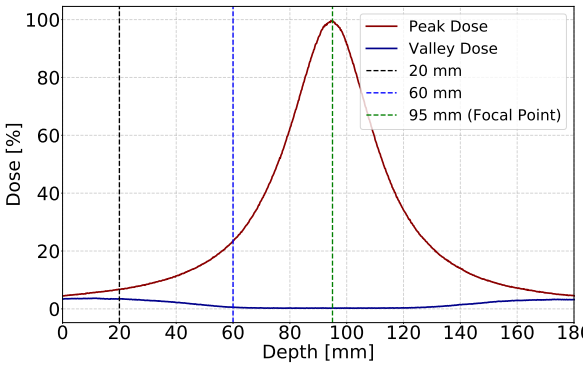

(b) PDD curves of HEFB, c-t-c = 8 mm.

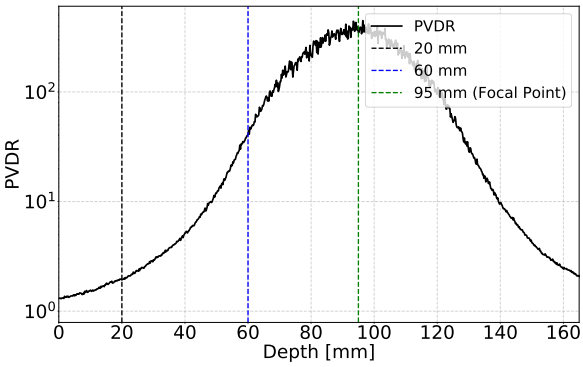

(c) PVDR of HEFB, c-t-c = 8 mm.

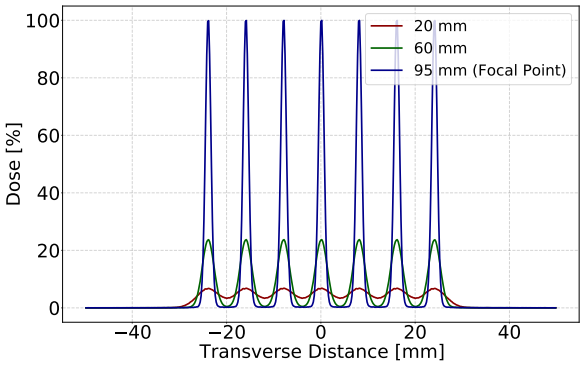

(d) Transverse dose profile, c-t-c = 8 mm.

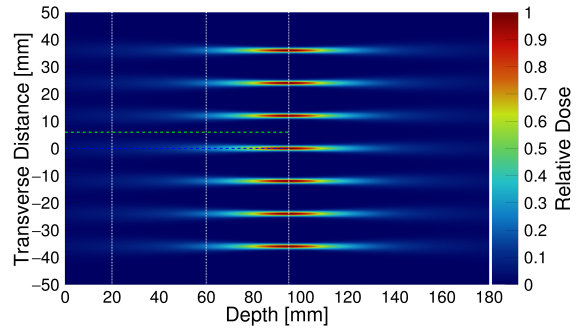

(e) 2D dose profile, c-t-c = 12 mm.

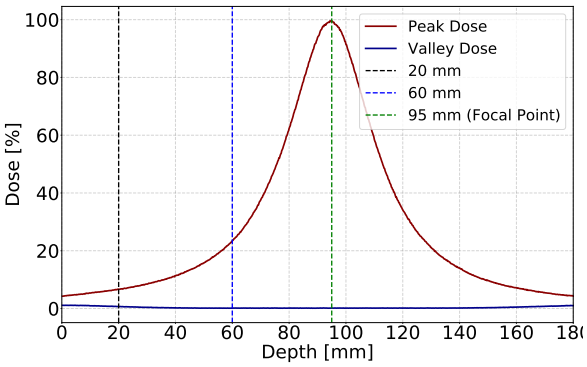

(f) PDD curves of HEFB, c-t-c = 12 mm.

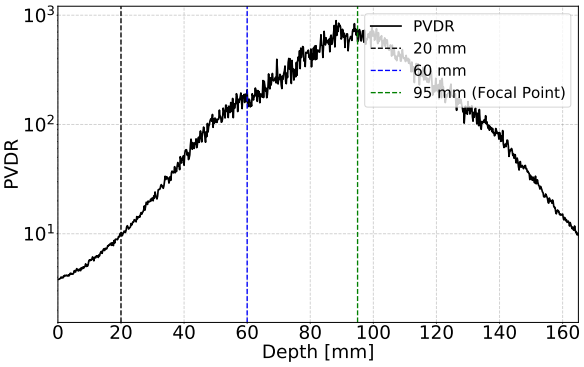

(g) PVDR of HEFB, c-t-c = 12 mm.

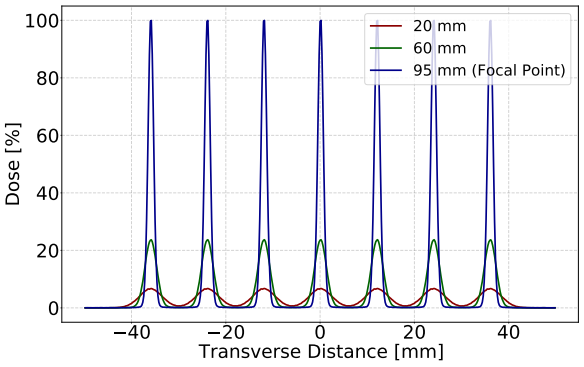

(h) Transverse dose profile, c-t-c = 12 mm.

Figure C.3: **GRID irradiation of HEFB:** Dose profile of fractionated irradiation of 350 MeV HEFB obtained with c-t-c = 8 mm (left column) and c-t-c = 12 mm (right column). Focused at 95 mm with initial beam size (σ) is 3.0 mm . **Top row:** Two-dimensional dose profile. The dose is normalized to the peak value. **Second row:** Comparison of the evolution of D_{Peak} and D_{Valley} as a function of depth. **Third row:** Evolution of PVDR of as a function of depth in the water phantom. **Bottom row:** Transverse dose profile at at 20 mm, 60 mm and 95 mm (focal length).

Bibliography

[1] *Understanding Cancer*. en. NIH Curriculum Supplement Series [Internet]. National Institutes of Health (US), 2007. URL: https://www.ncbi.nlm.nih.gov/books/NBK20362/.

[2] D. Eder, C. Aegerter, and K. Basler. "Forces controlling organ growth and size". en. In: *Mechanisms of Development*. Roles of physical forces in development 144 (Apr. 2017), pp. 53–61. ISSN: 0925-4773. DOI: 10.1016/j.mod.2016.11.005. URL: https://www.sciencedirect.com/science/article/pii/S0925477316300697.

[3] D. Hanahan and R. A. Weinberg. "The Hallmarks of Cancer". en. In: *Cell* 100.1 (Jan. 2000), pp. 57–70. ISSN: 0092-8674. DOI: 10.1016/S0092-8674(00)81683-9. URL: https://www.sciencedirect.com/science/article/pii/S0092867400816839.

[4] F. van Zijl, G. Krupitza, and W. Mikulits. "Initial steps of metastasis: Cell invasion and endothelial transmigration". In: *Mutation Research* 728.1-2 (July 2011), pp. 23–34. ISSN: 0027-5107. DOI: 10.1016/j.mrrev.2011.05.002. URL: https://www.ncbi.nlm.nih.gov/pmc/articles/PMC4028085/.

[5] J. Fares et al. "Molecular principles of metastasis: a hallmark of cancer revisited". en. In: *Signal Transduction and Targeted Therapy* 5.1 (Dec. 2020), p. 28. ISSN: 2059-3635. DOI: 10.1038/s41392-020-0134-x. URL: http://www.nature.com/articles/s41392-020-0134-x.

[6] F. Stephens et al. *Basics of Oncology*. Jan. 2009. ISBN: 978-3-540-92924-6.

[7] F. Bray et al. "Global cancer statistics 2018: GLOBOCAN estimates of incidence and mortality worldwide for 36 cancers in 185 countries". en. In: *CA: A Cancer Journal for Clinicians* 68.6 (2018). _eprint: https://acsjournals.onlinelibrary.wiley.com/doi/pdf/10.3322/caac.21492, pp. 394–424. ISSN: 1542-4863. DOI: 10.3322/caac.21492. URL: https://acsjournals.onlinelibrary.wiley.com/doi/abs/10.3322/caac.21492.

[8] *Global Cancer Facts & Figures — American Cancer Society*. en. URL: https://www.cancer.org/research/cancer-facts-statistics/global.html.

[9] R. Baskar et al. “Cancer and Radiation Therapy: Current Advances and Future Directions”. In: *International journal of medical sciences* 9 (Feb. 2012), pp. 193–9. DOI: 10.7150/ijms.3635.

[10] G. Delaney et al. “The role of radiotherapy in cancer treatment: estimating optimal utilization from a review of evidence-based clinical guidelines”. eng. In: *Cancer* 104.6 (Sept. 2005), pp. 1129–1137. ISSN: 0008-543X. DOI: 10.1002/cncr.21324.

[11] L. J. Schreiner. “Dosimetry in modern radiation therapy: limitations and needs”. en. In: *Journal of Physics: Conference Series* 56 (Dec. 2006), pp. 1–13. ISSN: 1742-6588, 1742-6596. DOI: 10.1088/1742-6596/56/1/001. URL: https://iopscience.iop.org/article/10.1088/1742-6596/56/1/001.

[12] B. Patyal. “Dosimetry Aspects of Proton Therapy”. In: *Technology in Cancer Research & Treatment* 6.4_suppl (Aug. 2007). Publisher: SAGE Publications Inc, pp. 17–23. ISSN: 1533-0346. DOI: 10.1177/15330346070060S403. URL: https://doi.org/10.1177/15330346070060S403.

[13] V. Dilalla et al. “Radiotherapy side effects: integrating a survivorship clinical lens to better serve patients”. In: *Current Oncology* 27.2 (Apr. 2020), pp. 107–112. ISSN: 1198-0052. DOI: 10.3747/co.27.6233. URL: https://www.ncbi.nlm.nih.gov/pmc/articles/PMC7253739/.

[14] S. M. Bentzen. “Preventing or reducing late side effects of radiation therapy: radiobiology meets molecular pathology”. en. In: *Nature Reviews Cancer* 6.9 (Sept. 2006), pp. 702–713. ISSN: 1474-175X, 1474-1768. DOI: 10.1038/nrc1950. URL: http://www.nature.com/articles/nrc1950.

[15] H. Rodney Withers, J. M. Taylor, and B. Maciejewski. “Treatment volume and tissue tolerance”. en. In: *International Journal of Radiation Oncology*Biology*Physics* 14.4 (Apr. 1988), pp. 751–759. ISSN: 03603016. DOI: 10.1016/0360-3016(88)90098-3. URL: https://linkinghub.elsevier.com/retrieve/pii/0360301688900983.

[16] J. W. Hopewell and K.-R. Trott. “Volume effects in radiobiology as applied to radiotherapy”. en. In: *Radiotherapy and Oncology* 56.3 (Sept. 2000), pp. 283–288. ISSN: 01678140. DOI: 10.1016/S0167-8140(00)00236-X. URL: https://linkinghub.elsevier.com/retrieve/pii/S016781400000236X.

[17] I. Martínez-Rovira, G. Fois, and Y. Prezado. “Dosimetric evaluation of new approaches in GRID therapy using nonconventional radiation sources: Dosimetric evaluation of new approaches in GRID therapy”. en. In: *Medical Physics* 42.2 (Jan. 2015), pp. 685–693. ISSN: 00942405. DOI: 10.1118/1.4905042. URL: http://doi.wiley.com/10.1118/1.4905042.

[18] J. A. Laissue, H. Blattmann, and D. N. Slatkin. “Alban Köhler (1874-1947): Inventor of grid therapy”. ger. In: *Zeitschrift Fur Medizinische Physik* 22.2 (June 2012), pp. 90–99. ISSN: 1876-4436. DOI: 10.1016/j.zemedi.2011.07.002.

[19] W. Yan et al. “Spatially fractionated radiation therapy: History, present and the future”. en. In: *Clinical and Translational Radiation Oncology* 20 (Jan. 2020), pp. 30–38. ISSN: 24056308. DOI: 10.1016/j.ctro.2019.10.004. URL: https://linkinghub.elsevier.com/retrieve/pii/S2405630819301041.

[20] *Protoner skal gi flere pasienter nytte av immunterapi*. en. URL: https://titan.uio.no/naturvitenskap-livsvitenskap-innovasjon/2019/protoner-skal-gi-flere-pasienter-nytte-av-immunterapi.

[21] J. Asperud et al. “Spatially fractionated radiotherapy: tumor response modelling including immunomodulation”. en. In: *Physics in Medicine & Biology* (2021). ISSN: 0031-9155. DOI: 10.1088/1361-6560/ac176b. URL: http://iopscience.iop.org/article/10.1088/1361-6560/ac176b.

[22] Z. Nikitaki et al. “Systemic mechanisms and effects of ionizing radiation: A new ”old” paradigm of how the bystanders and distant can become the players”. en. In: *Seminars in Cancer Biology* 37-38 (June 2016), pp. 77–95. ISSN: 1044579X. DOI: 10.1016/j.semcancer.2016.02.002. URL: https://linkinghub.elsevier.com/retrieve/pii/S1044579X16300049.

[23] A. Dilmanian et al. “Response of rat intracranial 9L gliosarcoma to microbeam radiation therapy”. In: *Neuro-oncology* 4 (Feb. 2002), pp. 26–38. DOI: 10.1215/Sq522851701000412.

[24] J. Meyer et al. “Spatially fractionated proton minibeams”. en. In: *The British Journal of Radiology* 92.1095 (Mar. 2019), p. 20180466. ISSN: 0007-1285, 1748-880X. DOI: 10.1259/bjr.20180466. URL: https://www.birpublications.org/doi/10.1259/bjr.20180466.

[25] C. Billena and A. J. Khan. “A Current Review of Spatial Fractionation: Back to the Future?” In: *International journal of radiation oncology, biology, physics* 104.1 (May 2019), pp. 177–187. ISSN: 0360-3016. DOI: 10.1016/j.ijrobp.2019.01.073. URL: https://www.ncbi.nlm.nih.gov/pmc/articles/PMC7443362/.

[26] P. Romanelli et al. “Synchrotron-Generated Microbeam Sensorimotor Cortex Transections Induce Seizure Control without Disruption of Neurological Functions”. en. In: *PLoS ONE* 8.1 (Jan. 2013). Ed. by M. Lim, e53549. ISSN: 1932-6203. DOI: 10.1371/journal.pone.0053549. URL: https://dx.plos.org/10.1371/journal.pone.0053549.

[27] F. H. Attix. *Introduction to Radiological Physics and Radiation Dosimetry*. en. 1st ed. Wiley, Nov. 1986. ISBN: 978-3-527-61713-5. DOI: 10.1002/9783527617135. URL: https://onlinelibrary.wiley.com/doi/book/10.1002/9783527617135.

[28] M. Niaz et al. "Reconstruction of the history of the photoelectric effect and its implications for general physics textbooks". en. In: *Science Education* 94.5 (2010), pp. 903–931. ISSN: 1098-237X. DOI: 10.1002/sce.20389. URL: https://onlinelibrary.wiley.com/doi/abs/10.1002/sce.20389.

[29] D. G. Grant. "RADIATION THERAPY PHYSICS". en. In: *Radiation Therapy Physics* (1983), p. 15.

[30] F. M. Khan and J. P. Gibbons. *Khan's the physics of radiation therapy*. en. Fifth edition. Philadelphia, PA: Lippincott Williams & Wilkins/Wolters Kluwer, 2014. ISBN: 978-1-4511-8245-3.

[31] D. Soliman. "Augmented microscopy: Development and application of high-resolution optoacoustic and multimodal imaging techniques for label-free biological observation". PhD thesis. Oct. 2016. DOI: 10.13140/RG.2.2.24410.03525.

[32] W. D. Newhauser and R. Zhang. "The physics of proton therapy". en. In: *Physics in Medicine and Biology* 60.8 (Apr. 2015), R155–R209. ISSN: 0031-9155, 1361-6560. DOI: 10.1088/0031-9155/60/8/R155. URL: https://iopscience.iop.org/article/10.1088/0031-9155/60/8/R155.

[33] Y. Helo et al. "The physics of Cerenkov light production during proton therapy". In: *Physics in Medicine and Biology* Phys. Med. Biol. (Nov. 2014), p. 7107. DOI: 10.1088/0031-9155/59/23/7107.

[34] H. Paganetti. *Proton Therapy Physics*. en. Google-Books-ID: IGPRBQAAQBAJ. CRC Press, Apr. 2016. ISBN: 978-1-4398-3645-3.

[35] H. A. Bethe. "Molière's Theory of Multiple Scattering". en. In: *Physical Review* 89.6 (Mar. 1953), pp. 1256–1266. ISSN: 0031-899X. DOI: 10.1103/PhysRev.89.1256. URL: https://link.aps.org/doi/10.1103/PhysRev.89.1256.

[36] V. L. Highland. "Some practical remarks on multiple scattering". en. In: *Nuclear Instruments and Methods* 129.2 (Nov. 1975), pp. 497–499. ISSN: 0029554X. DOI: 10.1016/0029-554X(75)90743-0. URL: https://linkinghub.elsevier.com/retrieve/pii/0029554X75907430.

[37] E. Ford. "Particle Interactions with Matter". en. In: *Primer on Radiation Oncology Physics*. 1st ed. CRC Press, May 2020, pp. 63–72. ISBN: 978-0-429-48888-7. DOI: 10.1201/9780429488887-7. URL: https://www.taylorfrancis.com/books/9780429950247/chapters/10.1201/9780429488887-7.

[38] *Particle Data Group*. en. URL: https://pdg.lbl.gov/2015/AtomicNuclearProperties/HTML/water_liquid.html.

[39] I. E. Tamm. "General Characteristics of Vavilov-Cherenkov Radiation". In: *Science* 131.3395 (1960). Publisher: American Association for the Advancement of Science, pp. 206–210. ISSN: 0036-8075. URL: https://www.jstor.org/stable/1705567.

[40] E. Draeger et al. "3D prompt gamma imaging for proton beam range verification". eng. In: *Physics in Medicine and Biology* 63.3 (Jan. 2018), p. 035019. ISSN: 1361-6560. DOI: 10.1088/1361-6560/aaa203.

[41] B. Gottschalk. "Physics of Proton Interactions in Matter". In: *Proton Therapy Physics. Series: Series in Medical Physics and Biomedical Engineering, ISBN: 978-1-4398-3644-6. CRC Press, Edited by Harald Paganetti, pp. 19-60* (Dec. 2011), pp. 19–60. DOI: 10.1201/b11448-3.

[42] B. Braunn et al. "Nuclear Physics and Hadron Therapy". In: *AIP Conference Proceedings* 1412 (Dec. 2011), pp. 303–310. DOI: 10.1063/1.3665328.

[43] W. H. Bragg and R. Kleeman. "XXXIX. On the α particles of radium, and their loss of range in passing through various atoms and molecules". In: *The London, Edinburgh, and Dublin Philosophical Magazine and Journal of Science* 10.57 (Sept. 1905). Publisher: Taylor & Francis _eprint: https://doi.org/10.1080/14786440509463378, pp. 318–340. ISSN: 1941-5982. DOI: 10.1080/14786440509463378. URL: https://doi.org/10.1080/14786440509463378.

[44] W. R. Leo. *Techniques for Nuclear and Particle Physics Experiments: A How-to Approach*. en. 2nd ed. Berlin Heidelberg: Springer-Verlag, 1994. ISBN: 978-3-540-57280-0. DOI: 10.1007/978-3-642-57920-2. URL: https://www.springer.com/gp/book/9783540572800.

[45] J. Schuemann et al. "Site-specific range uncertainties caused by dose calculation algorithms for proton therapy". In: *Physics in medicine and biology* 59.15 (Aug. 2014), pp. 4007–4031. ISSN: 0031-9155. DOI: 10.1088/0031-9155/59/15/4007. URL: https://www.ncbi.nlm.nih.gov/pmc/articles/PMC4136435/.

[46] H. E. S. Pettersen et al. "Accuracy of parameterized proton range models; a comparison". In: *Radiation Physics and Chemistry* 144 (Mar. 2018). arXiv: 1704.08854, pp. 295–297. ISSN: 0969806X. DOI: 10.1016/j.radphyschem.2017.08.028. URL: http://arxiv.org/abs/1704.08854.

[47] Y.-S. Park et al. "Proton Beam Energy Determination Using a Device for Range Measurement of an Accelerated High Energy Ion Beam". en. In: *Journal of the Korean Physical Society* 59.2 (Aug. 2011). Publisher: The Korean Physical Society, pp. 679–685. DOI: 10.393

8/jkps.59.679. URL: https://www.jkps.or.kr/journal/view.html?doi=10.3938/jkps.59.679.

[48] B. Gottschalk. "Radiotherapy Proton Interactions in Matter". In: *arXiv:1804.00022 [physics]* (Mar. 2018). arXiv: 1804.00022. URL: http://arxiv.org/abs/1804.00022.

[49] D. Schardt, T. Elsässer, and D. Schulz-Ertner. "Heavy-ion tumor therapy: Physical and radiobiological benefits". en. In: *Reviews of Modern Physics* 82.1 (Feb. 2010), pp. 383–425. ISSN: 0034-6861, 1539-0756. DOI: 10.1103/RevModPhys.82.383. URL: https://link.aps.org/doi/10.1103/RevModPhys.82.383.

[50] "ICRU Report 85 FUNDAMENTAL QUANTITIES AND UNITS FOR IONIZING RADIATION (Revised)". In: (Oct. 2012). DOI: doi:10.1093/jicru/ndr012.

[51] A. Lombardi, C. Algranati, and M. Schwarz. "Proton radiation therapy in oncology: Review of present clinical indications Review Article". In: *Cancer therapy* 4 (July 2006), pp. 231–231. URL: https://www.researchgate.net/publication/273146352_Proton_radiation_therapy_in_oncology_Review_of_present_clinical_indications_Review_Article.

[52] A. Brown and H. Suit. "The centenary of the discovery of the Bragg peak". English. In: *Radiotherapy and Oncology* 73.3 (Dec. 2004). Publisher: Elsevier, pp. 265–268. ISSN: 0167-8140, 1879-0887. DOI: 10.1016/j.radonc.2004.09.008. URL: https://www.thegreenjournal.com/article/S0167-8140(04)00449-9/abstract.

[53] F. Guan et al. "Analysis of the track-and dose-averaged LET and LET spectra in proton therapy using the geant4 Monte Carlo code". In: *Medical Physics* 42 (Oct. 2015), pp. 6234–6247. DOI: 10.1118/1.4932217.

[54] M. Lomax, L. Folkes, and P. O'Neill. "Biological Consequences of Radiation-induced DNA Damage: Relevance to Radiotherapy". en. In: *Clinical Oncology* 25.10 (Oct. 2013), pp. 578–585. ISSN: 09366555. DOI: 10.1016/j.clon.2013.06.007. URL: https://linkinghub.elsevier.com/retrieve/pii/S0936655513002471.

[55] K. Ledingham et al. "Towards Laser Driven Hadron Cancer Radiotherapy: A Review of Progress". In: *Appl. Sci.* 4 (May 2014).

[56] W. Hur and S. Yoon. "Molecular Pathogenesis of Radiation-Induced Cell Toxicity in Stem Cells". In: *International Journal of Molecular Sciences* 18 (Dec. 2017), p. 2749. DOI: 10.3390/ijms18122749.

[57] P. Maier et al. "Cellular Pathways in Response to Ionizing Radiation and Their Targetability for Tumor Radiosensitization". In: *International Journal of Molecular Sciences* 17.1 (Jan. 2016), p. 102. ISSN: 1422-0067. DOI: 10.3390/ijms17010102. URL: https://www.ncbi.nlm.nih.gov/pmc/articles/PMC4730344/.

[58] J. Valentin. “Relative biological effectiveness (RBE), quality factor (Q), and radiation weighting factor (wR): ICRP Publication 92: Approved by the Commission in January 2003”. In: *Annals of the ICRP* 33.4 (Oct. 2003). Publisher: SAGE Publications Ltd, pp. 1–121. ISSN: 0146-6453. DOI: 10.1016/S0146-6453(03)00024-1. URL: https://doi.org/10.1016/S0146-6453(03)00024-1.

[59] S. McMahon. “The linear quadratic model: usage, interpretation and challenges”. In: *Physics in Medicine and Biology* 64 (Nov. 2018). DOI: 10.1088/1361-6560/aaf26a.

[60] E. Rørvik et al. “Exploration and application of phenomenological RBE models for proton therapy”. eng. In: *Physics in Medicine and Biology* 63.18 (Sept. 2018), p. 185013. ISSN: 1361-6560. DOI: 10.1088/1361-6560/aad9db.

[61] H. Paganetti. “Relative biological effectiveness (RBE) values for proton beam therapy. Variations as a function of biological endpoint, dose, and linear energy transfer”. In: *Physics in Medicine and Biology* 59.22 (Nov. 2014), R419–R472. ISSN: 0031-9155, 1361-6560. DOI: 10.1088/0031-9155/59/22/R419. URL: https://iopscience.iop.org/article/10.1088/0031-9155/59/22/R419.

[62] M. C. Joiner and A. J. v. d. Kogel, eds. *Basic Clinical Radiobiology*. 5th ed. Boca Raton: CRC Press, Aug. 2018. ISBN: 978-0-429-49060-6. DOI: 10.1201/9780429490606.

[63] D. E. Gerber and T. A. Chan. “Recent Advances in Radiation Therapy”. In: *American Family Physician* 78.11 (Dec. 2008), pp. 1254–1262. ISSN: 0002-838X, 1532-0650. URL: https://www.aafp.org/afp/2008/1201/p1254.html.

[64] W. D. Bloomer and S. Hellman. “Normal Tissue Responses to Radiation Therapy”. en. In: *New England Journal of Medicine* 293.2 (July 1975), pp. 80–83. ISSN: 0028-4793, 1533-4406. DOI: 10.1056/NEJM197507102930206. URL: http://www.nejm.org/doi/abs/10.1056/NEJM197507102930206.

[65] A. Schüller et al. “The European Joint Research Project UHDpulse – Metrology for advanced radiotherapy using particle beams with ultra-high pulse dose rates”. en. In: *Physica Medica* 80 (Dec. 2020), pp. 134–150. ISSN: 11201797. DOI: 10.1016/j.ejmp.2020.09.020. URL: https://linkinghub.elsevier.com/retrieve/pii/S1120179720302362.

[66] C. Grassberger et al. “Variations in linear energy transfer within clinical proton therapy fields and the potential for biological treatment planning”. In: *International journal of radiation oncology, biology, physics* 80.5 (Aug. 2011), pp. 1559–1566. ISSN: 0360-3016. DOI: 10.1016/j.ijrobp.2010.10.027. URL: https://www.ncbi.nlm.nih.gov/pmc/articles/PMC3094592/.

[67] M. Hada and A. G. Georgakilas. “Formation of Clustered DNA Damage after High-LET Irradiation: A Review”. en. In: *Journal of Radiation Research* 49.3 (2008), pp. 203–210. ISSN: 0449-3060, 1349-9157. DOI: 10.1269/jrr.07123. URL: https://academic.oup.com/jrr/article-lookup/doi/10.1269/jrr.07123.

[68] X. Ding et al. “Proton Treatment Delivery Techniques”. In: *Target Volume Delineation and Treatment Planning for Particle Therapy*. Ed. by N. Y. Lee et al. Series Title: Practical Guides in Radiation Oncology. Cham: Springer International Publishing, 2018, pp. 17–44. DOI: 10.1007/978-3-319-42478-1_2. URL: http://link.springer.com/10.1007/978-3-319-42478-1_2.

[69] J. Son et al. “Development of Optical Fiber Based Measurement System for the Verification of Entrance Dose Map in Pencil Beam Scanning Proton Beam”. en. In: *Sensors* 18.1 (Jan. 2018). Number: 1 Publisher: Multidisciplinary Digital Publishing Institute, p. 227. DOI: 10.3390/s18010227. URL: https://www.mdpi.com/1424-8220/18/1/227.

[70] C. Guardiola, C. Peucelle, and Y. Prezado. “Optimization of the mechanical collimation for minibeam generation in proton minibeam radiation therapy”. eng. In: *Medical Physics* 44.4 (Apr. 2017), pp. 1470–1478. ISSN: 2473-4209. DOI: 10.1002/mp.12131.

[71] Y. Prezado et al. “Proton minibeam radiation therapy widens the therapeutic index for high-grade gliomas”. eng. In: *Scientific reports* 8.1 (2018). Place: England Publisher: Nature Publishing Group, pp. 16479–10. ISSN: 2045-2322. DOI: 10.1038/s41598-018-34796-8.

[72] Y. Prezado et al. “Tumor Control in RG2 Glioma-Bearing Rats: A Comparison Between Proton Minibeam Therapy and Standard Proton Therapy”. en. In: *International Journal of Radiation Oncology*Biology*Physics* 104.2 (June 2019), pp. 266–271. ISSN: 03603016. DOI: 10.1016/j.ijrobp.2019.01.080. URL: https://linkinghub.elsevier.com/retrieve/pii/S0360301619301713.

[73] A. Marín et al. “Bystander effects and radiotherapy”. In: *Reports of Practical Oncology and Radiotherapy* 20.1 (Aug. 2014), pp. 12–21. ISSN: 1507-1367. DOI: 10.1016/j.rpor.2014.08.004. URL: https://www.ncbi.nlm.nih.gov/pmc/articles/PMC4268598/.

[74] J.-P. Pouget, A. G. Georgakilas, and J.-L. Ravanat. “Targeted and Off-Target (Bystander and Abscopal) Effects of Radiation Therapy: Redox Mechanisms and Risk/Benefit Analysis”. en. In: *Antioxidants & Redox Signaling* 29.15 (Nov. 2018), pp. 1447–1487. ISSN: 1523-0864, 1557-7716. DOI: 10.1089/ars.2017.7267. URL: https://www.liebertpub.com/doi/10.1089/ars.2017.7267.

[75] J. R. Hughes and J. L. Parsons. “FLASH Radiotherapy: Current Knowledge and Future Insights Using Proton-Beam Therapy”. en. In: *International Journal of Molecular Sciences*

21.18 (Sept. 2020), p. 6492. ISSN: 1422-0067. DOI: 10.3390/ijms21186492. URL: https://www.mdpi.com/1422-0067/21/18/6492.

[76] M.-C. Vozenin, J. Hendry, and C. Limoli. "Biological Benefits of Ultra-high Dose Rate FLASH Radiotherapy: Sleeping Beauty Awoken". en. In: *Clinical Oncology* 31.7 (July 2019), pp. 407–415. ISSN: 09366555. DOI: 10.1016/j.clon.2019.04.001. URL: https://linkinghub.elsevier.com/retrieve/pii/S0936655519301517.

[77] K. P. Nesteruk and S. Psoroulas. "FLASH Irradiation with Proton Beams: Beam Characteristics and Their Implications for Beam Diagnostics". In: (2021). DOI: 10.3390/APP11052170.

[78] S. Jolly et al. "Technical challenges for FLASH proton therapy". en. In: *Physica Medica* 78 (Oct. 2020), pp. 71–82. ISSN: 11201797. DOI: 10.1016/j.ejmp.2020.08.005. URL: https://linkinghub.elsevier.com/retrieve/pii/S1120179720301964.

[79] H. Wiedemann. *Particle Accelerator Physics*. en. Springer, July 2015. ISBN: 978-3-319-18317-6.

[80] E. O. Lawrence and M. S. Livingston. "The Production of High Speed Light Ions Without the Use of High Voltages". en. In: *Physical Review* 40.1 (Apr. 1932), pp. 19–35. ISSN: 0031-899X. DOI: 10.1103/PhysRev.40.19. URL: https://link.aps.org/doi/10.1103/PhysRev.40.19.

[81] A. El-Saftawy. "Regulating the performance parameters of accelerated particles". PhD thesis. Jan. 2013.

[82] K. Peach, P. Wilson, and B. Jones. "Accelerator science in medical physics". In: *The British journal of radiology* 84 Spec No 1 (Dec. 2011), S4–10. DOI: 10.1259/bjr/16022594.

[83] *Quadrupole magnet*. en. Page Version ID: 1034776463. July 2021. URL: https://en.wikipedia.org/w/index.php?title=Quadrupole_magnet&oldid=1034776463.

[84] H. Grote et al. "(Methodical Accelerator Design) Version 5.02.08". en. In: (), p. 247.

[85] V. Kain. *Beam Dynamics and Beam Losses - Circular Machines*. en. Number: arXiv:1608.02449. Aug. 2016. DOI: 10.5170/CERN-2016-002.21. URL: https://cds.cern.ch/record/2206741.

[86] K. Wille and J. McFall. *The Physics of Particle Accelerators: An Introduction*. Oxford, New York: Oxford University Press, Feb. 2001. ISBN: 978-0-19-850549-5.

[87] H. Grote and F. Schmidt. "Mad-X - an upgrade from mad8". In: *Proceedings of the 2003 Particle Accelerator Conference*. Vol. 5. ISSN: 1063-3928. May 2003, pp. 3497–3499. DOI: 10.1109/PAC.2003.1289960.

[88] E. Stoian. “Fundamentals and Applications of the Monte Carlo Method”. In: *Journal of Canadian Petroleum Technology* 4.03 (July 1965), pp. 120–129. ISSN: 0021-9487. DOI: 10.2118/65-03-02.

[89] R. L. Harrison. “Introduction to Monte Carlo Simulation”. In: *AIP Conference Proceedings* 1204.1 (Jan. 2010). Publisher: American Institute of Physics, pp. 17–21. ISSN: 0094-243X. DOI: 10.1063/1.3295638. URL: https://aip.scitation.org/doi/abs/10.1063/1.3295638.

[90] R. Eckhardt. “STAN ULAM, JOHN VON NEUMANN, and the MONTE CARL0 METHOD”. en. In: *Los Alamos Science* Special Issue (1987), p. 11. URL: https://permalink.lanl.gov/object/tr?what=info:lanl-repo/lareport/LA-UR-88-9068.

[91] D. J. E. Turner, D. Downing, and J. Bogard. *Statistical Methods in Radiation Physics — Wiley*. en-us. ISBN: 978-3-527-41107-8.

[92] S. Okada et al. “MPEXS-DNA, a new GPU-based Monte Carlo simulator for track structures and radiation chemistry at subcellular scale”. In: *Medical Physics* 46.3 (Mar. 2019), pp. 1483–1500. ISSN: 0094-2405. DOI: 10.1002/mp.13370. URL: https://www.ncbi.nlm.nih.gov/pmc/articles/PMC6850505/.

[93] F. Salvat. *PENELOPE 2018: A code system for Monte Carlo simulation of electron and photon transport: Workshop Proceedings, Barcelona, Spain, 28 January – 1 February 2019*. en. Text. URL: https://www-oecd-ilibrary-org.ezproxy.uio.no/nuclear-energy/penelope-2018-a-code-system-for-monte-carlo-simulation-of-electron-and-photon-transport_32da5043-en.

[94] F. Salvat and J. Fernández-Varea. “Overview of physical interaction models for photon and electron transport used in Monte Carlo codes”. In: *Metrologia* 46 (Mar. 2009), S112. DOI: 10.1088/0026-1394/46/2/S08.

[95] I. J. Chetty et al. “Report of the AAPM Task Group No. 105: Issues associated with clinical implementation of Monte Carlo-based photon and electron external beam treatment planning”. en. In: *Medical Physics* 34.12 (2007), pp. 4818–4853. ISSN: 2473-4209. DOI: 10.1118/1.2795842. URL: https://aapm.onlinelibrary.wiley.com/doi/abs/10.1118/1.2795842.

[96] I. Kyriakou et al. “Influence of track structure and condensed history physics models of Geant4 to nanoscale electron transport in liquid water”. eng. In: *Physica medica: PM: an international journal devoted to the applications of physics to medicine and biology: official journal of the Italian Association of Biomedical Physics (AIFB)* 58 (Feb. 2019), pp. 149–154. ISSN: 1724-191X. DOI: 10.1016/j.ejmp.2019.01.001.

[97] P. Lazarakis et al. “Investigation of Track Structure and Condensed History physics models for applications in radiation dosimetry on a micro and nano scale in Geant4”. In: *Biomedical Physics & Engineering Express* 4 (Jan. 2018). DOI: 10.1088/2057-1976/aaa6aa.

[98] M. A. Tajik-Mansoury, H. Rajabi, and H. Mozdarani. “A comparison between track-structure, condensed-history Monte Carlo simulations and MIRD cellular S-values”. eng. In: *Physics in Medicine and Biology* 62.5 (Mar. 2017), N90–N106. ISSN: 1361-6560. DOI: 10.1088/1361-6560/62/5/N90.

[99] A. Bielajew. *Chapter 1 : History of Monte Carlo*. en. 2012. URL: https://www.semanticscholar.org/paper/Chapter-1-%3A-History-of-Monte-Carlo-Bielajew/cf86a7616fa558ef22924e12aa85cebb1ac547e2.

[100] D. P. Kroese et al. “Why the Monte Carlo method is so important today: Why the MCM is so important today”. en. In: *Wiley Interdisciplinary Reviews: Computational Statistics* 6.6 (Nov. 2014), pp. 386–392. ISSN: 19395108. DOI: 10.1002/wics.1314. URL: http://doi.wiley.com/10.1002/wics.1314.

[101] R. Carmona et al. “An introduction to particle methods in finance”. In: *Proceedings in Mathematics, No. XVII*. Vol. 12. Journal Abbreviation: Proceedings in Mathematics, No. XVII. Mar. 2012, pp. 1–46. ISBN: 978-3-642-25745-2.

[102] C. J. Mode. *Applications of Monte Carlo Methods in Biology, Medicine and Other Fields of Science*. en. Feb. 2011. ISBN: 978-953-307-427-6. DOI: 10.5772/634. URL: https://www.intechopen.com/books/applications-of-monte-carlo-methods-in-biology-medicine-and-other-fields-of-science.

[103] M. Moralles et al. “Applications of the Monte Carlo method in nuclear physics using the GEANT4 toolkit”. In: *AIP Conference Proceedings* 1139.1 (June 2009). Publisher: American Institute of Physics, pp. 51–56. ISSN: 0094-243X. DOI: 10.1063/1.3157829. URL: https://aip.scitation.org/doi/abs/10.1063/1.3157829.

[104] J. Collado et al. “Application of Monte Carlo Simulation in Industrial Microbiological Exposure Assessment”. en. In: *Applications of Monte Carlo Method in Science and Engineering* (Feb. 2011). Publisher: IntechOpen. DOI: 10.5772/15283. URL: https://www.intechopen.com/books/applications-of-monte-carlo-method-in-science-and-engineering/application-of-monte-carlo-simulation-in-industrial-microbiological-exposure-assessment.

[105] D. W. O. Rogers. “Fifty years of Monte Carlo simulations for medical physics”. en. In: *Physics in Medicine and Biology* 51.13 (July 2006), R287–R301. ISSN: 0031-9155, 1361-6560. DOI: 10.1088/0031-9155/51/13/R17. URL: https://iopscience.iop.org/article/10.1088/0031-9155/51/13/R17.

[106] P. Andreo. “Monte Carlo techniques in medical radiation physics”. In: *Physics in medicine and biology* 36 (Aug. 1991), pp. 861–920. DOI: 10.1088/0031-9155/36/7/001.

[107] J. S. Meena et al. “Overview of emerging nonvolatile memory technologies”. In: *Nanoscale Research Letters* 9.1 (Sept. 2014), p. 526. ISSN: 1556-276X. DOI: 10.1186/1556-276X-9-526. URL: https://doi.org/10.1186/1556-276X-9-526.

[108] S. Furber. “Microprocessors: the engines of the digital age”. In: *Proceedings. Mathematical, Physical, and Engineering Sciences* 473.2199 (Mar. 2017). ISSN: 1364-5021. DOI: 10.1098/rspa.2016.0893. URL: https://www.ncbi.nlm.nih.gov/pmc/articles/PMC5378251/.

[109] K. Jabbari. “Review of Fast Monte Carlo Codes for Dose Calculation in Radiation Therapy Treatment Planning”. In: *Journal of Medical Signals and Sensors* 1.1 (2011), pp. 73–86. ISSN: 2228-7477. URL: https://www.ncbi.nlm.nih.gov/pmc/articles/PMC3317764/.

[110] E. Spezi and G. Lewis. “An overview of Monte Carlo treatment planning for radiotherapy”. en. In: *Radiation Protection Dosimetry* 131.1 (Aug. 2008), pp. 123–129. ISSN: 0144-8420, 1742-3406. DOI: 10.1093/rpd/ncn277. URL: https://academic.oup.com/rpd/article-lookup/doi/10.1093/rpd/ncn277.

[111] H. Zaidi. “Relevance of accurate Monte Carlo modeling in nuclear medical imaging”. en. In: *Medical Physics* 26.4 (1999). _eprint: https://aapm.onlinelibrary.wiley.com/doi/pdf/10.1118/1.598559, pp. 574–608. ISSN: 2473-4209. DOI: 10.1118/1.598559. URL: https://aapm.onlinelibrary.wiley.com/doi/abs/10.1118/1.598559.

[112] M. A. Bernal et al. “Track structure modeling in liquid water: A review of the Geant4-DNA very low energy extension of the Geant4 Monte Carlo simulation toolkit”. en. In: *Physica Medica* 31.8 (Dec. 2015), pp. 861–874. ISSN: 1120-1797. DOI: 10.1016/j.ejmp.2015.10.087. URL: https://www.sciencedirect.com/science/article/pii/S1120179715010042.

[113] V. A. Semenenko, J. E. Turner, and T. B. Borak. “NOREC, a Monte Carlo code for simulating electron tracks in liquid water”. en. In: *Radiation and Environmental Biophysics* 42.3 (Oct. 2003), pp. 213–217. ISSN: 0301-634X, 1432-2099. DOI: 10.1007/s00411-003-0201-z. URL: http://link.springer.com/10.1007/s00411-003-0201-z.

[114] T. Liamsuwan et al. “Microdosimetry of low-energy electrons”. eng. In: *International Journal of Radiation Biology* 88.12 (Dec. 2012), pp. 899–907. ISSN: 1362-3095. DOI: 10.3109/09553002.2012.699136.

[115] S. Agostinelli et al. “Geant4—a simulation toolkit”. en. In: *Nuclear Instruments and Methods in Physics Research Section A: Accelerators, Spectrometers, Detectors and Associated Equipment* 506.3 (July 2003), pp. 250–303. ISSN: 01689002. DOI: 10.1016/S0168-9002(03)01368-8. URL: https://linkinghub.elsevier.com/retrieve/pii/S0168900203013688.

[116] J. Allison et al. “Geant4 Developments and Applications”. In: *IEEE Transactions on Nuclear Science* 53 (Feb. 2006), pp. 270–278. DOI: 10.1109/TNS.2006.869826.

[117] R. A. Forster and T. N. K. Godfrey. “MCNP - a general Monte Carlo code for neutron and photon transport”. en. In: *Monte-Carlo Methods and Applications in Neutronics, Photonics and Statistical Physics*. Ed. by R. Alcouffe et al. Vol. 240. Series Title: Lecture Notes in Physics. Berlin/Heidelberg: Springer-Verlag, 1985, pp. 33–55. ISBN: 978-3-540-16070-0. DOI: 10.1007/BFb0049033. URL: http://link.springer.com/10.1007/BFb0049033.

[118] A. Ferrari et al. “FLUKA: a multi-particle transport code”. In: *CERN Yellow report* 2005-10 (Jan. 2005). DOI: 10.2172/877507.

[119] J. Baró et al. “PENELOPE: An algorithm for Monte Carlo simulation of the penetration and energy loss of electrons and positrons in matter”. en. In: *Nuclear Instruments and Methods in Physics Research Section B: Beam Interactions with Materials and Atoms* 100.1 (May 1995), pp. 31–46. ISSN: 0168583X. DOI: 10.1016/0168-583X(95)00349-5. URL: https://linkinghub.elsevier.com/retrieve/pii/0168583X95003495.

[120] J. Allison et al. “Recent developments in GEANT4”. In: *Nuclear Instruments and Methods in Physics Research Section A: Accelerators, Spectrometers, Detectors and Associated Equipment* 835 (July 2016). DOI: 10.1016/j.nima.2016.06.125.

[121] H. Wenzel, J. Yarba, and A. Dotti. “The Geant4 physics validation repository”. In: *Journal of Physics: Conference Series* 664 (Dec. 2015), p. 062066. DOI: 10.1088/1742-6596/664/6/062066.

[122] D. Bolst et al. “Validation of Geant4 fragmentation for Heavy Ion Therapy”. en. In: *Nuclear Instruments and Methods in Physics Research Section A: Accelerators, Spectrometers, Detectors and Associated Equipment* 869 (Oct. 2017), pp. 68–75. ISSN: 01689002. DOI: 10.1016/j.nima.2017.06.046. URL: https://linkinghub.elsevier.com/retrieve/pii/S016890021730699X.

[123] Z. Chen et al. “COMPARISON OF BNCT DOSIMETRY CALCULATIONS USING DIFFERENT GEANT4 PHYSICS LISTS”. In: *Radiation protection dosimetry* 187 (May 2019). DOI: 10.1093/rpd/ncz144.

[124] J. Dudouet et al. “Benchmarking GEANT4 nuclear models for hadron therapy with 95 MeV/nucleon carbon ions”. In: *Physical Review C* 89.5 (May 2014). arXiv: 1309.1544, p. 054616. ISSN: 0556-2813, 1089-490X. DOI: 10.1103/PhysRevC.89.054616. URL: http://arxiv.org/abs/1309.1544.

[125] A. Makarova, B. Gottschalk, and W. Sauerwein. “Comparison of Geant4 multiple Coulomb scattering models with theory for radiotherapy protons”. en. In: *Physics in Medicine & Biology* 62.15 (July 2017), pp. 5959–5974. ISSN: 1361-6560. DOI: 10.1088/1361-6560/aa6ce3. URL: https://iopscience.iop.org/article/10.1088/1361-6560/aa6ce3.

[126] M. Pinto et al. “Assessment of Geant4 Prompt-Gamma Emission Yields in the Context of Proton Therapy Monitoring”. In: *Frontiers in Oncology* 6 (Jan. 2016). DOI: 10.3389/fonc.2016.00010.

[127] J.-F. Carrier et al. “Validation of GEANT4, an object-oriented Monte Carlo toolkit, for simulations in medical physics”. In: *Medical physics* 31 (Apr. 2004), pp. 484–92. DOI: 10.1118/1.1644532.

[128] P. Cirrone et al. “Implementation of a new Monte Carlo-GEANT4 Simulation tool for the development of a proton therapy beam line and verification of the related dose distributions”. In: *Nuclear Science, IEEE Transactions on* 52 (Mar. 2005), pp. 262–265. DOI: 10.1109/TNS.2004.843140.

[129] B. A. Faddegon et al. “Benchmarking of Monte Carlo simulation of bremsstrahlung from thick targets at radiotherapy energies”. In: *Medical Physics* 35.10 (Oct. 2008), pp. 4308–4317. ISSN: 0094-2405. DOI: 10.1118/1.2975150. URL: https://www.ncbi.nlm.nih.gov/pmc/articles/PMC2736754/.

[130] T. T. Böhlen et al. “Benchmarking nuclear models of FLUKA and GEANT4 for carbon ion therapy”. en. In: *Physics in Medicine and Biology* 55.19 (Oct. 2010), pp. 5833–5847. ISSN: 0031-9155, 1361-6560. DOI: 10.1088/0031-9155/55/19/014. URL: https://iopscience.iop.org/article/10.1088/0031-9155/55/19/014.

[131] X. Xu and K. Eckerman. *Handbook of Anatomical Models for Radiation Dosimetry*. Sept. 2009. ISBN: 978-0-429-15024-1. DOI: 10.1201/EBK1420059793.

[132] P. Cirrone et al. “Hadrontherapy: a Geant4-Based Tool for Proton/Ion-Therapy Studies”. In: *Progress in Nuclear Science and Technology* 2 (Oct. 2011). DOI: 10.15669/pnst.2.207.

[133] A. Resch et al. “Evaluation of electromagnetic and nuclear scattering models in GATE /Geant4 for proton therapy”. In: *Medical Physics* 46 (Mar. 2019). DOI: 10.1002/mp.13472.

[134] C. Winterhalter et al. “Evaluation of GATE-RTion (GATE/Geant4) Monte Carlo simulation settings for proton pencil beam scanning quality assurance”. en. In: *Medical Physics* 47.11 (2020). _eprint: https://aapm.onlinelibrary.wiley.com/doi/pdf/10.1002/mp.14481, pp. 5817–5828. ISSN: 2473-4209. DOI: 10.1002/mp.14481. URL: https://aapm.onlinelibrary.wiley.com/doi/abs/10.1002/mp.14481.

[135] P. Arce et al. “Report on G4-Med, a Geant4 benchmarking system for medical physics applications developed by the Geant4 Medical Simulation Benchmarking Group”. eng. In: *Medical Physics* 48.1 (Jan. 2021), pp. 19–56. ISSN: 2473-4209. DOI: 10.1002/mp.14226.

[136] L. Grevillot et al. “Optimization of GEANT4 settings for Proton Pencil Beam Scanning simulations using GATE”. In: *Nuclear Instruments and Methods in Physics Research Section B: Beam Interactions with Materials and Atoms* 268 (Oct. 2010), pp. 3295–3305. DOI: 10.1016/j.nimb.2010.07.011.

[137] T. Bortfeld and W. Schlegel. “An analytical approximation of depth - dose distributions for therapeutic proton beams”. In: *Physics in Medicine and Biology* 41.8 (Aug. 1996), pp. 1331–1339. ISSN: 0031-9155, 1361-6560. DOI: 10.1088/0031-9155/41/8/006. URL: https://iopscience.iop.org/article/10.1088/0031-9155/41/8/006.

[138] P. Vaníček and D. Wells. “The Least Squares Approximation”. In: (Jan. 1972).

[139] *SciPy.org — SciPy.org*. URL: https://www.scipy.org/.

[140] F. A. Dilmanian, J. G. Eley, and S. Krishnan. “Minibeam Therapy With Protons and Light Ions: Physical Feasibility and Potential to Reduce Radiation Side Effects and to Facilitate Hypofractionation”. eng. In: *International journal of radiation oncology, biology, physics* 92.2 (2015). Place: United States Publisher: Elsevier Inc, Elsevier BV, pp. 469–474. ISSN: 0360-3016. DOI: 10.1016/j.ijrobp.2015.01.018.

[141] K. Sjobak and H. Holmestad. “MiniScatter, a Simple Geant4 Wrapper”. en. In: *Proceedings of the 10th Int. Particle Accelerator Conf.* IPAC2019 (2019). Artwork Size: 4 pages, 0.951 MB ISBN: 9783954502080 Medium: PDF Publisher: JACoW Publishing, Geneva, Switzerland, 4 pages, 0.951 MB. DOI: 10.18429/JACOW-IPAC2019-WEPTS025. URL: http://jacow.org/ipac2019/doi/JACoW-IPAC2019-WEPTS025.html.

[142] S. Vynckier, D. Bonnett, and D. Jones. “Supplement to the code of practice for clinical proton dosimetry”. en. In: *Radiotherapy and Oncology* 32.2 (Aug. 1994), pp. 174–179. ISSN: 01678140. DOI: 10.1016/0167-8140(94)90104-X. URL: https://linkinghub.elsevier.com/retrieve/pii/016781409490104X.

[143] F. Romano et al. “A Monte Carlo study for the calculation of the average linear energy transfer (LET) distributions for a clinical proton beam line and a radiobiological carbon ion beam

line". eng. In: *Physics in Medicine and Biology* 59.12 (June 2014), pp. 2863–2882. ISSN: 1361-6560. DOI: 10.1088/0031-9155/59/12/2863.

[144] T. Schneider et al. "Advancing proton minibeam radiation therapy: magnetically focussed proton minibeams at a clinical centre". en. In: *Scientific Reports* 10.1 (Jan. 2020). Number: 1 Publisher: Nature Publishing Group, p. 1384. ISSN: 2045-2322. DOI: 10.1038/s41598-020-58052-0. URL: https://www.nature.com/articles/s41598-020-58052-0.

[145] U. Schneider and R. Hälg. "The Impact of Neutrons in Clinical Proton Therapy". English. In: *Frontiers in Oncology* 5 (2015). Publisher: Frontiers. ISSN: 2234-943X. DOI: 10.3389/fonc.2015.00235. URL: https://www.frontiersin.org/articles/10.3389/fonc.2015.00235/full.

[146] J. B. Farr et al. "Development , commissioning , and evaluation of a new intensity modulated minibeam proton therapy system". In: (2018). Accepted: 2013. URL: https://dl.uswr.ac.ir/handle/Hannan/82058.

[147] A. Bozkurt. "Monte Carlo calculation of proton stopping power and ranges in water for therapeutic energies". en. In: *EPJ Web of Conferences* 154 (2017). Ed. by A. Aydin et al., p. 01007. ISSN: 2100-014X. DOI: 10.1051/epjconf/201715401007. URL: http://www.epj-conferences.org/10.1051/epjconf/201715401007.

[148] K. Kokurewicz et al. "Focused very high-energy electron beams as a novel radiotherapy modality for producing high-dose volumetric elements". en. In: *Scientific Reports* 9.1 (July 2019). Number: 1 Publisher: Nature Publishing Group, p. 10837. ISSN: 2045-2322. DOI: 10.1038/s41598-019-46630-w. URL: https://www.nature.com/articles/s41598-019-46630-w.

[149] K. Kokurewicz et al. "An experimental study of focused very high energy electron beams for radiotherapy". en. In: *Communications Physics* 4.1 (Dec. 2021), p. 33. ISSN: 2399-3650. DOI: 10.1038/s42005-021-00536-0. URL: http://www.nature.com/articles/s42005-021-00536-0.

[150] M.J. Berger et al. *Stopping-Power & Range Tables for Electrons, Protons, and Helium Ions*. en. text. Last Modified: 2019-11-15T20:46-05:00. Oct. 2009. URL: https://www.nist.gov/pml/stopping-power-range-tables-electrons-protons-and-helium-ions.

[151] V. Bellinzona et al. "On the parametrization of lateral dose profiles in proton radiation therapy". en. In: *Physica Medica* 31.5 (July 2015), pp. 484–492. ISSN: 11201797. DOI: 10.1016/j.ejmp.2015.05.004. URL: https://linkinghub.elsevier.com/retrieve/pii/S1120179715001143.

[152] *Danish Centre for Particle Therapy*. en-US. URL: https://www.en.auh.dk/departments/the-danish-centre-for-particle-therapy/.

[153] C. Skou Søndergaard. *Private communication*. June 2020.

[154] H. Fuse et al. "An isocenter detection and verification device for use in proton therapy". In: *The Review of Scientific Instruments* 83.12 (Dec. 2012), p. 125109. ISSN: 0034-6748. DOI: 10.1063/1.4771576. URL: https://www.ncbi.nlm.nih.gov/pmc/articles/PMC3537708/.

[155] *Scanditronix*. URL: https://www.scanditronix-magnet.se/.

[156] Y. R. Lawrence et al. "Radiation Dose–Volume Effects in the Brain". en. In: *International Journal of Radiation Oncology*Biology*Physics* 76.3 (Mar. 2010), S20–S27. ISSN: 03603016. DOI: 10.1016/j.ijrobp.2009.02.091. URL: https://linkinghub.elsevier.com/retrieve/pii/S0360301609032878.

[157] D. Maes et al. "Parametric characterization of penumbra reduction for aperture-collimated pencil beam scanning (PBS) proton therapy". en. In: *Biomedical Physics & Engineering Express* 5.3 (Mar. 2019), p. 035002. ISSN: 2057-1976. DOI: 10.1088/2057-1976/ab0953. URL: https://iopscience.iop.org/article/10.1088/2057-1976/ab0953.

[158] E. Pedroni et al. "Experimental characterization and physical modelling of the dose distribution of scanned proton pencil beams". In: *Physics in Medicine and Biology* 50.3 (Feb. 2005), pp. 541–561. ISSN: 0031-9155, 1361-6560. DOI: 10.1088/0031-9155/50/3/011. URL: https://iopscience.iop.org/article/10.1088/0031-9155/50/3/011.

[159] F. A. Dilmanian et al. "Charged Particle Therapy with Mini-Segmented Beams". In: *Frontiers in Oncology* 5 (Dec. 2015). ISSN: 2234-943X. DOI: 10.3389/fonc.2015.00269. URL: http://journal.frontiersin.org/article/10.3389/fonc.2015.00269.

[160] C.-W. Chang et al. "A standardized commissioning framework of Monte Carlo dose calculation algorithms for proton pencil beam scanning treatment planning systems". en. In: *Medical Physics* 47.4 (Apr. 2020), pp. 1545–1557. ISSN: 0094-2405, 2473-4209. DOI: 10.1002/mp.14021. URL: https://onlinelibrary.wiley.com/doi/10.1002/mp.14021.

[161] L. Kastrati, G. Nafezi, and G. Shehi. "THE PENUMBRA OF IRRADIATIONS IN LINEAR ACCELERATORS, ITS USE IN RADIOTHERAPY OF CANCER DISEASES, NEGATIVE EFFECTS, AND THE POSSIBILITIES OF REDUCING THEM". en. In: *RAD Conference Proceedings*. RAD Association, 2016. DOI: 10.21175/RadProc.2016.26. URL: http://www.rad-proceedings.org/paper.php?id=42.

[162] B. Emami et al. "Tolerance of normal tissue to therapeutic irradiation". en. In: *International Journal of Radiation Oncology*Biology*Physics* 21.1 (May 1991), pp. 109–122. ISSN: 03603016. DOI: 10.1016/0360-3016(91)90171-Y. URL: https://linkinghub.elsevier.com/retrieve/pii/036030169190171Y.

[163] J. Grimm et al. “Dose tolerance limits and dose volume histogram evaluation for stereotactic body radiotherapy”. en. In: *Journal of Applied Clinical Medical Physics* 12.2 (Mar. 2011), pp. 267–292. ISSN: 15269914. DOI: 10.1120/jacmp.v12i2.3368. URL: http://doi.wiley.com/10.1120/jacmp.v12i2.3368.

[164] T. M et al. “Experimental validation of the TOPAS Monte Carlo system for passive scattering proton therapy.” English. In: *Medical Physics* 40.12 (Dec. 2013), pp. 121719–121719. ISSN: 0094-2405, 2473-4209. DOI: 10.1118/1.4828781. URL: http://europepmc.org/article/PMC/4109425.

[165] Y. Kase et al. “Microdosimetric calculation of relative biological effectiveness for design of therapeutic proton beams†”. In: *Journal of Radiation Research* 54.3 (May 2013), pp. 485–493. ISSN: 0449-3060. DOI: 10.1093/jrr/rrs110. URL: https://www.ncbi.nlm.nih.gov/pmc/articles/PMC3650736/.

[166] C. Peucelle et al. “Proton minibeam radiation therapy: Experimental dosimetry evaluation”. en. In: *Medical Physics* 42.12 (2015), pp. 7108–7113. ISSN: 2473-4209. DOI: 10.1118/1.4935868. URL: https://aapm.onlinelibrary.wiley.com/doi/abs/10.1118/1.4935868.

[167] M. Gao et al. “Spatially Fractionated (GRID) Radiation Therapy using Proton Pencil Beam Scanning (PBS): Feasibility Study and Clinical Implementation”. In: *Medical Physics* 45 (Feb. 2018). DOI: 10.1002/mp.12807.

[168] Y. Prezado and G. R. Fois. “Proton-minibeam radiation therapy: A proof of concept”. English. In: *Medical Physics* 40.3 (Mar. 2013). ISSN: 0094-2405. DOI: 10.1118/1.4791648. URL: https://www.osti.gov/biblio/22130553-proton-minibeam-radiation-therapy-proof-concept.

[169] Y. Prezado et al. “X-ray energy optimization in minibeam radiation therapy”. en. In: *Medical Physics* 36.11 (2009), pp. 4897–4902. ISSN: 2473-4209. DOI: 10.1118/1.3232000. URL: https://aapm.onlinelibrary.wiley.com/doi/abs/10.1118/1.3232000.

[170] L. De Marzi et al. “Implementation of planar proton minibeam radiation therapy using a pencil beam scanning system: A proof of concept study”. en. In: *Medical Physics* 45.11 (Nov. 2018), pp. 5305–5316. ISSN: 0094-2405, 2473-4209. DOI: 10.1002/mp.13209. URL: https://onlinelibrary.wiley.com/doi/abs/10.1002/mp.13209.

[171] M. Mohiuddin et al. “High-dose spatially-fractionated radiation (GRID): a new paradigm in the management of advanced cancers”. en. In: *International Journal of Radiation Oncology*Biology*Physics* 45.3 (Oct. 1999), pp. 721–727. ISSN: 03603016. DOI: 10.1016/S0360-3016(99)00170-4. URL: https://linkinghub.elsevier.com/retrieve/pii/S0360301699001704.

[172] M. Mohiuddin et al. “High-Dose Radiation as a Dramatic, Immunological Primer in Locally Advanced Melanoma”. In: *Cureus* 7.12 (Dec. 2015), e417. ISSN: 2168-8184. DOI: 10.7759/cureus.417. URL: https://www.ncbi.nlm.nih.gov/pmc/articles/PMC4725734/.

[173] S. Girst et al. “Proton Minibeam Radiation Therapy Reduces Side Effects in an In Vivo Mouse Ear Model”. en. In: *International Journal of Radiation Oncology*Biology*Physics*. Particle Therapy Special Edition 95.1 (May 2016), pp. 234–241. ISSN: 0360-3016. DOI: 10.1016/j.ijrobp.2015.10.020. URL: https://www.sciencedirect.com/science/article/pii/S0360301615265856.

[174] C. Shang-Wen et al. “The Implication of Geometrical Sparing Factor of Reference Points for Late Complications Following Uniform External Radiotherapy and High-Dose-Rate Brachytherapy for Cervical Cancer”. In: *The Journal of JASTRO* 17.1 (Mar. 2005), pp. 17–24. ISSN: 10409564. URL: https://ci.nii.ac.jp/naid/10027060494.

[175] C. G. Orton. *Fractionation: Radiobiological Principles and Clinical Practice*. en-US. Oct. 2016. URL: https://oncohemakey.com/fractionation-radiobiological-principles-and-clinical-practice/.

[176] D. Möhl. “Sources of emittance growth - CERN Document Server”. In: (Apr. 2009). URL: http://cds.cern.ch/record/941314/files/.

[177] A. S. Müller. *Description of Beam-Matter Interaction in the Covariance Matrix Formalism : Application to Modification of Emittance and Twiss Parameters*. en. Number: CERN-PS-2001-013-AE. May 2001. URL: https://cds.cern.ch/record/499590.